Field precision pesticide application technology and ground intelligent sprayer

Edited by
Wei Qiu, Yan Gong and Ramón Salcedo

About Frontiers

Frontiers is more than just an open access publisher of scholarly articles: it is a pioneering approach to the world of academia, radically improving the way scholarly research is managed. The grand vision of Frontiers is a world where all people have an equal opportunity to seek, share and generate knowledge. Frontiers provides immediate and permanent online open access to all its publications, but this alone is not enough to realize our grand goals.

Frontiers journal series

The Frontiers journal series is a multi-tier and interdisciplinary set of open-access, online journals, promising a paradigm shift from the current review, selection and dissemination processes in academic publishing. All Frontiers journals are driven by researchers for researchers; therefore, they constitute a service to the scholarly community. At the same time, the *Frontiers journal series* operates on a revolutionary invention, the tiered publishing system, initially addressing specific communities of scholars, and gradually climbing up to broader public understanding, thus serving the interests of the lay society, too.

Dedication to quality

Each Frontiers article is a landmark of the highest quality, thanks to genuinely collaborative interactions between authors and review editors, who include some of the world's best academicians. Research must be certified by peers before entering a stream of knowledge that may eventually reach the public – and shape society; therefore, Frontiers only applies the most rigorous and unbiased reviews. Frontiers revolutionizes research publishing by freely delivering the most outstanding research, evaluated with no bias from both the academic and social point of view. By applying the most advanced information technologies, Frontiers is catapulting scholarly publishing into a new generation.

What are Frontiers Research Topics?

Frontiers Research Topics are very popular trademarks of the *Frontiers journals series*: they are collections of at least ten articles, all centered on a particular subject. With their unique mix of varied contributions from Original Research to Review Articles, Frontiers Research Topics unify the most influential researchers, the latest key findings and historical advances in a hot research area.

Find out more on how to host your own Frontiers Research Topic or contribute to one as an author by contacting the Frontiers editorial office: frontiersin.org/about/contact

Field precision pesticide application technology and ground intelligent sprayer

Topic editors

Wei Qiu — Nanjing Agricultural University, China
Yan Gong — Chinese Academy of Agricultural Sciences (CAAS), China
Ramón Salcedo — Universitat Politecnica de Catalunya, Spain

Citation

Qiu, W., Gong, Y., Salcedo, R., eds. (2024). *Field precision pesticide application technology and ground intelligent sprayer*. Lausanne: Frontiers Media SA. doi: 10.3389/978-2-8325-4641-3

Table of
contents

Computational model of pesticide deposition distribution on canopies for air-assisted spraying

Hanjie Dou[1], Qi Li[2], Changyuan Zhai[3]*, Shuo Yang[1], Chunjiang Zhao[1,2]*, Yuanyuan Gao[2] and Yakai He[4]

[1]National Engineering Research Center for Information Technology in Agriculture, Beijing, China, [2]College of Agricultural Engineering, Jiangsu University, Zhenjiang, China, [3]Intelligent Equipment Research Center, Beijing Academy of Agriculture and Forestry Sciences, Beijing, China, [4]Institute of New Materials Technology & Equipment, Chinese Academy of Agricultural Mechanization Sciences Group Co., Ltd, Beijing, China

The deposited pesticide distribution in fruit tree canopies is crucial for evaluating the efficacy of air-assisted spraying in orchards. Most studies have determined the impact of pesticide application on pesticide deposition on canopies without a quantitative computational model. In this study, an air-assisted orchard sprayer with airflow control was used to perform spraying experiments on artificial and peach trees. In the spraying experiment on an artificial tree, a canopy with leaf areas ranging from 2.54~5.08 m^2 was found to require an effective air speed of 18.12~37.05 m/s. The canopy leaf area, air speed at the sprayer fan outlet and spray distance were used as test factors in a three-factor five-level quadratic general rotational orthogonal test to develop a computational model for pesticide deposition at the inner, outer and middle regions of a fruit tree canopy with R^2 values of 0.9042, 0.8575 and 0.8199, respectively. A significance analysis was used to rank the influencing factors for the deposited pesticide distribution in decreasing order of significance as follows: the spray distance, leaf area and air speed for the inner region of the canopy, followed by the spray distance, air speed and leaf area for the middle and outer regions of the canopy. The results of the verification test conducted in a peach orchard showed that the computational errors of the pesticide deposition model for the inner, middle and outer regions of the canopy were 32.62%, 22.38% and 23.26%, respectively. The results provide support for evaluating the efficacy of an air-assisted orchard sprayer and optimizing the sprayer parameters.

KEYWORDS

crop protection, air-assisted spraying, canopy, pesticide deposition, computational model

1 Introduction

Chemical pesticides play a dominant role in pest control for fruit trees. Pesticides are applied on fruit trees approximately 8-15 times a year, which contributes approximately 30% to the total workload (Van de Zande et al., 2008; Dekeyser et al., 2014). Air-assisted sprayers are widely used for orchard protection because using an airflow to transport droplets enhances pesticide penetration and adhesion to leaves (He, 2020; Zheng et al., 2020). The use of a high air speed for air-assisted spray application induces pesticide drift, whereas using an airflow that is too small to penetrate the canopy affects the efficacy of pest control (Zhai et al., 2018). Pesticide deposition on fruit tree canopies is key for evaluating the efficacy of air-assisted sprayers. Establishing a rule and a computational model for pesticide deposition on a canopy are very important for improving the efficacy of orchard air-assisted sprayers and optimizing the sprayer operation parameters (Teske et al., 2011).

Scholars in China and around the world have carried out many studies to determine how the deposited pesticide distribution in fruit tree canopies is affected by the pesticide application operation parameters (the spraying speed, fan speed, spray distance, spray pressure, nozzle flow rate, etc.). Jadav et al. (2019) studied the impact of different operation parameters for pesticide spraying on the deposited pesticide distribution in canopies. The spraying speed was found to significantly affect the deposited pesticide distribution. Jiang et al. (2016) combined air-assisted pesticide application and Internet of Things (IoT) technologies to perform a comparative test on sprayers with and without an air-assisted spraying function. Higher pesticide deposition was found using air-assisted spraying than without air-assisted spraying and saved over 30% of the pesticide used. Qiu et al. (2016) studied the impact of different fan speeds on pesticide deposition for pear trees. Fan speed was found to significantly affect pesticide deposition, although fan speeds exceeding 1,300 r/min reduced the deposition rate and coverage. Gu et al. (2020) studied the influence of spraying parameters, such as the fan speed and spray distance, on the deposited pesticide distribution in a kiwi fruit orchard using the orthogonal test method and established a regression equation to optimize and verify the parameters. Ding et al. (2020) studied the impact of spraying parameters, such as air speed, on pesticide deposition to provide a data reference for field spraying operations. Hong et al. (2018) conducted a computational fluid dynamics (CFD) simulation on the airflow inside a canopy and found that air speeds above a well-defined range reduced the quantity of pesticide deposited on the canopy. Duga et al. (2015) reported that the airflow distribution of a sprayer can affect pesticide deposition in the vertical section of the canopy and that canopy characteristics, such as leaf area and volume, significantly impact pesticide deposition. Sun and Liu (2019) studied a variety of fruit trees to establish a mathematical model for the second exponential of the droplet penetration ratio based on the leaf area density, canopy sampling depth and air speed. The sampling depth was found to have the most significant impact on droplet penetration into the canopy. Zhu et al. (2022) and Zhai et al.

(2021) employed a porous media model, and Duga et al. (2017) and Zhang et al. (2022) used a simplified equivalent porous media model to study the influence of canopy shape and leaf area density on the airflow field. The complex process of transporting droplets by airflow was simulated, and the effect of the airflow on the pesticide droplet distribution in the canopy was determined.

Studies have shown that the effective deposition of droplets inside the canopy can be improved by changing the spraying parameters according to the characteristics of the fruit tree canopy. The deposition of droplets involves the complex motion of trajectory spreading on the surface of branches and leaves through the canopy gap. It is difficult to determine the penetration law and pesticide deposition distribution characteristics for different areas of a target canopy (Endalew et al., 2010; Otto et al., 2018; Liu et al., 2021). A current challenging research problem is how to quantify pesticide deposition on different canopy areas based on the droplet deposition law for the canopy. Li et al. (2020) studied the impact of the spray distance, air speed at the air outlet of the sprayer fan and droplet size on pesticide deposition on the leaf surface and established a prediction model for the deposition state of droplets on the leaf surface. Farooq et al. (2001) established a simulation model to predict pesticide deposition on a fruit tree canopy. Shani (2020) used dimensional analysis to evaluate the influence of spraying parameters on the weight of pesticides deposited on a canopy and established a mathematical model to predict the weight of deposited pesticides. Shani (2021) subsequently analyzed the relationship between the spraying operation parameters and pesticide deposition for a fruit tree canopy and established a computational model for pesticide deposition under different operating conditions. This model was theoretically derived, and its applicability must be verified by orchard tests.

The objective of this study was to establish a computational model for pesticide deposition on different canopy areas considering the main influencing factors for pesticide deposition (canopy leaf area, air speed at the air outlet of the fan and spray distance). The impact of the main influencing factors on pesticide deposition in the inner, middle and outer regions of the canopy was determined. Thus, the results provide support for evaluating the efficacy of an orchard air-assisted sprayer and optimizing the sprayer performance parameters.

2 Materials and methods

2.1 Orchard air-assisted sprayer with airflow control

Figure 1 shows the orchard air-assisted sprayer with airflow control that was used to perform tests in this study. The fan speed and areas of the air inlet and outlet of the sprayer could be independently regulated. The main components of the sprayer are a crawler base, a control system, light detection and ranging system (LiDAR), a nozzle, a fan, louvers and slide rails. LiDAR obtains information on the fruit tree canopy characteristics (the position,
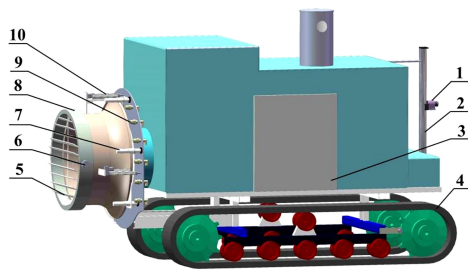
FIGURE 1
Structure chart for the complete crawler-type air-assisted sprayer.
1. LiDAR 2. Screw rod module 3. Control system 4. Crawler base
5. Louvers 6. Stepping motor 7. Slide rail 8. Fan 9. Nozzle 10. Electric
drive pusher.

canopy volume, leaf area, etc.) in real time. The fan is driven by an AC motor, and its speed can be adjusted in the range of 0–2923 r/min. The louvers are installed at the air inlet through an expansion cylinder, and the area of the air inlet can be adjusted by controlling the angle of the louvers using a stepping motor. The fan cylinder is connected to the back panel through an electric drive pusher, which can be moved to adjust the area and thereby the opening of the air outlet.

The effect of the air speed at the fan outlet on the deposition and distribution laws of droplets in different regions of a fruit tree canopy was determined. Air speed was regulated by adjusting the frequency of the fan's drive motor inverter. Because the nozzles at the fan outlet were positioned at equal intervals, one air speed measurement point was set at each nozzle position of the fan outlet. A soft blue ribbon of a certain length was tied to each nozzle position to determine the airflow direction at that position, which was used to document the direction of the air speed sensor (8455-300, TSI Company, USA) to rapidly measure the air speed at each nozzle position. The average value of air speed of each nozzle position was taken as the air speed at the fan outlet. The relationship between the inverter frequency and the air speed at the fan outlet was shown in Figure 2. There was a good linear relationship between the inverter frequency and the air speed, which was used to calculate the air speed at the fan outlet under different inverter frequencies.

2.2 Artificial tree canopy

An artificial tree canopy was used to simulate changes in fruit tree canopies in different growth periods. The artificial tree had a height of 2.0 m, a crown width of 1.6 m and a canopy height of 1.2 m. The canopy density was changed by manually picking and attaching leaves based on leaf changes of peach canopy at different growth stages obtained by pre-experiment. The artificial tree consisted of 4583 large leaves and 913 small leaves, based on leaf statistics. An instrument for measuring the leaf area (Shandong Fangke Instrument Co., Ltd., YMJ-G) was used to scan 10 groups of leaves. The average leaf areas for large and small leaves were 19.21 cm^2 and 14.79 cm^2, respectively. Specific numbers of leaves were then picked and arranged to create a canopy with different leaf areas, as shown in Figure 3.

2.3 Tests to determine the required air speed range for the artificial tree canopy

The range of required air speed for air-assisted spraying on canopies with different leaf areas was determined using spraying tests that were designed according to the national standards of China, i.e., GB/T 3244-2015 Crop Protection Equipment - Field Measurement of Spray Distribution in Tree and Bush Crops (Yan et al., 2015). The tests were carried out by placing water-sensitive papers (size: 2.5 × 5 cm) on the front and back sides of the leaf along the plane of the tree trunk center on the sprayed side of the artificial tree canopy to evaluate droplet deposition under different air speeds. The layout of the papers is shown in Figure 4A. During the test, the spray pressure was set to 1.0 MPa, and the inverter frequency was adjusted to set the air speed to 12.76 m/s, 17.58 m/s, 22.74 m/s, 28.42 m/s, 33.93 m/s, 37.38 m/s and 41.03 m/s. A remote-controlled sprayer was used to spray a solution at 1.0 m/s along the spray center 3.0 m from the tree trunk. After the droplets on the water-sensitive papers dried, the papers were placed in a bag, which was labelled according to the number of papers and taken to the laboratory for analysis.

2.4 Tests for droplet deposition on an artificial-tree canopy

The following test factors were used: leaf area, air speed for fan outlet and spray distance. The quantities of pesticide deposited at the inner, middle and outer positions of the artificial tree canopy were used as the response values. A three-factor five-level quadratic general rotational orthogonal test was designed using Design-Expert 8.06 software (Xu and He, 2010). Table 1 shows the factor coding. The canopy leaf area and the air speed were determined using the test procedure described in Sections 2.2 and 2.3. The planting pattern of orchards in China was used to determine the
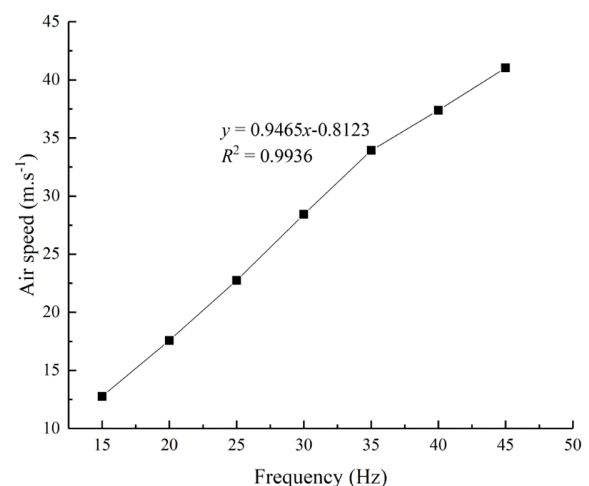
FIGURE 2
Relationship between the inverter frequency and the air speed at the fan outlet. In the equation, *x* represents the inverter frequency, Hz, and *y* denotes the air speed at the air outlet of the fan, m/s.

FIGURE 3
An artificial canopy with different leaf areas. (1) leaf area = 5.08 m^2, (2) leaf area = 4.57 m^2, (3) leaf area = 3.81 m^2, (4) leaf area = 3.05 m^2, (5) leaf area = 2.54 m^2.

spray distance from the tree trunk to the sprayer center as 1.5 to 3.0 m, and the value of γ was 1.682. The γ stands for asterisk arm.

The test was conducted at the National Precision Agriculture Research and Demonstration Base in Xiaotangshan, Changping District, Beijing, China. The droplet pesticide depositions for different test combinations were obtained by arranging filter papers for sampling (9 cm in diameter, Special Paper Co., Ltd., Hangzhou, China) at different positions in the fruit tree canopy. The layout of the filter papers is shown in Figure 4A.

A tracer (rhodamine B, Tianjin Kemiou Chemical Reagent Co., Ltd.) was used instead of a pesticide in the test. The spray pressure was set to 1.0 MPa. We used the specifications in Table 1 to regulate the air speed, vary the leaf area of the artificial tree canopy, and remotely control the distance of the sprayer to achieve a spray velocity of 1.0 m/s, as shown in Figure 5. During the test, a self-developed small field weather station was used to monitor the ambient temperature, humidity, wind velocity and wind direction in real time. For a southeast wind, the average ambient temperature, relative humidity and wind velocity were 21.71°C, 45.95% and 0.70 m/s, respectively. The test results showed that a small quantity of pesticide was deposited on the nonsprayed side of the fruit tree canopy. Deposition on the nonsprayed side of the canopy was neglected in calculating the quantity of pesticide deposited on different regions of the sprayed canopy side.

2.5 Orchard tests

The established computational model for pesticide deposition on a canopy was validated by conducting a spraying test in a peach orchard at the National Precision Agriculture Research and Demonstration Base in Xiaotangshan, Changping District, Beijing, China. The test was performed on 5-year-old peach trees, Ruiguang No. 8, with a row spacing of 4.5 m and a tree spacing of 5.0 m. Point cloud data for the canopy were obtained with LiDAR placed in front of the sprayer. The canopy volume was determined to be 5.39 m^3 using a detection method that was previously developed by the research team (Gu et al., 2021). The method used to calculate the canopy leaf area of the artificial tree was used to compile statistics to determine the number of leaves in the fruit tree canopy. A preliminary test was carried out to statistically analyze canopy leaf changes, and the statistical results show that the area of a single leaf was divided by 25 cm^2 into large leaves and small leaves, and the distribution proportion of the two types of leaves in the canopy was close to the same, which was used to classify large leaves and small leaves in orchard test. We randomly picked leaves and used the statistical method to determine the leaves areas. We scanned the leaves with the instrument for measuring the leaf area and determined the average areas of the leaves to be 36.44 cm^2 and 21.59 cm^2 for large leaves and small leaves, and the number

FIGURE 4
Layout of sampling points and test. **(A)** Sampling layout. **(B)** Spraying test. X = spray direction, Y = sprayer travel direction, and Z = tree height.

TABLE 1 Factor coding table.

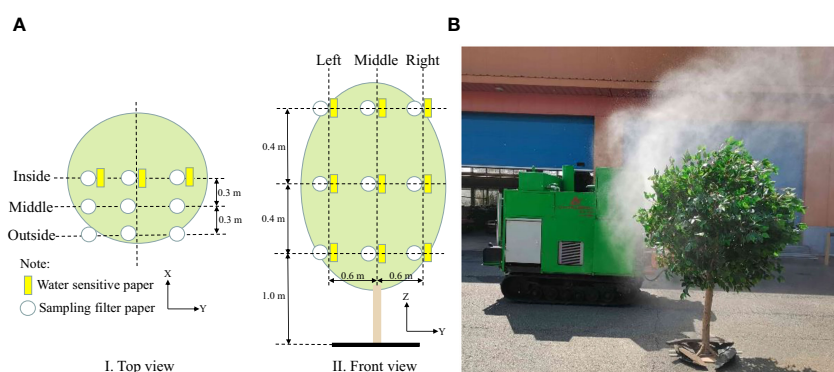| Factor level	Leaf area (m²)	Air speed (m·s⁻¹)	Spray distance (m)
Zero level (z_0)	3.81	27.59	2.25
Radius variation (△)	0.76	5.62	0.45
-γ	2.54	18.12	1.50
-1	3.05	21.96	1.80
0	3.81	27.59	2.25
1	4.57	33.21	2.70
γ	5.08	37.05	3.00

of large leaves and small leaves were 914 and 782, respectively. The canopy leaf area was 5.02 m². We used the test results for the artificial tree canopy to design a spraying test for the orchard. The test combinations are shown in Table 2.

The method described in Section 2.4 was used to arrange filter papers for sampling the peach tree canopy, as shown in Figure 6. A rhodamine tracer was used instead of a pesticide. The spray pressure was set to 1.0 MPa. The fan speed was set according to the air speed values given in Table 2. We drove the sprayer to achieve a 1.0 m/s spray from east to west and collected the filter papers in a marked opaque white plastic box. Upon completion of the test, the collected filter papers were taken to the laboratory for data analysis. For a southeast wind, the average ambient temperature, relative humidity and wind velocity were 20.85°C, 48.03% and 0.74 m/s, respectively.

2.6 Test data analysis

The water-sensitive papers were scanned using a TSN450 scanner developed by ShenZhen Tiancai Electronic Co., Ltd. to obtain greyscale images. These images were analyzed using droplet deposition analysis software developed by Chongqing Liuliu Shanxia Co., Ltd. to determine changes in the droplet coverage and deposition point density at different air speeds. A fluorometer

FIGURE 5
Pesticide deposition test for a fruit tree canopy.

(Turner Designs, Inc., San Jose, Cal) was employed to measure the content of the rhodamine solution on the filter papers used for sampling, as shown in Figure 7. Each filter paper was placed in a beaker, and distilled water was added to the beaker up to a volume of 80 mL. The filter paper was allowed to soak in the water for 10 min and removed from the beaker. A portion of the solution was transferred to a cuvette, which was placed in a fluorometer to measure the content of the rhodamine solution. Each sample was measured three times, and the average value is reported as the final measured value.

The measured content of the rhodamine solution on the filter paper was used in Equation (1) to calculate the quantity of pesticide deposited per unit area of the filter paper at different positions in the canopy (Dou et al., 2021).

$$Deposition = \frac{C_{paper} \times V}{C_{tank} \times S_{paper} \times R} \tag{1}$$

where $Deposition$ is the quantity of the tracer agent deposited on the filter paper, mL/m²; C_{paper} is the concentration of the rhodamine solution on the filter paper, mg/mL; V is the volume of distilled water used for washing, mL; C_{tank} is the concentration of the mother solution, mg/mL; S_{paper} is the area of the filter paper, m²; and R is the recovery rate of the solution, which was measured to be 87.29%.

The single filter paper at each sampling point covered a circular area with a diameter of 9 cm. To calculate the spray deposition quantity at different canopy regions, a rectangular area surrounding each filter paper was outlined. The quantities of spray deposition in the rectangular area were the product of the quantities of pesticide deposition on each filter paper and the area of the rectangle, and the total quantities of spray deposition in all the rectangles was considered the quantities of pesticide deposited at current canopy area. The quantities of pesticide deposited at the inner, middle and outer positions of the canopy was calculated using Equation (2).

$$Deposition_{Canopy} = \frac{\sum_{i=1,j=1} Deposition_{ij} c_{ij}}{S_i} \tag{2}$$

Where $Deposition_{Canopy}$ is the quantities of pesticide deposited at the inner, middle and outer positions of the canopy, mL/m²; $Deposition_{ij}$ is the quantity of the tracer agent deposited on the filter

TABLE 2 Parameters used for the orchard spraying test.

Test No.	Leaf area (m^2)	Air speed (m·s^{-1})	Spray distance (m)
1		38.94	3.00
2		35.15	3.00
3	5.02	33.26	2.70
4		37.05	2.70
5		32.62	2.25

paper for the j sampling point in the i region, mL/m^2; c_{ij} is the area of the rectangle for the j sampling point in the i region, m^2; S_i is the canopy section area, m^2; i is 1, 2 and 3 for the inner, middle and outer positions of the canopy, respectively; j is the number of sampling points at different canopy regions.

3 Test results and analysis

3.1 Tests to determine the required air speed range for the artificial tree canopy

The data obtained using the water-sensitive paper were used to determine changes in droplet coverage and deposition point density for different air speeds, as shown in Figure 8.

Figure 8 shows that the spray coverage on the front and back sides of the canopy leaf changes as the air speed increases. At an air speed of 13.39 m/s, there is low coverage on the back of the leaf, and the deposit density is less than 20 deposits/cm^2. The number of droplets deposited on a crop must exceed 20 deposits/cm^2 during the spraying process for effective pest control (Salcedo et al., 2020). Therefore, the air speed should be maintained above 13.39 m/s during the testing process. By comparison, at an air speed of 37.05 m/s, there is comparable coverage on the front and back sides of a tree leaf, and the mist spray is uniform. Increasing the air speed further results in a significant difference in droplet coverage on the front and back sides of the leaf and deteriorates the uniformity of

FIGURE 6
Orchard spraying test.

the mist spray, because the droplet size increases with the air speed. However, the adhesiveness of a droplet to the leaf surface decreases beyond a well-defined range of drop sizes. In summary, an air speed range of 18.12–37.05 m/s is required for canopy leaf areas between 2.54 m^2 and 5.08 m^2.

3.2 Test for droplet deposition on an artificial tree canopy

3.2.1 Computational model for pesticide deposition in different canopy regions

We used the analysis method for the test data described in Section 2.6 to calculate the quantity of pesticide deposited on different canopy regions for different test combinations. The results are shown in Table 3.

Design-Expert 8.06 software was used to determine the regression equation, regression coefficient and lack-of-fit for the regression model. The variance analysis results are shown in Table 4. The overall P values of the computational model for the inner, middle and outer regions of the canopy are 0.0092, 0.0032 and 0.0005, respectively, which are less than 0.05, indicating that the regression models relating the test factors (A, B and C) to the response variables (Y_1, Y_2 and Y_3) are significant. The P values for the lack-of-fit of the model for the inner, middle and outer regions of the canopy are 0.7401, 0.2943 and 0.2065, respectively, which are all greater than 0.05, indicating that the lack-of-fit values are not significant, the lack-of-fit error between the model equation and the fit to the data is small, and the regression model effectively fits the experimental data. The signal-to-noise ratios (SNRs) for the measurements of the model accuracy for the inner, middle and outer regions of the canopy are 9.354, 7.917 and 12.907, respectively. These ratios are all greater than 4, indicating that the model has high reliability. A regression analysis was used to obtain Equations (3)-(5) for the quantities of spray deposited per unit area (mL/m^2) in the inner, middle and outer regions of the canopy (denoted by $Desposition_{Inner}$, $Desposition_{Middle}$ and $Desposition_{Outer}$, respectively) in terms of the canopy leaf area (A, m^2), air speed (B, m/s) and spray distance (C, m). The R^2 values of Equations (3), (4) and (5) are 0.8199, 0.8575 and 0.9042, respectively.

$$Deposition_{Inner} = 7.73 + 12.36A - 0.04B - 13.26C + 0.07A \cdot B$$

$$- 1.90A \cdot C + 0.58B \cdot C - 1.36A^2 - 0.03B^2$$

$$+ 0.20C^2 \qquad (3)$$

FIGURE 7
Measurement of the rhodamine solution content on the filter papers used for sampling. **(A)** Collection container. **(B)** Cuvette. **(C)** Fluorometer.

$Deposition_{Middle}$

$$= 44.49 + 19.98A - 2.60B - 18.49C + 0.07A \cdot B - 1.42A \cdot C$$

$$+ 0.36B \cdot C - 2.39A^2 + 0.02B^2 + 1.55C^2 \qquad (4)$$

$$Deposition_{Outer} = 18.04 + 23.60A - 1.37B - 7.92C - 0.14AB$$

$$- 5.03AC + 0.47BC - 1.26A^2 + 7.91$$

$$\times 10^{-3}B^2 + 1.40C^2 \qquad (5)$$

3.2.2 Analysis of normal plot of residuals

The accuracy of the regression model was further analyzed by using Design-Expert 8.06 to generate a normal plot of residuals for the regression model and the corresponding relation between the values predicted by the regression model and the actual values. The results are shown in Figure 9. Figure 9A shows that 95% of the residuals are distributed within the standard range around a straight line, indicating a normal error distribution. Figure 9B shows that the model predictions and actual values are consistent and follow good linear distributions. In summary, the normal distribution of the regression model and the standard prediction of errors can be used to calculate the quantity of pesticide deposited on the fruit-free canopy.

3.2.3 Response surface analysis

Figure 10 shows the response surface for the regression equation to analyze the influence of the interaction of any two factors of A, B and C on Y_1, Y_2 and Y_3.

Figure 10.A.I shows that for C = 2.25 m, increasing A and B causes Y_1 to first increase and then decrease. When A is between 3.65 and 3.96 m^2 and B is between 25.30 and 27.25 m/s, the response surface exhibits a peak, that is, Y_1 reaches a maximum. Figure 10.A.II shows that for B = 27.59 m/s, increasing A and C causes Y_1 to decrease: when A is below 3.65 m^2, Y_1 declines slowly with increasing C, whereas when A is above 3.65 m^2, Y_1 rapidly decreases with increasing C; at C = 1.8 m, increasing A causes Y_1 to first increase to a maximum at A = 3.96 m^2 and then decrease; at C = 2.7 m, Y_1 gradually decreases with increasing A. Figure 10.A.III shows that at B = 21.96 m/s, Y_1 decreases rapidly with increasing C, whereas at B = 33.21 m/s, Y_1 remains nearly unchanged as C changes; at C = 1.8 m, Y_1 decreases slowly with increasing B; and at C = 2.7 m, Y_1 grows slowly with increasing B.

Figure 10.B.I shows that Y_2 decreases noticeably with increasing B for small A values; with increasing A, Y_2 increases up to A = 3.96 m^2 and then decreases. Figure 10.B.II shows that Y_2 decreases with increasing C. For large A, Y_2 changes significantly with increasing A; that is, Y_2 first increases slowly and then decreases. Y_2 reaches a maximum at the smallest value of C and when A is within the range of 3.96-4.26 m^2. Figure 10.B.III shows that Y_2 decreases with increasing B and C, where Y_2 changes significantly with C: these
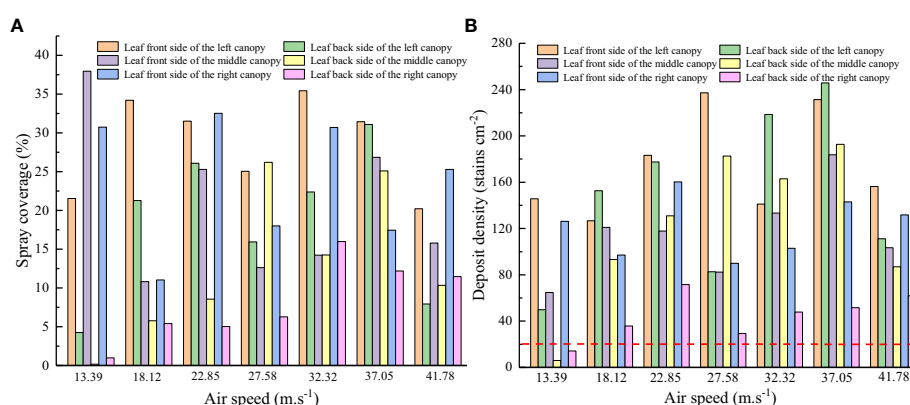

FIGURE 8
Changes in spray coverage and deposit density for different air speeds. **(A)** Spray coverage. **(B)** Deposit density.

TABLE 3 Test data for pesticide deposition on a canopy for different test combinations.

Test No.	Factors			Responses		
	A (m^2)	B (m·s^{-1})	C (m)	Y_1 (mL.m^{-2})	Y_2 (mL·m^{-2})	Y_3 (mL·m^{-2})
1	4.57	33.21	2.70	6.80	9.96	9.67
2	4.57	33.21	1.80	9.56	18.75	20.89
3	4.57	21.96	2.70	5.48	11.91	15.65
5	3.05	33.21	2.70	9.18	10.37	17.17
6	3.05	33.21	1.80	7.29	14.25	17.69
7	3.05	21.96	2.70	6.91	10.60	16.96
8	3.05	21.96	1.80	12.98	21.10	26.12
9	2.54	27.59	2.25	9.16	10.75	18.83
10	5.08	27.59	2.25	7.95	11.33	14.82
11	3.81	18.12	2.25	7.54	20.29	22.27
12	3.81	37.05	2.25	8.94	13.41	16.85
13	3.81	27.59	1.50	13.36	18.86	23.97
14	3.81	27.59	3.00	8.38	12.70	15.33
15	3.81	27.59	2.25	8.83	13.71	17.55
16	3.81	27.59	2.25	10.02	13.90	18.18
17	3.81	27.59	2.25	10.74	16.16	19.97
18	3.81	27.59	2.25	11.39	16.75	19.19
19	3.81	27.59	2.25	12.91	16.72	21.27
20	3.81	27.59	2.25	9.36	13.04	18.14

In the table, A represents the canopy leaf area; B represents the air speed; C represents the spray distance; and Y_1, Y_2 and Y_3 represent the quantities of pesticide deposited at the inner, middle and outer positions of the canopy, respectively.

results are consistent with those presented in Table 4. This result shows that C has a significant impact on Y_2.

Figure 10.C.I shows that Y_3 declines with increasing A and B, where Y_3 changes more significantly with increasing B than with increasing A, which indicates that changes in B impact Y_3 more significantly than changes in A. Figure 10.C.II shows that with increasing C, Y_3 decreases slowly up to A = 3.65 m^2 and then rapidly decreases; with increasing A, Y_3 increases slowly up to C = 2.25 m and then decreases. Figure 10.C.III shows that Y_3 decreases with increasing B and C and reaches a maximum at B = 21.96 m/s and C = 1.80 m.

Combining the results of the analysis presented above with the variance analysis results presented in Table 4 produces the following ranking (in order of decreasing significance) for the test factors: C, A and B for Y_1 and C, B and A for Y_3.

3.3 Orchard tests

The test data analysis method described in Section 2.6 was used to determine the quantities of spray deposited on different canopy regions for different test combinations. Table 5 presents a comparison of these results with those calculated by the proposed computational model.

The model accuracy varies with the test combinations. As the spray distance decreases and the air speed increases, the calculation error of the model increases for the inner and middle regions of the canopy but decreases for the outer region of the canopy, and the calculation error of the model is relatively large when the air speed and spray distance are taken to the maximum or minimum value. The reason may be that there are some differences in contour between the artificial tree and the peach tree, and with the change of spray distance and air speed at the fan outlet, the deposition distribution of spray droplets in the vertical direction of the sprayer changes, resulting in differences in the spray deposited on the canopy of the at the fan outlet and the peach tree, which leads to the calculation error of the model. The calculated mean values of the relative error per unit area in the inner, middle and outer regions of the canopy are 23.26%, 22.38% and 32.62%, respectively.

4 Discussion

The calculation model for pesticide deposition on fruit tree canopies can be used to evaluate the efficacy of pesticide spraying in orchards and optimize sprayer parameters while providing data to help manage the tracing and quantification of pesticide application

TABLE 4 Variance analysis for the regression model.

Sources	Pesticide deposition (mL·m^{-2})									
	Inner			Middle			Outer			
	Degree of freedom	F value	P -values Prob>F	Degree of freedom	F value	P -values Prob>F	Degree of freedom	F value	P -values Prob>F	
Model	9	5.06	0.0092	9	6.69	0.0032	9	10.48	0.0005	significant
A	1	0.88	0.3701	1	0.86	0.3751	1	2.75	0.1284	
B	1	0.21	0.6550	1	10.50	0.0089	1	21.82	0.0009	
C	1	20.74	0.0011	1	36.03	0.0001	1	54.15	<0.0001	
AB	1	0.38	0.5527	1	0.21	0.6567	1	0.88	0.3698	
AC	1	1.96	0.1914	1	0.50	0.4972	1	7.62	0.0201	
BC	1	10.24	0.0095	1	1.77	0.2130	1	3.72	0.0826	
A^2	1	5.13	0.0469	1	7.11	0.0236	1	2.41	0.1515	
B^2	1	6.74	0.0267	1	1.83	0.2055	1	0.29	0.5991	
C^2	1	0.013	0.9102	1	0.38	0.5531	1	0.38	0.5522	
Lack of fit	5	0.54	0.7401	5	1.67	0.2943	5	2.18	0.2065	not significant
SNRs		9.354			7.917			12.907		

in orchards. Hong et al. (2018); Duga et al. (2015) and Zhu et al. (2022) studied the qualitative relationship between the operation parameters of orchard sprayers and the deposited pesticide distribution in canopies. However, the quantity of pesticide deposited on the canopy was not calculated. In this study, the key influencing factors for the deposited pesticide distribution in the canopy were used in an orthogonal test to establish a computational model for the quantity of pesticide deposited in different canopy regions.

The characteristics of fruit trees vary considerably with the tree type and growth period. To improve the application scope of the model, a reasonable range of test factors should be used the orthogonal regression modelling method, which is difficult to implement for real orchards. In this study, artificial trees were

FIGURE 9
Analysis of a normal plot of the model residuals. (A) Normal plot of residuals. (B) Corresponding relation between the values predicted by the regression model and the actual values.

FIGURE 10
Response surface showing the influence of factor interactions on pesticide deposition on the inner, middle and outer regions of the canopy.
(A) Inner region of the canopy. **(B)** Middle region of the canopy. **(C)** Outer region of the canopy.

used to simulate real fruit frees. The canopy leaf area was manually changed to simulate changes in real fruit-tree canopies and thereby control the orthogonal test factors. A regression analysis was used to establish a computational model for the quantity of pesticide

deposited on different canopy regions, and the model was verified using data for real fruit trees. The modelling method proposed in this paper can complement the existing CFD simulation modelling methods, which provides a novel insight for the construction of

TABLE 5 Model verification test results.

Test No.	Inner deposition (mL·m^{-2})			Middle deposition (mL·m^{-2})			Outer deposition (mL·m^{-2})		
	Calculated value	Measured value	Error (%)	Calculated value	Measured value	Error (%)	Calculated value	Measured value	Error (%)
1	5.65	4.52	25.06	10.12	6.63	52.71	5.04	8.21	38.60
2	5.82	5.38	8.22	8.33	8.82	5.46	5.25	9.06	42.02
3	6.30	6.51	3.25	9.12	8.66	5.39	8.28	10.66	22.30
4	5.87	9.37	37.29	10.19	10.42	2.20	7.42	12.04	38.34
5	7.57	5.31	42.46	11.80	8.07	46.16	13.32	10.94	21.83

quantitative computational modelling of pesticide deposition on canopies using air-assisted orchard sprayers.

The computational model established using artificial trees can be applied to orchards. The maximum mean error of the model does not exceed 32.62%, showing that the model exhibits high accuracy for fruit tree canopies of different shapes. Recently, our research team made a breakthrough in LiDAR-based online computation of the fruit tree canopy leaf area (Gu et al., 2022). This method has considerable application value for determining the canopy leaf area of different types of fruit trees using LiDAR and can be used to investigate the universality of models and improve the calculation accuracy of models.

5 Conclusion

In this study, leaves were manually arranged to create artificial tree canopies with the following leaf areas: 2.54 m^2, 3.05 m^2, 3.81 m^2, 4.57 m^2 and 5.08 m^2. An orchard air-assisted sprayer with airflow control was used to conduct pesticide application tests on artificial trees at different air speeds. Water-sensitive papers and filter papers used for sampling were placed at different positions in the canopies to determine the required range of the effective air speed as 18.12-37.05 m/s for canopy leaf areas ranging between 2.54 and 5.08 m^2. The test factors included the canopy leaf area, air speed and airflow travel distance. A computational model for pesticide deposition in the inner, middle and outer regions of the canopy was established using a three-factor five-level quadratic general rotational orthogonal test; the R^2 values were 0.8199, 0.8575 and 0.9042, respectively. There is considerable variation among the characteristics of fruit tree canopies in real orchards. It is challenging to perform orthogonal regression modelling based on design parameters appropriate for real orchards. The computational model established in this study was developed using data for artificial trees, which provides novel concepts for formulating quantitative computational models for pesticide deposition on fruit tree canopies.

The significance of the influencing factors for pesticide deposition was analyzed based on a regression equation, regression coefficient and the lack-of-fit of the regression model. The results show that the influencing factors for the deposited pesticide distribution in the canopy can be ranked in decreasing order of significance as follows: the airflow travel distance, leaf area and air speed for the inner canopy region, followed by the airflow travel distance, air speed and leaf area for the middle and outer regions of the canopy. Tests were conducted on peach tree canopies to verify the model. The mean calculation errors of the computational model for pesticide deposition in the inner, middle and outer regions of the canopy were determined to be 23.26%, 22.38% and 32.62%, respectively. Studies will be conducted in the future to determine the canopy leaf areas of different types of fruit trees based on LiDAR, the universality of the model and ways to improve the calculation accuracy of the model.

Data availability statement

The original contributions presented in the study are included in the article/supplementary material. Further inquiries can be directed to the corresponding authors.

Author contributions

HD, ChaZ and ChuZ: conceptualization, validation, investigation and methodology. HD, SY and YG: software and visualization. HD, QL and SY: formal analysis. HD, ChaZ and KY: data curation. QL and ChuZ: resources and supervision. HD, QL and ChaZ: writing—original draft preparation. HD, ChaZ, SY, and YG: writing—review and editing and funding acquisition. ChaZ: project administration. All authors contributed to the article and approved the submitted version.

Funding

Conflict of interest

Author YH was employed by Chinese Academy of Agricultural Mechanization Sciences Group Co., Ltd.

The remaining authors declare that the research was conducted in the absence of any commercial or financial relationships that could be construed as a potential conflict of interest.

The handling editor WQ declared a past co-authorship with the author ZC.

Publisher's note

References

Dekeyser, D., Foqué, D., Duga, A. T., Verboven, P., Hendrickx, N., and Nuyttens, D. (2014). Pesticide deposition assessment using different application techniques in artificial orchard trees. *Crop Prot.* 64, 187–197. doi: 10.1016/j.cropro.2014.06.008

Ding, S. M., Xue, X. Y., Dong, X., Gu, W., and Zhou, Q. Q. (2020). Effects of spraying parameters on droplet deposition performance. *Trans. Chin. Soc. Agric. Machinery* 51 (s2), 308–315. doi: 10.6041/j.issn.1000-1298.2020

Dou, H., Zhai, C., Chen, L., Wang, X., and Zou, W. (2021). Comparison of orchard target-oriented spraying systems using photoelectric or ultrasonic sensors. *Agriculture* 11 (8), 753. doi: 10.3390/agriculture11080753

Duga, A. T., Delele, M. A., Ruysen, K., Dekeyser, D., Nuyttens, D., Bylemans, D., et al. (2017). Development and validation of a 3D CFD model of drift and its application to air-assisted orchard sprayers. *Biosyst. Eng.* 154, 62–75. doi: 10.1016/j.biosystemseng.2016.10.010

Duga, A. T., Ruysen, K., Dekeyser, D., Nuyttens, D., Bylemans, D., Nicolai, B. M., et al. (2015). Pesticide deposition profiles in pome fruit trees: effects of sprayer design, training system and tree canopy characteristics. *Crop Prot.* 67, 200–213. doi: 10.1016/j.cropro.2014.10.016

Endalew, A. M., Debaer, C., Rutten, N., Vercammen, J., Delele, M. A., Ramon, H., et al. (2010). Modelling pesticide flow and deposition from air-assisted orchard spraying in orchards: a new integrated CFD approach. *Agric. For. Meteorol.* 150 (10), 1383–1392. doi: 10.1016/j.agrformet.2010.07.001

Farooq, M., Balachandar, R., Wulfsohn, D., and Wolf, T. M. (2001). PA–precision agriculture: agricultural sprays in cross-flow and drift. *J. Agric. Eng. Res.* 78 (4), 347–358. doi: 10.1006/jaer.2000.0660

Gu, C., Liu, Z., Pan, G., Pu, Y., and Yang, F. (2020). Optimization of working parameters for 3MGY-200 axial air-assisted sprayer in kiwifruit orchards. *Int. J. Agric. Biol. Eng.* 13 (2), 81–91. doi: 10.25165/j.ijabe.20201302.5078

Gu, C. C., Zhai, C. Y., Wang, X., and Wang, S. L. (2021). CMPC: an innovative lidar-based method to estimate tree canopy meshing-profile volumes for orchard target-oriented spray. *Sensors* 21 (12), 4252. doi: 10.3390/s21124252

Gu, C. C., Zhao, C. J., Zou, W., Yang, S., Dou, H. J., and Zhai, C. Y. (2022). Innovative leaf area detection models for orchard tree thick canopy based on LiDAR point cloud data. *Agriculture* 12 (8), 1241. doi: 10.3390/agriculture12081241

He, X. K. (2020). Research progress and developmental recommendations on precision spraying technology and equipment in China. *Smart Agric.* 2 (1), 133–146. doi: 10.12133/j.smartag.2020.2.1.201907-SA002

Hong, S. W., Zhao, L., and Zhu, H. (2018). CFD simulation of airflow inside tree canopies discharged from air-assisted sprayers. *Comput. Electron. Agric.* 149, 121–132. doi: 10.1016/j.compag.2017.07.011

Jadav, C. V., Jain, K. K., and Khodifad, B. C. (2019). Spray of chemicals as affected by different parameters of air assisted sprayer: a review. *Curr. Agric. Res. J.* 7 (3), 289–295. doi: 10.12944/CARJ.7.3.03

Jiang, H. H., Bai, P., and Liu, L. M. (2016). Caterpillar self-propelled and air-assisted orchard sprayer with automatic target spray system. *Trans. Chin. Soc. Agric. Machinery* 47 (S1), 189–195. doi: 10.6041/j.issn.1000-1298.2016.S0.029

Li, J., Cui, H., Ma, Y., Xun, L., Li, Z., Yang, Z., et al. (2020). Orchard spray study: a prediction model of droplet deposition states on leaf surfaces. *Agronomy* 10 (5), 747. doi: 10.3390/agronomy10050747

Liu, X. M., Liu, X. H., Cui, H. Y., and Yuan, J. (2021). Research progress and trend analysis of crop canopy droplet deposition. *Trans. Chin. Soc. Agric. Machinery* 52 (11), 1–20. doi: 10.6041/j.issn.1000-1298.2021.08.011

Otto, S., Loddo, D., Schmid, A., Roschatt, C., Venturelli, M., and Innerebner, G. (2018). Droplets deposition pattern from a prototype of a fixed spraying system in a sloping vineyard. *Sci. Total Environ.* 639, 92–99. doi: 10.1016/j.scitotenv.2018.05.167

Qiu, W., Zhao, S. Q., Ding, W. M., Sun, C. D., Lu, J., Li, Y. N., et al. (2016). Effects of fan speed on pesticide deposition and drift for targeting air-assisted sprayer in pear orchard. *Int. J. Agric. Biol. Eng.* 9 (4), 53–62. doi: 10.3965/j.ijabe.20160904.1938

Salcedo, R., Zhu, H., Zhang, Z., Wei, Z., Chen, L., Ozkan, E., et al. (2020). Foliar deposition and coverage on young apple trees with PWM-controlled spray systems. *Comput. Electron. Agric.* 178, 105794. doi: 10.1016/j.compag.2020.105794

Shani, B. B. (2020). Development of mathematical modelling for predicting spray mass flux on tree canopies. *J. Eng. Res. Dev.* 3 (2), 66–79.

Shani, B. B. (2021). Development of a mathematical model for forecasting pesticide deposition on tree canopies. *Dutse J. Pure Appl. Sci.* 7 (2b), 216–227.

Sun, C. D., and Liu, C. D. (2019). Construction and application of droplet canopy penetration model for air-assisted spraying pattern. *Trans. Chin. Soc. Agric. Eng.* 35 (15), 25–32. doi: 10.11975/j.issn.1002-6819.2019.15.004

Teske, M. E., Thistle, H. W., Schou, W. C., Miller, P. C. H., Strager, J. M., Richardson, B., et al. (2011). A review of computer models for pesticide deposition prediction. *Trans. ASABE* 54 (3), 789–801. doi: 10.13031/2013.37094

Van de Zande, J. C., Huijsmans, J. F. M., Porskamp, H. A. J., Michielsen, J. M. G. P., Stallinga, H., Holterman, H. J., et al. (2008). Spray techniques: how to optimise pesticide deposition and minimise spray drift. *Environmentalist* 28 (1), 9–17. doi: 10.1007/s10669-007-9036-5

Xu, X. H., and He, M. Z. (2010). Experimental design and application of design-expert SPSS. Beijing, China: China Science Press, 109–133.

Yan, H. R., Chen, J. B., Lin, Y. H., Xue, X. Y., and Qiu, B. J. (2015). *Crop protection equipment–field measurement of spray distribution in tree and bush crops* (Beijing, China: National Agricultural Machinery Standard Technical Committee, GB/T 3244-2015, Standardization Administration of China).

Zhai, C. Y., Zhang, Y. N., Dou, H. J., Wang, X., and Chen, L. P. (2021). CFD modeling and experiment of airflow at the air outlet of orchard air-assisted sprayer. *Smart Agric.* 3 (3), 70–81. doi: 10.12133/j.smartag.2021.3.3.202106-SA007

Zhai, C., Zhao, C., Ning, W., Long, J., Wang, X., Weckler, P., et al. (2018). Research progress on precision control methods of air-assisted spraying in orchards. *Trans. Chin. Soc. Agric. Eng.* 34 (10), 1–15. 10.11975/j.issn.1002-6819.2018.10.001

Zhang, H., Qi, L., Wan, J., Musiu, E. M., Zhou, J., Lu, Z., et al. (2022). Numerical simulation of downwash airflow distribution inside tree canopies of an apple orchard from a multirotor unmanned aerial vehicle (UAV) sprayer. *Comput. Electron. Agric.* 195, 106817. doi: 10.1016/j.compag.2022.106817

Zheng, Y. J., Chen, B. T., Lyu, H. T., Kang, F., and Jiang, S. J. (2020). Research progress of orchard plant protection mechanization technology and equipment in China. *Trans. Chin. Soc. Agric. Eng.* 36 (20), 110–124. doi: 10.11975/j.issn.1002-6819.2020.20.014

Zhu, Y., Guo, Q., Tang, Y., Zhu, X., He, Y., Huang, H., et al. (2022). CFD simulation and measurement of the downwash airflow of a quadrotor plant protection UAV during operation. *Comput. Electron. Agric.* 201, 107286. doi: 10.1016/j.compag.2022.107286

Check for updates

Design and operation of a Peucedani Radix weeding device based on YOLOV5 and a parallel manipulator

Xuechen Zhang[1], Chengmao Cao[1]*, Kun Luo[1], Zhengmin Wu[2,3], Kuan Qin[1], Minhui An[1], Wuyang Ding[1] and Wang Xiang[1]

[1]School of Engineering, Anhui Agricultural University, Hefei, China, [2]School of Tea and Food Science and Technology, Anhui Agricultural University, Hefei, China, [3]State Key Laboratory of Tea Plant Biology and Utilization, Hefei, China

To avoid excessive use of herbicides in the weeding operations of Peucedani Radix, a common Chinese herb, a precision seedling avoidance and weeding agricultural robot was designed for the targeted spraying of herbicides. The robot uses YOLOV5 combined with ExG feature segmentation to detect Peucedani Radix and weeds and obtain their corresponding morphological centers. Optimal seedling avoidance and precise herbicide spraying trajectories are generated using a PSO-Bezier algorithm based on the morphological characteristics of Peucedani Radix. Seedling avoidance trajectories and spraying operations are executed using a parallel manipulator with spraying devices. The validation experiments showed that the precision and recall of Peucedani Radix detection were 98.7% and 88.2%, respectively, and the weed segmentation rate could reach 95% when the minimum connected domain was 50. In the actual Peucedani Radix field spraying operation, the success rate of field precision seedling avoidance herbicide spraying was 80.5%, the collision rate between the end actuator of the parallel manipulator and Peucedani Radix was 4%, and the average running time of the parallel manipulator for precision herbicide spraying on a single weed was 2 s. This study can enrich the theoretical basis of targeted weed control and provide reference for similar studies.

KEYWORDS

Peucedani Radix, YOLOv5, trajectory planning, precision weeding, parallel manipulator

1 Introduction

Peucedani Radix (Chinese name Qianhu), the dried root of *Peucedanum praeruptorum* Dunn (The State Pharmacopoeia Commission of P.R. China, 1997; Pharmacopoeia, 2010; The State Pharmacopoeia, C., 2010), is a common Chinese herb. Peucedani Radix has been widely used for centuries to treat colds and coughs (Chang et al., 1986). Competition for

water, nutrients, space, and sunlight between weeds and Peucedani Radix (Li et al., 2021) significantly reduces the yield of Peucedani Radix, causing huge economic losses. However, the main economic value of Peucedani Radix lies in its buried rhizome, which mechanical weeding operations can damage along with plant stems (Quan et al., 2022). At present, Peucedani Radix weeding is mainly achieved using sprayed herbicides; however, spraying herbicides over a large area on water, air, and soil can lead to environmental problems (Villette et al., 2022). Therefore, reducing the use of herbicides and ensuring the yield of Peucedani Radix is a major challenge. Precision seedling avoidance spraying is an effective way to maintain the use of herbicides and effectively control weeds in Peucedani Radix fields (Özlüoymak, 2022).

The prerequisite for accurate seedling avoidance spraying of herbicides is accurate spraying without damaging the crop. Some researchers have proposed distinguishing weeds from crops using features such as color space, leaf texture, spectrum characteristics, and morphological size (Hamuda et al., 2017; Strothmann et al., 2017; Sujaritha et al., 2017; Zheng et al., 2017). However, the performances of these methods are influenced by a complex variety of factors, including weed density, light conditions, crop–weed overlap, weather, and crop growth stage. Therefore, an efficient and stable algorithm is needed to handle the complex and diverse field operation situations (Zou et al., 2021). In recent years, deep learning techniques have developed rapidly. Chavan and Nandedkar (2018) combined Alexnet and Vggnet models to form the AgroAVNET network for classification of crops and weeds. Dos Santos Ferreira et al. (2017) classified soybean and weeds using ConvNets. Tang et al. (2017) used K-means combined with Convolutional Neural Network (CNN) to identify and classify weeds. Although the accuracy of these classification methods is relatively high, the operation requires the segmentation of crops and weeds, and the classification time of a single image will increase with the number of weeds and crops in the image. Picon et al. (2022) achieved semantic segmentation of multiple weed and maize crops using Dual Pyramid Scene Parsing Network (PSPNet). Quan et al. (2019) used an improved Fast Region-based Convolutional Network (Fast-RCNN) model with Visual Geometry Group 19 (VGG19) to achieve maize seedling detection at different growth stages and under various weather conditions. Ahmad et al. (2021) and Quan et al. (2022) used the You Only Look Once Version 3 (YOLOV3) network model to detect and classify common weeds in maize fields and the results showed that the average detection accuracy of YOLOV3 was above 93% in all cases. Although these methods have high identification accuracy in actual field operations, they require extensive labeling of weeds and crops, which greatly increases the workload of detection (Hasan et al., 2021; Li et al., 2022).

It is challenging to use an end-effector to precisely spray herbicide onto weed surfaces without collisions between the end-effector and crop (Li et al., 2022). Utstumo et al. (2018) designed an Asterix autonomous robotic platform that enables drop-on-demand spraying of herbicides from the top to the bottom of the crop through nozzles with a lateral spacing of 6 cm. Partel et al. (2019) designed precision spraying systems adapted to crop row spacing. Villette et al. (2021; 2022) compared different nozzle spray shapes, nozzle spacing, and six spraying strategies to obtain the

optimal pattern of triangular-shaped sprays combined with overlapping sprays, which significantly reduced the amount of herbicide used. However, the above method cannot avoid potential damage to the crop if the nozzles are too high due to improper nozzle spacing and height setting, causing the herbicide to be sprayed onto the surface of the crop during equipment travel.

A key objective of this research was to design an algorithm that identifies crops and weeds quickly and accurately, while reducing the workload of dataset production. Another important goal was to ensure that the spray actuation equipment avoids crop injury during accurate herbicide spraying. To achieve these two goals, this study developed an intelligent Peucedani Radix weeding agricultural robot, which uses You Only Look Once Version 5 (YOLOV5) with Extra-Green (ExG) feature segmentation for crop and weed recognition, and a parallel spraying device with Particle Swarm Optimization (PSO)-Bezier seedling avoidance trajectory for herbicide spraying. By applying YOLOV5 for crop identification and ExG feature segmentation for weed identification, the crop and weed identification problem is transformed into a binary problem, thus simplifying the complex weed labeling work. In addition, the PSO-Bezier curve is used to achieve accurate seedling avoidance spraying of herbicides based on crop characteristics to reduce pesticide usage and achieve seedling avoidance during operation, which significantly reduces the amount of pesticide residues on the crop surface and energy consumption.

2 Materials and methods

2.1 System overview

The biology of Peucedani Radix seedlings is characterized by an erect growth type (Figure 1). Therefore, to facilitate subsequent studies, the morphology of Peucedani Radix plants was simplified in this study as cylinders of different diameters. An intelligent Peucedani Radix weeding agricultural robot was designed, as shown in Figure 2. The agricultural robot is driven by Direct Current motors and is equipped with parallel robotic arms and circular nozzles on the end-effectors. The crop and weeds on the field ridge are photographed by a camera mounted at 90° to the horizontal and the locations of Peucedani Radix and weeds are identified in real time by a computer. The computer performs PSO-Bezier trajectory planning for the robotic arm end-effector based on the position and morphological parameters of Peucedani Radix and the position of the weed to achieve precise seedling avoidance for herbicide spraying. The corresponding workflow schematic is shown in Figure 3.

2.2 Image dataset construction

The growth cycle of Peucedani Radix plants used in this study was one year, planted in December 2021. Peucedani Radix fields are usually weeded when the plants are approximately 15 cm tall. Peucedani Radix planted in the Nongcui Garden of Anhui Agricultural University, Hefei, Anhui Province, China (117°14'E,

FIGURE 1
Semiannual morphological parameters of Peucedani Radix growth.
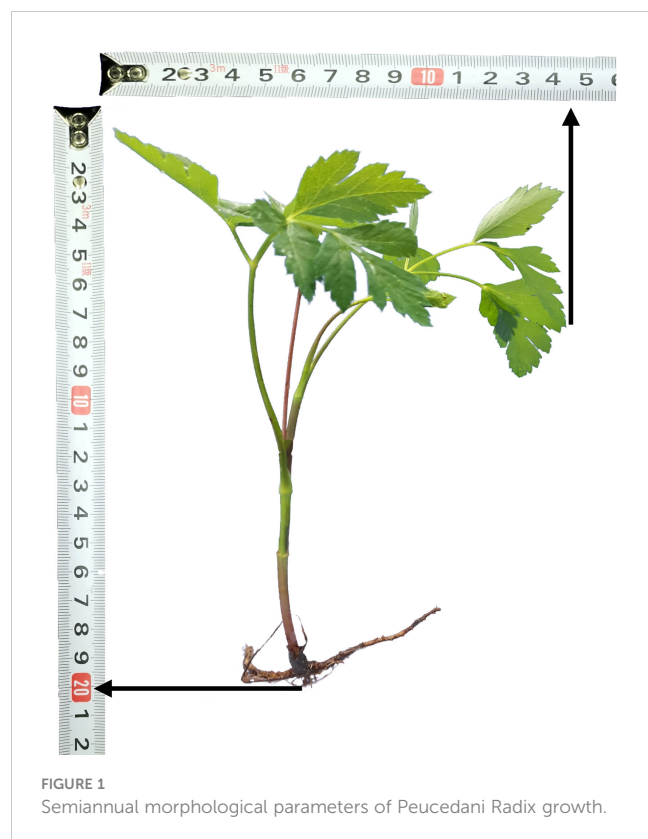
31°52'N) were photographed in April, June, and August 2022 to produce the dataset. A Balser industrial camera (acA1920-150uc, Germany) was used for image acquisition, cropping the left and right unrelated areas of the image to improve acquisition speed. In total, 5,092 images with a resolution of 1200×1200 were collected. Since the dataset pictures were taken at 1 s intervals in a cycle, the differences between adjacent pictures were not obvious. In addition, some pictures of poor quality were obtained during the dataset acquisition process and these pictures could not meet the experimental requirements. Therefore, it was necessary to filter the dataset manually. Finally, 2,347 images were selected as the dataset and the dataset was enhanced by changing the brightness and darkness of the images, mirroring, and other adjustments to improve the richness of the sample. In contrast to other dataset annotations, this annotation only labeled Peucedani Radix plants. Finally, the dataset of 2,347 images was expanded to 9,388 images and the enhanced dataset was divided into a training set and a validation set at a 4:1 ratio (Table 1).

2.3 Crop and weed identification

Since the YOLO network is currently one of the best-performing algorithms in the target detection field, this study used the fast and accurate YOLOV5 network combined with ExG feature segmentation to detect crops and weeds. The structure of the crop and weed detection model is shown in Figure 4, which is mainly divided into two parts: Peucedani Radix detection and weed segmentation. The Peucedani Radix detection component consists
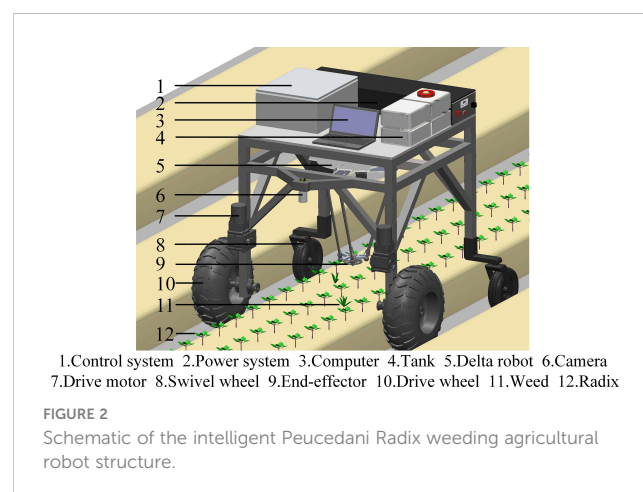
of the YOLOV5 network, which was developed from the previous YOLOV4 and YOLOV3 (Redmon and Farhadi, 2018) networks. The YOLOV5 network is divided into three parts: Backbone, Neck, and Head. Compared with that of YOLOV4, the first layer of the Backbone network in YOLOV5 has an additional 6×6 sized convolutional layer. In the Neck part, YOLOV5 uses Spatial Pyramid Pooling – Fast (SPPF) network structure, compared to the previous version which uses Spatial Pyramid Pooling (SPP) structure. SPPF modifies the 9×9 and 13×13 sized MaxPool layers into two and three 5×5 sized MaxPool layers, respectively. The modified network achieves the same result but is two times faster. The weed segmentation component is composed of four parts: crop image, 2G-R-B (ExG feature segmentation), maximum between-cluster variance (OSTU), and rectangle.

In this study, the YOLOV5 network model was first used to process the images captured by the camera to determine the locations of the Peucedani Radix plants (Output1). The Peucedani Radix plants were then separated from the original image by cropping the minimum external rectangular box. Next, the cropped image was fed into the 2G-R-B (ExG) algorithm to obtain the foreground image of the weed after separation of the weed from the soil. Subsequently, the foreground image of the weed was grayed out and adaptive binarization was implemented using OSTU. The connectivity domain of the binarized image was processed by operations such as erosion expansion to obtain a reasonable weed connectivity domain. Finally, morphological center extraction and minimum outer rectangle drawing were performed on the weed connectivity domain to detect the weed and Peucedani Radix plants and their corresponding locations.

The training platform used a host containing an Intel Core i7-11700F (2.5 GHz) octa-core CPU, an NVIDIA RTX3060 (1,876 MHz) GPU, and 32 GB of RAM, running on Windows 10. The software tools included CUDA 11.4, CUDNN 8.2.2, and Python 3.8 and the experiments were implemented in the Pytorch framework.

2.4 Weed trajectory planning

YOLOV5 combined with the ExG feature segmentation algorithm was used to detect Peucedani Radix and weeds and

1.Control system 2.Power system 3.Computer 4.Tank 5.Delta robot 6.Camera
7.Drive motor 8.Swivel wheel 9.End-effector 10.Drive wheel 11.Weed 12.Radix

FIGURE 2
Schematic of the intelligent Peucedani Radix weeding agricultural robot structure.

FIGURE 3
Schematic of the Peucedani Radix weeding process.
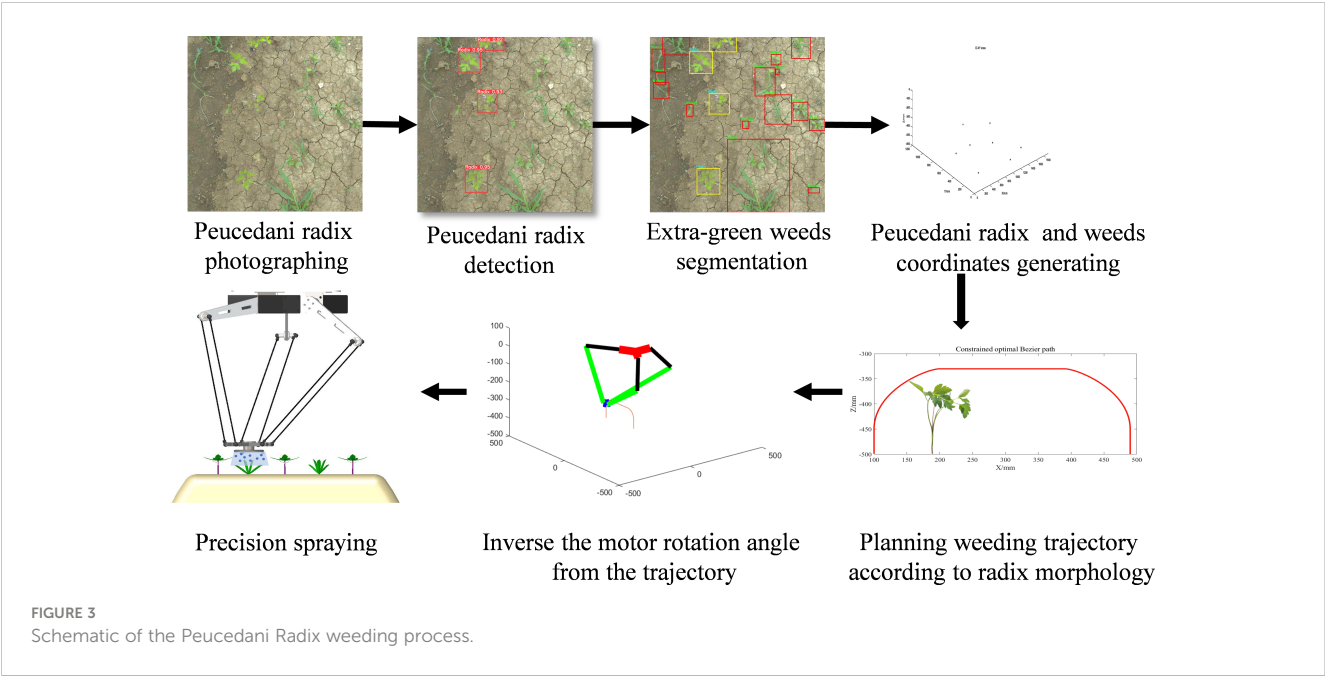
obtain their coordinate information under the robot coordinate system. To avoid collision of the end-effector of the robot arm with Peucedani Radix plants, an optimal motion path needs to be found for the specified coordinates of the start and end points of the end-effector motion to achieve efficient seedling avoidance and weed spraying.

The process of moving the end-effector from the current weed position to the next weed position is first defined as a weeding cycle. As shown in the red curve in Figure 5, the trajectory of the end-effector was designed in one weeding cycle and the center of the end-effector moves along the curve to achieve precise weeding and avoid spraying herbicide onto the crop surface. To reduce the overall vibration of the robotic arm during the transition phase and crop avoidance, Particle Swarm Optimization and third-order Bezier curves combined with crop morphology parameters were used to generate the optimal transition trajectory for the end-effector movement in the vertical to horizontal direction.

As shown in Figure 6, S and E are the starting and ending points of the trajectory, respectively, corresponding to the coordinates of the weed. The "∩" type trajectory of seedling avoidance and weeding was established in the vertical plane N of the SE line segment (Yang et al., 2021). For analysis, the plane N was rotated to the O-XZ plane, and the point S was set as the origin. To facilitate the calculation, a Peucedani Radix plant was regarded as a cylinder with constant height and changing diameter and the height h_2 of the

cylinder was set to 150 mm using numerous statistics. The radius of the cylinder was set to w_2 and the distance from the center of the cylinder bottom circle to the point S was $w_1 + w_2$. $S \rightarrow P_0$ is the ascent phase with height h_1, $P_0 \rightarrow P_1 \rightarrow P_2 \rightarrow P_3$ is the transition phase designed using a third-order Bezier curve with height h_2, $P_3 \rightarrow P_4$ is the horizontal shift phase, $P_4 \rightarrow P_5$ is the transition phase designed using a third-order Bezier curve, and $P_5 \rightarrow E$ is the descent phase. In Figure 6, P_0, P_3 are the starting and ending points of the Bezier curve, respectively, and P_1, P_2 are the first and second control points, respectively. The shape of the third-order Bezier curve is adjusted by adjusting the position of the P_1, P_2 points to ensure that the end-effector of the robot arm avoids the crop as it moves along the Bezier curve to the M point.

The Bezier curve equation is as follows:

$$P(t) = \sum_{i=0}^{n} P_i B_{i,n}(t), t \in [0, 1] \tag{1}$$

$$B_{i,n}(t) = C_n^i t^i (1 - t)^{n-i} [i = 0, 1, \ldots, n] \tag{2}$$

According to equations (1) and (2), the third-order Bezier curve calculation equation (3) can be obtained:

$$B(t) = (1 - t)^3 P_0 + 3t(1 - t)^2 P_1 + 3t^2(1 - t)P_2 + t^3 P_3, t$$
$$\in [0, 1] \tag{3}$$

TABLE 1 Main parameters of YOLOV5 network dataset.

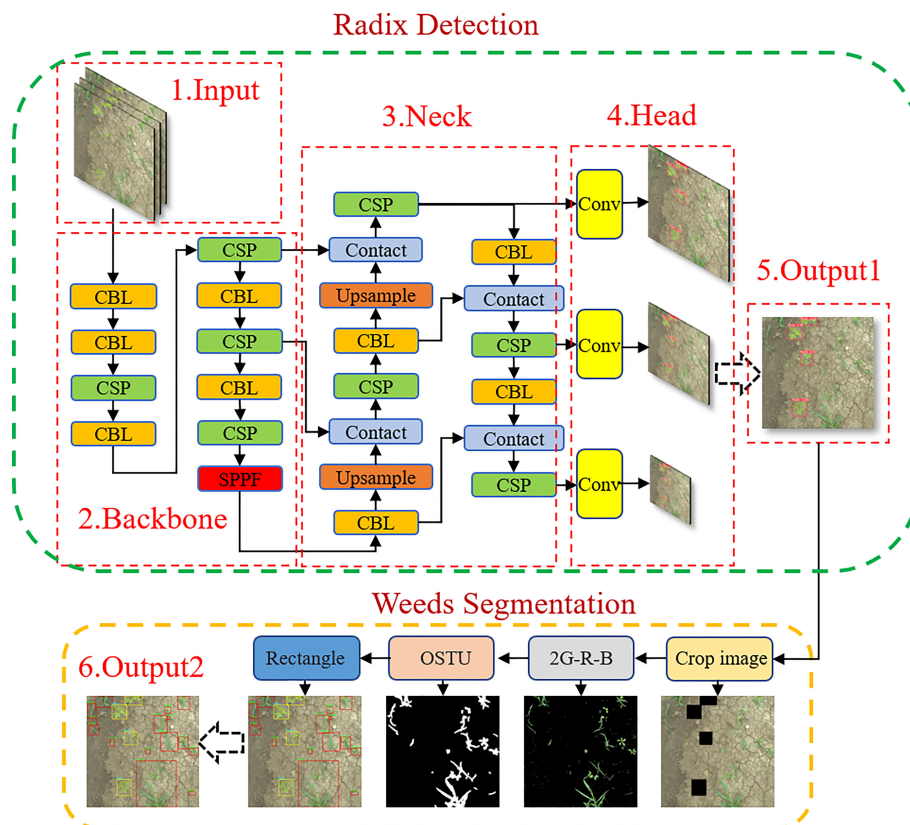| Name	Quantity (No.)	Peucedani Radix number (No.)
Preferred dataset	2,347	4,823
Image augmentation	9,388	19,297
Training dataset	7,577	15,439
Test dataset	1,811	3,858

FIGURE 4
Crop and weed identification model structure.

$$k(t) = \frac{|x_i \dot{y}_i - \ddot{x}_i y_i|}{(x_i^2 + y_i^2)^{\frac{3}{2}}}, [i = 0, 1, \ldots, n] \qquad (4)$$

In equation (4), $k(t)$ is the curvature of the path point, $(x(t), y(t))$ is the third-order Bezier curve obstacle avoidance path, and $\dot{x}$、$\dot{y}$、$\ddot{x}, \ddot{y}$ is the first- and second-order derivative of the path point $(x(t), y(t))$ on the X and Y axes.

To ensure that the third-order Bezier curve curvature $k(t)$ is smooth in the definition domain and there is no singularity,

curvature smoothing constrained Bezier curve planning was used. In this planning, the first control point P_1 moves in the direction of $\overrightarrow{SP_0}$ and the length of P_0P_1 does not exceed $0.8h_2$, and the second control point P_2 moves in the $\overrightarrow{P_4P_3}$ direction and the length of P_2P_3 does not exceed $0.8(w_1 + w_2)$. A particle swarm algorithm (eq. 5) based on the shortest path was established to solve the optimal path with the constraint that the vertical distance of point M from the horizontal plane is greater than h_3. An adaptive adjustment factor (eq. 6) based on the inverse tangent function was established so that the particle search range decreased with the number of iterations.
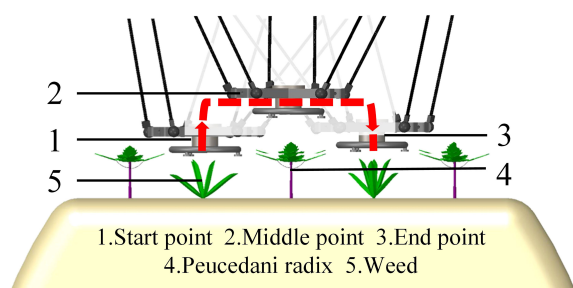

FIGURE 5
Schematic of end-effector weeding trajectory. Schematic diagram of the seedling avoidance and weeding trajectory of the end-effector.
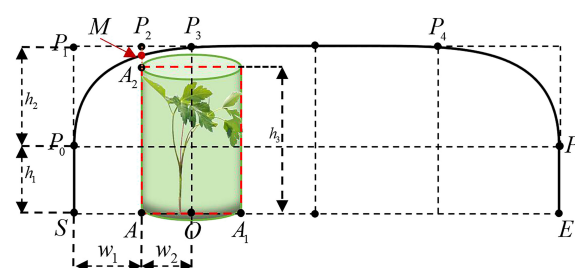

FIGURE 6
Bezier weeding trajectory execution paths and their corresponding control points.

$$\begin{cases} v_i^{n+1} = \omega \times v_i^n + c_1 \times R_1 \times (Pbest_i - x_i^n) + c_2 \times R_2 \times (Gbest_i - x_i^n) \\ x_i^{n+1} = x_i^n + r \times v_i^{n+1} \end{cases}$$

(5)

$$r = 1 - \tanh \frac{n}{1 + n_{max}}$$

(6)

where i is the particle number, n is the number of iterations, ω is the inertia factor, c_1, c_2 is the learning factor of the particle, r is the adjustment factor, R_1, R_2 is a random number between 0 and 1, v is the velocity of the particle, x is the position of the particle, $Pbest$ is the historical best position of particle i, and $Gbest$ is the historical best position of the particle population.

3 Evaluation of detection and trajectory planning

3.1 Evaluation of Peucedani Radix detection

For the evaluation of Peucedani Radix detection, this study used three evaluation metrics to assess the performance of the YOLOV5 network: precision, recall, and mean Average Precision (map). The Intersection over Union (IOU) is the ratio of the overlap area between the predicted bounding box and the true bounding box to the area contained in the predicted and true bounding boxes (eq. 7).

$$IOU = \left(\frac{A_1 \cap A_2}{A_1 \cup A_2} \right)$$

(7)

where A_1 is the area of the predicted bounding box and A_2 is the area of the real bounding box.

$$precision = \frac{TP}{TP + FP}$$

(8)

$$recall = \frac{TP}{TP + FN}$$

(9)

where TP, FP, and FN are the number of true positive cases, false positive cases, and false negative cases, respectively.

The datasets of Peucedani Radix plants collected in April, June, and August were fed into the model training and validation and the validation results are shown in Table 2. The validation results for the June and August datasets were better than those for the April dataset. Although the precision of the April dataset was high, the recall rate was only 76.3%. There are several reasons for the poor detection results of the April dataset: compared to the June and August datasets, the number of April datasets was relatively small and the model did not produce reliable results for the extraction of Peucedani Radix features in April. In addition, as shown in Figure 7, Peucedani Radix plants in April were smaller and less distinctive than those in June and August. As shown in Table 2, the validation effect improved as Peucedani Radix grew, with an accuracy of 99.2%, recall of 91.6%, and map (IOU=0.5) of 95.8% for the August dataset when the plants were largest.

TABLE 2   Results of validation detection in April, June, and August.

Period	TP	FP	FN	Precision (%)	Recall (%)	Map (IOU=0.5)	Map (IOU=0.5:0.95)
April	720	11	224	98.5	76.3	87.8	83.1
June	1,349	20	111	98.5	92.4	95.5	91.5
August	1,327	11	122	99.2	91.6	95.8	95
All	3,399	45	454	98.7	88.2	93.8	91.1

FIGURE 7
Peucedani Radix plants in different months.

3.2 Evaluation of weed split

As previously described in Figure 4, after extracting Peucedani Radix using YOLOV5, weeds of varying sizes were segmented by the ExG feature algorithm. To verify the validity of the method, a test set of Peucedani Radix field pictures with different weed sizes and densities was used for testing. Figure 8 shows the results of multiple images with different weed sizes and densities on the ExG feature algorithm for weed segmentation labeling. In Figures 8A–C, and d are the test images in order of increasing weed density. The minimum weed volume segmented by the ExG feature marker increased as the minimum connected domain size (MCDS) increased, as shown in the white boxed area in Figure 8D. When MCDS=50, the weed segmentation rate can attain over 95%. This means that the model can be adjusted to segment the minimum connected domain size according to the actual growth size state of the weed to achieve accurate weed identification.

To verify the development of the weed segmentation model, the weed identification model of YOLOV5 combined with ExG feature segmentation proposed in this study was compared with the YOLOV5 direct weed identification algorithm and validated. First, the dataset that was labeled with Peucedani Radix crops was secondarily labeled with all the weed samples in the dataset. The annotated dataset was enhanced in the same way. The composition of the enhanced weed Peucedani Radix dataset is shown in Table 3. Then, the dataset was fed into the YOLOV5 model for training. Finally, the two algorithms were tested independently using Peucedani Radix field images with different weed sizes and densities.

As shown in Figure 9, the five images present gradually increasing weed density from left to right. By comparing the experimental results, we found that the direct method of using YOLOV5 to identify weeds and Peucedani Radix crops could only identify some weeds with larger size and distinct features, but not all of them. However, combining YOLOV5 with ExG to first identify the Peucedani Radix plants and then perform weed segmentation allowed us to accurately segment most weeds despite the gradual increase in weed density. The strategy of combining YOLOV5 with ExG to identify Peucedani Radix plants and weeds showed superior performance compared to the direct use of YOLOV5 alone.

FIGURE 8
Results of weed segmentation at different minimum connected domain sizes (MCDS).
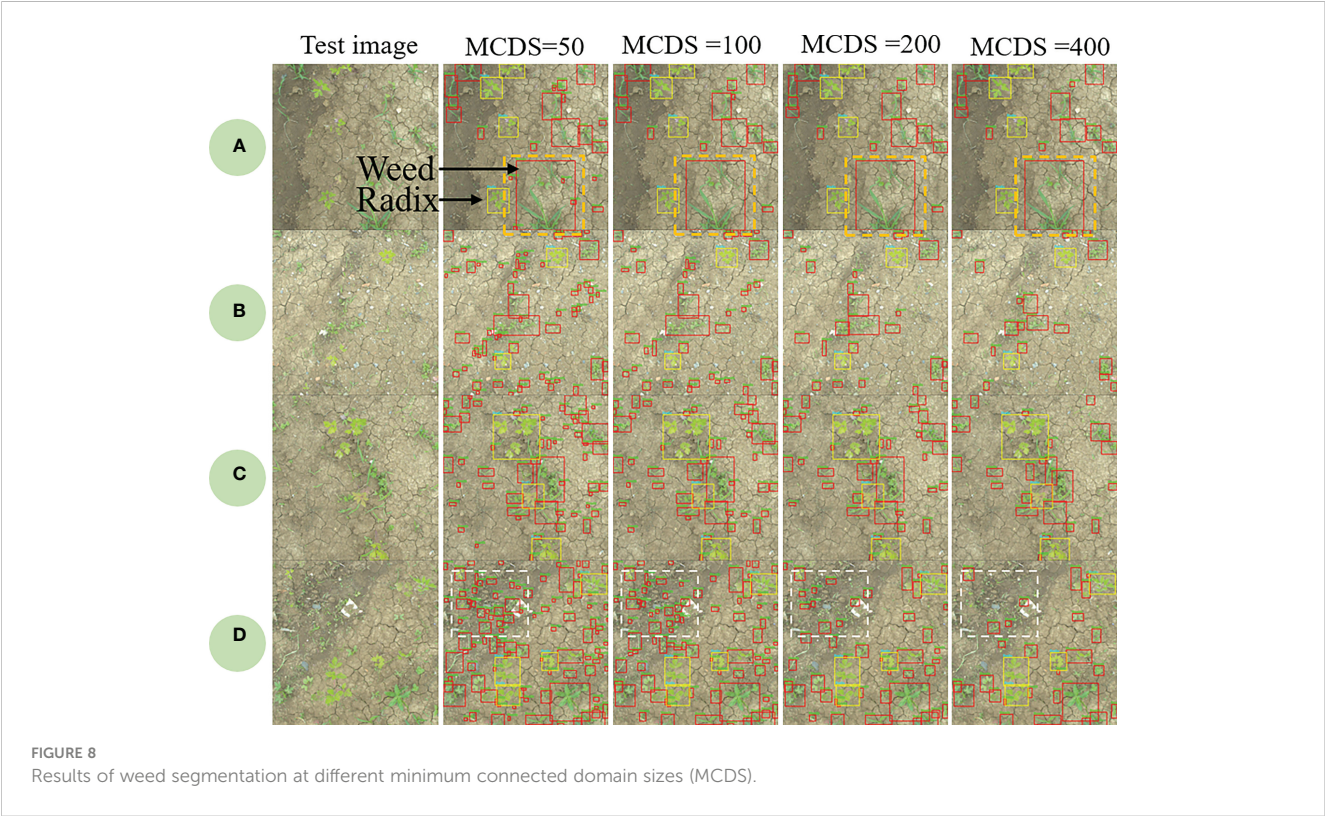
TABLE 3 Composition of weed dataset.

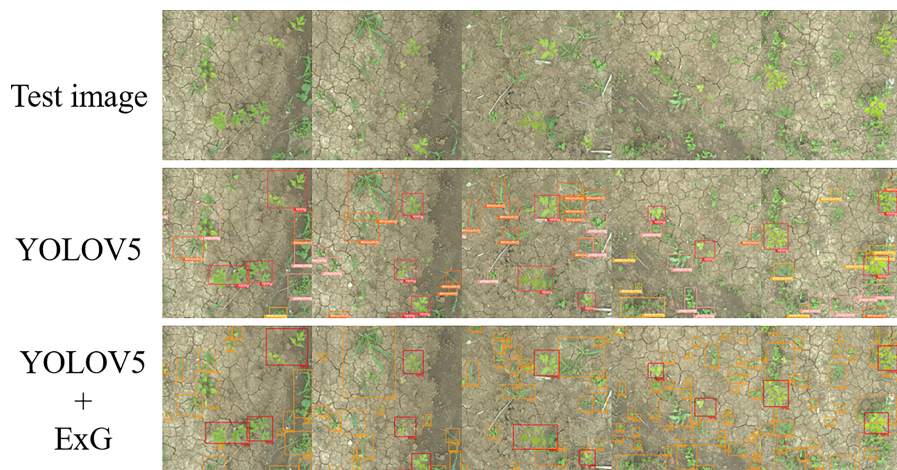| Name	Quantity (No.)	Graminaceae	Broadleaf	Sauraceae
Preferred dataset	2,347	3,472	2,889	1,236
Image augmentation	9,388	13,888	11,556	4,944
Training dataset	7,577	11,110	9,244	3,955
Test dataset	1,811	2,778	2,312	989

FIGURE 9
Schematic diagram comparing the effectiveness of the YOLOv5 and YOLOv5+ExG methods in identifying Peucedani Radix plants with weeds.

3.3 Evaluation of weed trajectory planning

The simulation was performed using the proposed PSO-Bezier trajectory generation method as described previously. In the simulation, the particle swarm number was set to 5 and the maximum number of iterations to 200. The height of the sample Peucedani Radix plants was $h_3 = 150$ and trajectory planning height was $h_1 + h_2 = 170$. The distance between the horizontal center of Peucedani Radix and the starting point of the trajectory was set as $SO = 100$, where $w_1 = 60$. The Bezier curve generated by the particle swarm is shown in Figure 10A. Where the Bezier trajectory (black dashed envelope) intersects with Peucedani Radix is shown using a red dashed envelope. The collision-free Bezier trajectory curve (Figure 10B) generated by the particle swarm was obtained by establishing the obstacle avoidance constraint through the height relationship between points M and A_2 in Figure 6.

As shown in the yellow dashed box in Figure 11A, the Bezier trajectory generated only by the height relationship between points M and A_2 shows a large change of direction at the end of the trajectory and the connection point P_3 of the horizontal movement stage, which leads to a large vibration of the robot arm when it passes through this

point at high speed. After introducing the curvature constraint (eq. 4), the first control point P_1 moves in the $\overrightarrow{SP_0}$ direction, the length of P_0P_1 does not exceed $0.8h_2$, the second control point P_2 moves in the direction $\overrightarrow{P_4P_3}$, and the length of P_2P_3 does not exceed $0.8(w_1 + w_2)$. The effect of the curvature constraint is shown in the yellow dashed box indicated by the arrow in Figure 11B. Compared with Figure 11A, the end of the trajectory is smoother at the connection point P_3 between the end of the trajectory and the horizontal moving stage after the curvature constraint, and the vibration of the frame will be significantly reduced when the robot arm moves at high speed.

The global obstacle avoidance trajectory planned with obstacle avoidance and curvature constraints is shown in Figure 12A. As shown in Figure 12B., the global obstacle avoidance trajectory is inverse kinematically solved by establishing the inverse kinematic inverse solution model of the parallel robotic arm in Python. The global obstacle avoidance trajectory is discretized into 100 trajectory points, and the angle that the three motors of the parallel robot arm need to rotate is obtained by solving the difference of the pose angle of the robot active arm corresponding to two adjacent trajectory points, and the robot arm end-effector moves along the planned trajectory through equal interpolation.
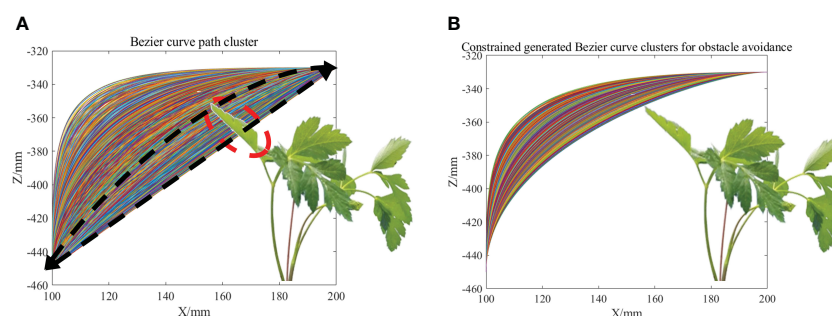

FIGURE 10
(A) Cluster of Bessel trajectories generated by PSO. **(B)** Cluster of seedling avoidance Bezier trajectories generated by PSO.
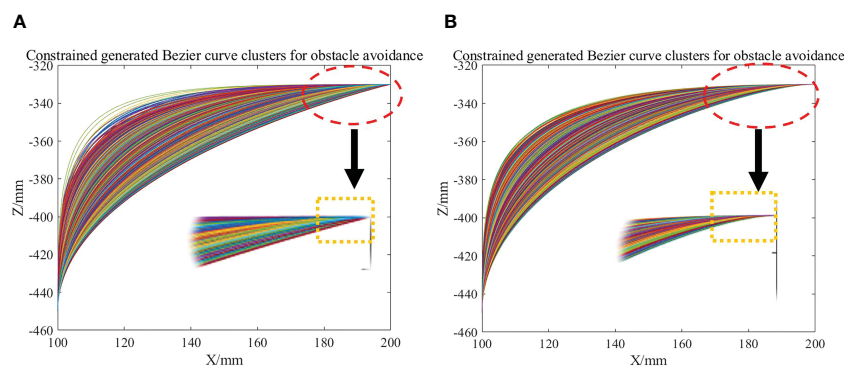
FIGURE 11
(A) Bezier trajectory before curvature constraint. **(B)** Bezier trajectory after curvature constraint.

4 Weeding experiments

4.1 Introduction of the experimental system

The machine used for the Peucedani Radix weeding experiment consisted mainly of an industrial camera, a computer, a control layer device, and a controlled layer device, as shown in Figure 13. The control layer contained the microcontroller STM32F407, the LORA communication module, the motor driver, and the relays. The controlled layer contained geared motors and drive wheels, Delta parallel manipulators, and end spray actuators. The Delta parallel manipulator was designed and made by our team (Zhang et al., 2023) and the repeat positioning accuracy was 4 mm.

In Figure 13, the robot first captures images of the crop and weeds on the monopoly using a camera mounted at an angle of 90° to the horizontal plane, and the computer identifies and locates the positions of the Peucedani Radix plants and weeds in real time. Subsequently, the computer performs PSO-Bezier trajectory planning for the end-effector of the robot arm based on the position and morphological parameters of the Peucedani Radix plants and the positions of the weeds. Then, the computer sends commands to the STM32 microcontroller to control the robot to advance a fixed distance based on the horizontal fixed distance between the origin of the camera coordinate system and the origin of the robot arm coordinates. Finally, the computer discretizes the planned trajectory and sends it to the STM32 microcontroller in sequence through the serial port. After

receiving the signal from the serial port, the STM32 microcontroller generates an interrupt and the number of pulses required for motor rotation in the interrupt service program. When the robot arm runs through all trajectory points and reaches above the weeds, the relay is activated, and the end-effector pump starts working to spray the herbicide. Through these steps, the robot achieves the function of spraying herbicide with precise seedling avoidance.

All algorithms were executed on a portable computing device (Lenovo) equipped with an Intel i5-7300HQ processor and 16 GB of RAM, operating on a Windows 10 64-bit system. The Peucedani Radix detection algorithm was implemented based on a modification of the YOLOV5 code open-source library (https://github.com/ultralytics/yolov5). The weed ExG feature segmentation algorithm was implemented based on a modification of the open-source Computer Vision library (OpenCV, https://opencv.org/). The PSO-Bezier optimal trajectory generation algorithm for seedling avoidance and weeding was designed and written by our team and deployed using Python. The STM32F407 hardware was programmed using the official firmware library (https://stmicroelectronics.com.cn) and the relevant code was written in the MDK compiler using the C language.

4.2 Results of weeding experiments

The weeding experiment was conducted on a sunny day in August 2022 at Nongcui Garden, Anhui Agricultural University,
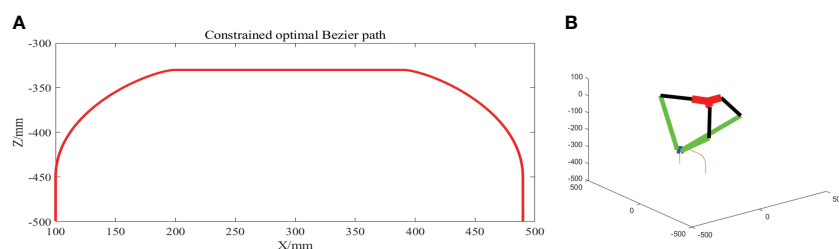

FIGURE 12
(A) Optimal Bezier curve path profile planned. **(B)** Schematic diagram of the inverse spatial state kinematic solution of the global obstacle avoidance trajectory.
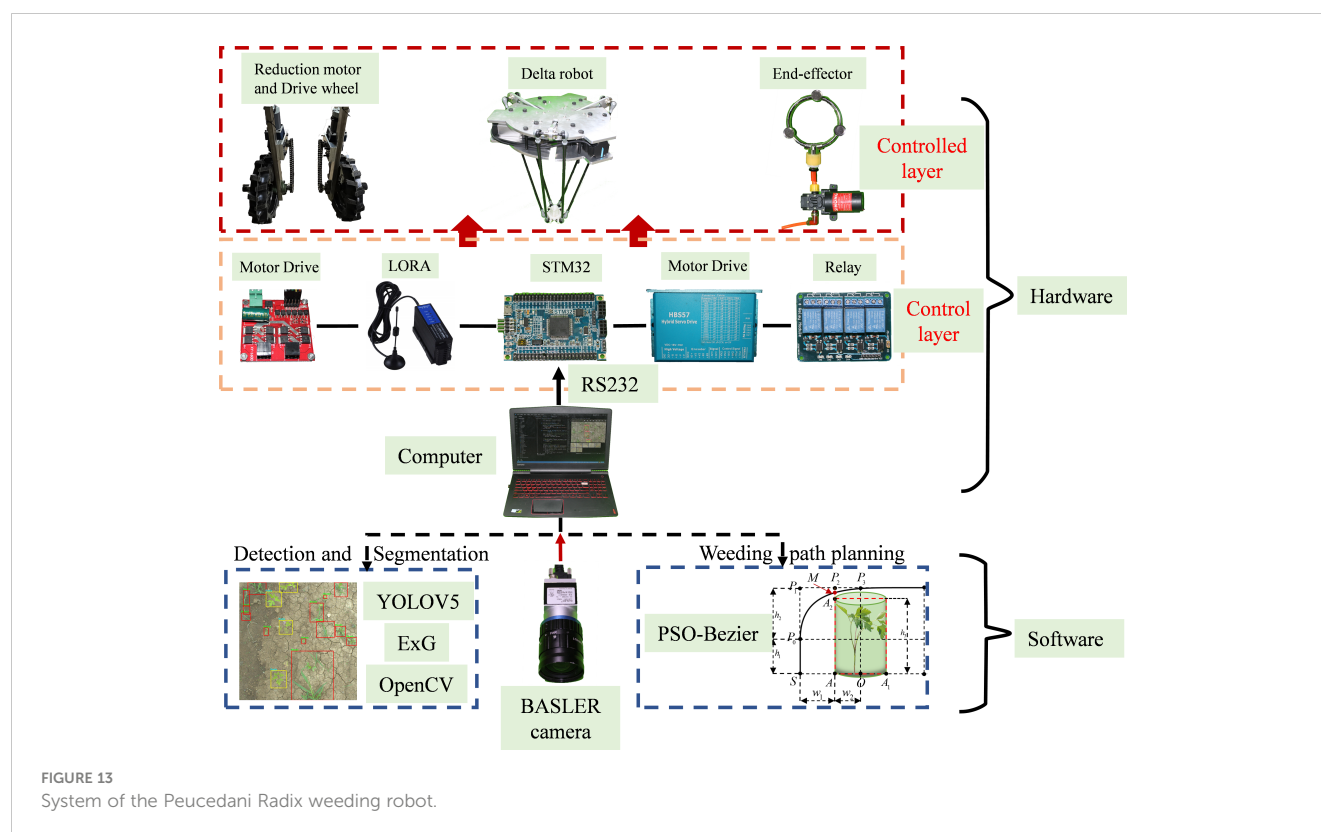
FIGURE 13
System of the Peucedani Radix weeding robot.

Anhui Province, China (Figure 14). In the experiment, Peucedani Radix was first identified by the YOLOV5 algorithm and the weeds were then segmented by the ExG feature segmentation algorithm to obtain the Peucedani Radix size parameters and the corresponding coordinates of Peucedani Radix and weeds. The trajectory of the manipulator arm end avoidance was generated by PSO-Bezier and the joint rotation angle of the parallel manipulator arm at each step of the interpolation was obtained by inverse solution of the kinematics of the avoidance trajectory by aliquot interpolation. The angle of joint rotation was converted into motor operation drive parameters and sent to the STM32 microcontroller *via* RS232 communication, which controlled the motor driver and drove the equipment to the specified position. The end-effector started spraying herbicide when it reached above the weed to complete a spraying operation. Fifty plants were selected for 100 spraying operations to verify the accuracy of the algorithm and the results were as follows:

(1) A total of 161 weeds were successfully and accurately sprayed out of 100 spraying operations, with 39 weeds not successfully sprayed; therefore, the success rate of accurate herbicide spraying was 80.5%.

(2) In the precision spraying operation, the end-effector made four collision contacts with the Peucedani Radix plants when moving according to the generated PSO-Bezier trajectory. Therefore, the success rate of seedling avoidance for the PSO-Bezier trajectory motion of the end-effector was 96%.

(3) The failure of agricultural robots to accurately spray herbicides on weeds was partly due to failure in

accurately identifying Peucedani Radix and weeds, and partly due to failure in accurately locating the weeds.

(4) The main reason for the collision contact between the end-effector of the agricultural robot and the Peucedani Radix plants was the differing heights of Peucedani Radix plants and the variable height of the terrain.

The results showed that the time to identify and locate Peucedani Radix and weeds in one frame was 0.75 s on average. The average time to generate the end-effector PSO-Bezier seedling avoidance motion trajectory was 0.35 s. The end-effector movement time increased with the linear distance between the weeds at the ends of the trajectory. The average time for the end-effector to execute the planned PSO-Bezier trajectory was 2.8 s when the weed linear spacing was 30 cm. In summary, the total time for precision herbicide spraying by the developed agricultural robot was 3–5 s, meaning that it takes an average of 2 s per weed to accurately spray herbicide. Therefore, the proposed method for precise seedling avoidance spraying of herbicides can be effectively applied to an agricultural robot platform.

5 Discussion

In the validation experiments of Peucedani Radix recognition, the accuracy of early Peucedani Radix recognition was relatively low because the dataset of April Peucedani Radix plants was small and plant morphology was not obvious compared with June and August. To improve this problem, we plan to add more images to

1.Computer   2.Water tank   3.Battery(24V)   4.Inverter(DC-AC)   5.Basler camera
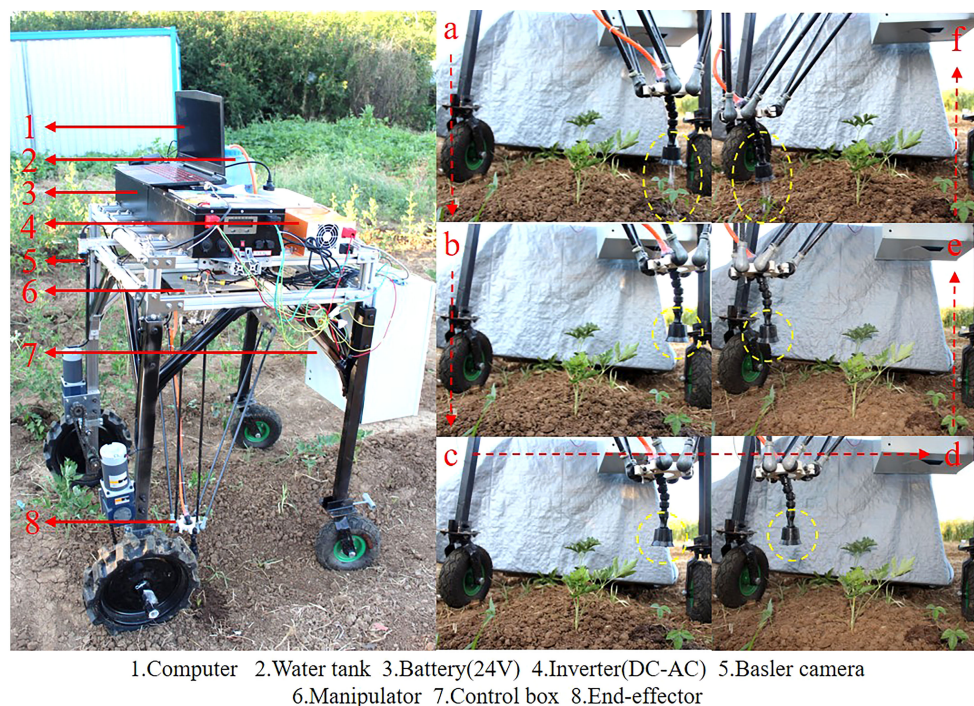6.Manipulator   7.Control box   8.End-effector

FIGURE 14
Agricultural robot field weeding experiment site.

the April Peucedani Radix plant dataset. In the ExG feature segmentation weed experiment, we achieved over 95% accuracy of weed segmentation at MCDM=50. In addition, through comparison experiments, the YOLOV5 method proposed in this study for identifying Peucedani Radix combined with ExG feature segmentation of weeds was able to maintain a higher recognition accuracy under different weed density conditions compared to the YOLOV5 direct weed recognition method. In particular, the ability to segment weeds with smaller targets indicates that the method is robust for weed recognition. Compared with the maize and weed detection algorithm proposed by Quan et al. (2022), the method proposed in this study eliminates the weed labeling work and significantly reduces the workload of crop and weed detection. However, as shown in the orange dashed box in Figure 8A, the segmented connected domain becomes larger when weeds are present in adhesion, which causes the center of the connected domain morphology to deviate from the center of the single weed morphology, thus leading to ineffective spraying of herbicides onto the weed foliage during subsequent spraying. To solve this problem, in the future, we will explore how to extract single weeds based on the weed skeleton line based on the ExG segmentation to achieve the accurate positioning of single weed centroids.

In the PSO-Bezier trajectory simulation experiments, the trajectory profile generation time was only 0.35 s. Moreover, our proposed end-effector motion trajectory can save 10–15% of the motion distance with the same start and end points compared to the Lamé3 type motion trajectory proposed by Yang et al. (2021), which effectively reduces energy consumption. This demonstrates the superior performance of our algorithm. In addition, our proposed

PSO-Bezier trajectory can be adaptively parameterized according to plant characteristics, and this adjustment can enable this trajectory to be used for weeding operations of other important cash crops such as tomatoes and eggplants. However, in our study we idealized a fixed height of the Peucedani Radix plant, which in practice will lead to collisions between the end-effector and some of the taller Peucedani Radix seedlings, thus causing some damage to the Peucedani Radix crop. The reason for this phenomenon is that the camera cannot effectively obtain the exact height of the Peucedani Radix plants, a disadvantage of the camera capturing the ground image vertically. To improve this problem, we plan to use an RGB-D (Xu et al., 2017) depth camera to combine depth and image information to obtain information such as height and pose of Peucedani Radix plants.

In the actual trial, a total of 39 weed plants were not successfully sprayed with herbicide. This was attributed to two main reasons:

(1) The actual experiment was conducted using Peucedani Radix plants in August, and the weather on the day of the experiment was sunny with sufficient sunlight at noon. The overexposure of direct sunlight on the foliage of some of the Peucedani Radix plants and weeds caused serious loss of color features of Peucedani Radix in the images, and the Peucedani Radix plants and weeds could not be identified accurately. There were eight times that the Peucedani Radix plants and weeds could not be identified in the experiment. To improve this problem, in the future, we will take field images at midday and add overexposed images to increase the diversity of our samples to increase the generalization

performance of the model. In addition, we will also explore the use of shades or creation of a stable lighting environment to improve the recognition accuracy of Peucedani Radix plants and weeds.

(2) Due to the linear distance between the camera coordinate system and the origin of the parallel robot arm coordinate system, the agricultural robot platform needs to travel a fixed distance for accurate spraying operation after the camera identifies the Peucedani Radix and weeds. In this process, ground topography has a large influence on the Peucedani Radix and weed positioning. As shown in Figure 15, the ground is not flat and the camera plane is not parallel to the ground, which leads to a large deviation in positioning and makes it difficult for the nozzle at the end of the robot arm to accurately locate the weeds. Therefore, in the future, we will explore the use of a depth camera to identify and locate crops and weeds, and measure the deviation of the image position from the actual position by the angle A between the camera plane and the monopoly plane through the on-board altitude sensor, which can be used to compensate the position to achieve accurate spray positioning.

In summary, in this study, we applied the YOLOV5 deep learning network with ExG feature segmentation to a Peucedani Radix crop and weed detection system for the first time. We transformed crop and weed recognition into a binary classification problem, thus avoiding tedious weed labeling and improving the overall recognition accuracy, especially for small target weeds. In addition, our proposed PSO-Bezier weed avoidance trajectory better incorporated the biological characteristics of the Peucedani Radix plants compared to existing trajectories, saving the robot arm 10–15% of the movement distance, which will significantly reduce the energy consumption of the robot's work in practical applications. However, there remain limitations to our research, such as the inability to accurately identify Peucedani Radix plants and weeds under high exposure conditions and the lack of accuracy in herbicide spraying due to changes in the robot's body position. In future work, we plan to address these issues by expanding the image dataset for high exposure conditions, using RGB-D depth cameras, and building a position error compensation model.

6 Conclusions

An intelligent agricultural robot was designed to accurately spray weeds in Peucedani Radix fields with herbicide. The agricultural robot identified Peucedani Radix plants and weeds in the field using YOLOV5 combined with the ExG segmentation algorithm, used the PSO-Bezier algorithm to plan the optimal seedling avoidance spraying path, and executed this based on Peucedani Radix growth parameters obtained by identification. We evaluated the performance of the agricultural robots and algorithms through simulation validation combined with real-world operations. The following specific conclusions can be drawn:

(1) The overall precision and recall of Peucedani Radix detection in the Peucedani Radix field environment used for the experiment were 98.7% and 88.2%, respectively, and the map was 93.8% at IOU=0.5. When the MCDS was 50, the ExG feature segmentation algorithm can achieve 95% segmentation rate for weeds. In addition, the study evaluated the results of Peucedani Radix testing at different periods and found that the best results were obtained in August, when the plants were the largest.

(2) The study introduced a novel scheme for precise herbicide spraying by seedling avoidance, which used the PSO-Bezier algorithm to effectively achieve precise herbicide spraying in combination with the growth characteristics of Peucedani Radix. Compared with the Lamé3 transition trajectory, the trajectory generated by the arm running the PSO-Bezier algorithm can reduce movement distance by 10–15%, which effectively reduces the energy consumption required for arm operation.

(3) The effectiveness of the proposed algorithm was verified in actual field weeding experiments. The results showed that the success rate of field precision seedling avoidance herbicide spraying was 80.5%, the collision rate between the robotic arm end-effector and Peucedani Radix was 4%, the average detection time of the proposed algorithm for weeds and Peucedani Radix was 0.75 s per image, the average generation time of a single PSO-Bezier motion
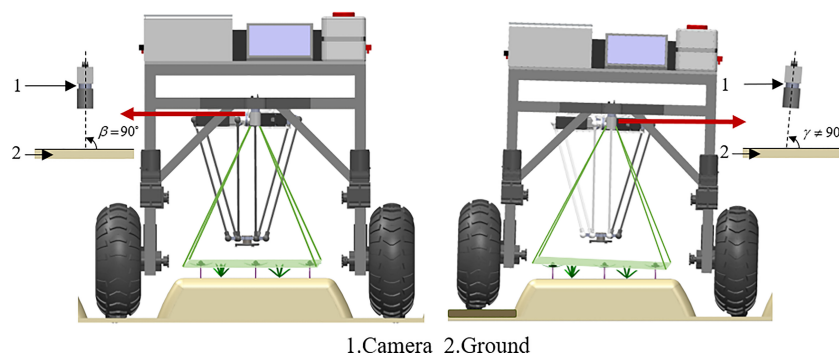

1.Camera 2.Ground

FIGURE 15
Reasons for the positioning error in camera recognition.

trajectory was 0.35 s, and the robotic arm could precisely spray a single weed an average of every 2 s.

Overall, the herbicide spraying method proposed in this study for precise seedling avoidance in a Peucedani Radix field was effective. The detection time of the proposed algorithm for weeds and the generation time of weeding trajectories are reasonable for agricultural robots. Also, this research can be widely applied to weed control in fields of tomato, eggplant, and other important crops worldwide. However, uneven terrain and large areas of weeds sticking between monopolies negatively impact weed center point positioning and accurate spraying. In addition, the precise timing of herbicide spraying in the field was not satisfactory. In future work, we will continue to study the above-mentioned points, improve the productivity of agricultural robots based on actual weeding operation scenarios, and contribute to the development of agricultural automation and precision agriculture.

Data availability statement

The raw data supporting the conclusions of this article will be made available by the authors, without undue reservation.

Author contributions

ZX designed the sorting robot structure, control system and experiments, conducted the data analyses, and drafted the manuscript. CC provided financial support for the article, designed the framework of the study, and acts as the corresponding author. WZ helped to design the framework of the study. LK implemented the software and helped to process the figures and tables. QK and AM helped in the design of the mechanical structure and prototype commissioning. DW helped in the design of the control system and tests. XW helped prepare materials and tests. All authors contributed to the article and approved the submitted version.

Conflict of interest

The authors declare that the research was conducted in the absence of any commercial or financial relationships that could be construed as a potential conflict of interest.

Publisher's note

All claims expressed in this article are solely those of the authors and do not necessarily represent those of their affiliated organizations, or those of the publisher, the editors and the reviewers. Any product that may be evaluated in this article, or claim that may be made by its manufacturer, is not guaranteed or endorsed by the publisher.

References

Ahmad, A., Saraswat, D., Aggarwal, V., Etienne, A., and Hancock, B. (2021). Performance of deep learning models for classifying and detecting common weeds in corn and soybean production systems. *Comput. Electron. Agric.* 184, 106081. doi: 10.1016/j.compag.2021.106081

Chang, H.-M., But, P.-P. H., Yao, S.-C., Wang, L.-L., and Yeung, S. C.-S. (1986). *Pharmacology and Applications of Chinese Materia Medica: (Volume I).* WORLD SCIENTIFIC doi: 10.1142/0284

Chavan, T. R., and Nandedkar, A. V. (2018). AgroAVNET for crops and weeds classification: a step forward in automatic farming. *Comput. Electron. Agric.* 154, 361–372. doi: 10.1016/j.compag.2018.09.021

Dos Santos Ferreira, A., Freitas, D. M., da Silva, G. G., Pistori, H., and Folhes, M. T. (2017). Weed detection in soybean crops using ConvNets. *Comput. Electron. Agric.* 143, 314–324. doi: 10.1016/j.compag.2017.10.027

Hamuda, E., Mc Ginley, B., Glavin, M., and Jones, E. (2017). Automatic crop detection under field conditions using the HSV colour space and morphological operations. *Comput. Electron. Agric.* 133, 97–107. doi: 10.1016/j.compag.2016.11.021

Hasan, A. M., Sohel, F., Diepeveen, D., Laga, H., and Jones, M. G. (2021). A survey of deep learning techniques for weed detection from images. *Comput. Electron. Agric.* 184, 106067. doi: 10.1016/j.compag.2021.106067

Li, N., Chen, Z., Zhang, X., and Liu, X. (2021). An ultra-fast bi-phase advanced network for segmenting crop plants from dense weeds. *Biosyst. Eng.* 212, 160–174. doi: 10.1016/j.biosystemseng.2021.10.008

Li, Y., Guo, Z., Shuang, F., Zhang, M., and Li, X. (2022). Key technologies of machine vision for weeding robots: a review and benchmark. *Comput. Electron. Agric.* 196, 106880. doi: 10.1016/j.compag.2022.106880

Özlüoymak, Ö.B. (2022). Development and assessment of a novel camera-integrated spraying needle nozzle design for targeted micro-dose spraying in precision weed control. *Comput. Electron. Agric.* 199, 107134. doi: 10.1016/j.compag.2022.107134

Partel, V., Kakarla, S. C., and Ampatzidis, Y. (2019). Development and evaluation of a low-cost and smart technology for precision weed management utilizing artificial intelligence. *Comput. Electron. Agric.* 157, 339–350. doi: 10.1016/j.compag.2018.12.048

Pharmacopoeia, C. (2010). *The state pharmacopoeia commission of PR China* Vol. 3 (Beijing: China Medical Science).

Picon, A., San-Emeterio, M. G., Bereciartua-Perez, A., Klukas, C., Eggers, T., and Navarra-Mestre, R. (2022). Deep learning-based segmentation of multiple species of weeds and corn crop using synthetic and real image datasets. *Comput. Electron. Agric.* 194, 106719. doi: 10.1016/j.compag.2022.106719

Quan, L., Feng, H., Lv, Y., Wang, Q., Zhang, C., Liu, J., et al. (2019). Maize seedling detection under different growth stages and complex field environments based on an improved faster r–CNN. *Biosyst. Eng.* 184, 1–23. doi: 10.1016/j.biosystemseng.2019.05.002

Quan, L., Jiang, W., Li, H., Li, H., Wang, Q., and Chen, L. (2022). Intelligent intra-row robotic weeding system combining deep learning technology with a targeted weeding mode. *Biosyst. Eng.* 216, 13–31. doi: 10.1016/j.biosystemseng.2022.01.019

Redmon, J., and Farhadi, A. (2018). YOLOv3: An Incremental Improvement. doi: 10.48550/arXiv.1804.02767

Strothmann, W., Ruckelshausen, A., Hertzberg, J., Scholz, C., and Langsenkamp, F. (2017). Plant classification with in-field-labeling for crop/weed discrimination using spectral features and 3d surface features from a multi-wavelength laser line profile system. *Comput. Electron. Agric.* 134, 79–93. doi: 10.1016/j.compag.2017.01.003

Sujaritha, M., Annadurai, S., Satheeshkumar, J., Sharan, S. K., and Mahesh, L. (2017). Weed detecting robot in sugarcane fields using fuzzy real time classifier. *Comput. Electron. Agric.* 134, 160–171. doi: 10.1016/j.compag.2017.01.008

Tang, J., Wang, D., Zhang, Z., He, L., Xin, J., and Xu, Y. (2017). Weed identification based on K-means feature learning combined with convolutional neural network. *Comput. Electron. Agric.* 135, 63–70. doi: 10.1016/j.compag.2017.01.001

The State Pharmacopoeia, C. (2010). *The state pharmacopoeia commission of PR China* Vol. 3 (Beijing: China Medical Science).

The State Pharmacopoeia Commission of P.R. China (1997). *Pharmacopoeia of the people's republic of China* (Beijing, China: Chemical Industry Press).

Utstumo, T., Urdal, F., Brevik, A., Dørum, J., Netland, J., Overskeid, Ø., et al. (2018). Robotic in-row weed control in vegetables. *Comput. Electron. Agric.* 154, 36–45. doi: 10.1016/j.compag.2018.08.043

Villette, S., Maillot, T., Guillemin, J. P., and Douzals, J. P. (2021). Simulation-aided study of herbicide patch spraying: influence of spraying features and weed spatial distributions. *Comput. Electron. Agric.* 182, 105981. doi: 10.1016/j.compag.2020.105981

Villette, S., Maillot, T., Guillemin, J. P., and Douzals, J. P. (2022). Assessment of nozzle control strategies in weed spot spraying to reduce herbicide use and avoid under-or over-application. *Biosyst. Eng.* 219, 68–84. doi: 10.1016/j.biosystemseng.2022.04.012

Xu, X., Li, Y., Wu, G., and Luo, J. (2017). Multi-modal deep feature learning for RGB-d object detection. *Pattern Recogn.* 72, 300–313. doi: 10.1016/j.patcog.2017.07.026

Yang, H., Chen, L., Ma, Z., Chen, M., Zhong, Y., Deng, F., et al. (2021). Computer vision-based high-quality tea automatic plucking robot using delta parallel manipulator. *Comput. Electron. Agric.* 181, 105946. doi: 10.1016/j.compag.2020.105946

Zhang, X., Wu, Z., Cao, C., Luo, K., Qin, K., Huang, Y., et al. (2023). Design and operation of a deep-learning-based fresh tea-leaf sorting robot. *Comput. Electron. Agric.* 206, 107664. doi: 10.1016/j.compag.2023.107664

Zheng, Y., Zhu, Q., Huang, M., Guo, Y., and Qin, J. (2017). Maize and weed classification using color indices with support vector data description in outdoor fields. *Comput. Electron. Agric.* 141, 215–222. doi: 10.1016/j.compag.2017.07.028

Zou, K., Chen, X., Wang, Y., Zhang, C., and Zhang, F. (2021). A modified U-net with a specific data argumentation method for semantic segmentation of weed images in the field. *Comput. Electron. Agric.* 187, 106242. doi: 10.1016/j.compag.2021.106242

Check for updates

Modeling of the control logic of a UASS based on coefficient of variation spraying distribution analysis in an indoor flight simulator

Adhitya Saiful Hanif[1], Xiongzhe Han[1,2]*, Seung-Hwa Yu[3], Cheolwoo Han[4], Sun Wook Baek[5], Chun-Gu Lee[3], Dae-Hyun Lee[6] and Yeong Ho Kang[7]

[1]College of Agricultural and Life Sciences, Interdisciplinary Program in Smart Agriculture, Kangwon National University, Chuncheon, Republic of Korea, [2]College of Agricultural and Life Sciences, Department of Biosystem Engineering, Kangwon National University, Chuncheon, Republic of Korea, [3]Upland Mechanization Team, National Institute of Agricultural Sciences, Department of Agriculture Engineering, Rural Development Administration, Jeonju, Republic of Korea, [4]Department of Agriculture and Biosystem, Korea Polytechnic, Gimje, Republic of Korea, [5]Department of Smart Agriculture, Korea Agriculture Technology Promotion Agency, Iksan, Republic of Korea, [6]Department of Biosystems Machinery Engineering, Chungnam National University, Daejeon, Republic of Korea, [7]Department of Crops and Food, Jeollabukdo Agricultural Research & Extension Service, Iksan, Republic of Korea

Introduction: In the past decade, unmanned aerial spraying systems (UASS) have emerged as an effective crop treatment platform option, competing with other ground vehicle treatments. The development of this platform has provided an effective spraying system that can be used on all crop types and in all weather conditions. However, related research has not been able to develop a UASS that can be operated in windy conditions with a low drift percentage.

Methods: In this research, spraying was simulated in an indoor flight simulator by considering flight speed, altitude, wind speed, wind direction, rotor rotation, interval, spraying pattern, and nozzle type, which were used as the parameters affecting the output value of the coefficient of variation (CV) of spraying. These parameters were referenced as properties that occur in the field, and using machine learning methods, the CV value was used as a dataset to develop a model that can execute pump opening by controlling the flow rate. There are four machine learning methods used, i.e. random forest regression, gradient boosting, ada boost, and automatic relevance determination regression which are compared with simple linear regression and ridge regression as linear regression.

Results: The results revealed that the random forest regression model was the most accurate, with R2 of 0.96 and root mean square error (RMSE) of 0.04%. The developed model was used to simulate spraying with pump opening A, which

connects two nozzles in front, and pump opening AB, which connects all four nozzles.

Discussion: Using the logic based on CV value and pesticide quantity, the model can execute the pump opening against the environment and UASS operation.

1 Introduction

Plant pests and diseases are the main factors responsible for a significant reduction in crop production, including crop yield and quality (Godfray et al., 2016). Guo et al. reported that pests, weeds, and plant diseases accounted for 30% of global crop losses annually (Guo et al., 2019). Therefore, measures must be taken to reduce the enormous impact of pests and diseases. Currently, the spraying of chemical pesticides on crops is the most widely used method for preventing and controlling diseases and pests (Chen et al., 2021; Sparks and Bryant, 2021; Zhang et al., 2021). Various methods have been developed to improve the spraying efficiency and control the effect of pesticides, such as ground spraying, aerial spraying, air-assisted spraying, and knapsack spraying (Qin et al., 2016; Pan et al., 2017; Wang et al., 2019).

In the last decade, the price of pesticides for plant maintenance has soared (Wilson and Tisdell, 2001). Moreover, the use of pesticides in the past year reached an average of 5–7 liters/ha (Maria Travisi et al., 2006). However, the inappropriate use of pesticides results in a decrease in productivity owing to decreased soil nutrients. In addition, the indiscriminate use of pesticides affects crop yield because pesticides affect soil nutrients, interfering with plant growth and directly affecting crop yield (Tudi et al., 2021). Accordingly, the impact of indiscriminately used pesticides is felt on crops. In addition, the exposure of pests and diseases to large quantities of pesticides results in the development of resistance. In some plant pests, this resistance can be passed on to the 5th–7th generation, increasing difficulties in controlling these pests via chemical control in the next planting periods (Shi et al., 2011). This indicates that the correct application of pesticide-based plant treatments can improve the quality of the plants. In addition, this can affect the productivity and optimal growth of plants on fertile lands (Kalia and Gosal, 2011). This indicates the importance of the appropriate application of pesticides in terms of quantity and accuracy of the needs of plants.

Spraying systems that utilize aerial vehicles have a greater application range and can overcome the negative impacts of pesticide use, as most of these impacts are related to the ground rather than air (Li et al., 2022). Compared to conventional spraying methods, such as knapsack sprayers or ground vehicles, unmanned aerial spraying systems (UASS) exhibit a greater spread distance (Maheswaran et al., 2020). However, as this system operates by

flying over the ground, it is susceptible to strong winds, which results in drift. In addition, owing to the maximum light payload and high energy output of the system, the power source, which is a battery, runs out quickly, resulting in a limited operational time. The use of a flexible platform makes it simpler to meet the intended needs. However, this platform encounters problems operating UASS for spraying fields in windy situations. Compared to conventional knapsack spraying techniques and ground vehicle plant protection, UASS exhibits significantly increased operational efficiency with reduced labor costs and pesticide exposure (Zhu et al., 2010). In addition, UASS exhibits numerous advantages, including a higher rate of pesticide penetration into the crop, owing to the ability of the rotors to overturn the leaves (Meng et al., 2019). To date, significant studies have been conducted on the use of plant protection techniques to reduce pests, such as the development of precision UASSs (Zhu et al., 2010; Li et al., 2022), autonomous ground vehicle plant treatment (Maheswaran et al., 2020), and in specific sectors, such as crop protection machinery for vegetables (Wang et al., 2019). Consequently, this has resulted in a significant increase in the use of plant-protection UASS.

The fundamental factor in agrochemical capacity control is the accuracy of the spray target in spray deposition pesticides. The use of a different platform slightly disrupts these fundamental plant protections; thus, it is essential to develop a new spraying system that will comply with applicable regulations. In addition, UASS manufacturers must consider variables that may emerge during operation (Chen et al., 2022; Huang et al., 2023). This is because ignoring these factors may reduce the effectiveness of UASS owing to malfunctions, such as drift (Lan and Chen, 2018; Liao et al., 2019; Hussain et al., 2022). Recently, UASSs have been widely employed in the agricultural sector and combined with cutting-edge technology to meet aerial spraying needs (Chen et al., 2022; Huang et al., 2023). In addition, research findings have been used as feature upgrades to develop new platforms. Typically, UASS developers do not produce upgraded components traded separately from the main platform, and they want to capitalize by increasing the selling value of their products by incorporating research features (Gregorio et al., 2014; Butler Ellis et al., 2017).

Pesticides are typically applied uniformly across the land. Even if not all areas of the agricultural land are infected and require treatment, the treatment requirements of disease-infected plants determine the pesticide dose. As the distribution of pests and

diseases determines treatment, the amount of pesticides sprayed is unevenly distributed. In contrast, a plant-targeted protection treatment with the right dose will enable the rapid completion of the process before the disease spreads throughout the land (Bottrell and Schoenly, 2018).

Previous studies have reported several limitations of each UASS category. Operation parameters are the main factors that are still an operational consideration. Rotor rotation is an advantage not exhibited by other sprayer systems (Meng et al., 2020), but should be considered in the operation of the UASS (Lan and Chen, 2018). Some UASS manufacturers advise that they should be operated in a conducive environment. This is because an unstable condition affects the effectiveness of the flexible platform; particularly, the use of the UASS during inclement weather may result in the uncontrollable loss of pesticides. Manufacturers have addressed this weakness by upgrading the system via the development of a new platform rather than the addition of feature-enhancing components, such as new control systems. To overcome the limitations of UASSs, their features must be improved to meet the needs of their users. For optimal performance, not only the quantity of pesticides required but target location requiring a specific treatment should be considered, and these must be fulfilled under any operating conditions or environment, indicating that the system must overcome all negative parameters for the UASS to complete the target as soon as possible before the spread of pests and diseases (Hanif et al., 2022).

The quality of effective spray width and overlap identifies the effectiveness of a UASS spray, as shown in the method in ISO 5682-1 (ISO (International Organization for Standardization), 2017a), and another indication is uniformity. The uniform distribution of pesticides on plants indicates a good spraying distribution and the safety of pesticide penetration on plants (Lv et al., 2019). The spray' uniformity across the nozzle's working width demonstrates an even distribution. This context has been demonstrated by the low coefficient of variation (CV), which has been reported that the maximum acceptable level of CV is 30% (Parkin and Wyatt, 1982; Richardson et al., 2004; Richardson et al., 2020). CV value obtained from overlapping between spray lines in the operation of spray distribution (Griesang et al., 2022). Nevertheless, a lower CV indicates a uniform and even distribution in agricultural spraying. The output is expected to meet the goal of spraying as uniformly as possible while using a minimum amount of pesticides.

The most common method for assessing these characteristics is by recording droplet deposition using water-sensitive paper (WSP) and conventional optical techniques to assess the droplet images of the WSP. The WSP can rapidly and easily calculate droplet deposition, coverage, and distribution (Zhu et al., 2010; Cerruto et al., 2019; Brandoli et al., 2021). However, it only qualitatively displays the occurrence of deposition, approximates the droplet size distribution portion, and cannot be used to investigate the dynamic. Cunha et al. evaluated the capability of the imaging systems of WSPs and found that most imaging systems cannot precisely measure the coverage density of droplets when the coverage rate exceeds 17%. Consequently, with the growing concern about the adoption and growth of UASS, it is essential to develop a specific standard method or equipment that can determine the spraying

deposition pattern of UASS, either in target or off-target regions (Cunha et al., 2012).

This study conducted UASS tests in an indoor simulator under varied controlled conditions, such as wind effect and UASS operation conditions, focusing on developing a spraying control system for row crops. Data collection as a modeling dataset in the indoor simulator had also been adapted to the layout of row crops in the field, with the same planting distance and planting rows in accordance with the standard planting of row crops. The main objective was to develop a machine learning-based model for spraying distribution and characteristic data using the indoor simulator analysis results. Most studies used indoor simulators to analyze the spray distribution characteristics of the UASS type, nozzle type, or spraying scheme. The specific objectives of this study were: 1) analyzing UASS operational conditions, such as flight speed, flight height, rotor rotation, and even spraying pattern, and environmental factors, such as wind condition, as the parameters that need to be considered during UASS operation and assign their values as condition variations, 2) conducting simulations using indoor flight simulators under various conditions to analyze the spray distribution characteristics, and 3) modeling the control system logic using the dataset generated by the simulation in the mission to obtain a uniform spraying distribution.

2 Materials and methods

2.1 Prototype instrumentation

2.1.1 Main platform (UASS)

The control system model in this study was developed using a Korean octocopter UASS platform. The SG-10P (Hankook Samgong Co. Ltd., Seoul, South Korea) UASS was used, as shown in Figure 1. This UASS employs four nozzles with an under-main rod rotor system rather than a series configuration like a boom sprayer. The unfolded dimension of the 8-rotor UASS is 1500 mm (length) × 2075 mm (width) × 700 mm (height) with a propeller diameter of 57.5 cm and a spray tank volume of 10.3 L. The system's

FIGURE 1
SG-10P UASS used as a prototype.

net weight (excluding the battery) is 10 kg, and the maximum take-off weight is 24 kg. Four nozzles are mounted below the four lateral rotators of the UASS with a horizontal spacing of 150 cm.

This nozzle placement enables spraying by collectively operating the front and rear nozzles separately. The tank capacity (10.3 liters) will affect the rotor rotation speed in spraying applications. This is because the volume of pesticides in the tank, which decreases with the operation, causes the adjustment of the rotor rotation to the same flight altitude. Increasing rotor rotational speed is the same as operating the UASS at a specific flight speed. The rotor rotation will increase with an increase in the platform's flying speed setting. In addition, the pitch angle of the platform on the SG-10P increases with an increase in the flying speed.

2.1.2 Type of nozzles used in UASS

Although the main body of the platform does not affect the spraying application, the nozzle type contributes to a high spray quality. Alternatively, this study selected AI series nozzles that have been modified and developed (Rural Development Administration, Jeonju, South Korea) and XR series nozzles 110015 type (TeeJet Technologies, Glendale Heights, USA) were selected. Table 1 shows the specifications of the two types of nozzles used.

The AI series nozzle can overcome drift but sprays larger-sized droplets, making crop penetration difficult. The XR series nozzle exhibits flexible specifications in terms of spray pressure. This nozzle type can better cope with drift when used in UASS for low-altitude spraying. Using the XR series nozzle at a high pump pressure enables smoother droplets and improved coverage. These two types of nozzles were used to investigate the possibility of using different types of nozzles in UASSs. These two nozzles are an option if the user uses a nozzle type with similar specifications.

2.2 Indoor simulator

The UASS performance data can be retrieved in two ways: 1. The direct application of the system in the field or land, but this method has the disadvantage of random and uncontrollable parameter values. 2. An indoor flight simulator was used in this study (Korean Agriculture Technology Promotion Agency, Iksan, South Korea; Supplementary figure 1). The indoor flight simulator enables the adjustment of the parameter values according to the needs of various conditions. The total operating conditions used in this study combined all operational and environmental parameters. The combined variations also included two types of nozzles and two types of pump openings, where pump opening A opens two nozzles connected at the front, and opening AB opens all four nozzles at the front and rear.

2.2.1 Spray distribution recording device

The most standard device for measuring the spread of plant treatment sprays was TeeJet water-sensitive paper (WSP) (TeeJet Technologies, Glendale Heights, USA). The WSP was layered with a yellow film, which changes to a dark blue color upon contact with droplets owing to the interaction of the bromophenol blue indicator on the surface of the WSP with water (Fox et al., 2003; Zhu et al., 2011). The area of the WSP that changes color indicates the deposition quantity (Semião et al., 1996; Sies et al., 2017). The primary constraint of the WSP is the inability of droplets of diameter below 50 mm to create a measurable stain (Semião et al., 1996; Hoffmann and Hewitt, 2005; Mahmud et al., 2016). The size of the WSP used was 50.26 mm × 76 mm, which can resolve droplet diameters of approximately ~30 μm. According to ISO 5682-1 (ISO (International Organization for Standardization), 2017a), measurements can be performed with devices that have an equal surface area, and in this study, WSP was used as a measuring device instead of petri dishes. In Figure 2, the use of WSP as a spraying distribution recorder was utilized in the indoor simulator by placing it in WSP placement as shown in Figure 2A and Figure 2B shows the spray result recorded on WSP from one of the simulations of AI series nozzle.

2.2.2 UASS attachment devices

The indoor simulators used in this study are suitable for obtaining controlled datasets required for model development

TABLE 1 Specifications of the AI and XR series nozzles used in developing the control system.

| Nozzle type	Specifications	Figure
AI series by RDA	• The optimal spraying pressure is between 4 and 8 bar. • The AI nozzle has a spraying angle of 80° which is good at overcoming drift. • It has a finer droplet size at high pressure • More capable of overcoming drift with larger droplet sizes.	
XR series by TeeJet	• It has excellent spray distribution over a wide range of pressures 15-60 PSI (1-4 bar). • The XR nozzle has 110° spray angles • Reduces drift at lower pressures and better coverage at higher pressures. • An excellent nozzle for Pulse Width Modulation Nozzle Control	
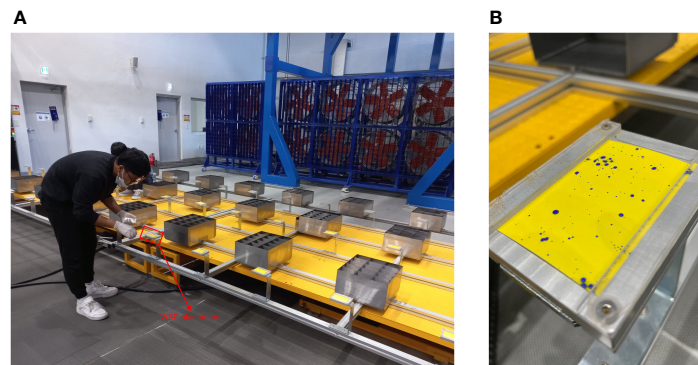
FIGURE 2
The use of WSP in recording spray distribution, **(A)** by installing WSP on the WSP placement layout, and **(B)** is one of the spray results from the AI series nozzle.

with machine learning methods. Although the UASS platform can be used directly in the field, the parameter values will vary according to the weather conditions during the tests. Therefore, the prototype platform was installed in an indoor simulator to get controlled parameter values. The main component where the UASS was placed in the simulator is the UASS attachment. The UASS attachment in the indoor simulator can fit on all types of UASS because it uses four combination rods that can rotate 360°, making it universal for various kinds of UASS. The four rods connected the main rod of the UASS to the simulator using a different-sized manufacture jig for each UASS.

The main jig functions to install and connect the UASS with the simulator. The diameter of the jigs matched that of the SG-10P main rods; four jigs were installed on each connecting rod simulator, which then adjusted the degree of rotation of the connecting rods. Owing to the nature of the universal simulator, which can be used on all types of UASS, this simulator also adjusts the system type of each UASS. The simulator can move forward and backward using a rail track whose speed can be adjusted through command control, and according to ISO 5682-1 (ISO (International Organization for Standardization), 2017a), the test shall be carried out with the spraying system moving towards the horizontal spray area, which is in accordance with the test method. In addition, considering that this type of UASS exhibits a different kind of flight system, with some of them adding speed by tilting the pitch angle, as well as increasing rotational speed, this indoor simulator can adjust the degree of roll, pitch and yaw tilt, each of which can be adjusted with paired UASS features. The UASS was installed in this indoor simulator by considering the operation and making the working direction perpendicular to the WSP, which was placed above the ground adjuster.

2.2.3 Ground height and fan generator adjustment

The height of the UASS spraying was not adjusted directly on the UASS attacher, but through the ground adjuster. This component enables the moving up and down of the distribution value recording device (i.e., WSP) and the adjustment of its height

according to the operating altitude of the UASS. To consider wind in the simulation, the simulator was equipped with a wind generator with three fans of two different sizes. In Supplementary figure 2, the fan in the center position has six blades, and the two fans on the sides have four blades, and the blowing direction of all fans can be adjusted by sliding with the equipped rolling wheels. First, the device must be calibrated to determine the maximum speed at 100% performance to adjust the wind speed. The calibration process was performed using a wind effect measurement system, which also records the value of the direction of the gusts. After calibration, the calibration scale was used to set the desired wind speed.

2.2.4 RPM recorder

The rotation of the rotor or propeller needs to be considered in the operation of the UASS because the resulting fluid dynamics are also one of the factors that affect the quality of the spraying distribution (Chang et al., 2023). Rotor rotation data was retrieved in two stages. The first stage was the estimation of the number of rotors rotations in rotations per minute (RPM) as a function of the flight speed, and the second stage was the rotor rotation value, corresponding to the reduction of tank capacity. Later the two will be correlated with each other because if the user uses a certain flight speed, the rotational speed when spraying will decrease as the UASS operates; for example, if the maximum rotational speed obtained when the UASS flies at 3 m/s is 3000 RPM, the speed reduces with a decrease in the tank capacity. The primary function of testing the flight speed against the rotational speed of the rotor is as a reference for the initial value for the linearity equation obtained from the second stage of the test.

2.3 Simulation process

2.3.1 Determination of the variable values

The properties of each parameter should be determined before the simulation is conducted in the indoor simulator so that the settings can be adapted to the parameter platforms in the simulator. However, some parameters, such as flight speed and altitude, can be

set directly in the simulator through the command control. The wind speed parameter must be set through the command control, as shown in Supplementary figure 3, with the calibration scale that has been performed. In addition, this command control also functions in signaling the simulator to start the simulation, stop the simulation, and emergency stop if an incident occurs in the simulation process.

The flight altitude in the simulator was not achieved by adjusting the UASS' height but by adjusting the height of the ground where the WSP was placed. The adjustment of the ground height was enabled by the hydraulic rod supports and the regulation of the height of the WSP placement. No precision measurement was provided on this hydraulic rod, so manual measurement using a laser rangefinder was performed. Figure 3 describes setting the operating spray height by measuring the distance between the WSP placement and the nozzle tip on the UASS. The flying height measurement was obtained from the total distance of the nozzle tip to the simulator floor minus the distance from the floor to the WSP placement. The distance between the nozzle tip and the simulation floor was 4 m, and the maximum distance from the WSP placement to the floor was 2 m, so the minimum flight height that could be achieved was 2 m.

Furthermore, to measure the parameters of the wind effect, the determination and setting were performed in the simulator, but first, the performance calibration of the wind generator was performed. The fan operating performance settings were performed through command control by specifying the percentage value of fan performance. Supplementary figure 4A shows a mini weather station used to calibrate the wind speed value generated by the fan. The primary function of this device was to capture wind properties, such as wind speed and direction, and this tool must be set to face the fan perpendicularly. Thereafter, the wind speed and direction values will appear and be recorded, as shown in Supplementary figure 4B. The values were recorded for ten variations to get a calibration value where the results obtained are 30% generator performance producing a wind speed of 2 m/s and 60% performance producing a speed of 4 m/s.

Another factor of the platform condition that affects the quality of spraying distribution is the rotor rotation condition that directly produces fluid dynamics at the bottom (Qin et al., 2016). This area is where the pesticide comes out of the nozzle towards the target crop. Thus, in addition to the wind blowing in the environment, the downwind produced by the UASS itself is also influential and must be addressed. Therefore, in this study, the rotor rotation factor was considered as one of the influential parameters.

Each UASS exhibits a different rotor rotation mechanism. Still, most UASS products use a higher rotor rotation mechanism combined with an increased pitch angle, directly proportional to the increased flight speed. In addition, during the spraying operation, the weight of the UASS will decrease as the pesticide is sprayed. This kind of UASS mechanism is similar to the theory outlined by González and Garanger, where the number of UASS rotor rotations will be directly proportional to the payload of the platform, and according to ISO 5682-2 (ISO (International Organization for Standardization), 2017b), the liquid should be measured by the volumetric degradation during the operation of horizontal surface spraying (González et al., 2011; Garanger et al., 2020). These two factors need to be processed to be used as one of the parameters, namely by determining the linearity between rotor rotation with flight speed and tank capacity. Thereafter, the value inputted into the system depends on the flight speed used; then, the rotor rotation parameter can be used with the theory of linearity against tank capacity.

2.3.2 Prototype installation in the indoor simulator

There are supporting components used to install the platform in the simulator. As shown in Figure 4, the SG-10P was modified as a UASS simulator using three types of jigs. Figure 4A shows the jig type that unites the UASS with the simulator with four jigs attached to each main rod of the SG-10P UASS. Figure 4B shows the jig supporting the optical sensor ROS-HT-W-25 (Monarch Instrument, Amherst, USA) that sends rotor rotation data to the data acquisition (DAQ) system, and Figure 4C shows the jig used to

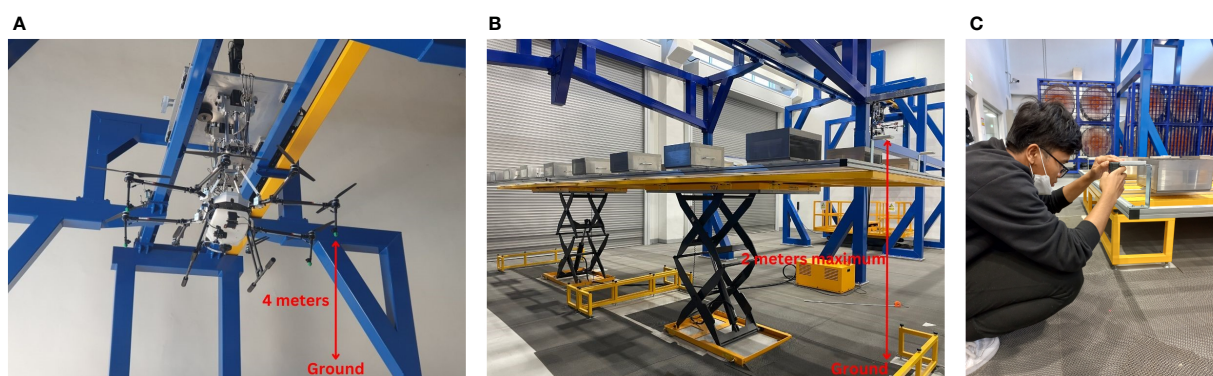**FIGURE 3**
Ground measurement to adjust the spraying altitude; **(A)** maximum distance of nozzle tip to the ground, **(B)** distance of WSP placement to the ground, **(C)** distance measurement process using laser distance stabilizer device.
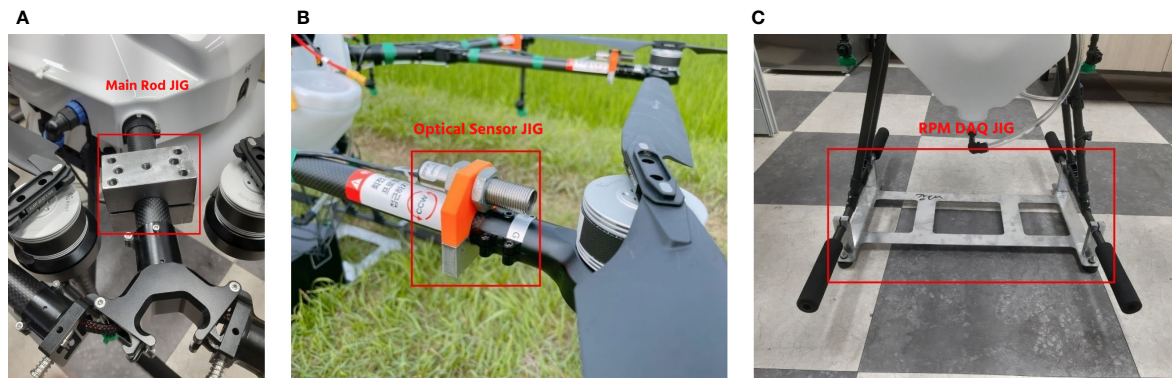
mount the RPM DAQ system (Rural Development Administration, Jeonju, South Korea).

The rotor rotation parameter was determined separately regarding the tank capacity and flight speed. A rotor rotation value was determined using a device that can record rotor rotation. Four optical sensors were placed on two rotors on the front side and two rotors on the rear side to calculate the number of rotations per minute. Figure 5 shows the RPM recorder device used in the preliminary test with reflection tape attached to the rotor to reflect the light that will be captured by the optical sensors. The RPM recorder was installed inside the UASS during data collection, so the tank capacity data collection accumulated 2 kg. To collect the rotor rotation data as a function of the tank capacity, the number of RPM was calculated at different tank capacities from empty to filled (maximum of 10 liters). Additional data were collected on the rotor speed as a function of the flight speed. Flying speeds of 2, 3, and 4 m/s were used, and this data was taken when the UASS tank was empty. The relationship between the rotor rotational speed against the tank capacity and flight speed was derived to obtain the equation used in the system in real time, and the tank capacity and flight speed were used to determine the RPM parameters.

2.4 Parameter analysis and simulation output

2.4.1 Schematic combination of parameter variations

Several factors need to be considered by farmers before operating the UASS in terms of weather and platform conditions. The selection of the performance of the UASS features was also prepared before spraying. A flight speed value of 3 m/s is sometimes used by farmers, so this value was used as the middle value in this study, so that the variation values were 2, 3, and 4 m/s, and the altitude value was set at 2, 2.75, and 3.5 m (Zhang et al., 2021). Thereafter, the wind speed value was set at 0, 2, and 4 m/s with a change in the angle of incidence of the wind to 0, 22.5, and 45°. The rotor rotation used in this study followed the previous data collection and determined the variation value of 2900, 3100, and 3300 RPM. The predetermined parameters were combined scientifically using the orthogonal matrix method. Using five parameters and three levels in this study enabled the extraction of the most effective combination data by the orthogonal matrix so that the simulations performed do not overlap each other and with
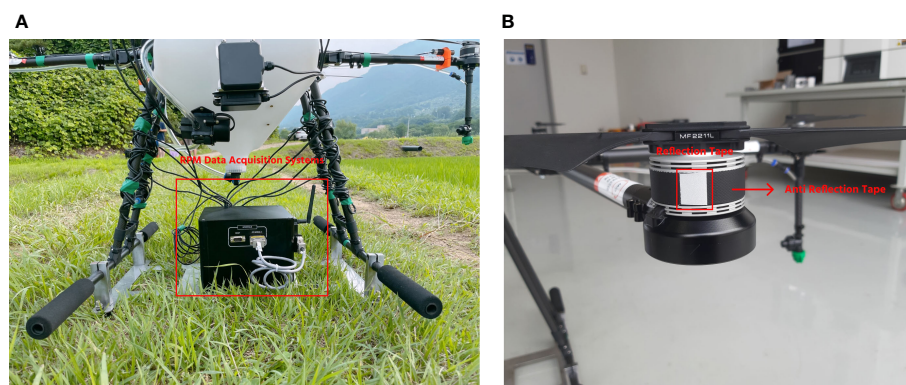
the maximum amount. The combination of parameters can be seen in Table 2.

2.4.2 Image processing, coverage, and coefficient of variation analysis

The combinations used in the setup of each device produce parameter values in a controlled environment. Using these conditions, the simulation was first performed using one of the nozzle types. One simulation run was performed for each combination of conditions, and the coverage output, which the WSP recorded, was simultaneously generated. To process the simulated WSP to obtain the coverage data, an image processing device was used to read the spray distribution on each WSP sheet. Supplementary figure 5 visualizes a set of tools that process WSP data into coverage values on each sheet. The attached camera processes the WSP spectrum indicated with water to calculate the number of droplets. The coverage value can be obtained by comparing the sprayed area on the WSP.

The coverage value data analyzed was extracted into CV values using two types of spraying patterns. The average result of the three rows of WSPs had output coverage values at the effective swath width. In Figure 6, seventeen WSP sheets were used to record the coverage value of one of the simulations, and the order of the WSPs represents the spraying route from the bottom to the top. The CV value calculation was done with three lines of spraying routes in one interval distance; thus, in Figure 6A, the CV value was calculated

using the same WSP arrangement with a race track spraying pattern with the same spray route direction. However, in Figure 6B, back-and-forth has the opposite direction on both sides. Based on the back-and-forth spraying rule (Carvalho et al., 2020), the WSP arrangement order can be rotated vertically to indicate the spray direction from top to bottom. Thus, CV values were calculated using coverage values with the order of values reversed on both sides.

The uniformity of pesticide spray distribution is one of the essential factors of pesticide application quality, which is indicated by the CV. The smaller the CV value, the more uniform the droplet distribution and the better the spray quality. The calculation formula is given in Equations (1) to (3) according to ISO 5682-3 (ISO (International Organization for Standardization), 2017c) as follows:

$$\bar{a} = \frac{1}{n} \sum_{i=1}^{n} a_i \tag{1}$$

$$s = \left[\frac{1}{n-1} \sum_{i=1}^{n} (a_i - \bar{a})^2 \right] \tag{2}$$

$$CV = \left| \frac{s}{\bar{a}} \right| \times 10 \tag{3}$$

Where $\bar{a}$ is the average coverage value at the effective swath width (in %), n is the number of effective swath widths, and a_i is the coverage value at the working width range (in %). Thereafter, s is the

TABLE 2 Combination of parameters with three levels randomized by orthogonal matrix.

| Flight Speed (m/s)	Altitude (m)	Wind Speed (m/s)	Wind direction (°)	Rotor rotation (RPM)	Result code
2	2	0	22,5	2900	11111
2	2	2	0	3300	11223
2	2.75	0	45	3300	12133
2	2,75	4	22,5	3100	12312
2	3,5	2	45	3100	13232
2	3,5	4	0	2900	13321
3	2	0	45	3100	21132
3	2	4	22,5	3300	21313
3	2,75	2	0	3100	22222
3	2,75	4	45	2900	22331
3	3,5	0	0	3300	23123
3	3,5	2	22,5	2900	23211
4	2	2	45	2900	31231
4	2	4	0	3100	31322
4	2,75	0	0	2900	32121
4	2,75	2	22,5	3300	32213
4	3,5	0	22,5	3100	33112
4	3,5	4	45	3300	33333
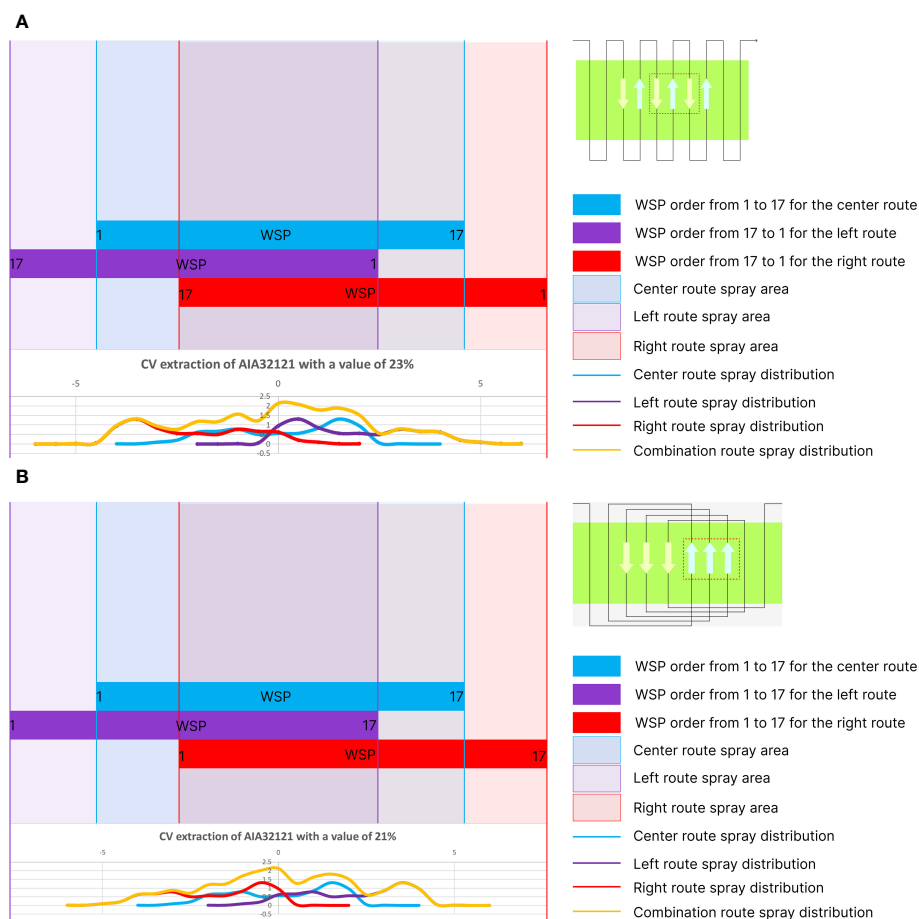
FIGURE 6
Processing coverage values into CV using: **(A)** back-and-forth and **(B)** race track spraying patterns.

standard deviation of each coverage mean, which is then divided by $\bar{a}$ to get the *CV* value (in %).

The influence of parameters used on the CV obtained through the indoor simulator should be validated, and the validation was performed using analysis of variance (ANOVA), which aims to determine the validity of each parameter used in obtaining the CV value.

2.5 Development of spray control system model

The main objective of the simulation was to obtain the CV under various spraying system operating conditions. The variation of conditions determined was in line with the simulation rules, namely using an orthogonal matrix design that enables these combinations to cover all conditions of the various levels specified. Thereafter, this output data was used as the dataset to determine what treatment should be executed to provide a uniform spraying distribution if values are outside the variation of conditions.

In this study, two methods were used to develop the prediction model for the operating state of the UASS: the first method uses

linear regression, and the second method is machine learning. Two types of linear regression methods were selected, namely simple linear regression and ridge regression, and four types of machine learning (random forest regression, ada boost, gradient boosting, and automatic relevance determination regression (ARDR)). The R^2 and root mean square error (RMSE) values of these two methods were compared. During the development of the model, 70% of the dataset was used for calibration and 30% for validation.

The number of datasets used in calibration significantly affects the accuracy of the resulting model. The ability of the model to find a regression function to predict the situation improves as the dataset of variation results increases. Therefore, the datasets obtained during the simulation were combined by giving the identity of each output so that they were not mixed up, considering that the same conditions were used in two types of nozzles. The datasets of the AI series nozzle and XR series nozzle were merged by representing the AI nozzle with number 1 and XR with number 2. In addition, the datasets were merged on the spraying pattern used in processing the coverage value into CV, namely back-and-forth represented with number 1 and race track with number 2. After combining the nozzle types and spraying patterns, the total dataset for pump opening A was 648, and 648 for pump opening AB. The pump opening here is an option that will be the actuator in

the control system, where pump A operates the front nozzle and pump B operates both rear nozzles. The control system has actuators with openings A and AB; therefore, the two datasets obtained from the simulation of different openings cannot be merged for modeling. These two pump openings will have different equations and be used as a logic model in determining which pump opening (A or AB) is better used in determining the real-time operating state of the UASS.

3 Result

3.1 Equation of RPM parameter

The combination of the flight speed, altitude, wind speed, wind direction, and RPM parameters are shown in the orthogonal matrix (Table 2). The three levels of each parameter were determined by taking the value often used by farmers in operating the UASS as the center value, followed by the two upper and lower border values. The rotor rotation value was measured to calculate the RPM of each rotor at different flying speeds and tank capacities.

Two types of RPM data collection methods were conducted in the preliminary test to determine the parameter values. The first test involved calculating the rotational speed with a change in the flight speed, both of which exhibited a linear performance (Figure 7A): the rotor rotation value increases with an increase in the flight speed. The rotor rotation values were calculated using the resulting linearity formula value at speeds of 1 to 5 m/s at an increase of 1 m/s for data processing purposes.

In addition, it is essential to understand the relationship between the rotational speed and tank capacity, as the number of rotor rotations is directly proportional to the weight of the UASS. The results revealed that the rotor revolutions decreased with a decrease in the tank capacity to adjust the flight altitude. Under full tank conditions where the UASS is in maximum payload, the resulting rotational speed was 3400 RPM, which exceeds the rotational speed of the specified maximum flight speed parameter of 3 m/s (Figure 7B). Therefore, the RPM parameter was derived using the tank capacity and flight speed.

The data for the two variables (flight speed and tank capacity) were processed using the statistical analysis software Minitab (ver.

20.3, Minitab, LLC., State College, USA) application to obtain equation linearity, as expressed in Equation (4) as follows:

$$RPM = 2574.3 + 122.2v + 88.36m \qquad (4)$$

Where RPM value is determined by v as flight speed (m/s) and m as tank capacity (liter), which is multiplied by a constant value, and an interception value is given, which was derived using the regression method, the R-squared value was 87.77%, indicating that the model was quite valid and can be used.

Thereafter, this equation was used as one of the parameters in the system control, where the flight speed and tank capacity can be input in real time so that the calculation can be performed as the UASS operates.

3.2 Comparison of the spraying distribution under different nozzles and spraying patterns

Simulations were performed using the indoor flight simulator based on all the predetermined parameters. The combination with code 32121, primarily used by farmers, was analyzed at a flight speed of 4 m/s, an average height of 2.75 m, no wind effect, and an average rotor rotation of 2900 RPM. In Figure 8, the coverage value was obtained from a simulation where the UASS moved and operated the spray over the three rows of WSPs arranged on the layout.

The characteristics of the AI nozzle, which can spread further and spray large-diameter droplets, are shown in Figures 8A, B, where both A and AB openings exhibit a wide spray spread of up to 6 m. At pump opening A, the spread on the left side indicates a coverage value of above 2%, which can be attributed to the anomalies of nozzles. The spray distribution results of the TeeJet XR series nozzle in openings A (Figure 8C) and AB (Figure 8D) revealed that the uniformity of the distribution was high at a distance of 1–1.5 m from the center point. The shape of the distribution was consistent with the spray mechanism: there was a more significant amount at the center owing to overlapping from both sides of the nozzle. The coverage of pump opening A at the center point was approximately 1%, and that of opening AB was 10%. There was an anomaly with pump opening AB, in which water
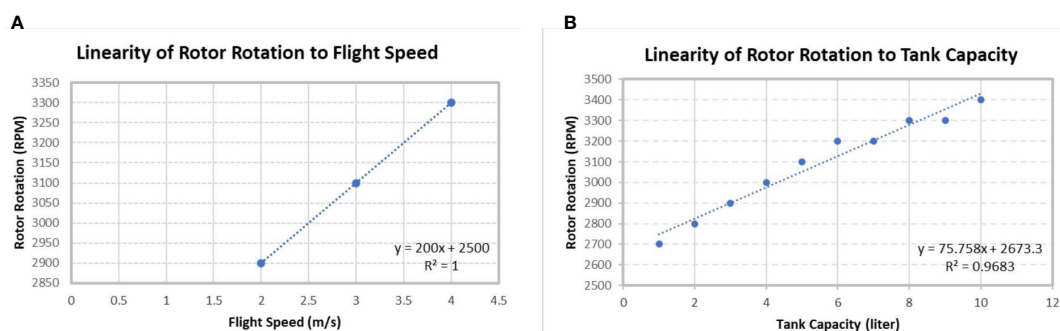

FIGURE 7

Linear graph of the relationship between **(A)** flight speed and rotor rotation and **(B)** tank capacity and rotor rotation.
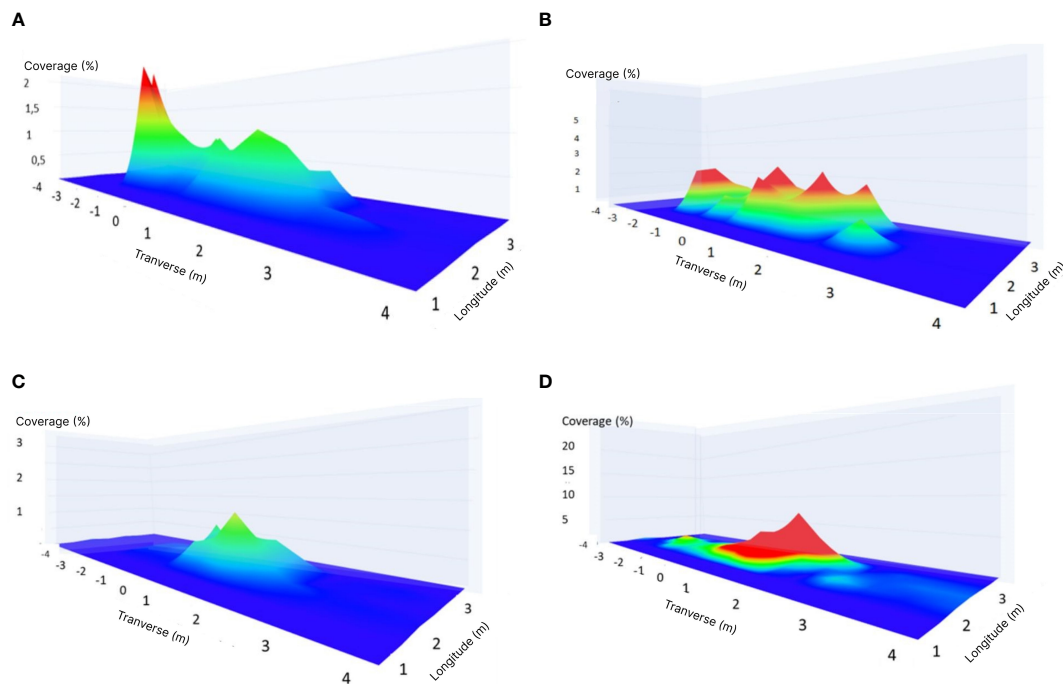
FIGURE 8
Mapping of the spray distribution under general conditions with **(A)** AI series pump opening A, B. AI series pump opening AB, **(C)** TeeJet XR series pump opening A and **(D)** TeeJet XR pump opening AB.

that should be sprayed actually drips by the time the UASS reaches the spray point, resulting in a significant increase in the diameter of the droplets that fell on the WSP and an increase in the coverage to 10%.

3.2.1 CV value of race track spraying pattern at 1−9 m intervals

The race track spraying pattern exhibited good CV values at narrow intervals. Figure 9 shows the CV results using the race track spraying pattern. AI series nozzle opening A in the resulting graph indicates that the CV value was good up to an interval of 4 m under some conditions. However, the CV of opening AB on the AI series nozzle type is<30% at high intervals of up to 9 m under some conditions. The CV results generated from the TeJeet XR series nozzle opening A indicate very rare CV values of<30%, which were even below standards under some conditions. However, the CV result of opening AB on TeeJet XR series, with CV values of<30% at scattered intervals, as in the simulation results of TJAB23123, where the standard CV was obtained at intervals of 1–5 m and 8–9 m.

3.2.2 CV value of back-and-forth spraying pattern at 1−9 m intervals

The back-and-forth spraying pattern exhibited improved distribution with CV values of<30% for pump opening A on both nozzle types than the race track spraying pattern, as shown in Figure 10. With pump opening A, the AI nozzle showed CV values of<30% up to an interval of 6 m under some conditions and

exhibited CV values of<30% up to 9 m for both openings. The Tejeet XR series nozzle showed good CV values under wide intervals of up to 7 m with pump openings A under some conditions. An interesting phenomenon was observed in the AB pump opening with the Tejeet XR series nozzle exhibited a CV value of<30%, which is very rare and even tends to be narrower than that of A pump opening, from 1–3 m.

3.3 ANOVA analysis to validate the contribution of each parameter to the CV results

Based on the CV results on all range intervals, the variance analysis of each parameter was performed by merging all the data using the output CV value. The results revealed that parameters with a P-value of less than 0.05 exhibited a high relationship with the CV value. In contrast, parameters with a P-value above 0.05 were considered not to influence the CV value. Supplementary Tables 1–4 show the results of the ANOVA tests conducted on each nozzle type and pump opening type. In Supplementary Table 1, which is the ANOVA of the AI series nozzle opening A, only the single parameter of wind direction has a P-value >0.05, and the parameter combination between RPM and flight was the only one that did not exert on the CV values (P-value >0.05). While in the AI series nozzle opening AB presented in Supplementary Table 2, only the parameter combination of wind direction and flight speed had a
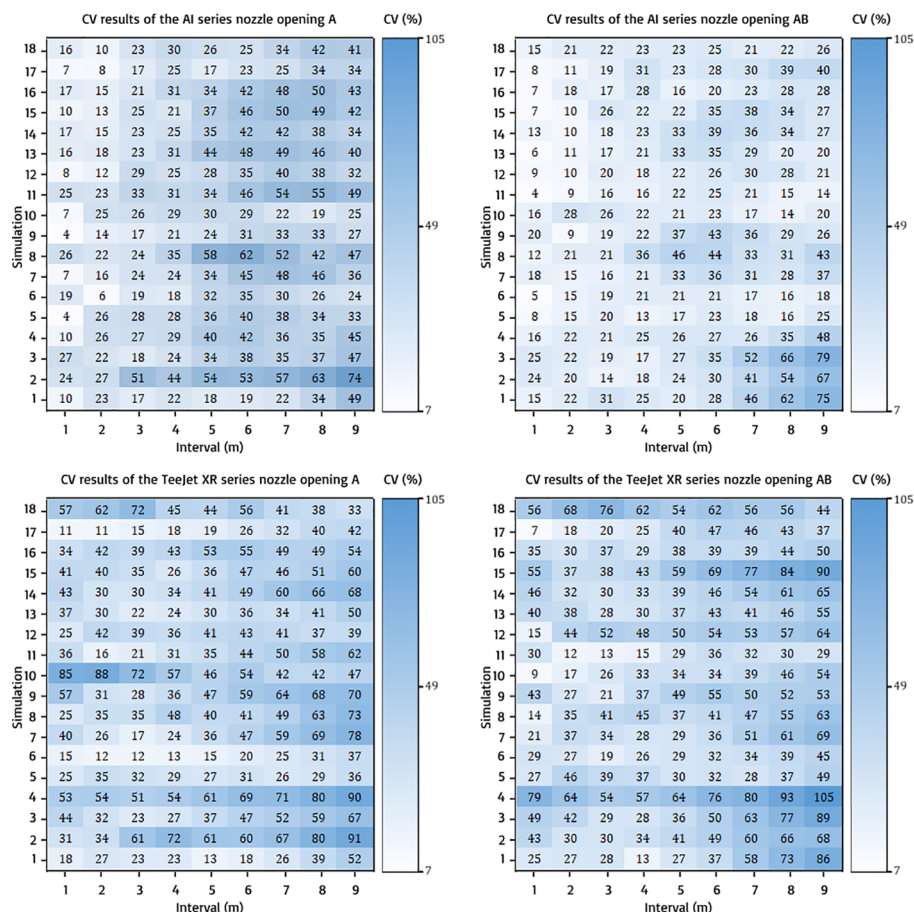
FIGURE 9
CV results of race track spraying pattern on all nozzle types and openings.

P-value >0.05. Referring to Supplementary Table 3, which analyzes the TeeJet XR series nozzle opening A, wind direction as a single parameter and its combination with flight speed has a P-value >0.05. In the ANOVA results for the TeeJet XR series nozzle opening AB represented in Supplementary Table 4, only the single parameter RPM and its combination with flight speed had a P-value >0.05. In this condition, wind direction significantly influenced the formation of CV values.

In addition, the combination of parameters in generating CV values was determined from the three-parameter levels used in the simulation. Some parameter combinations that have a P-value >0.05 produced similar CVs at each parameter level. Similar CV values, even with different levels, indicate that the combination of parameters does not have an extra impact on CV establishment. Most of these indications were generated by the wind direction and RPM parameters. The wind direction parameter has a zero value at one of its levels. In contrast, the RPM parameter had settings that were not constant in the simulation because it was done manually by the pilot. These two circumstances allow the combination of wind direction and RPM parameters to not highly influence the establishment of CV values.

3.4 Modeling of the control system based on the CV results

Obtaining data on the effects of variables on the output value is one of the crucial steps in developing the control system model; if the parameters that have been determined have a low level of influence on the output, then model development will be futile. Thus, the effects of the parameters of the CV value were confirmed, and the model was developed using each of the aforementioned methods. The following are the models generated from the six types of modeling used in this study. Modeling was divided into two for the CV output of each pump opening during simulation. The system control model was developed using four types of nonlinear models (random forest regression, ada boost, gradient boosting, and ARDR) and two types of linear models (simple linear regression and ridge regression). Modeling was performed for the different pump openings because both were actuator options. The y-axis and x-axis in Figures 11, 12 represent the predicted CV and actual measured CV, respectively. The predicted values were used to plot the predicted fit line to the actual measured CV values. Each figure below has an R-squared value representing the prediction
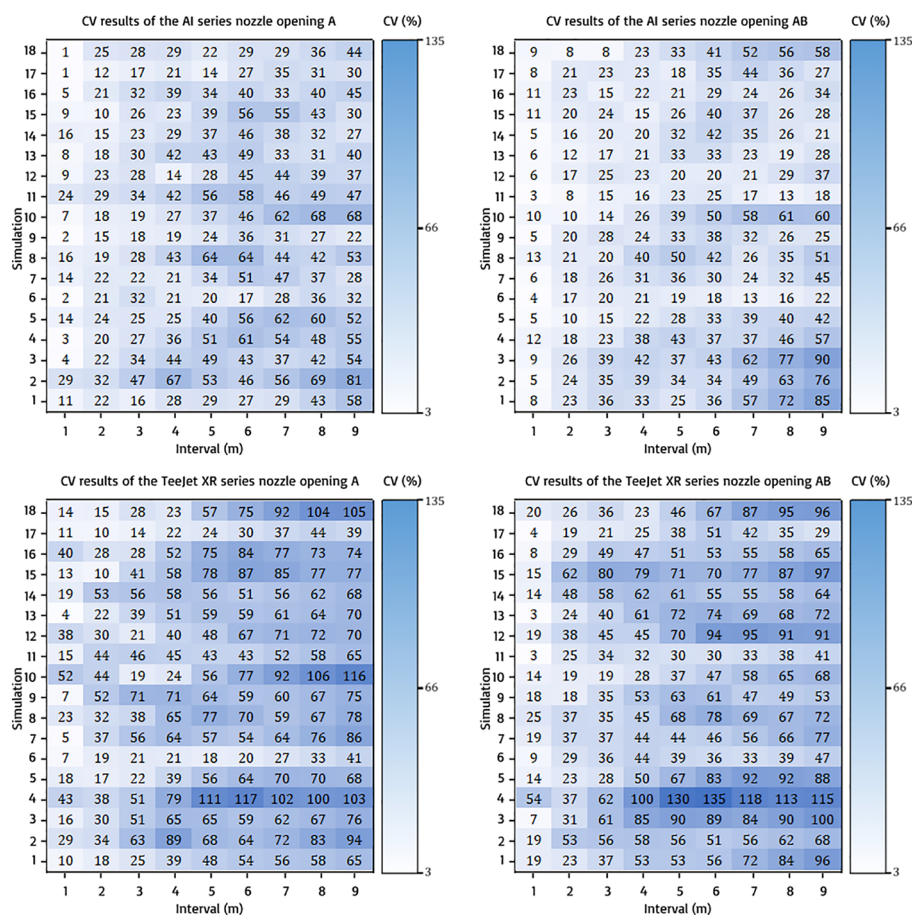
FIGURE 10
CV results of back-and-forth spraying pattern on all nozzle types and openings.

accuracy, and the RMSE represents the prediction error. Figure 11 shows the results of nonlinear regression and linear regression calibration for CV opening A, and Figure 12 shows the result for CV opening AB. The random forest model exhibited the best accuracy ($R^2 = 0.96$) and the lowest error value (RMSE = 0.04%) for both A and AB pump openings. The R^2 values of the ARDR model for pump openings A and AB were 0.48 and 0.53, respectively, the lowest among the three machine learning models, with RMSE of 0.15% for both pump openings, which was larger than those of the others. Under the linear regression models, the ridge regression model exhibited an R^2 value of 0.57 for pump opening A, which was slightly higher than that of the simple linear regression for the same pump opening. However, both exhibited the same error values for pump openings A (RMSE = 0.14%) and AB (RMSE = 0.15%).

The developed models were validated using 30% of the dataset not included in the model calibration dataset. Figure 13 shows the validation result of nonlinear regression and linear regression for CV opening A, and Figure 14 shows the validation result of the models for opening AB. The random forest model did not exhibit the best accuracy in the model validation result for CV opening A. The R^2 value of the validation of the gradient boosting model for pump opening A was 0.74. Although this R^2 value of the gradient boosting model was the same as that of the random forest. However, the

RMSE of random forest remained the best among other validation models at 0.05%, which is smaller than that of gradient boosting (0.12%). In the validation for CV opening AB, as shown in Figure 14, the random forest still performed best compared to other models with an R^2 value of 0.82 and RMSE of 0.09%. For the nonlinear models, the ARDR model exhibited the lowest R^2 and RMSE values for pump opening A (0.53 and 0.14%, respectively) and pump opening AB (0.56 and 0.15%, respectively). The linear regression models did not exhibit improved R^2 or RMSE values for calibration and validation compared to the random forest regression model. The simple linear and ridge regression exhibited poor R^2 and RMSE values for model validation. The R^2 and RMSE of the simple linear model for opening A were 0.5 and 0.14%, respectively, and those of the ridge regression model were 0.45 and 0.15%, respectively; for pump opening AB, the R^2 and RMSE of the simple linear model were 0.54 and 0.15%, respectively, and those of the ridge regression model were 0.55 and 0.16%, respectively. Accordingly, the validation R^2 value of each test process was generated, which strengthens the validity of the model that has been formed.

Among the models used to predict the CV values, the control system was modeled using the model with the best accuracy (R^2) and error (RMSE) values (i.e., the random forest regression model). Particularly, the residual distribution values during calibration and
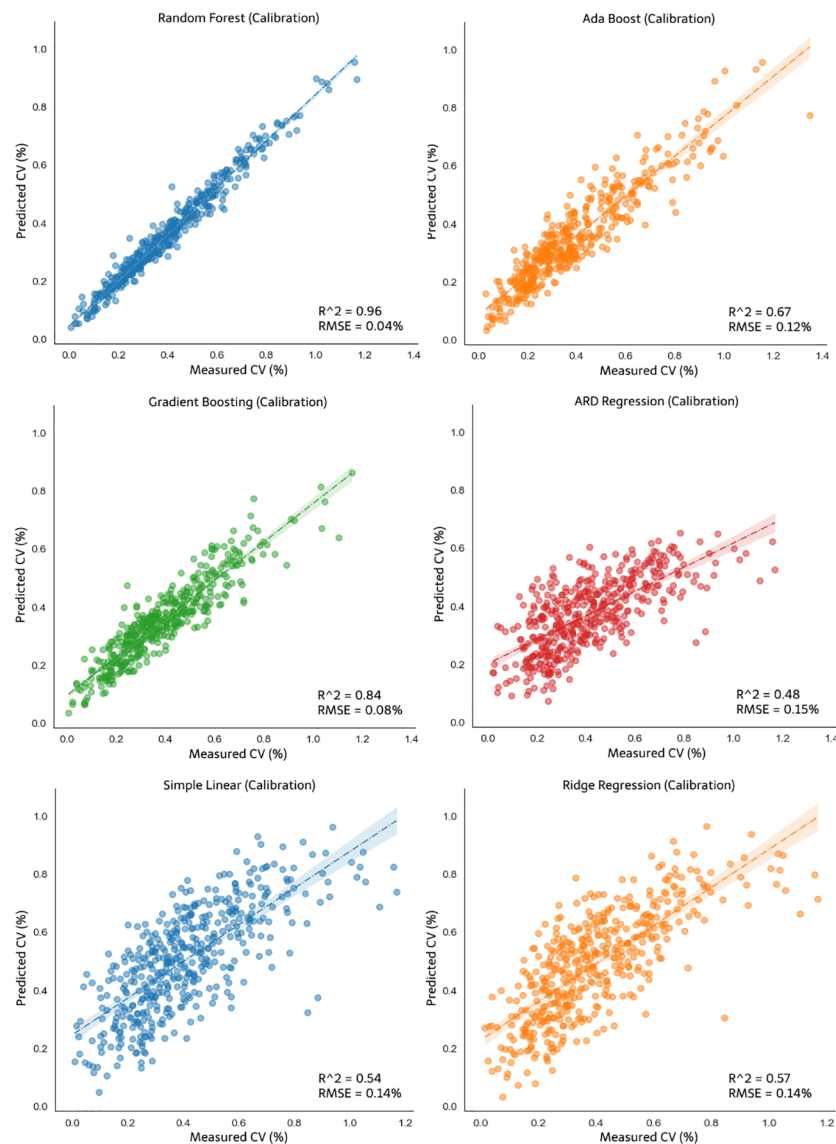
FIGURE 11
Calibration of the nonlinear models: random forest, ada boost, gradient boosting and ARDR, and linear models: simple linear and ridge regression for CV opening A.

validation are presented in Figure 15. The x-axis of the two figures illustrates the predicted CV value obtained during calibration and validation, and the error between the predicted value and the actual CV value is presented on the y-axis. Figure 15A shows the residual graph from the random forest regression modeling using pump opening dataset A. The error value was balanced, ranging from -0.3 to 0.4% CV. However, most errors occurred close to the CV number equal to 0, which illustrates an R^2 of 0.96 for calibration and an R^2 of 0.72 for validation. In Figure 15B, the prediction error value for the modeling of the pump opening AB exceeds -0.5% during the validation process. However, the R^2 values for calibration and validation are higher than those in Figure 15A, where $R^2 = 0.97$ for calibration and $R^2 = 0.77$ for validation.

Python-based computational simulations were performed using a random combination of parameter values. This random combination was obtained using the orthogonal matrix method to obtain the most effective combination value from several levels of values of the eight parameters used, including flight speed, altitude, wind speed, wind direction, RPM, interval, spraying pattern, and nozzle. Each combination of parameter values that have been formed was used as a simulation condition for the random forest regression model for modeling both pump openings A and AB. Subsequently, both results of CV values from openings A and AB were used to provide a frame of reference in developing logic in the system to determine which pump opening can better fulfill the needs of the pesticides in the field. In this study, the CV value was first prioritized, where a value of less than 30% was considered as the best spray quality, whereas a value above 30% was assumed to be an unusable value. However, spraying must still be performed even if the two pumps cannot overcome the situation under certain conditions, so the second priority was applied in this circumstance to use the minimum amounts of pesticides possible to meet crop maintenance needs.
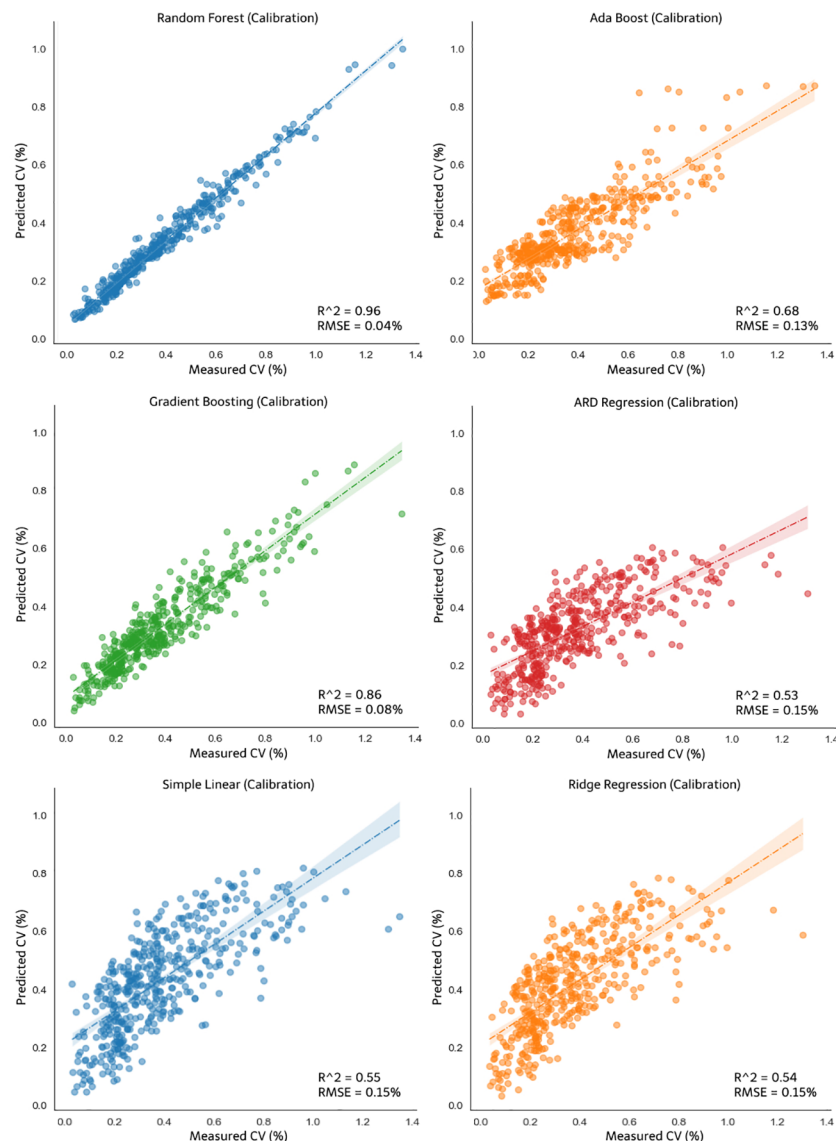
FIGURE 12

Calibration of the nonlinear models: random forest, ada boost, gradient boosting and ARDR, and linear models: simple linear and ridge regression for CV opening AB.

Table 3 shows the simulation results conducted using the AI series nozzle under the spraying pattern race track, and the spraying distance was 8 m wide. The operating and environmental conditions were set using a speed of 3 m/s, flying height of 2 m, wind speed varied from 2.1 m/s, 2.7 m/s, 3.5 m/s, to 4.0 m/s, and random wind direction from 15° for minimum value to 45° for maximum value. Table 3 indicates that the CV value from the pump opening model A and AB in condition number 15 was less than 30%, then the decision given is to only open pump A where this logic is the same as the first priority. In addition, in condition number 1, when the pump opening model A produced a CV of above 30%, and the AB opening model produced a CV of less than 30%, the decision given is to open the AB pump where the pump opening model A does not meet the priority criteria. The second priority regarding providing the minimum possible pesticide treatment can be seen in condition number 9, where both pump

opening models produced CVs greater of above 30%, then the decision given is to open pump A. Practically opening pump A will provide a lower flow rate than opening both pumps and automatically, the pesticide is expelled at the minimum amount. Table 4 shows the same simulation results when the XR series nozzle was used with a back-and-forth flight pattern at a spraying distance of 1 m under the same operating conditions and environment as the AI series nozzle simulation. Through the same logic commands as the XR series nozzle simulation, Table 4 shows the following simulation results. For instance, in column number 1, when the CV of opening A exceeds 30% and that of opening AB is lesser, the decision given is to select pump opening AB. In all decisions that open only pump A, both actually had a CV value in the standard set, but when the state of both pump openings had a CV value of less than 30%, then the second priority applies, which is to choose the opening with a smaller flowrate value,
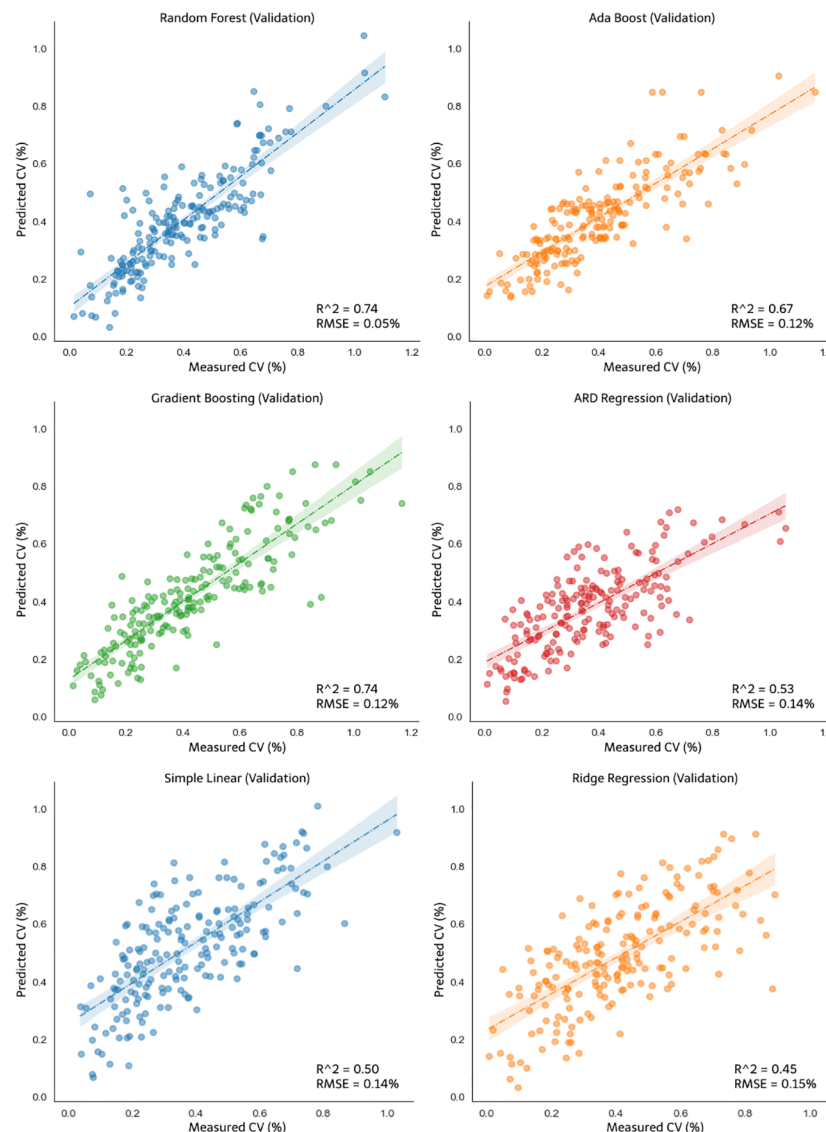
FIGURE 13
Validation of the nonlinear models: random forest, ada boost, gradient boosting, ARDR, and linear models: simple linear and ridge regression for CV opening A.

namely pump opening A, to reduce the quantity of pesticide used. In accordance with both simulation results from Tables 3 and 4, the pump opening is in line with expectations in addressing the operating conditions of the UASS.

4 Discussion

Nozzle opening control systems to support the requirements of precision and uniform pesticide spraying in UASS were modeled based on the occurring parameters and are most influential in pesticide spraying operations. The determination of parameters was based on literature studies and UASS operating standard settings, both from nozzle type, pump pressure, pesticide dilution ratio, and spraying interval to UASS operating properties, such as flight speed, spray height, spraying pattern used, and fluid dynamics that occur,

to produce sprays that must also meet standards, such as uniformity and precise quantity (Zhang et al., 2021). These conditions, particularly the UASS operating properties, cannot be determined based on user preferences. However, crop treatment operations must be adapted to the current needs in the field. In some cases, as reported by Martin et al. in 2019, the operation of UASS is highly influenced by weather conditions. They also analyzed the environmental conditions, particularly wind properties, that affect the results of the spray patterns and droplet spectra from UASS; thus, some are recommended to be kept from being operated in windy weather conditions (Martin et al., 2019), which are similar problems and phenomena that prompted this research.

The previously mentioned parameters were used as a reference in determining the parameters used in the simulation so that the environmental conditions can be adjusted according to the values of the predetermined parameters when using machine learning, where
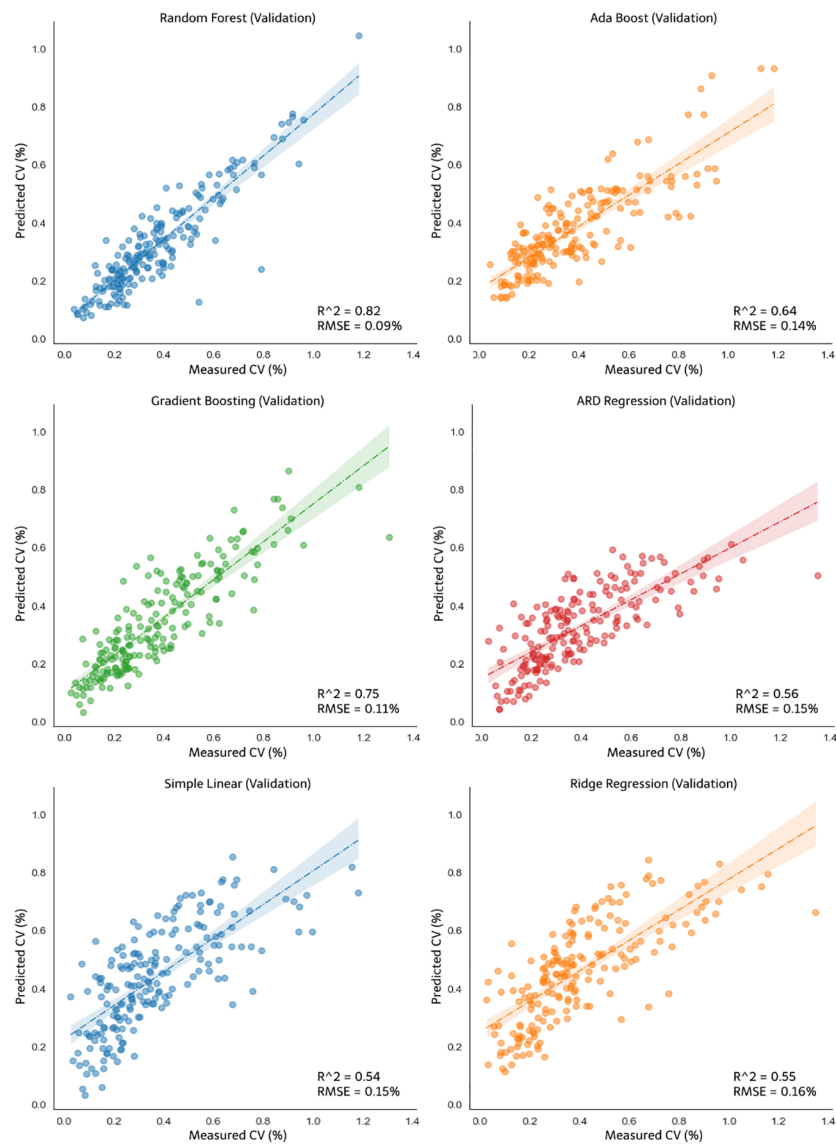
FIGURE 14
Validation of the nonlinear models: random forest, ada boost, gradient boosting, ARDR, and linear models: simple linear and ridge regression for CV opening AB.
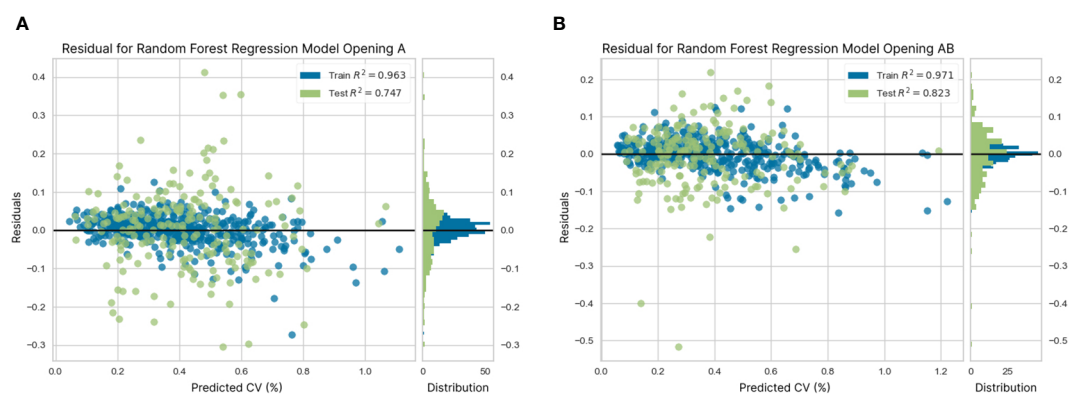

FIGURE 15
Distribution of residuals from random forest regression modeling **(A)** with pump opening A and **(B)** pump opening AB.

TABLE 3 Simulation results of random forest regression for AI series nozzle.

No.	Parameter condition								CV (%)		Decision
	FS (m/s)	Alt. (m)	WS (m/s)	WD (°)	RPM	Interval (m)	FM	Nozzle	A	AB	
1.	3	2	2.1	15	2900	8	2	1	32.8	25.7	A+B
2.	3	2	2.1	29	2900	8	2	1	32.8	25.2	A+B
3.	3	2	2.1	37	3100	8	2	1	43.6	29.3	A+B
4.	3	2	2.1	45	3100	8	2	1	43.6	29.3	A+B
5.	3	2	2.7	15	2900	8	2	1	32.8	25.7	A+B
6.	3	2	2.7	29	2900	8	2	1	32.8	25.2	A+B
7.	3	2	2.7	37	3100	8	2	1	43.6	29.3	A+B
8.	3	2	2.7	45	3100	8	2	1	43.6	29.3	A+B
9.	3	2	3.5	15	3100	8	2	1	39.9	30.1	A
10.	3	2	3.5	29	3100	8	2	1	40.1	29.0	A+B
11.	3	2	3.5	37	2900	8	2	1	26.6	23.8	A
12.	3	2	3.5	45	2900	8	2	1	26.6	23.8	A
13.	3	2	4.0	15	3100	8	2	1	39.9	30.1	A
14.	3	2	4.0	29	3100	8	2	1	40.1	29.0	A+B
15.	3	2	4.0	37	2900	8	2	1	26.6	23.8	A
16.	3	2	4.0	45	2900	8	2	1	26.6	23.8	A

a dataset must be formed and used in the calibration and validation process. Obtaining CV values in this simulation requires a long data processing series and particular circumstances must also be discussed to validate this study. The rest of this chapter will go over the phenomena that occur during project development until there are variables that affect the output data. Furthermore, the discussion continues with the practical application of the results of this study to enable the evaluation of the practical application of the model to ensure its application in agriculture.

Various observations were made during the simulation, as shown in Figure 8D, where one of the simulations using the XR series nozzle produced an abnormal coverage value. A similar thing can happen in simulation when the operational conditions of the simulator are unstable. This specific kind of data can still be used because there is an R^2 value in modeling that indicates the accuracy of the prediction when the dataset is used, as well as the accuracy of other machine learning methods (Wen et al., 2019) and this type of phenomenon contributes to the development of the model while considering a situation that may occur in actual use.

The ANOVA results revealed that all the parameters in calculating the CV value of each spraying pattern and interval range were valid with a P-value of less than 0.05 (Wang et al., 2023), indicating that the parameters significantly affected the output results (i.e., CV value). Few parameters, whether used as a single value or combined, have a P-value above 0.05. This begs the question of whether such parameters should still be used or whether they can be eliminated. RPM and wind direction are the only parameters with a P-value greater than the default. First, the parameters are discussed to discover the facts in the field. Almost all parameter values, except the RPM value, can be set

precisely in the simulator. The use of optical sensors in calculating the number of rotor rotations does help in monitoring. Still, the rotor rotation was controlled manually, so the possibility of error is considerably high. Moreover, the wind direction parameter, which has a high P-value, indicates that this parameter does not really affect the output value because wind direction is directly affected by the wind speed value. If the wind speed value is zero, any predetermined wind direction value will not affect the output CV value. According to the orthogonal matrix used for the simulation, there are three levels of wind speed parameter, one of which is 0 m/s. This value will have no effect regardless of the wind direction value, which directly reduces the influence of the parameter on the CV.

Initially, the modeling in this study was performed separately for both nozzle types and spraying patterns used in the processing coverage data. However, these two classifications can be combined by assigning identities with numbers, increasing the data used in modeling. Recognizing that the number of datasets used influences the accuracy of the resulting model, this merging step was performed to improve the accuracy. Furthermore, as various investigations were performed, several modeling methods are still used as a comparative aspect where nonlinear or machine learning techniques have performed better than linear methods. The regression equation generated from four nonlinear methods also exhibited different performances, so random forest regression was selected as the modeling method with the best performance and was used for the development of the system control.

Using the simulator as a data collection platform had many advantages for this study. The predetermined parameters could be achieved with considerable ease and precisely. On the other hand,

TABLE 4 Simulation results of random forest regression for XR series nozzle.

No.	Parameter condition								CV (%)		Decision
	FS (m/s)	Alt. (m)	WS (m/s)	WD (°)	RPM	Interval (m)	FM	Nozzle	A	AB	
1.	3	2	2.1	15	2900	1	1	2	31.2	15.8	A+B
2.	3	2	2.1	29	2900	1	1	2	30.3	15.8	A+B
3.	3	2	2.1	37	3100	1	1	2	29.8	13.8	A
4.	3	2	2.1	45	3100	1	1	2	29.8	13.8	A
5.	3	2	2.7	15	2900	1	1	2	31.2	15.8	A+B
6.	3	2	2.7	29	2900	1	1	2	30.5	15.8	A+B
7.	3	2	2.7	37	3100	1	1	2	29.8	13.8	A
8.	3	2	2.7	45	3100	1	1	2	29.8	13.8	A
9.	3	2	3.5	15	3100	1	1	2	29.8	17.5	A
10.	3	2	3.5	29	3100	1	1	2	28.9	17.5	A
11.	3	2	3.5	37	2900	1	1	2	28.1	15.5	A
12.	3	2	3.5	45	2900	1	1	2	28.1	15.5	A
13.	3	2	4.0	15	3100	1	1	2	29.8	17.5	A
14.	3	2	4.0	29	3100	1	1	2	28.9	17.5	A
15.	3	2	4.0	37	2900	1	1	2	28.1	15.5	A
16.	3	2	4.0	45	2900	1	1	2	28.1	15.5	A

testing directly in the field would result in random parameter values that are difficult to establish. Developing an independent UASS spraying control system using machine learning is also an exciting advancement in precision agriculture. Achieving uniform spray distribution is one of the most critical factors in effective aerial spraying. The fact that the system processes data of CV values below 30% indicates that the machine learning algorithm can detect and correct uneven spray distribution. In addition, the amount of pesticide sprayed is another priority for developing precision spraying. Both scenarios improve the effectiveness of spraying and reduce the waste of chemicals, thus saving costs for farmers.

Another significant advantage of using machine learning for spraying control is the ability to target all UASS types in the future. This indicates that the system will be adaptable to a wide range of UASS, making it accessible to more farmers and agricultural businesses. Additionally, the ability to adapt and learn from new data means that the system can be continually improved and evolved over time, ultimately leading to even better results. However, there are also some potential challenges and considerations that should be addressed. One concern is the need for consistent and accurate data input, as the performance of the machine learning algorithm will depend heavily on the quality and accuracy of the data it receives. There also might be regulatory and ethical considerations regarding using autonomous UASS for spraying, particularly regarding safety and potential environmental impacts. Overall, developing an independent UASS spraying control system using machine learning is a promising advancement in agriculture technology, and it has the potential to improve spraying effectiveness, reduce waste, and increase cost savings for farmers. As the system is

completed and ready to be fully examined, field tests will be conducted to determine the control system's performance in addressing environmental conditions and the operation of the UASS. However, carefully considering potential challenges and ethical implications will be important moving forward.

5 Conclusions

The overall objective of this study was answered during the experiments. The essential results of this study are briefly summarized in the following conclusion:

Spraying distribution data was collected under the simulator environment conditions with 72 simulations. Using the spraying pattern and interval from 1–9 m, 648 kinds of CV datasets were obtained for each pump opening. AI nozzle produced a better ability to overcome drift at 1–7 m intervals under several simulation conditions and exhibited a CV value of<30%. The TeeJet nozzle type XR exhibited a narrower interval width with a CV of<30%, which ranges from 1–3 m in some simulation conditions. The CV values obtained in the spraying pattern race track tend to be greater, ranging from 4 to 26% at a spray interval of 1 m using the AI series nozzle and 7 to 57% at the XR series TeeJet nozzle. In contrast, in the back-and-forth spraying pattern, the CV values obtained ranged from 1 to 24% at a spray interval of 1 m while using the AI series nozzle and 3 to 54% at a spray interval of 1 m while using the XR series TeeJet nozzle. The control system was modeled using machine learning and linear regression methods based on the CV datasets for each pump opening. Using nine levels of interval parameters and

two spraying pattern types also helps increase the number of datasets. In this study, the random forest regression model achieved the best accuracy and intercept error value compared to other models: it exhibited an R^2 of 0.96 and RMSE of 0.04% for pump openings A and AB. This model could predict the CV value under parameters outside the modeling boundary. As confirmed in the simulation, the model can predict the CV value and make decisions on pump operation. The findings of this study confirmed the ability of random forest regression to develop a model for a functioning control system to establish an independent precision spraying control system.

Data availability statement

The original contributions presented in the study are included in the article/Supplementary Material. Further inquiries can be directed to the corresponding author.

Ethics statement

Written informed consent was obtained from the individual(s) for the publication of any potentially identifiable images or data included in this article.

Author contributions

Conceptualization, AH, and XH. Methodology, AH, XH, S-HY, CH, and SB. Analysis, AH, S-HY, CH, and SB. Visualization, AH, S-HY, CH, and SB. Supervision, XH. Reviewing the manuscript, XH, S-HY, CH, SB, C-GL, D-HL, and YK. All authors contributed to the article and approved the submitted version.

Funding

Acknowledgments

We acknowledge the contributions of certain colleagues who have helped make this project possible, institutions, or agencies that aided the efforts of the authors.

Conflict of interest

The authors declare that the research was conducted in the absence of any commercial or financial relationships that could be construed as a potential conflict of interest.

Publisher's note

All claims expressed in this article are solely those of the authors and do not necessarily represent those of their affiliated organizations, or those of the publisher, the editors and the reviewers. Any product that may be evaluated in this article, or claim that may be made by its manufacturer, is not guaranteed or endorsed by the publisher.

Supplementary material

The Supplementary Material for this article can be found online at: https://www.frontiersin.org/articles/10.3389/fpls.2023.1235548/full#supplementary-material

SUPPLEMENTARY FIGURE 1
Indoor flight simulator for spraying distribution testing with **(A)** UASS mounted into the simulator and spraying on **(B)** water-sensitive paper layout.

SUPPLEMENTARY FIGURE 2
Positioning of the fan as a wind generator in the simulator.

SUPPLEMENTARY FIGURE 3
Control command used to control the device during the simulation.

SUPPLEMENTARY FIGURE 4
Weather station device with **(A)** ultrasonic anemometer and **(B)** data acquisition systems displaying wind property values.

SUPPLEMENTARY FIGURE 5
The image processing device for analyzing the spraying distribution data recorded on the WSP.

SUPPLEMENTARY TABLE 1
ANOVA of AI series nozzle opening A for single parameter and combination of parameters.

SUPPLEMENTARY TABLE 2
ANOVA of AI series nozzle opening AB for single parameter and combination of parameters.

SUPPLEMENTARY TABLE 3
ANOVA of TeeJet XR series nozzle opening A for single parameter and combination of parameters.

SUPPLEMENTARY TABLE 4
ANOVA of TeeJet XR series nozzle opening AB for single parameter and combination of parameters.

References

Bottrell, D. G., and Schoenly, K. G. (2018). Integrated pest management for resource-limited farmers: challenges for achieving ecological, social and economic sustainability. *J. Agric. Sci.* 156, 408–426. doi: 10.1017/S0021859618000473

Brandoli, B., Spadon, G., Esau, T., Hennessy, P., Carvalho, A. C. P. L., Amer-Yahia, S., et al. (2021). DropLeaf: A precision farming smartphone tool for real-time quantification of pesticide application coverage. *Comput. Electron. Agric.* 180, 105906. doi: 10.1016/j.compag.2020.105906

Butler Ellis, M. C., Alanis, R., Lane, A. G., Tuck, C. R., Nuyttens, D., and Van De Zande, J. C. (2017). Wind tunnel measurements and model predictions for estimating spray drift reduction under field conditions. *Biosyst. Eng.* 154, 25–34. doi: 10.1016/j.biosystemseng.2016.08.013

Carvalho, F. K., Chechetto, R. G., Mota, A. A. B., and Antuniassi, U. R. (2020). Challenges of aircraft and drone spray applications. *Outlooks. Pest Manage.* 31, 83–88. doi: 10.1564/v31_apr_07

Cerruto, E., Manetto, G., Longo, D., Failla, S., and Papa, R. (2019). A model to estimate the spray deposit by simulated water sensitive papers. *Crop Prot.* 124, 104861. doi: 10.1016/j.cropro.2019.104861

Chang, K., Chen, S., Wang, M., Xue, X., and Lan, Y. (2023). Numerical simulation and verification of rotor downwash flow field of plant protection UAV at different rotor speeds. *Front. Plant Sci.* 13. doi: 10.3389/fpls.2022.1087636

Chen, P., Ouyang, F., Zhang, Y., and Lan, Y. (2022). Preliminary evaluation of spraying quality of multi-unmanned aerial vehicle (UAV) close formation spraying. *Agriculture* 12, 1149. doi: 10.3390/agriculture12081149

Chen, J., Zhang, D., Zeb, A., and Nanehkaran, Y. A. (2021). Identification of rice plant diseases using lightweight attention networks. *Expert Syst. Appl.* 169, 114514. doi: 10.1016/j.eswa.2020.114514

Cunha, M., Carvalho, C., and Marcal, A. R. S. (2012). Assessing the ability of image processing software to analyse spray quality on water-sensitive papers used as artificial targets. *Biosyst. Eng.* 111, 11–23. doi: 10.1016/j.biosystemseng.2011.10.002

Fox, R. D., Derksen, R. C., Cooper, J. A., Krause, C. R., and Ozkan, H. E. (2003). Visual and image system measurement of spray deposit using water–sensitive paper. *Appl. Eng. Agric.* 19, 549–552. doi: 10.13031/2013.15315

Garanger, K., Epps, J., and Feron, E. (2020). "Modeling and experimental validation of a fractal tetrahedron UAS assembly," in *2020 IEEE Aerospace Conference* (Big Sky, MT, USA: IEEE), 1–11. doi: 10.1109/AERO47225.2020.9172614

Godfray, H. C. J., Mason-D'Croz, D., and Robinson, S. (2016). Food system consequences of a fdisease epidemic in a major crop. *Philos. Trans. R. Soc B Biol. Sci.* 371, 20150467. doi: 10.1098/rstb.2015.0467

González, J. O. W., Gutiérrez, M. M., Murray, A. P., and Ferrero, A. A. (2011). Composition and Biological Sctivity of Essential Oils from Labiatae against *Nezara viridula* (Hemiptera: Pentatomidae) Soybean Pest: Activity of Essential Oils from Labiatae against *N. viridula*. *Pest Manage. Sci.* 67, 948–955. doi: 10.1002/ps.2138

Gregorio, E., Rosell-Polo, J. R., Sanz, R., Rocadenbosch, F., Solanelles, F., Garcerá, C., et al. (2014). LIDAR as an alternative to passive collectors to measure pesticide spray drift. *Atmos. Environ.* 82, 83–93. doi: 10.1016/j.atmosenv.2013.09.028

Griesang, F., Spadoni, A. B. D., Urah Ferreira, P. H., and Da Costa Ferreira, M. (2022). Effect of working pressure and spacing of nozzles on the quality of spraying distribution. *Crop Prot.* 151, 105818. doi: 10.1016/j.cropro.2021.105818

Guo, S., Li, J., Yao, W., Zhan, Y., Li, Y., and Shi, Y. (2019). Distribution characteristics on droplet deposition of wind field vortex formed by multi-rotor UAV. *PloS One* 14, e0220024. doi: 10.1371/journal.pone.0220024

Hanif, A. S., Han, X., and Yu, S.-H. (2022). Independent control spraying system for UAV-based precise variable sprayer: A review. *Drones* 6, 383. doi: 10.3390/drones6120383

Hoffmann, W. C., and Hewitt, A. J. (2005). Comparison of three imaging systems for water-sensitive papers. *Appl. Eng. Agric.* 21, 961–964. doi: 10.13031/2013.20026

Huang, Z., Wang, C., Li, Y., Zhang, H., Zeng, A., and He, X. (2023). Field evaluation of spray drift and nontargeted soybean injury from unmanned aerial spraying system herbicide application under acceptable operation conditions. *Pest Manage. Sci.* 79, 1140–1153. doi: 10.1002/ps.7285

Hussain, M., Wang, Z., Huang, G., Mo, Y., Guo, Y., Kaousar, R., et al. (2022). Evaluation of droplet deposition and efficiency of 28-homobrassinolide sprayed with unmanned aerial spraying system and electric air-pressure knapsack sprayer over wheat field. *Comput. Electron. Agric.* 202, 107353. doi: 10.1016/j.compag.2022.107353

ISO (International Organization for Standardization). (2017a). *ISO 5682-1, equipment for crop protection-spraying equipment-part 1: test methods for sprayer nozzles.* Available at: https://www.iso.org/standard/60053.html (Accessed July 17, 2023).

ISO (International Organization for Standardization). (2017b). *ISO 5682-2, Equipment for Crop Protection-Spraying Equipment-Part 2: Test Methods to Assess The Horizontal Transverse Distribution for Hydraulic Sprayers.* Available at: https://www.iso.org/standard/60054.html (Accessed July 17, 2023).

ISO (International Organization for Standardization). (2017c). *ISO 5682-3, Equipment for Crop Protection-Spraying Equipment-Part 3: Test Methods to Assess The Performance of Volume/Area Adjustment Systems.* Available at: https://www.iso.org/standard/60055.html (Accessed July 17, 2023).

Kalia, A., and Gosal, S. K. (2011). Effect of pesticide application on soil microorganisms. *Arch. Agron. Soil Sci.* 57, 569–596. doi: 10.1080/03650341003787582

Lan, Y., and Chen, S. (2018). Current status and trends of plant protection UAV and its spraying technology in China. *Int. J. Precis. Agric. Aviat.* 1, 1–9. doi: 10.33440/j.ijpaa.20180101.0002

Li, L., Hu, Z., Liu, Q., Yi, T., Han, P., Zhang, R., et al. (2022). Effect of flight velocity on droplet deposition and drift of combined pesticides sprayed using an unmanned aerial vehicle sprayer on A peach orchard. *Front. Plant Sci.* 13. doi: 10.3389/fpls.2022.981494

Liao, J., Zang, Y., Luo, X., Zhou, Z., Lan, Y., Zang, Y., et al. (2019). Optimization of variables for maximizing efficacy and efficiency in aerial spray application to cotton using unmanned aerial systems. *Int. J. Agric. Biol. Eng.* 12, 10–17. doi: 10.25165/j.ijabe.20191202.4288

Lv, M., Xiao, S., Tang, Y., and He, Y. (2019). Influence of UAV flight speed on droplet deposition characteristics with the application of infrared thermal imaging. *Int. J. Agric. Biol. Eng.* 12, 10–17. doi: 10.25165/j.ijabe.20191203.4868

Maheswaran, S., Murugesan, G., Duraisamy, P., Vivek, B., Selvapriya, S., Vinith, S., et al. (2020). "Unmanned ground vehicle for surveillance," in *2020 11th International Conference on Computing, Communication and Networking Technologies (ICCCNT)* (Kharagpur, India: IEEE), 1–5. doi: 10.1109/ICCCNT49239.2020.9225313

Mahmud, H. M. I., Moinuddin, K. A. M., and Thorpe, G. R. (2016). Experimental and numerical study of high-pressure water-mist nozzle sprays. *Fire. Saf. J.* 81, 109–117. doi: 10.1016/j.firesaf.2016.01.015

Maria Travisi, C., Nijkamp, P., and Vindigni, G. (2006). Pesticide risk valuation in empirical economics: A comparative approach. *Ecol. Econ.* 56, 455–474. doi: 10.1016/j.ecolecon.2004.06.026

Martin, D. E., Woldt, W. E., and Latheef, M. A. (2019). Effect of application height and ground speed on spray pattern and droplet spectra from remotely piloted aerial application systems. *Drones* 3, 83. doi: 10.3390/drones3040083

Meng, Y., Song, J., Lan, Y., Mei, G., Liang, Z., and Han, Y. (2019). Harvest aids efficacy applied by unmanned aerial vehicles on cotton crop. *Ind. Crops. Prod.* 140, 111645. doi: 10.1016/j.indcrop.2019.111645

Meng, Y., Su, J., Song, J., Chen, W.-H., and Lan, Y. (2020). Experimental evaluation of UAV spraying for peach trees of different shapes: effects of operational parameters on droplet distribution. *Comput. Electron. Agric.* 170, 105282. doi: 10.1016/j.compag.2020.105282

Pan, H.-W., Lei, H.-J., He, X.-S., Xi, B.-D., Han, Y.-P., and Xu, Q.-G. (2017). Levels and distributions of organochlorine pesticides in the soil–groundwater system of vegetable planting area in tianjin city, Northern China. *Environ. Geochem. Health* 39, 417–429. doi: 10.1007/s10653-016-9899-9

Parkin, C. S., and Wyatt, J. C. (1982). The determination of flight-lane separations for the aerial application of herbicides. *Crop Prot.* 1, 309–321. doi: 10.1016/0261-2194(82)90006-0

Qin, W.-C., Qiu, B.-J., Xue, X.-Y., Chen, C., Xu, Z.-F., and Zhou, Q.-Q. (2016). Droplet deposition and control effect of insecticides sprayed with an unmanned serial vehicle against planthoppers. *Crop Prot.* 85, 79–88. doi: 10.1016/j.cropro.2016.03.018

Richardson, B., Kimberley, M. O., and Schou, W. C. (2004). Defining acceptable levels of herbicide deposit variation from aerial sraying. *Appl. Eng. Agric.* 20, 259–267. doi: 10.13031/2013.16059

Richardson, B., Rolando, C. A., Somchit, C., Dunker, C., Strand, T. M., and Kimberley, M. O. (2020). Swath pattern analysis from A multi-rotor unmanned serial vehicle configured for pesticide application. *Pest Manage. Sci.* 76, 1282–1290. doi: 10.1002/ps.5638

Semião, V., Andrade, P., and Carvalho, M. D. G. (1996). Spray characterization: numerical prediction of sauter mean diameter and droplet size distribution. *Fuel* 75, 1707–1714. doi: 10.1016/S0016-2361(96)00163-9

Shi, X., Jiang, L., Wang, H., Qiao, K., Wang, D., and Wang, K. (2011). Toxicities and sublethal effects of seven neonicotinoid insecticides on survival, growth and reproduction of imidacloprid-resistant cotton aphid, *aphis gossypii*: toxicities and sublethal effects of seven neonicotinoid. *Pest Manage. Sci.* 67, 1528–1533. doi: 10.1002/ps.2207

Sies, M. F., Madzlan, N. F., Asmuin, N., Sadikin, A., and Zakaria, H. (2017). Determine spray droplets on water sensitive paper (WSP) for low pressure deflector nozzle using image J. *IOP. Conf. Ser. Mater. Sci. Eng.* 243, 12047. doi: 10.1088/1757-899X/243/1/012047

Sparks, T. C., and Bryant, R. J. (2021). Crop protection compounds – trends and perspective. *Pest Manage. Sci.* 77, 3608–3616. doi: 10.1002/ps.6293

Tudi, M., Daniel Ruan, H., Wang, L., Lyu, J., Sadler, R., Connell, D., et al. (2021). Agriculture development, pesticide application and its impact on the environment. *Int. J. Environ. Res. Public. Health* 18, 1112. doi: 10.3390/ijerph18031112

Wang, G., Lan, Y., Yuan, H., Qi, H., Chen, P., Ouyang, F., et al. (2019). Comparison of spray deposition, control efficacy on wheat aphids and working efficiency in the wheat field of the unmanned aerial vehicle with boom sprayer and two conventional knapsack sprayers. *Appl. Sci.* 9, 218. doi: 10.3390/app9020218

Wang, C., Wongsuk, S., Huang, Z., Yu, C., Han, L., Zhang, J., et al. (2023). Comparison between drift test bench and other techniques in spray drift evaluation of an eight-rotor unmanned aerial spraying system: the influence of meteorological parameters and nozzle types. *Agronomy* 13, 270. doi: 10.3390/agronomy13010270

Wen, S., Zhang, Q., Yin, X., Lan, Y., Zhang, J., and Ge, Y. (2019). Design of plant protection UAV variable spray system based on neural networks. *Sensors* 19, 1112. doi: 10.3390/s19051112

Wilson, C., and Tisdell, C. (2001). Why farmers continue to use pesticides despite environmental, health and sustainability costs. *Ecol. Econ.* 39, 449–462. doi: 10.1016/S0921-8009(01)00238-5

Zhang, S., Qiu, B., Xue, X., Sun, T., Gu, W., Zhou, F., et al. (2021). Effects of crop protection unmanned aerial system flight speed, height on effective spraying width, droplet deposition and penetration rate, and control effect analysis on wheat aphids, powdery mildew, and head blight. *Appl. Sci.* 11, 712. doi: 10.3390/app11020712

Zhu, H., Lan, Y., Wu, W., Hoffmann, W. C., Huang, Y., Xue, X., et al. (2010). Development of A PWM precision spraying controller for unmanned aerial vehicles. *J. Bionic. Eng.* 7, 276–283. doi: 10.1016/S1672-6529(10)60251-X

Zhu, H., Salyani, M., and Fox, R. D. (2011). A portable scanning system for evaluation of spray deposit distribution. *Comput. Electron. Agric.* 76, 38–43. doi: 10.1016/j.compag.2011.01.003

Effect of adjuvants on physicochemical properties of lime sulfur on flower/ paraffin and application on flower thinning

Yuanyuan Li[1,2], Yang Liu[1], Changjie Wu[1], Rui Zhao[1],
Minghua Li[1], Jing Cai[3], Li Ma[3], Xiongkui He[1], Xuemin Wu[1]
and Zhang Zhenhua[1*]

[1]College of Science, China Agricultural University, Beijing, China, [2]College of Plant Protection, China
Agricultural University, Beijing, China, [3]Qingshengyuan Agricultural Development Co., Ltd., Chengde,
Hebei, China

Introduction: Adjuvants can effectively enhance the utilization rate of pesticides, but the application of adjuvants in plant growth regulators is rarely studied.

Methods: This work explored the effects of adjuvants dioctyl sulfosuccinate sodium salt (AOT) and methyl oleate (MO) on lime sulfur (LS), especially the drop behavior on flower and paraffin surface.

Results: The results showed that the addition of AOT and AOT+MO can significantly reduce the static and dynamic surface tension of LS from 72mN/m to 28mN/m and 32mN/m respectively, and increase the spreading factor from 0.18 to 1.83 and 3.10 respectively, reduce the bounce factor from 2.72 to 0.37 and 0.27 respectively. The fluorescence tracer test showed that the addition of adjuvants could promote the spreading and permeation of droplets. The field test results revealed that the flower thinning rate of adjuvant and non-adjuvant were 80.55% and 54.4% respectively, and the flower thinning effect of adding adjuvant was the same as that of artificial which the flower thinning rate was 84.77%. The quality of apples treated with adjuvants was similar to that treated with artificial, and the weight of single fruit increased by 24.08% compared with CK (spray water).

Discussion: The application of tank-mixture adjuvant could reduce the dosage of LS for thinning agent application, improve apple's quality, and decrease labor cost and improve the economic benefits of fruit planting and the environmental benefits of plant growth regulators.

KEYWORDS

tank-mixture adjuvant, lime sulfur, flower thinning, dioctyl sulfosuccinate sodium salt, apple cultivation, sustainable agriculture

1 Introduction

Flower and fruit thinning is an important technology in apple cultivation, which can reduce the number of fruits per plant to improve the quality of apples and promote the growth of apple trees (Ngugi and Schupp, 2009). At present, manual, mechanical, and chemical thinning strategies are commonly used for fruit thinning. However, mechanical thinning can damage flower and leaf, reduce photosynthesis, and in some cases, facilitate the spreading of fire blight in apple orchards. Manual thinning is an expensive, labor-intensive form of field management. With an aging population, skilled labor for thinning is not easy to be found in China.

Chemical thinning for flowers and fruits is conducted as it can save time and labor, and can achieve desired thinning in a time-effective manner. When metamitron, a chemical fruit thinning agent, was applied to fruit trees, fruit number per plant reduced, average fruit color improved, and fruit weight per plant and diameter significantly increased by thinning (Gonzalez et al., 2020). The thinning efficiency of metamitron was found to strongly correlate with night temperature. Lucas De Ross Marchioretto et al. have reported that spraying ammonium thiosulfate (ATS) affects the germination of pollen and achieves flower thinning (Marchioretto et al., 2019). Lime sulfur (LS) mixture treatment can not only control fungi, bacteria and insects, but also inhibit the growth of pollen tubes (Holb et al., 2003; Marchioretto et al., 2019). Mineral oil and ATS can achieve flower thinning under field conditions (Marchioretto et al., 2019). Growth regulators, such as 6-benzylaminopurine hydrochloride (6-BA), gibberellic acid (GA_{4+7}) + 6-BA, 1-naphthaleneacetic acid (NAA), can significantly reduce crop load and improve fruit quality (Marchioretto et al., 2019). In these chemical thinnings of fruit and flower, the effect needs to be accurate and predictable, and the chemical agents needs to be reduced to have a wide window of concentration for safe usage (Lordan et al., 2018).

The addition of adjuvants can improve the wetting behavior of pesticide droplets, increase deposition of liquid on the target, facilitate the infiltration and transfer of active ingredients (Kovalchuk et al., 2014; Grundke et al., 2015). Oil adjuvants, mainly including mineral oil, vegetable oil, and vegetable oil derivatives, can promote the diffusion, adhesion, infiltration, and absorption of pesticide drops on leaves (Buchholz, 2006; Arand et al., 2010; Xu et al., 2011). As mineral oil is harmful, it should be sparingly used (Meng et al., 2016). Surfactants can significantly inhibit the fragmentation and rebound behavior of droplets impacting the leaf surface of hydrophobic plants and can improve the wetting and spreading behavior of droplets. For example, Wu, Zhang, Xu and coworkers reported that the use of appropriate tank-mix adjuvants at low dilution ratios for UAV application in paddy fields could improve the performance of spray dilutions, increase the effective deposition and wetting spread of pesticides on rice leaves, and further reduce the dosage of pesticide products and improve pesticide utilization (Zhao et al., 2022). In recent years, double-chain ionic surfactants, which have superspreading and superwetting effects, such as dioctyl sulfosuccinate sodium salt (AOT) and didecyldimethylammonium bromide (DDAB), have attracted great attention in pesticide application (Song et al., 2017; Song et al., 2019; Li et al., 2021).

Jiang, Wang, Dong and coworkers showed that binary additive (0.005% PEO and 0.1% AOT) droplet have excellent spreading performance on superhydrophobic leaves, including rice, cauliflower, chive and cabbage (Song et al., 2019). Du, Gao and coworkers reported that DDAB can not only inhibit droplet regression and rebound but also significantly improve the herbicide control effect as observed through field experiments (Li et al., 2021). However, only few studies are available on the synergistic effects of adjuvants in plant growth regulation, and the study their behaviors on flower and paraffin surface are also rare.

Herein, we aimed to study the tank-mixture of AOT and methyl oleate (MO) into LS thinning agent to improve droplet performance on flower and paraffin, to achieve efficient, accurate, and appropriate flower thinning, to reduce the use of flower thinning agents, and to improve the efficacy on apple cultivation. We systematically studied the physicochemical properties of AOT and AOT + MO, their combination with LS. The impact behavior of different droplets on the target lowers and paraffins, and the spread and penetration characteristics of different droplets assessed using the fluorescent tracer method were estimated. The addition of adjuvants can reduce the dosage of LS thinning agent and the effect is as good as that of thinning by artificial. As a result, the dosage of thinning agent application was reduced, the apple's quality was improved, and labor cost was further decreased and improve the economic benefits of fruit planting and the environmental benefits of plant growth regulators.

2 Materials and methods

2.1 Materials

Lime sulfur (LS) comprised of calcium oxide, sulfur and water in a ratio of 1:2:10 was made at Qingshengyuan Agricultural Development Co., Ltd. (China). The adjuvants, namely, bis(2-ethylhexyl) sodium sulfosuccinate (AOT, 97%), methyl oleate (MO), and emulsifier were purchased from Aladdin Co., Ltd. (China), Hebei Ming Shun Agricultural Science and Technology Co., Ltd. (China) and Nantong deyi Chemical Co., Ltd. (China) respectively. 1,3,6-Pyrenetrisulfonicacid,8-hydroxy-trisodiumsalt (pyranine) was purchased from Shanghai Maclin Biochemical Technology Co., Ltd. (China). An AOT + MO mixture of AOT (35%) + MO (55%) + emulsifier (10%) was prepared at China Agricultural University. Flat paraffin plates were prepared by melting solid paraffin, using it to cover the slide, and letting it cool to room temperature.

2.2 Static surface tension

Static surface tension was measured using the Wilhelmy plate method using an automatic tension meter, JK99B (Shanghai Zhong Chen Digital Technology Equipment Co., Ltd.). The adjuvant solutions were diluted in distilled water, and the critical micellar concentration curve was plotted by taking the average of three measurements.

2.3 Wetting experiments

Contact angles were measured using the sessile drop method using an OCA 15 Plus optical contact angle measuring device (Data Physics Instruments GmbH, Filderstadt, Germany). Each treatment was repeated 5 times. Recording was performed at a speed of 0.45 fps, and the shooting process lasted for 5 min.

2.4 Adhesion work

The adhesion work (Wa) of the solutions can be calculated using Eq. (1) (Lee and Lee, 2011):

$$Wa = \gamma SV + \gamma LV - \gamma SL \qquad (1)$$

The Young"s equation is expressed as Eq. (2):

$$\gamma SV - \gamma SL = \gamma LV \, cos\Phi \qquad (2)$$

Substituting Eq. (1) into Eq. (2), we obtain:

$$Wa = \gamma LV (1 + cos\Phi) \qquad (3)$$

According to Eq. (3), by measuring the contact angle and surface tension of pesticide solution on the surface of paraffin and petals, the adhesion work can be calculated (Zheng et al., 2021).

2.5 Impact experiments

Impact experiments were performed by high-speed photography method using a camera (I - Speed 220, IX - cameras, UK). The impact progress was recorded at 4021 fps and 592 × 534 px from 0° and 30° views. The droplets fell from a peristaltic pump (LD - P2020II, Shanghai Lande Medical Equipment Co. Ltd.) on to the surface of a flat paraffin plate. Droplets were generated using flat-tipped syringe needles with internal diameters of 0.17 or 0.6 mm. Plant targets were of the same size and a constant impact velocity was maintained. The droplets had a diameter of approximately 2 ± 0.2 mm, and they fell on the surface at an impact velocity of 2 m/s. The images were analyzed using ImageJ to quantitatively track the droplet's impact process.

2.6 Dynamic surface tension

Dynamic surface tension was measured using the maximum bubble pressure method using the bubble pressure tensiometer BPA - 2P (SINTERFACT, Germany). The tendency of surface tension within 10 ms to 10 s was measured to characterize the dynamics of adsorption of surface-active compounds.

2.7 Fluorescent tracer experiments

The spreading and penetrating properties of droplets on plant targets were measured using fluorescent tracer method using 1% pyranine, a fluorescent dye, and ultraviolet light. Pyranine was applied on the stamens, pistils, and petals of apple flowers. After 12

h without dew and rain, the apple flowers were removed for indoor photography experiments to observe the behavior of pyranine, excited using a handheld 365 nm ultraviolet lamp.

2.8 Field Experiments

2.8.1 Field experimental design and treatment

The chemical thinning experiments on apple cultivation were performed at Qingshengyuan Agricultural Development Co. LTD., Pingquan city, Hebei Province, from May 1 to October 20, 2021. The Yueguan variety, an experimental variety (hybrid of Hanfu and Yueshuai varieties), was used. The following solutions were sprayed at a volume of 2 L/tree: LS at 0.5, 0.75, and 1 B° and 0.75 B° LS + 0.1% AOT and 0.75 B° LS + 0.1% AOT + 0.16% MO. Water, 0.1% AOT, 0.1% AOT + 0.16% MO, and artificially thinning were set as the controls in May 2021. Each treatment was performed on 2 trees; therefore, the experiment involved a total of 18 trees. Fruit trees with approximately the same perimeter (25-28 cm) of trunks, crown width(1.8-2 m × 2.2-2.5 m), and tree growth were selected before the experiment.

2.8.2 Field experimental indices and determination methods
2.8.2.1 Flower number and inflorescence number

Two repetitions were set per process, and on each tree two branches for four directions (north, east, south, and west) were marked. The fruit number and branch growth were similar among the trees. The flower and inflorescence numbers in each group of branches were counted before spraying the solutions.

2.8.2.2 Fruit setting rate

In June, the rates of inflorescence fruit-set, total flower fruit-set, single/double fruit-set, single fruit-set, empty fruit, and flower thinning were calculated from the marked branches in each treatment group as follows.

inflorescence fruit set rate (%)

$\quad$ = inflorescence fruit set number/total inflorescence number

$\quad \times 100\%$

total flower fruit set rate (%)

$\quad$ = number of fruits on inflorescence

$\qquad$ /number of flowers on inflorescence × 100%

single/double fruit set rate (%)

$\quad$ = inflorescence of single or double fruits set number

$\qquad$ /total inflorescence fruits set number × 100%

single fruit set rate (%)

$\quad$ = inflorescence of single fruits set number

$\qquad$ /total inflorescence fruits set number × 100%

empty fruit rate (%)

    = inflorescence fruits not set number
            /total inflorescence fruits set number × 100 %

flower thinning rate (%)

    = thinning flowers number on inflorescence
            /number of flowers on inflorescence × 100 %

2.8.2.3 Determination of fruit quality

After apple fruits were mature, 10 apples were randomly and evenly picked from the upper, middle, and lower levels of each tree in each treatment group. Therefore, 20 apples were selected from each treatment group, and their individual weight, hardness, soluble solid content, and vertical and horizontal diameters were measured. Fruit hardness was measured using GY - 3 fruit hardness tester; soluble solids were measured using BM - 0532 digital refractometer-saccharometer.

2.8.2.4 Economic valuation

The amount of sprayed solution and expenditure were calculated in terms of hectares, and the ratio of chemical thinning cost to artificial thinning cost was calculated with artificial thinning as the denominator and each treatment as the numerator.

2.9 Statistical analyses

Data analysis involves taking the average of all duplicate values in the processing group. The obtained data were processed and analyzed using SPSS Statistics software (version 20.0), Origin (version 2021), and Excel data processing software. The fruit quality index was expressed as mean ± standard deviation.

3 Results and discussion

3.1 Critical micellar concentration curves of adjuvants

The critical micellar concentration is determined by the minimum concentration of surfactant molecules required to form micelles in solution. When the solution has critical micellar concentration, the surface tension of the solution decreases to the minimum value. At this time, even when the surfactant concentration is further increased, the surface tension of the solution is no longer reduced, but more micelles are formed.

We measured the critical micellar concentration of (AOT) and AOT+ MO and plotted the critical micellar concentration curve (Figures 1A, B). At identical adjuvant concentrations (Figure 1A), AOT reached the inflection point earlier than AOT + MO. The critical micellar concentration of AOT was 0.1%, and that of AOT + MO was approximately 1%. The surface tension corresponding to the critical micellar concentration was approximately 27 mN/m.

The critical micellar concentration curve when the AOT concentration of the two adjuvants was the same is shown in Figure 1B. When the critical micellar concentration was less than 0.01%, the surface tension of AOT + MO at the same AOT concentration was smaller than that of AOT. However, when the critical micellar concentration was greater than 0.01%, it was the opposite. The concentration of AOT used in the experiment was 0.1% and the concentrations of AOT/MO were 0.1%/0.16%, respectively. The surface tensions of the two were 28 and 32 mN/m, respectively.

3.2 Wetting and spreading of the droplets

When a droplet touches a solid surface, a three-phase contact line is formed. When the droplet three-phase contact line stops moving, the droplet reaches the optimal wetting state (He et al.,
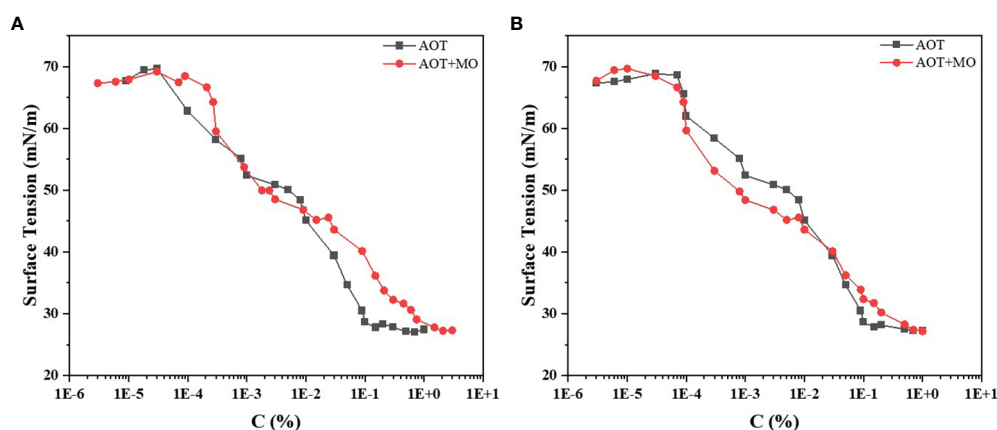

FIGURE 1
Critical micellar concentration curves of AOT and AOT + MO. **(A)** Critical micellar concentration curves of the two adjuvants, AOT and AOT + MO. **(B)** Critical micellar concentration curves of the two adjuvants at the same AOT concentration. AOT: dioctyl sulfosuccinate sodium salt MO: methyl oleate.

2021). Wenzel model, Cassie-Baxter model, and Wenzel model and Cassie-Baxter transition state models are suitable for simulating the wettability of rough hydrophobic solid surfaces because of the presence of micro-nano structures (Quéré, 2003; Bormashenko, 2015). We evaluated the contact states of different droplets with and without adjuvants on flat paraffin plates and on petals of apple flowers, and observed the wetting states of different droplets (Figure 2).

On the flat paraffin plate, the wetting state of water and lime sulfur (LS) (0.75 B°) was close to the Cassie-Baxter model. However, after the addition of adjuvants, the droplets exhibited Wenzel and Cassie-Baxter transition state models, and the transition from Cassie-Baxter state to Wenzel state occurred. The contact angle of water on the petal surface (122°) is shown in Figure 2G. Petals, one of the targets of the flower thinning agent, have a hydrophobic surface. After adding AOT and AOT + MO, the state of the petal changed from Cassie-Baxter to Wenzel state. Particularly after adding AOT, the wetting state of the droplet was close to the Wenzel state. In the Cassie-Baxter state, the friction between the droplet and solid surfaces decreases, and the rolling angle becomes smaller, which makes it easier to roll off. In the Wenzel state, the friction between the droplet and solid surfaces increases, and the rolling angle becomes larger, which makes it easier to deposit (Quéré, 2003).

The contact angles of water and LS on the surface of paraffin were 116° and 108°, respectively (Figure 2J). However, after adding adjuvants, the contact angles of droplets were significantly reduced. The contact angles of AOT and AOT + MO on the surface of paraffin were approximately 30° and 51°, respectively. The contact angle of AOT with LS increased slightly compared with AOT alone; however, only a small difference was observed in the contact angle between the two adjuvants and LS mixtures. We hypothesize that the emulsifier in AOT + MO emulsifies the agent to reduce the droplet contact angle.

3.3 Mechanism of wettability of droplets on paraffin and petal surfaces

It is important to understand the interaction of pesticide droplets with plant surfaces. Target wettability largely determines the retention of pesticide droplets on the surface of crops and target plants (Armstrong et al., 2020; Gao et al., 2020; Zheng et al., 2021).

The wetting behavior of pesticide droplets on paraffin and petal surfaces were studied using adhesion work. The principal mechanism of the effect of surface tension and contact angle on wetting behavior is discussed below.

As shown in Table 1, the adhesion work of different droplets on the surface of paraffin surface was as follows. The adhesion work of water and pesticide droplets was slightly smaller, approximately 41 mJ/m^2, and the adhesion work of droplets increased with the addition of the two adjuvants (approximately 54 mJ/m^2). Compared with that of LS, the adhesion work of the LS and adjuvant combinations increased, particularly that of LS + AOT + MO, where the adhesion work was approximately higher by 10 mJ/m^2 than LS. The higher the work of adhesion, the more the liquid can wet the solid (He et al., 2021).

Additionally, the adhesion on petal surface exhibited the same rule as that on paraffin surface. As previously mentioned, the contact angle on the surface of apple flower petals was greater. Furthermore, the larger adhesion function is conducive to the deposition and adhesion of pesticide droplets on the surface of the target petals (Table 2), thus, reducing the splash and bounce of pesticide.

3.4 Impact behavior of droplets on a flat paraffin plate

In the field, the effective deposition of droplets on the target interface is key to improving the efficacy of pesticides. We
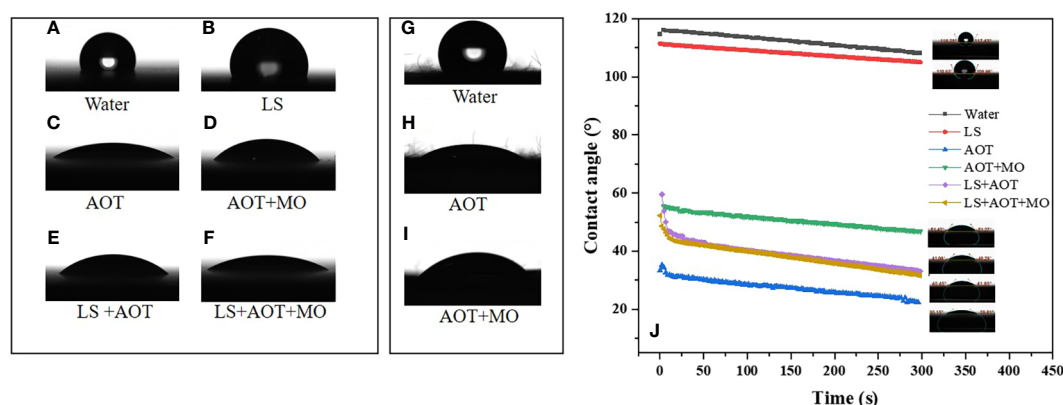

FIGURE 2

Contact angle of droplets on flat paraffin plate and petal surfaces. **(A−F)** The wetting and spreading of droplets on paraffin surfaces. **(A)** water, **(B)** 0.75 B° LS, **(C)** 0.1% AOT, **(D)** 0.1% AOT + 0.16% MO, **(E)** 0.75 B° LS + 0.1% AOT, and **(F)** 0.75 B° LS + 0.1% AOT + 0.16% MO. **(G−I)** The wetting and spreading of droplets on petal surfaces. **(G)** water, **(H)** 0.1% AOT, and **(I)** 0.1% AOT + 0.16% MO **(J)** The tendency of contact angles of the solutions on paraffin surfaces at 5 min. The treatments were water, 0.75 B° LS, 0.1% AOT, 0.1% AOT + 0.16% MO, 0.75 B° LS + 0.1% AOT, and 0.75 B° LS + 0.1% AOT + 0.16% MO. AOT, dioctyl sulfosuccinate sodium salt; MO, methyl oleate; LS, lime sulfur.

TABLE 1 Adhesion work (Wa) of different droplets on paraffin.

Treatment	Surface Tension (mN/m)	Contact Angle (°)	Adhesion Work (mJ/m^2)
Water	72.00	116.00	40.50
0.75 B° LS	59.89	108.12	41.31
0.1% AOT	28.63	28.11	53.88
0.1% AOT + 0.16% MO	32.26	47.55	54.05
0.75 B° LS + 0.1% AOT	25.31	35.96	45.80
0.75 B° LS + 0.1% AOT + 0.16% MO	28.23	37.58	50.61

AOT, dioctyl sulfosuccinate sodium salt; MO, methyl oleate; LS, lime sulfur; B°, baume degrees.

compared the effect of droplets of different solutions on the surface of flat paraffin plates, revealing the dynamics of droplets when they collided with the paraffin surface, spread out, and subsequently rebounded. The impact velocity of the droplet was 2 m/s. Considering the influence of adjuvants on the droplet size, we used needles of two specifications (GB/T 1962.1-2015) to ensure that the droplet size was 2 ± 0.2 mm (Figure 3). When the droplets of water or LS solutions (Figures 3A, B) fell on the surface of the flat paraffin plate, they first spread out after contacting the surface of the plate followed by a high bounce. During the bounce process, the droplets broke and finally fell on the surface of the plate in a Cassie-Baxter state. When the droplets of adjuvants or adjuvants and LS (Figures 3C–F) fell on the surface of the flat paraffin plate, the diffusion phenomenon occurred first. Unlike droplets of water or LS, those of adjuvants did not bounce, but diffused on the surface of the flat paraffin plate in different states; the combination of 0.1% AOT and LS + 0.1% AOT + 0.16% MO had a larger diffusion area than water and LS.

Further, we measured the dynamic surface tension (Figure 3G) of the solutions over time and calculated the change in spreading factor D_t/D_0 (Figure 3H) and bounce factor H_t/D_0 (Figure 3I) with time, during post-impact spreading on the flat paraffin plate. Dynamic surface tension affects droplet behavior at the target interface, and the surfactant with low dynamic surface tension is more helpful in inhibiting droplet rebound on superhydrophobic surfaces. The dynamic surface tension between water and LS was

70-75 mN/m (Figure 3G). However, the dynamic surface tension of LS with adjuvants was considerably reduced to 30-40 mN/m, which could reduce or inhibit the splash bounce of pesticide droplets at the target interface; this was consistent with the results of high-speed photography.

The curve of the spreading factor D_t/D_0 and bounce factor H_t/D_0 over time revealed the impact behavior of the droplets at the target interface. These help accurately describe the spreading and bouncing behavior of the droplet at the target interface in detail. The diameter of the nearly spherical droplet before hitting the target was D_0, and the droplet spread out after contacting the target interface. All the droplets spread out to a maximum area within 3 ms, but the droplet spreading factors were different. Water and LS droplets rapidly shrank back after spreading to the maximum area, and the spreading factor was less than 0.5 on the target surface within 30 ms. When water or LS droplets with adjuvants were spread to the largest area, the droplets of LS + 0.1% AOT tended to shrink; however, the droplets of 0.1% AOT and LS + 0.1% AOT + 0.16% MO maintained a large diffusion area, which was conducive to further absorption, penetration, and conduction of droplets. The diameter of the nearly spherical droplet before hitting the target was D_0, the droplet maybe bounces in different degrees after touching the target interface. Droplets of water and LS bounce when they touch the interface, the bounce factor of water and LS are 5.21 and 2.72 respectively, however, the droplets added with adjuvants did not exhibit bouncing behavior at the target interface.

TABLE 2 Adhesion work (Wa) of different droplets on petal surfaces.

Treatment	Surface tension (mN/m)	Contact Angle(°)	Adhesion Work (mJ/m2)
Water	72.00	122.71	33.16
0.75 B°LS	59.89	115.43	34.22
0.1%AOT	28.63	36.18	51.74
0.3% (AOT+MO)	32.26	43.89	55.52
0.75 B°LS+0.1% AOT	25.31	42.16	44.07
0.75 B°LS + 0.1% AOT+0.16% MO	28.23	48.42	46.98

AOT, dioctyl sulfosuccinate sodium salt; MO, methyl oleate; LS, lime sulfur; B°, baume degrees.
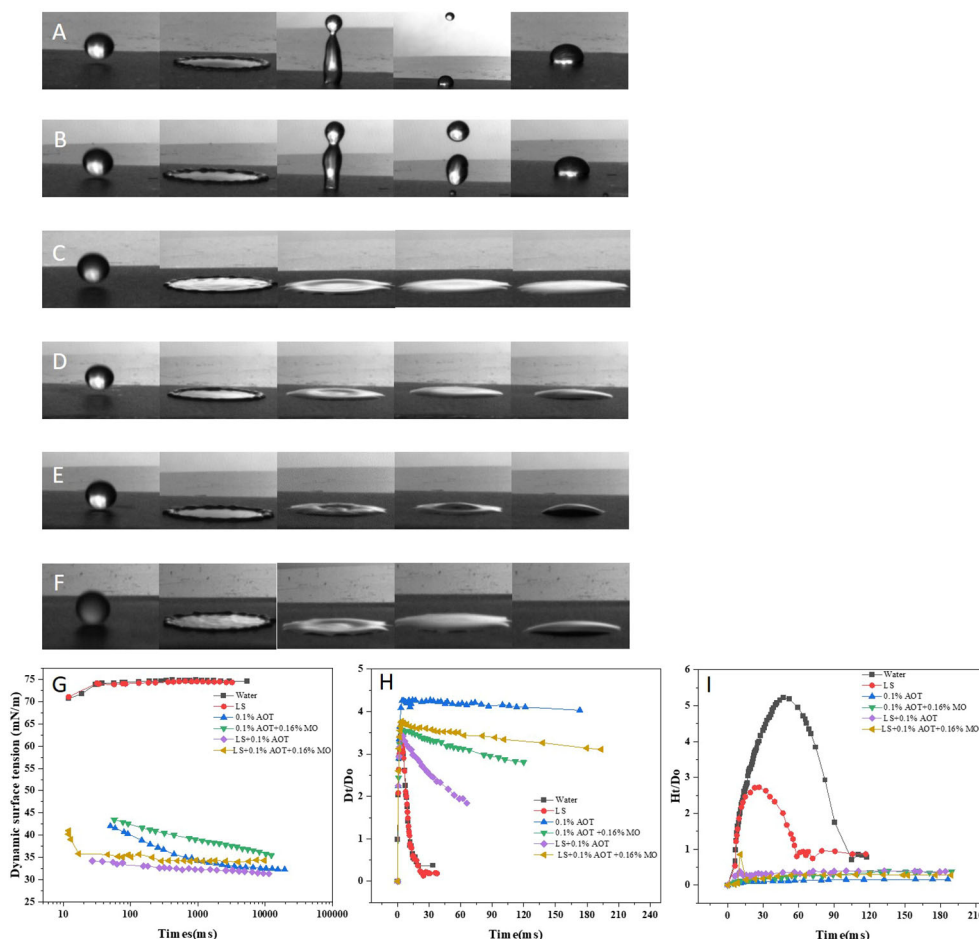
FIGURE 3

Impact process of droplets on a flat paraffin plate. (A−F) Impact behaviors of different droplets on a flat paraffin plate. (A) Water, (B) 0.75 B° LS, (C) 0.1% AOT, (D) 0.1% AOT + 0.16% MO, (E) 0.75 B° LS + 0.1% AOT, and (F) 0.75 B° LS + 0.1% AOT + 0.16% MO. (G) Dynamic surface tension of water, LS, AOT, AOT + MO, LS + AOT, and LS + AOT + MO. (H) Temporal variations in the spreading factors during post-impact spreading on a flat paraffin plate. The treatments were water, 0.75 B° LS, 0.1% AOT, 0.1% AOT + 0.16% MO, 0.75 B° LS + 0.1% AOT, 0.75 B° LS + 0.1% AOT + 0.16% MO. (I) Temporal variations in the bounce factor during post-impact spreading on a flat paraffin plate. The treatments were water, 0.75 B° LS, 0.1% AOT, 01% AOT + 0.16% MO, 0.75 B° LS + 0.1% AOT, 0.75 B° LS + 0.1% AOT + 0.16% MO. AOT: dioctyl sulfosuccinate sodium salt MO: methyl oleate LS: lime sulfur B°: baume degrees.

3.5 Impact behavior of a droplet on a petal surface

Since the leaves and flowers apparatus of most plants are inclined, it is necessary to study the effect of droplets on inclined hydrophobic surfaces. Apple petals with a tilt angle of 30° were used as the hydrophobic surface to measure the impact behavior of droplets on the target interface (Figure 4). At 30°, water and pesticide droplets broke up into smaller droplets and slid off, settling on the petal surface in a Cassie-Baxter state (Figures 4A, B). After the addition of adjuvants to water or LS, the droplet deposition state on the petals significantly improved. The droplets deposited in a larger area on the petal surface, close to the Wenzel state; this was conducive to the deposition of flower thinning agent on the surface of petals and promoted the absorption, penetration, and conduction of pesticide and further improved the efficacy of flower thinning.

3.6 The spreading behavior of a droplet on pistils and stamens

The mechanism of action of a flower thinning agent is to burn the flower organs and hinder pollination and fertilization processes so that fruits cannot be fertilized, and fall off from the tree body. Therefore, we studied the spreading behavior of droplets on the flower organs, pistils and stamens. We used droplets with the same diameter and impact velocity. When water or LS droplets impacted the pistil or stamen, the droplets would hang on the pistil or stamen as shown by the red circle and arrow in Figures 5A, B, and the droplets hung in a spherical shape for a sustained period of time. When the adjuvant droplet impinged on the stamen or pistil, the droplet hung on the stamen. However, after a while, the droplet spread on the stamen and finally deposited in a large area on the stamen, as shown by the arrow in Figures 5C–F. The dynamic impact process of droplets on pistils and stamens can be seen in
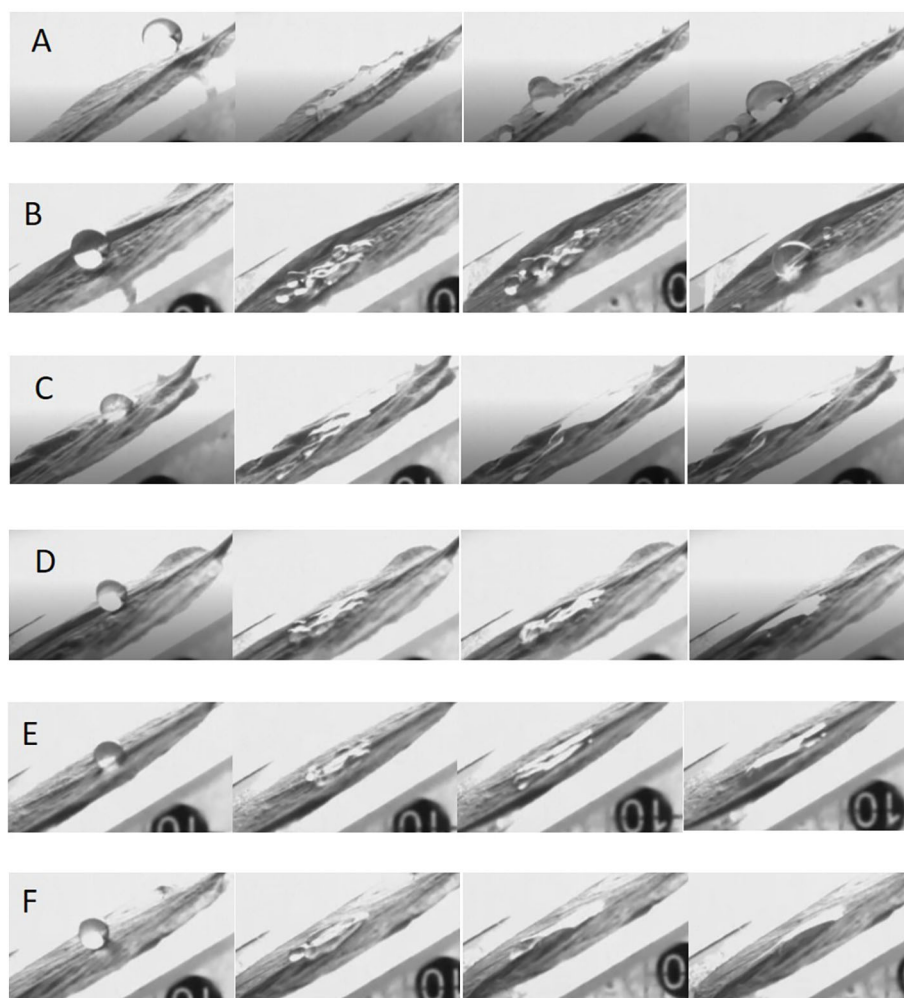
FIGURE 4
Impact process of droplets on the petal surfaces. **(A−F)** Impact behaviors of different droplets on petal surface. **(A)** water, **(B)** 0.75 B° LS, **(C)** 0.1% AOT, **(D)** 0.1% AOT + 0.16% MO, **(E)** 0.75 B° LS + 0.1% AOT, and **(F)** 0.75 B° LS + 0.1% AOT + 0.16% MO. AOT, dioctyl sulfosuccinate sodium salt; MO, methyl oleate; LS, lime sulfur; B°, baume degrees.

Movies S7-S12. The spreading effect of LS + 0.1% AOT droplets on the stamen was not as good as that of LS + 0.1% AOT + 0.16% MO droplets. This may be because the behavior of droplets on curved surfaces is different from that on plane surfaces, this process requires both good spreading and infiltration effects.

Because of the small contact area between stamens and pistils, surface properties, such as contact angle, cannot be measured. By measuring the impact behavior of droplets, the spreading behavior of droplets on this curved target surface can clearly be seen. The effect of the flower thinning agent provides a theoretical guidance for the study of the behavior of the adjuvants on curved surfaces.

3.7 The permeability and spreading ability of the droplets using the fluorescence tracer method

To assess the spreading and penetration effect of adjuvants more directly, we used the fluorescent tracer method. The fluorescent dye chosen was pyranine, which exhibits green fluorescence at 365 nm under ultraviolet illumination. The platform for fluorescence tracing is shown in Figure S1. A dark environment is required during photography to ensure that the fluorescence color can be captured clearly and accurately. During the experiment, we first applied pyranine with or without adjuvants on naturally growing petals and stamens, as shown by the red circle on the petals and stamens in Figure 6. To avoid the influence of sunlight, rain, and dew on the test results, the petals and stamens were removed for indoor testing after 12 h of application. No spreading and permeating behavior occurred on petals and stamens after spot coating of pyranine, and fluorescence remained unchanged at the spot coating position (Figures 6A–C). In contrast, such behaviors did occur after the application of pyranine with adjuvants [Figures 6D–F (pyranine + AOT) and Figures 6G-I (pyranine + AOT + MO)].

In particular, after application of the pyranine + AOT + MO combination, the droplet deposition on the curved target increased. This indicated that owing to the special structure of the curved target,
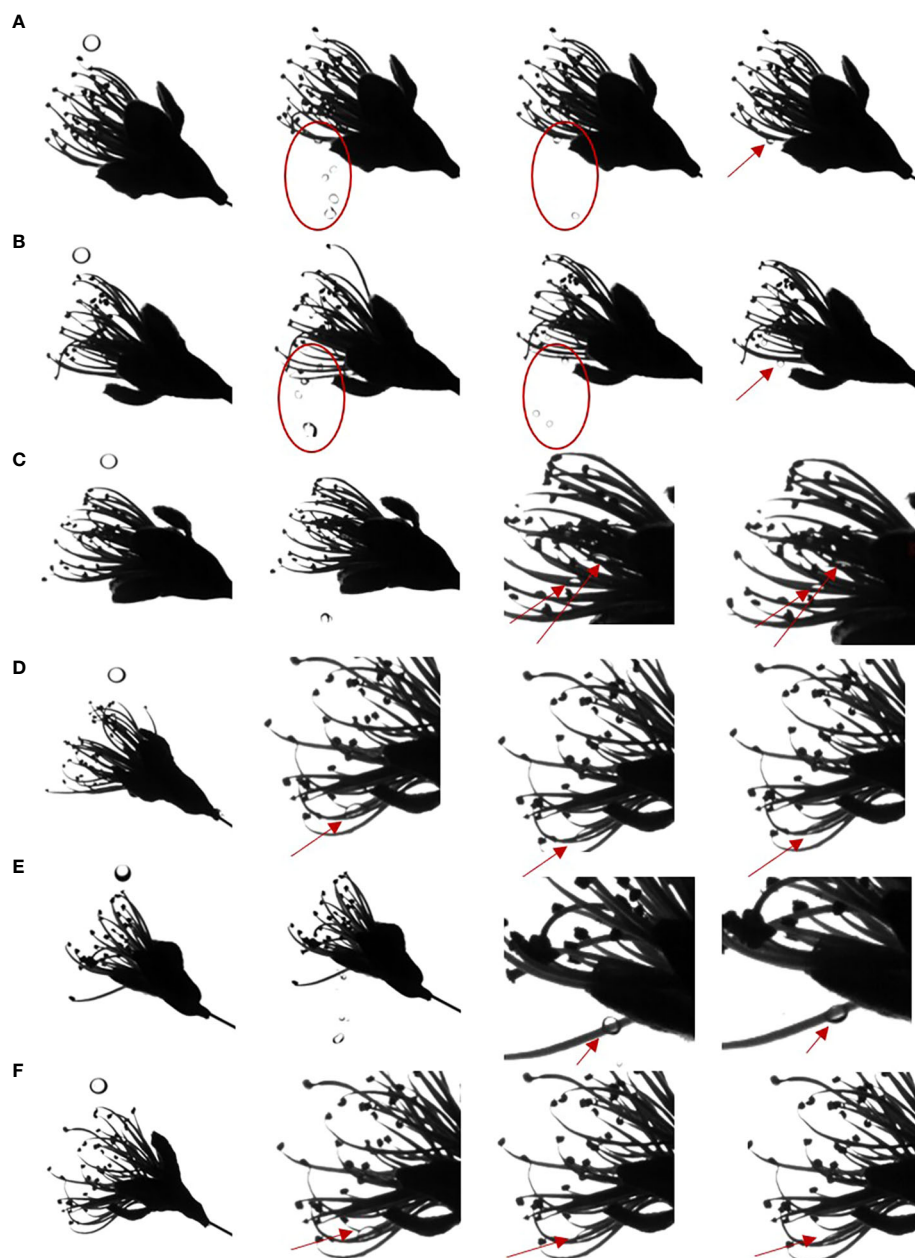
FIGURE 5
Spreading process of droplets on the pistil and stamen. **(A–F)** The spreading behavior of droplets on the pistil and stamen. **(A)** Water, **(B)** 0.75 B° LS, **(C)** 0.1% AOT, **(D)** 0.1% AOT + 0.16% MO, **(E)** 0.75 B° LS + 0.1% AOT, and **(F)** 0.75 B° LS + 0.1% AOT + 0.16% MO. AOT, dioctyl sulfosuccinate sodium salt; MO, methyl oleate; LS, lime sulfur; B°, baume degrees.

adjuvants need to be added to liquids to increase permeability and spread ability to promote absorption of the liquid. This can reduce the loss of pesticides, and improve its use rate.

3.8 Field experiments

3.8.1 Effects of various thinning treatments on flowers

Experimental information on the effects of different treatments on flowers is summarized in support Information (SI).

Spraying water had no effect on flower growth. Spraying 0.1% AOT, 0.165% MO, and 0.03% emulsifier negatively affected the growth of petals but had no effect on the growth of stamens and pistils. Spraying various concentrations of LS or LS + 0.1% AOT + 0.16% MO significantly negatively affected the growth of flowers. The 0.75 B° + 0.1% AOT + 0.16% MO solution was selected for further study as it provided optimum experimental results.

3.8.2 Analysis of parameters of apple thinning

The effect of adjuvants on the spreading, wetting, and penetration behavior of droplets on petal and stamen surfaces has been established.
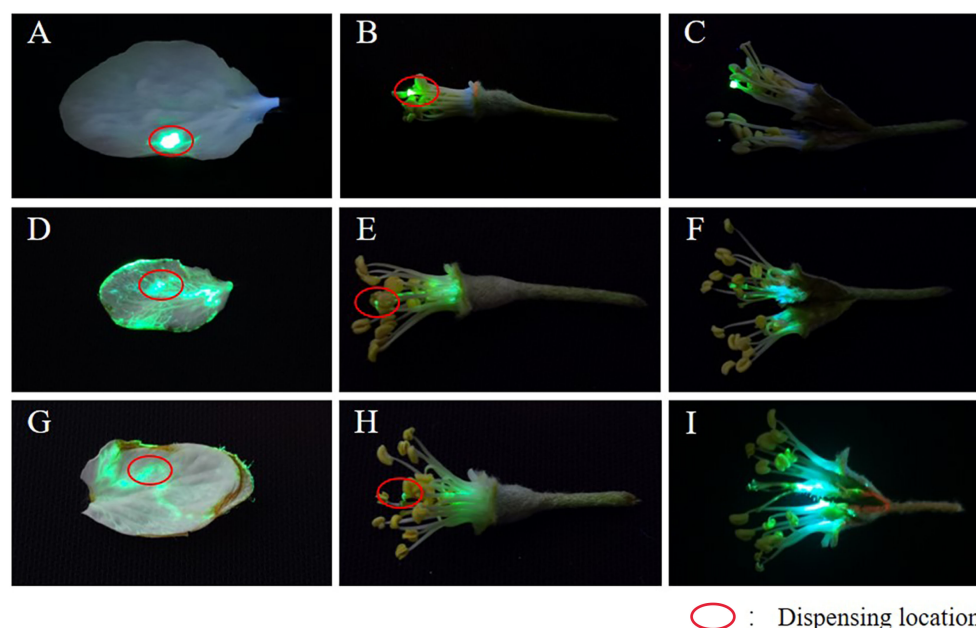
FIGURE 6
Permeability and spreadability behavior of the droplets estimated using the fluorescent tracer method. **(A–I)** The permeability and spreadability behavior of the droplets using the fluorescent tracer method. **(A-C)** pyranine, **(D-F)** pyranine + 0.1% AOT, and **(G-I)** pyranine + 0.1% AOT + 0.16% MO. AOT, dioctyl sulfosuccinate sodium salt; MO, methyl oleate.

Based on the results, field experiments on flower thinning were performed to further evaluate the effect of LS with or without adjuvants on thinning. Pesticide spraying was performed twice in the flowering stage, and statistical analysis of the field data was performed after the apples were set (Figure 7).

Various levels of LS exhibited significantly different flower thinning effects on apples, but the effects were better than the water control. At 0.5, 0.75, and 1 B° LS, the inflorescence fruit setting rates were 88.73%, 81.87%, and 74.93%, respectively (Figure 7A), which were higher than those by artificial thinning. However, the inflorescence fruit setting rate of LS and adjuvants combination was similar to that of artificial thinning (52.51%), and that of 0.1% AOT + 0.16% MO (62%) was better than that of 0.1% AOT (68.38%). Further, we sprayed adjuvants alone (treatments 2 and 3 in the Figure 7), and the inflorescence fruit setting rate was comparable to that of water. The empty fruit rate exhibited the same trend as that of the inflorescence fruit set rate (Figure 7D).

At 0.5, 0.75, and 1 B° LS, the total flower fruit setting rate was 63.75%, 54.65%, and 30.42%, respectively, whereas that of artificial thinning was 27.33%. The total flower fruit set rate of the LS and adjuvants combinations was 38.64 (treatment 7) and 30.87 (treatment 8). Further, after spraying the adjuvant alone (treatments 2 and 3 in the Figure 7), the total flower fruit setting rate was over 60%. The differences in single fruit set rate and flower thinning rate among various treatments can be seen in Table S1. The total flower fruit setting rate is closely related to the single and double fruit set rates, and the single and double fruit rates positively affect the quality of the fruit. In Figure 7C, we can see that the single and double fruit set rates of treatments 6, 7, 8, and 9 were close to 100%. However, as mentioned before, the inflorescence fruit set rate

of treatment 6 was too high, and that of treatments 7 and 8 was close to that of artificial thinning.

3.8.3 Determination of fruit quality and economic valuation

After analyzing the data of the thinning test, an artificial thinning treatment was conducted for some treatments (except water treatment) to avoid overhanging fruits and detrimental effects on fruit growth. Fruit that has not been thinned loses approximately 20% of its weight, which affects not only the quality of the fruit but also the healthy growth of the tree. For Yueguan apples, the addition of flower thinning agent and adjuvants had no adverse effect on the sensory quality of apples, which is an important consideration while using flower thinning agents (Table 3).

At the same time, we calculated the input cost difference between a chemical flower thinning agent and artificial thinning (Table 4). The experimental values of the thinning agent were taken as the standard, and costs calculated into hectares. The cost of chemical flower thinning was only 20% of that of the labor cost for manual thinning. Moreover, the combination of chemical flower thinning agent and adjuvants not only achieved better effects than higher concentrations of thinning agent alone, but also costed less and had a higher usage value.

4 Conclusion

In summary, this study systematically explored the synergistic effects of addition of adjuvant AOT and (AOT +MO) into LS in the chemical desensitization process from three perspectives: indoor physical and chemical properties, nature of the physical target, and
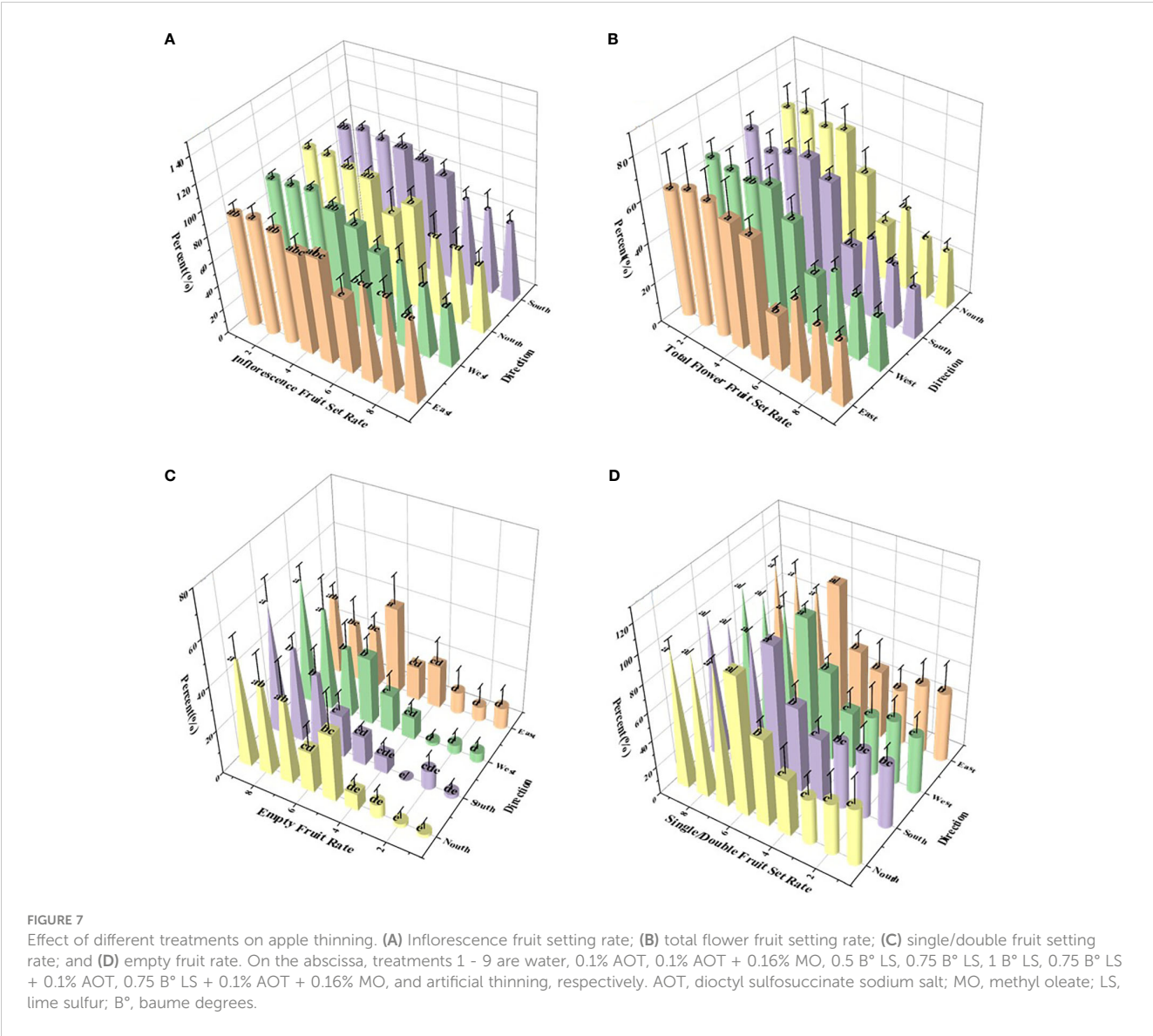
FIGURE 7
Effect of different treatments on apple thinning. **(A)** Inflorescence fruit setting rate; **(B)** total flower fruit setting rate; **(C)** single/double fruit setting rate; and **(D)** empty fruit rate. On the abscissa, treatments 1 - 9 are water, 0.1% AOT, 0.1% AOT + 0.16% MO, 0.5 B° LS, 0.75 B° LS, 1 B° LS, 0.75 B° LS + 0.1% AOT, 0.75 B° LS + 0.1% AOT + 0.16% MO, and artificial thinning, respectively. AOT, dioctyl sulfosuccinate sodium salt; MO, methyl oleate; LS, lime sulfur; B°, baume degrees.

TABLE 3 Effect of various thinning treatments on fruit quality.

Treatment	Fruit Mass (g)	Soluble Solids (%)	Fruit Firmness (Kg/cm^2)	Fruit Shape Index
Water	103.46 ± 6.80b	12.09 ± 0.91ab	10.83 ± 0.84bc	0.85 ± 0.05a
0.1%AOT	108.32 ± 3.41b	11.67 ± 0.86b	11.04 ± 0.55ab	0.87 ± 0.07a
0.1% AOT + 0.16% MO	108.45 ± 6.59b	12.00 ± 0.80ab	11.06 ± 0.49ab	0.86 ± 0.06a
0.5 B° LS	126.94 ± 5.52a	12.15 ± 0.95ab	10.38 ± 0.46c	0.86 ± 0.03a
0.75 B° LS	126.35 ± 7.62a	12.11 ± 0.87ab	10.77 ± 0.95bc	0.88 ± 0.05a
1 B° LS	129.42 ± 5.93a	12.11 ± 0.76ab	10.91 ± 0.49bc	0.88 ± 0.05 a
0.75 B° LS +0.1%AOT	129.01 ± 8.52a	12.33 ± 0.61ab	11.57 ± 0.51a	0.87 ± 0.08a
0.75 B° LS + 0.1% AOT + 0.16% MO	127.80 ± 4.71a	12.56 ± 0.52a	11.13 ± 0.53ab	0.89 ± 0.05a
Artificial	130.82 ± 4.96a	12.03 ± 0.8ab	11.25 ± 0.51ab	0.84 ± 0.05a

The data in the table is the average value of 20 repeated treatments shown in materials and methods, and the data in the same column marked with different lowercase letters indicate significant differences (p<0.05).
AOT, dioctyl sulfosuccinate sodium salt; MO, methyl oleate; LS, lime sulfur; B°, baume degrees.
The variety of apple is "Yue Guan".

TABLE 4   Average dosage and cost comparison chart of various thinning treatments.

Treatment	Dosage (kg/ha^2)	Cost (yuan/ha^2)	Account for the Percentage of Artificial (%)
0.5 B° LS	7.50	367.5 + 450	22.71
0.75 B° LS	8.55	418.95 + 450	24.14
1 B° LS	10.00	490.25 + 450	26.12
0.75 B° LS +0.1%AOT	7.5 + 0.015	418.95 + 15 + 450	24.55
0.75 B° LS + 0.1% AOT + 0.16% MO	7.5 + 0.045	418.95 + 18 + 450	24.64
Artificial		3600.00	100.00

AOT, dioctyl sulfosuccinate sodium salt; MO, methyl oleate; LS, lime sulfur; B°, baume degrees.
The variety of apple is "Yue Guan".

field experiments. The addition of adjuvants could effectively reduce the static surface tension from 72mN/m to 28mN/m and 32mN/m respectively, increase the spreading factor from 0.18 to 1.83 and 3.10 respectively, reduce the bounce factor from 2.72 to 0.37 and 0.27 respectively, and increase the deposition amount of the droplets on target interface. In particular, the increase in solution spread ability and permeability caused by adjuvants increased droplet deposition in the flower and paraffin surfaces, such as stamens, and promoted the absorption. The field test results revealed that the flower thinning rate of adjuvant and non-adjuvant were 80.55% and 54.4% respectively, and the flower thinning effect of adding adjuvant was the same as that of artificial which the flower thinning rate was 84.77%. The quality of apples treated with adjuvants was similar to that treated with artificial, and the weight of single fruit increased by 24.08% compared with CK (spray water). In this study, AOT and MO were used as adjuvants to improve the efficiency of flower thinning agents. Most of the current studies focus on the effect of adjuvants on pesticide, but there are seldom related studies on the effect of additives on plant growth regulators. This work not only provided guidance for increasing the deposition and spreading of droplets on the hydrophobic interface of petals, stamens and leaves, but also expanded the application of adjuvants in plant growth regulators, and promoted the sustainable green development of agriculture.

Author's note

Due to the high seasonal requirements of test materials and the small volume stamens and pistils of apples, the stamens and pistils used in the test were peach blossoms belonging to the Rosaceae family.

Data availability statement

The raw data supporting the conclusions of this article will be made available by the authors, without undue reservation.

Author contributions

ZZ: Conceptualization, Funding acquisition, Project administration, Resources, Supervision, Validation, Writing – review & editing. YYL: Data curation, Formal Analysis, Investigation, Methodology, Software, Writing – original draft, Writing – review & editing. YL: Data curation, Investigation, Writing – review & editing. CW: Data curation, Writing – review & editing. RZ: Data curation, Software, Writing – review & editing. ML: Investigation, Writing – review & editing. JC: Methodology, Writing – review & editing. LM: Methodology, Writing – review & editing. XH: Conceptualization, Supervision, Writing – review & editing. XW: Conceptualization, Supervision, Writing – review & editing.

Funding

Acknowledgments

Conflict of interest

Authors JC and LM were employed by the company Qingshengyuan Agricultural Development Co., Ltd.

The remaining authors declare that the research was conducted in the absence of any commercial or financial relationships that could be construed as a potential conflict of interest.

Publisher's note

Supplementary material

The Supplementary Material for this article can be found online at: https://www.frontiersin.org/articles/10.3389/fpls.2023.1257672/full#supplementary-material

References

Arand, K., Stock, D., Burghardt, M., and Riederer, M. (2010). pH-dependent permeation of amino acids through isolated ivy cuticles is affected by cuticular water sorption and hydration shell size of the solute. *J. Of Exp. Bot.* 61, 3865–3873. doi: 10.1093/jxb/erq193

Armstrong, S., McHale, G., Ledesma-Aguilar, R., and Wells, G. G. (2020). Evaporation and electrowetting of sessile droplets on slippery liquid-like surfaces and slippery liquid-infused porous surfaces (SLIPS). *Langmuir* 36, 11332–11340. doi: 10.1021/acs.langmuir.0c02020

Bormashenko, E. (2015). Progress in understanding wetting transitions on rough surfaces. *Adv. In Colloid Interface Sci.* 222, 92–103. doi: 10.1016/j.cis.2014.02.009

Buchholz, A. (2006). Characterization of the diffusion of non-electrolytes across plant cuticles: properties of the lipophilic pathway. *J. Of Exp. Bot.* 57, 2501–2513. doi: 10.1093/jxb/erl023

Gao, M., Wang, X. G., Lv, W. F., Zhou, Z. H., Zhang, Q., Ma, D. S., et al. (2020). Adsorption behaviors of branched cationic gemini surfactants and wettability in quartz-solution-air systems. *Soft Matter* 16, 5450–5457. doi: 10.1039/D0SM00689K

Gonzalez, L., Torres, E., Àvila, G., Bonany, J., Alegre, S., Carbó, J., et al. (2020). Evaluation of chemical fruit thinning efficiency using Brevis® (Metamitron) on apple trees ('Gala') under Spanish conditions. *Scientia Hortic.* 261, 109003. doi: 10.1016/j.scienta.2019.109003

Grundke, K., Pöschel, K., Synytska, A., Frenzel, R., Drechsler, A., Nitschke, M., et al. (2015). Experimental studies of contact angle hysteresis phenomena on polymer surfaces — Toward the understanding and control of wettability for different applications. *Adv. In Colloid Interface Sci.* 222, 350–376. doi: 10.1016/j.cis.2014.10.012

He, L., Ding, L., Li, B., Mu, W., Li, P., and Liu, F. (2021). Regulating droplet wetting and pinning behaviors on pathogen-modified hydrophobic surfaces: strategies and working mechanisms. *J. Agric. Food Chem.* 69, 11720–11732. doi: 10.1021/acs.jafc.1c04216

Holb, I., Jong, P., and Heijne, B. (2003). Efficacy and phytotoxicity of lime sulfur in organic apple production. *Ann. Appl. Biol.* 142, 225–233. doi: 10.1111/j.1744-7348.2003.tb00245.x

Kovalchuk, N. M., Trybala, A., Starov, V., Matar, O., and Ivanova, N. (2014). Fluoro-vs hydrocarbon surfactants: Why do they differ in wetting performance? *Adv. In Colloid Interface Sci.* 210, 65–71. doi: 10.1016/j.cis.2014.04.003

Lee, J. B., and Lee, S. H. (2011). Dynamic wetting and spreading characteristics of a liquid droplet impinging on hydrophobic textured surfaces. *Langmuir* 27, 6565–6573. doi: 10.1021/la104829x

Li, Z., Ma, Y., Zhao, K., Zhang, C., Gao, Y., and Du, F. (2021). Regulating droplet impact and wetting behaviors on hydrophobic weed leaves by a double-chain cationic surfactant. *ACS Sustain. Chem. Eng.* 9, 2891–2901. doi: 10.1021/acssuschemeng.0c08883

Lordan, J., Alins, G., Àvila, G., Torres, E., Carbó, J., Bonany, J., et al. (2018). Screening of eco-friendly thinning agents and adjusting mechanical thinning on 'Gala', 'Golden Delicious' and 'Fuji' apple trees. *Scientia Hortic.* 239, 141–155. doi: 10.1016/j.scienta.2018.05.027

Marchioretto, L. D. R., De Rossi, A., Amaral, L. O. D., and Ribeiro, A.M.A.D. l (2019). Efficacy, and mode of action of blossom thinners on 'Fuji More' apple trees. *Scientia Hortic.* 17, 2619–2621. doi: 10.1016/j.scienta.2018.11.039

Meng, G., Zhou, J., and Jin, C. (2016). Research Progress on Plant Source Herbicide Adjuvants. *Hunan agricultural science & technology newsletter: HASTN* 17, 2619–2621. doi: 10.16175/j.cnki.1009-4229.2016.11.043

Ngugi, H. K., and Schupp, J. R. (2009). Photosynthesis inhibition as a tool for apple fruitlet thining. *Hortscience* 3, 862–865. doi: 10.21273/HORTSCI.44.3.862

Quéré, A. L. A. D. (2003). Superhydrophobic states. *Nat. Materials* 2, 457–460. doi: 10.1038/nmat924

Song, M., Hu, D., Zheng, X., Wang, L., Yu, Z., An, W., et al. (2019). Enhancing droplet deposition on wired and curved superhydrophobic leaves. *ACS Nano* 13, 7966–7974. doi: 10.1021/acsnano.9b02457

Song, M., Ju, J., Luo, S., Han, Y., Dong, Z., Wang, Y., et al. (2017). Controlling liquid splash on superhydrophobic surfaces by a vesicle surfactant. *Sci. Adv.* 3, e1602188–e1602188. doi: 10.1126/sciadv.1602188

Xu, L., Zhu, H., Ozkan, H. E., Bagley, W. E., and Krause, C. R. (2011). Droplet evaporation and spread on waxy and hairy leaves associated with type and concentration of adjuvants. *Pest Manage. Sci.* 67, 842–851. doi: 10.1002/ps.2122

Zhao, R., Sun, Z., Bird, N., Gu, Y., Xu, Y., Zhang, Z., et al. (2022). Effects of tank-mix adjuvants on physicochemical properties and dosage delivery at low dilution ratios for unmanned aerial vehicle application in paddy fields. *Pest Manage. Sci.* 78, 1582–1593. doi: 10.1002/ps.6777

Zheng, L., Cao, C., Chen, Z., Cao, L., Huang, Q., and Song, B. (2021). Efficient pesticide formulation and regulation mechanism for improving the deposition of droplets on the leaves of rice (Oryza sativa L.). *Pest Manage. Sci.* 77, 3198–3207. doi: 10.1002/ps.6358

Check for updates

Development and evaluation of 4WSS electric-driven chassis for high-clearance sprayer

Siwei He, Yue Shen*, Yafei Zhang and Hui Liu

School of Electrical and Information Engineering, Jiangsu University, Zhenjiang, China

Introduction: The high clearance sprayer with conventional steering mechanisms, as an intelligent spraying machine, is frequently stuck or broken in muddy fields due to the excessive torque load.

Methods: A Four-Wheel Self-Steering (4WSS) electric-driven chassis with a smaller turning radius and better passability is developed to handle complex agricultural terrains. The 4WSS chassis is mainly composed of two custom-designed steering bridges and four in-wheel drive motors. It can achieve steering and driving forward simultaneously through coordinate differential speed control of drive motors, saving a set of dedicated servo steering systems and requiring less torque during steering compared to conventional structures. A kinematic model depicting the speed relationships between four wheels is established via geometric analysis, and a Speed Distribution Controller (SDC) is designed to accomplish locomotion objectives.

Results: Experimental results demonstrate the effectiveness of the new prototype 4WSS chassis system in tracking speed and steering angle. Compared to conventional agricultural chassis, the 4WSS chassis has a smaller turning radius of 2,877 mm.

Discussion: The 4WSS chassis exhibits superior performance in typical field conditions, including muddy terrain, deep gullies, and ridges.

KEYWORDS

crop protection, high clearance sprayer, four-wheel self-steering chassis, electrically driven, speed distribution controller

1 Introduction

The high-clearance sprayer is an important type of agricultural machinery that aims to protect crops from diseases, insects, and weeds. Its steering performance and obstacle-surmounting performance directly affect working efficiency (Oksanen and Linkolehto, 2013; Ding et al., 2018).

Paddy soil has thixotropic properties. When the sprayer chassis repeatedly walks or turns in the paddy field, the soil structure of the paddy field will be damaged, the bearing

capacity and shear capacity will be reduced, and the adhesion will be aggravated (Zeng et al., 2019). This often results in the chassis getting stuck in the mud. It is also easy to cause damage to the chassis transmission system and vertical shaft while struggling (Chen et al., 2020). Zeng et al. (2019) designed a wheel-track compound power chassis for a high-clearance sprayer aimed at preventing excessive sinking in paddy fields. The rear wheel was transformed into a tracked structure, leading to a reduction in its sinking depth. But it will crush more plants when turning. Wang et al. (2017) designed a high-clearance roll-waist multifunctional power chassis aimed at improving the stability of field driving and surmounting ridge performance. However, the muddy situation was not well discussed in that paper. Li et al. (2018) designed a high-clearance self-walking full-hydraulic independent driver for the universal operating chassis. The walking variable pump was directly driven by the engine. Torque was transmitted to the walking system and steering system through a hydraulic pump. Compared with the mechanical transmission chassis, the hydraulic transmission chassis was not only more convenient in layout but also more reliable. It also had a certain effect on the improvement of the ability to surmount obstacles. Actual research on the chassis in the academic community was mostly concentrated on the hydraulic transmission chassis for such advantages (Hui et al., 2018; Li et al., 2019; Liu et al., 2019).

Nevertheless, an electric chassis is more efficient (Park et al., 2019) and causes less pollution (Sato et al., 2022) than a hydraulic chassis, and its proportion in the vehicle field is gradually increasing (Park et al., 2023). Moreover, the electric chassis has better performance on controllability, particularly the four-wheel independent drive (4WID) structure (Wang et al., 2022). Each wheel's torque or speed can be controlled independently, giving it strong potential in terms of handling stability and flexibility (Liang et al., 2020; Liu et al., 2021).

Based on the 4WID chassis, some academics had further proposed the concept of differential steering, which generated steering torque by separately controlling the speed or torque of each in-wheel motor. Wang et al. (2008) proposed a novel power-assisted differential steering system based on the front two-wheeled differential steering (FTDS) electric vehicle (EV). Then, a vehicle dynamics model with the steering system was built in SIMULINK, and a phase lead compensator was designed to modulate differential torque of the front wheels. Wu et al. (2013); Wu et al. (2014) investigated an FTD EV by analyzing the kinematic model with the Ackermann–Jeantand steering. A speed-following control was designed to achieve electrical differential. Oke et al. (2016) designed a dynamic output feedback controller for an all-wheeled differential steering (AWDS) EV. The vehicle dynamic system with road adhesion was analyzed, and the $H\infty$ controller was utilized to improve yaw dynamics performances. Kuslits and Bestle (2019) analyzed the motion of the AWDS EV and proved that differential steering had a comparable steering performance as that of conventional passenger cars through various simulation experiments. This demonstrated that simplifying or omitting the dedicated steering actuators of the vehicle was reasonable. Summing up the above, the methods of differential chassis were mainly based

on the kinematic speed-following method or dynamic traction force distribution method. Considering the demand for field chassis and the advantages of electric chassis, the four-wheel self-steering (4WSS) electric chassis was proposed in this paper. Based on the research experience of other differential chassis, the research route was determined to start from kinematics.

Therefore, the main contributions of this paper are as follows: 1) The 4WSS chassis is designed with four independently driven power motors, and the special steering structure improves the steering and surmounting ability in mud; 2) The linkages, designed to constrain the front and rear steering bridge, are analyzed, and the calculation method of its installation point is demonstrated; 3) The 4WSS chassis kinematics model is established, and its SDC is designed; 4) Field tests prove a small steering radius and better passability of the 4WSS chassis.

2 Materials and methods

2.1 Chassis structure design

The actual demand for paddy field machinery is considered for the design of 4WSS chassis, which is sketched in Figure 1. The 4WSS chassis is driven independently by in-wheel motors, and the wheels which are embedded Brushless Direct Current Motor (BLDC) motors are installed on both sides of the steering bridges. The steering bridges are both connected to the frame with slewing bearings. So, steering bridges are separately rotated around slewing bearings to form steering angles. The linkages between the front and rear steering bridges make the amplitudes of steering angles equal. Compared with the hydraulic transmission chassis, the electric chassis has advantages of larger torque and stronger capability to surmount obstacles (Ragheb et al., 2013). The 4WSS chassis, steering by controlling four-wheel differentials, is significantly different from the existing differential chassis.

The novel structure of the 4WSS chassis brings challenges to modeling and steering control. And its basic components are divided into three sections: Backbone Structure, Linkage Structure, and Drive System.

2.1.1 Backbone structure

Unlike most existing Ackermann steering chassis, the 4WSS chassis backbone structure mainly consists of three parts: the freely rotating front steering bridge and rear steering bridge and the frame. The front and rear steering bridges are inverted U-shaped structures, and in-wheel motors (wheels with BLDC motors embedded inside) are mounted on both sides. The steering bridges are connected to the frame with slewing bearings.

The basic structure of the 4WSS chassis is shown in Figure 2. As shown in Figure 2A, A and B are the center point of the front and rear steering bridge separately. The bridges are connected to the frame with slewing bearings. The assembled figure is shown in Figure 2B. The four wheels are named the front left (*fl*) wheel, front right (*fr*) wheel, rear left (*rl*) wheel, and rear right (*rr*) wheel according to their positions on the chassis.
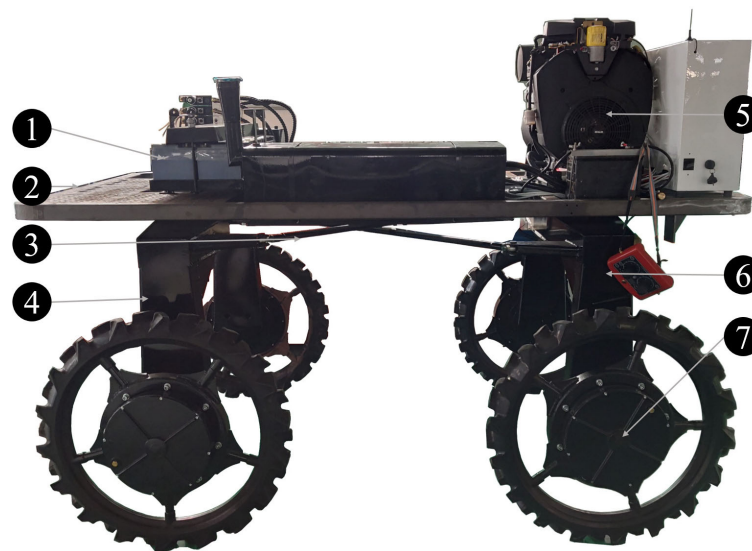
FIGURE 1
The four-wheel self-steering (4WSS) chassis. 1: lead-acid batteries; 2: frame; 3: linkages; 4: front steering bridge; 5: generator; 6: front steering bridge; 7: wheel (BLDC motor embedded inside).

To better demonstrate the working principle of the chassis, the three Cartesian coordinate systems are established as sketched in Figure 3. At the geometric center of the frame, the coordinate system O is attached. Axis x is parallel to OA and points to A. At the geometric center of the front steering bridge, the coordinate system A is attached. Axis y_A is parallel to the bridge and points to the front left wheel. In the same way, at the geometric center of the rear steering bridge, the coordinate system B is attached. Axis y_B is parallel to the bridge and points to the rear left wheel. Take the front steering bridge as an example, define the front steering angle as the angle rotated from x to x_A and the anticlockwise direction represents positive. Four in-wheel motors are mounted on the front and rear steering bridges, and each motor can be driven independently.

The chassis runs straight when the front and rear steering angles are 0. In the case that the front steering angle is greater than the rear steering angle, the chassis will turn left and vice versa. The front and rear steering angles can be changed by the speed of the corresponding in-wheel motors. So, the critical problem of

controlling this chassis is controlling the speed of the four in-wheel motors.

2.1.2 Linkage structure

The linkage structure is designed to improve the stability and anti-disturbance ability of the chassis by formulating hard constraints on steering angles of the front and rear bridges. With such constraint, the steering angles are consistently kept opposite and numerically equal.

Figure 4 is the linkage structure diagram. $a_1 \sim a_4$ are the four installation points of the linkage structure. The two linkages a_1a_2 and a_3a_4 are cross-connected at four connecting points. The major challenge of the linkage structure lies in the position selection of the linkage installation points $a_1 \sim a_4$. The points $p_1 \sim p_4$ are on the center line of the steering bridge respectively, and the distance from the center of the steering bridge is d. The distance between point a_i and point p_i is $c(i = 1 \sim 4)$. The line $p_i a_i$ is perpendicular to axis y_B or y_A.

The straight run state is shown in Figure 4A, and the steering run state is shown in Figure 4B. The optimal
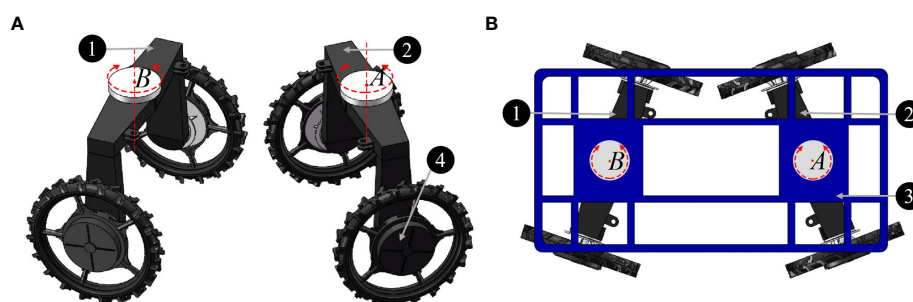

FIGURE 2
Basic structure of the four-wheel self-steering (4WSS) chassis. **(A)** Front bridge and rear bridge. **(B)** Connection of one main frame and two steering bridges.
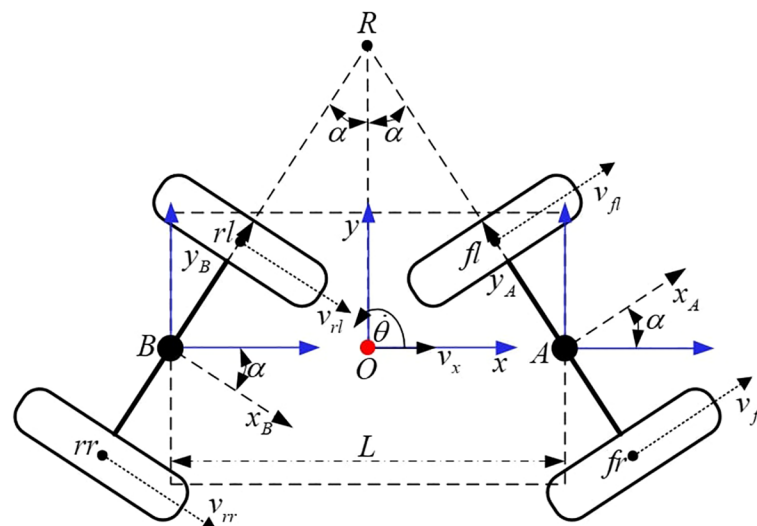
FIGURE 3
Self-steering structure diagram.

installation points, the positions of a_1 to a_4, should be settled where the two linkages remain the same length throughout the steering process. Only one linkage will be analyzed by considering the symmetrical property. With regard to the length between a_1 and a_2, when the steering bridge angle is α, the length of the linkage is:

$$H(\alpha) = \sqrt{4d^2\cos^2(\alpha) + (L - 2c\cos(\alpha))^2} \qquad (1)$$

The linkage steering error $E(\alpha)$ is defined as the difference between $H(0)$ and $H(\alpha)$.

$$E(\alpha) = H(0) - H(\alpha) = \sqrt{4d^2 + (L - 2c)^2} \\ -\sqrt{4d^2\cos^2(\alpha) + (L - 2c\cos(\alpha))^2} \qquad (2)$$

When the chassis is moving, the range of the steering angle should be limited. The maximum steering angle is called the mechanics-limited steering angle, and the value is 25°. As the steering angle increases, the stability progressively decreases. The mechanics-limited steering angle is $\alpha \in [-25°, 25°]$. Since $E(a)$ is an even function, it is just analyzed when $\alpha \in [0°, 25°]$. The derivative of $E(\alpha)$ is:

$$\dot{E}(\alpha) = \frac{4d^2\sin(\alpha)\cos(\alpha)}{\sqrt{4d^2\cos^2(\alpha) + (L - 2c\cos(\alpha))^2}} \\ - \frac{2c(L - 2c\cos(\alpha))\,\text{son}(\alpha)}{\sqrt{4d^2\cos^2(\alpha) + (L - 2c\cos(\alpha))^2}} \qquad (3)$$

An optimal installation point d and c can be solved from Equation 4, which implies $E(\alpha) = E(0) = 0$ under such solution.

$$\dot{E}(\alpha) = 0 \qquad (4)$$

And the solution of Equation 4 is

$$\begin{cases} d = 0 \\ c = 0 \end{cases} \qquad (5)$$

This is not a feasible installation point. So, there is no perfect installation point to keep the linkage remaining in the same length at all steering angles. Thus, a linkage with a slightly deformable capability is taken into consideration.

When handling the position of the installation point, d is selected first, determined by the chassis manufacturer. Then, an appropriate c can be obtained by fixing the steering angles α and d, and the results can be verified at last.
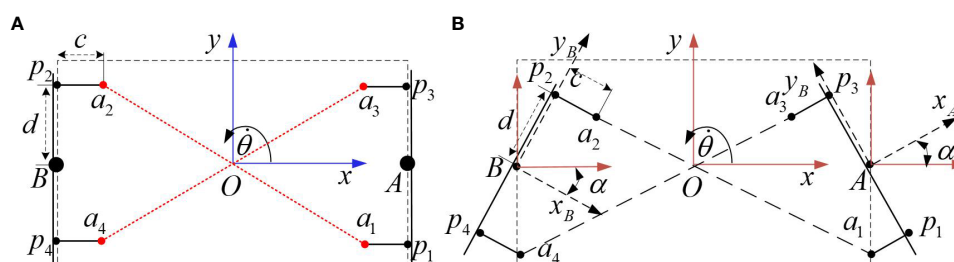

FIGURE 4
Linkage structure diagram. **(A)** The straight run state. **(B)** The steering run state.

Solve Equation 6 to achieve a suitable c.

$$E(\alpha) = 0 \tag{6}$$

The two solutions to c are

$$c_1 = \frac{L - \sqrt{(L - 2d\cos\ (\alpha) - 2d)(L + 2d\cos\ (\alpha) + 2d)}}{2(\cos\ (\alpha) + 1)} \tag{7}$$

$$c_1 = \frac{L + \sqrt{(L - 2d\cos\ (\alpha) - 2d)(L + 2d\cos\ (\alpha) + 2d)}}{2(\cos\ (\alpha) + 1)} \tag{8}$$

Design the parameters $L = 1.7$ m, $d = 0.406$ m, $\alpha = 25°$. Then, the solutions can be solved from Equations 7 and 8 that

$$\begin{cases} c_1 = 0.262 \\ c_2 = 0.630 \end{cases} \tag{9}$$

Use the calculated c_1 and c_2 to plot the error graphic (Figure 5) of $E(\alpha)$ with respect to α.

The corresponding maximum error varies as c changes. When $c = c_1$, the maximum error is 0.75 mm, and when $c = c_2$, the maximum error is 2.73 mm. So c_1 is a suitable solution. The linkage remains deformation during steering, which is less than 0.75 mm within the elastic range.

2.1.3 Drive system

Four in-wheel motors mounted on the steering bridges provide tractive force. Therefore, the design of the drive system is mainly based on the power distribution system, the in-wheel motor and driver system, and the drive control system.

2.1.3.1 Power distribution system

For the chassis to function smoothly, a stable power distribution system is essential, which is sketched in Figure 6. The electrical bus connects the batteries and generator to the drivers of the motors, DC-DC converter, and other work systems. One battery pack with six cells is attached to the front of the chassis. Each battery provides a nominal voltage of 12 V, and six batteries together proved a nominal bus voltage of 72 V. A power generation unit, composed of

FIGURE 5
Error graph with different values about c.

a petrol engine, generator, and AC-DC converter, is housed at the rear of the chassis. There are mainly three kinds of electrical equipment on the chassis: VCU, motor drivers, and other work systems (spray, chemical mixer, etc.). VCU draws 12 V of direct electric current from the DC-DC converter, while the motor drivers and other working systems are connected to the 72-V bus directly.

2.1.3.2 The in-wheel motor and driver system

As shown in Figure 7, an in-wheel motor mainly consists of four parts: a hub, an embedded permanent magnet synchronous motor (BLDC), a reduction mechanism, and a tire. Five spokes are used between the rim and the center, so the wheel is mostly hollow. The wheels do not use conventional pneumatic tires but solid rubber tires. Solid rubber tires require less maintenance and can be made with a deeper tread for better grip in muddy paddy fields. The tire width is 11 cm, and a wider tire has a larger contact area with the road surface, making movement easier in muddy fields.
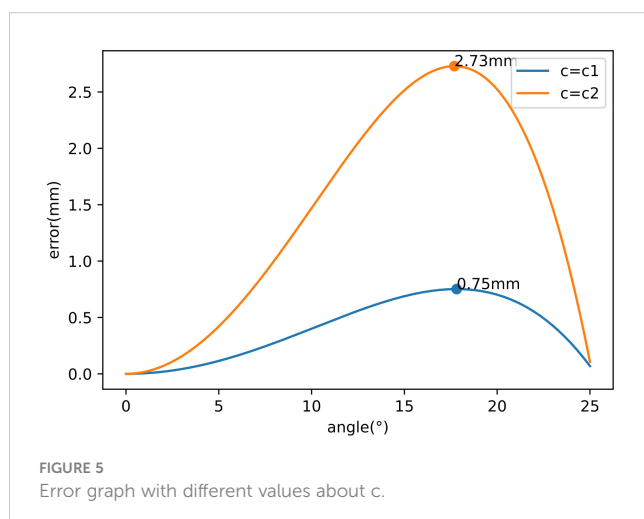
The embedded motor has a rated power of 4 kW, a rated voltage of 72 V, and a rated speed of 1,000 rpm. The in-wheel motor is composed of a planetary gear coaxial deceleration structure with a reduction ratio of 1:19, which reduces the speed of the in-wheel motor to 52.6 rpm. The wheel radius is 0.483 m, so the rated chassis speed of the in-wheel motor is near 10 kmh^{-1}.
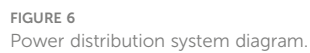
The motor driver (Kelly QSKLS8430H) is selected for driving the embedded motor. It has a rated current of 100 A and an input voltage of 24 V~105 V. The driver adjusts the input voltage of the BLDC motor, according to the control signal from the VCU, to control the speed of the wheel. The CAN bus is used between the driver and the controller.

Kelly QSKLS8430H is a general-purpose EV driver, its basic functions including torque output and regenerative braking. The driver will actively ignore the given reverse torque output when the motor speed is positive. Therefore, in this case, it needs to be set to the regenerative braking mode, so that the reverse torque is small but sufficient for speed control.

2.1.3.3 Drive control system

Figure 8 depicts a diagram of the communication-level system. The platform is controlled by a high-performance microcontroller unit (MCU) STM32F407VET6. This MCU communicates with four motor drivers via the CAN bus interface. The drivers receive the control message from the MCU, and its output wheel velocity gives feedback to the MCU. The wireless module, the motor drive system, and the angle sensors constitute the minimum system of chassis operation. The wireless module communicates with the remote controller to receive commands from the operator. Two linear hall angle sensors are mounted on the front and the rear steering bridge, respectively. Therefore, the front and rear steering angles can be obtained in real time through the 12-bit ADC of the MCU. The MCU handles control tasks by assembling the operator's commands and the feedback signals. The in-wheel motors are braked via the power-off of the brake coils, which is controlled by the brake controller. This can be used when braking or parking. The brake controller communicates with the MCU via Modbus, receiving

FIGURE 6
Power distribution system diagram.

FIGURE 7
The wheel of the four-wheel self-steering (4WSS) chassis. 1: hub; 2: embedded permanent magnet synchronous motor; 3: reduction mechanism; 4: solid rubber tire.

FIGURE 8
Communication-level system diagram.

MCU control instructions and returning the error of the brake system. The relay controller mainly controls the operation of the generator and other operating systems.

2.1.4 Structural comparison and challenges

Controlling movement and steering of vehicles are two major functions of the chassis. For conventional 4WID chassis, movement is manipulated by drive motors directly and steering is handled by steering motors separately. As shown in Figure 9A, the wheels of the conventional 4WID structure rotate around their center points. The steering of the chassis is restricted by the deflection angle of each wheel. Each wheel rotates around its center point, and the mounting shaft directly bears the reverse torque when steering. When the steering mechanism gets deep sinking in the mud, the wheel has to push the side mud directly away to steer. Under such circumstances, the chassis often fails to provide sufficient torque to turn, or the steering structure cannot withstand excessive torque, resulting in damage.

Different from the conventional 4WID chassis as described above, each wheel of the novel 4WSS chassis rotates around the centers of its corresponding steering bridge, as shown in Figure 9B. The front bridge, taken as an example, when the differential speed of *fl* wheel and *fr* wheel exists, rotates around the mounted point *A*, completely motivated by in-wheel motors. It is not necessary to completely push the side mud during steering. Consequently, the 4WSS chassis requires less steering torque, provides the longer force arm, and replaces the dedicated steering motors with more powerful in-wheel motors. The 4WID 4WSS structure has the potential to get better passability in dealing with muddy conditions.

The conventional 4WID chassis requires dedicated steering servo motors to steer, while the 4WSS chassis employs the differential speed of the in-wheel motors to steer. The 4WSS chassis saves four steering servo motors, reducing the complexity and cost of the hardware system. With the comparison analysis, the structure of the 4WSS chassis is simpler to make higher reliability. On the other hand, challenges in designing the controller arise from the coupling between the in-wheel motors, which completely control the action of the chassis.

2.2 Kinematic model build

The characteristics of the 4WSS chassis indicate its difference in nature from the Ackermann steering structure. The movement of the 4WSS chassis is based on the four-wheel differential speed. Therefore, the study of the relationship between the wheel speed and the chassis movement is the basis for designing the control system.

Figure 3 depicts a diagram of the self-steering structure. On the premise of linkage constraint as described in the section *Linkage Structure*, it can be considered that the front and rear steering angle amplitudes are equal. The prolongation lines of the front and rear steering bridge meet at point *R*. According to geometric relations, $\angle BRO = \angle AOR = \alpha$ can be obtained. Assuming no skidding between the in-wheel motors and the ground, point *R* is the steering center of the 4WSS chassis.

v_{fl}, v_{fr}, v_{rl}, and v_{rr} represent the corresponding speed of each wheel. v_x is 4WSS chassis speed. *L* is the wheelbase, and α is the steering angle. The radius of the steering bridge *I* and the radius of the 4WSS chassis *K* can be obtained.

$$I = RA = \frac{L}{2 \sin \alpha} \tag{10}$$

$$K = RO = \frac{L}{2 \tan \alpha} \tag{11}$$

D is wheel track, and $\dot{\theta}$ is yaw rate. In the case of no slippage, the relationship between the yaw rate and the speed of the four in-wheel motors can be obtained in Equation 12.

$$\dot{\theta} = \frac{v_{fl}}{I - \frac{D}{2}} = \frac{v_{fr}}{I + \frac{D}{2}} = \frac{v_{rl}}{I - \frac{D}{2}} = \frac{v_{rr}}{I + \frac{D}{2}} \tag{12}$$

Rewriting Equation 12 yields the relationship between the in-wheel motor speed and the yaw rate.

$$\dot{\theta} = \frac{v_{fl} + v_{fr} + v_{rl} + v_{rr}}{4I} \tag{13}$$

According to the kinematic relationship, the speed of the chassis v_x can be written as Equation 14.

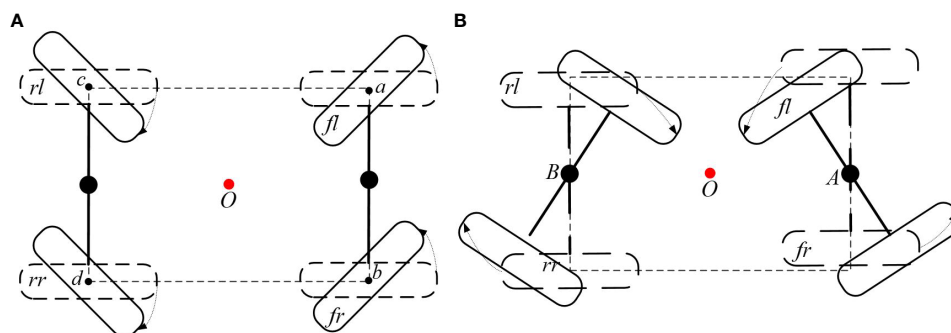$$v_x = \dot{\theta}k \tag{14}$$

FIGURE 9
Comparison of different steering structures. **(A)** Conventional four-wheel independent drive (4WID) structure with dedicated steering actuators. **(B)** The four-wheel self-steering (4WSS) utilizes only drive motors without steering actuators.

Based on Equations 10–14, Equation 15 can be derived.

$$v_x = \frac{v_{fl} + v_{fr} + v_{rl} + v_{rr}}{4} \cos \alpha \qquad (15)$$

Generally, $\alpha \in [-25\,°, 25\,°]$ can be approximated as $\cos\alpha = 1$. Thus, the approximated chassis speed meets Equation 16.

$$v_x = \frac{v_{fl} + v_{fr} + v_{rl} + v_{rr}}{4} \qquad (16)$$

According to Equations 13 and 16, the result can be derived.

$$\dot{\theta} = \frac{v_x}{I} \qquad (17)$$

The speed of each in-wheel motor can be decomposed of the speed around the chassis steering center R and the speed around the bridge steering center A or B.

The velocities of the four in-wheel motors can be obtained as shown in Equations 18–21.

$$v_{fl} = \dot{\theta}\left(I - \frac{D}{2}\right) - \dot{\alpha}\frac{D}{2} \qquad (18)$$

$$v_{fr} = \dot{\theta}\left(I + \frac{D}{2}\right) + \dot{\alpha}\frac{D}{2} \qquad (19)$$

$$v_{rl} = \dot{\theta}\left(I - \frac{D}{2}\right) + \dot{\alpha}\frac{D}{2} \qquad (20)$$

$$v_{rr} = \dot{\theta}\left(I + \frac{D}{2}\right) - \dot{\alpha}\frac{D}{2} \qquad (21)$$

Substitute Equation 17 into Equations 18–21, replace $\dot{\theta}$ with v_x, and then obtain Equations 22–25.

$$v_{fl} = v_x\left(1 - \frac{D}{2I}\right) - \dot{\alpha}\frac{D}{2} \qquad (22)$$

$$v_{fr} = v_x\left(1 + \frac{D}{2I}\right) + \dot{\alpha}\frac{D}{2} \qquad (23)$$

$$v_{rl} = v_x\left(1 - \frac{D}{2I}\right) + \dot{\alpha}\frac{D}{2} \qquad (24)$$

$$v_{rr} = v_x\left(1 + \frac{D}{2I}\right) - \dot{\alpha}\frac{D}{2} \qquad (25)$$

The theoretical model of the 4WSS chassis reveals the correlation between the chassis speed, the steering angle, and the speed of the four wheels. Chassis speed, composed of the in-wheel motor speed and steering angular velocity, is restricted by the limited in-wheel motor speed.

According to the principle of differential steering, the speed of the in-wheel motors on the inner and outer sides varies during steering. It must be ensured that the speed of each of the four wheels shall not be greater than the maximum speed V of the in-wheel motor, as shown in Equation 26.

$$\begin{cases} |v_{fl}| \le V \\ |v_{fr}| \le V \\ |v_{rl}| \le V \\ |v_{rr}| \le V \end{cases} \qquad (26)$$

Union of Equations 22–25 can get Equation 27.

$$|v_x| \le \frac{\left|VL - |\dot{\alpha}|\frac{DL}{2}\right|}{L + D|\sin \alpha|} \qquad (27)$$

To ensure stability during walking, the maximum steering angular speed of the steering bridge will be limited during operation. Let $|\dot{\alpha}| \le \dot{\alpha}_{max}$, and rewrite Equation 27 to get Equation 28.

$$\left|v_{x,max}\right| = \frac{\left|VL - \dot{\alpha}_{max}\frac{DL}{2}\right|}{L + D|\sin \alpha|} \qquad (28)$$

It can be seen that the maximum speed during the operation of the chassis is limited by the maximum speed of the in-wheel motor, the steering angle, and the steering angular speed. Once the maximum speed of the in-wheel motor is determined, the maximum speed of the chassis decreases as the steering angle increases.

Assuming that the chassis is in a steady state and turned at its maximum steering angle. That is $V = 10$ kmh^{-1} (\dot{\alpha}{max} =0) = 2.78 ms^{-1}, $\alpha = 24°$ and parameter of the 4WSS chassis is $L = 1.7$ m, $D = 1.5$ m. To avoid the situation where the mechanics-limited steering angle cannot be reached due to sensor errors and mechanical manufacturing errors, α is set to 24°. The value is called program-limited steering angle. The maximum speed of the chassis in the steady state is

$$\left|v_{x,max}\right| = 2.0 \, ms^{-1} \qquad (29)$$

According to Equations 28 and 29, when the steering angle is 24°, the speed of the chassis cannot exceed 2.0 ms^{-1}. And speed cannot exceed 2.8 ms^{-1} when going straight.

2.3 Speed Distribution controller design

The 4WSS chassis bases its action on target speed and steering angle from the remote control. Set the target steering angle positive or negative to make the chassis turn left or right, while zero to make it go straight. The essence of the 4WSS chassis control system is a servo system that follows the target speed and steering angle from the remote control.

The key to 4WSS chassis motion control is to properly distribute the speeds of the four in-wheel motors according to the control objectives. The correlation between the speed of the four in-wheel motors, the speed of the chassis, and the steering angle can be obtained from the section *Kinematic Model Build*. According to Equations 22–25, the expression about in-wheel motor speeds with the target speed can be directly obtained.

$$\bar{v}_{fl} = v_T\left(1 - \frac{D}{2I}\right) - \dot{\alpha}_p\frac{D}{2} \qquad (30)$$

$$\bar{v}_{fr} = v_T \left(1 + \frac{D}{2I} \right) + \dot{\alpha}_p \frac{D}{2} \tag{31}$$

$$\bar{v}_{rl} = v_T \left(1 - \frac{D}{2I} \right) + \dot{\alpha}_p \frac{D}{2} \tag{32}$$

$$\bar{v}_{rr} = v_T \left(1 + \frac{D}{2I} \right) - \dot{\alpha}_p \frac{D}{2} \tag{33}$$

where V_T is the target speed, and $\dot{\alpha}_p$ is the steering angular velocity. $\bar{v}_{fl}$, $\bar{v}_{fr}$, $\bar{v}_{rl}$, and $\bar{v}_{rr}$ are the target speeds of the corresponding in-wheel motors.

The steering angle error is $\alpha_T - \alpha_s$. When it is positive, $\dot{\alpha}_p$ should be made positive to lower such error, and vice versa. So, a P controller, where α_s is the feedback signal, can be designed.

$$\dot{\alpha}_p = sat\ (k(\alpha_T - \alpha_s), \dot{\alpha}_{max}) \tag{34}$$

where k is the P controller parameter, α_T is the target steering angle, α_s is the actual steering angle, and $\dot{\alpha}_{max}$ is the maximum output limit of the controller.

The function $sat\ (x,M)$ is a saturation function. And its definition is shown in Equation 35. It is mainly to limit the maximum steering angular velocity to prevent instability caused by excessive steering angle deviation.

$$sat\ (x,M) = \begin{cases} M, (x \geq M) \\ x, (-M < x < M) \\ -M, (x \leq -M) \end{cases} \tag{35}$$

To ensure that the in-wheel motor can have sufficient speed margin to deal with disturbances, the maximum speed of the 4WSS chassis needs to be limited in real time. The target speed should be limited according to Equation 36.

$$v_T = sat\ (v_{user}, v_{x,max}) \tag{36}$$

where v_{user} is the target value directly given by the user via remote control.

Since the motor driver does not assemble the speed servo function, a PID controller is selected for the speed servo inner loop (Mohanraj et al., 2022). The difference is that, for the Kelly QSKLS8430H, the speed servo controller needs to truncate the reverse output and set the driver to brake mode.

3 Testing

The 4WSS chassis with a spraying system is sketched in Figure 10. The chassis weighs 1,380 kg, with a wheelbase of 1.5 m, ground clearance of 1.1 m, and overall dimensions of 3,680 × 1,720 × 2,130 mm³. The water tank, spray boom, and water pump required for the spraying system are mounted on the chassis. The 500-L water tank is located in the middle of the chassis. The generator and water pump are installed on the rear of the chassis. These components are protected by dust covers, which prevent dust from getting into the machine and avoid accidental touch by the operator. The battery pack is mounted on the front, and the seat is located above the battery pack. The spray arm is mounted on the chassis head. It unfolds to 12 m and folds on both sides when not in operation.

Experimental tests were conducted to evaluate the kinematic performance of the 4WSS chassis and the effectiveness of the kinematic-based control algorithms. A section of a flat road and a piece of muddy field were chosen as representative scenes.

3.1 Control of speed and steering angle

This experiment aims to verify the control ability of the 4WSS chassis with SDC for speed and steering angle tracking. The experiment site is a flat concrete road with a length of 30 m and a width of 30 m. The test flow is shown in Figure 11: the line represents the chassis trajectory. The 4WSS held still, and the steering angle held 0 at the start point before operating. Then, target speed was set to an exact value. After the chassis was accelerated to the corresponding speed, the target steering angle was set to 24° because 24°, the program-limited steering angle, was the most frequently employed angle for making turns at field boundaries. Then, the chassis speed and steering control results can be achieved.

Referring to Equation 29, the maximum test speed is 2 ms⁻¹. So, the 4WSS chassis test speed was set from 0.4 ms⁻¹ to 2 ms⁻¹ with an interval of 0.2 ms⁻¹. The test results are shown in Figure 12, and their response characteristics are presented in Table 1. Figure 12A shows the tracking curve of the chassis speed at different target speeds. The dashed line is the target speed, and the solid line is the chassis speed (Equation 16 is used to calculate the 4WSS chassis speed using the four in-wheel motor speeds.). The target speeds vary from 0.4 ms⁻¹ to 2 ms⁻¹, with an interval of 0.2 ms⁻¹. The rise times and overshoots of speed tracking control are shown in Table 1. It is obvious that as the speed increases, the rise time also increases linearly due to the acceleration that is set to 0.24 ms⁻² for safety. When the chassis starts, the feedback speed is numerically 0 for nearly 1 s, while the actual value is increasing. Because the hall position sensors for the wheel motors are of low resolution, the driver cannot obtain effective speed feedback at very low speeds. When the velocity is 0.4 ms⁻¹, the speed controller overshoots by 16.3%, whereas with 2.0 ms⁻¹, it overshoots by only 1.7%. Because of the abnormal speed feedback, the wheel speed controller does not work correctly for the first 1 s. Therefore, the integral controller is integrated to a larger value, and then a more significant overshoot occurs. With a larger target speed, the acceleration time is longer and weakens such initial abnormal integration over time, resulting in a minor speed overshoot. And with different target speeds, the chassis speed can finally converge to the target speeds.

Figure 12B shows the tracking curve of the front steering angle during the turning test (The values of the front and rear steering angles are equal, so take one of them as an example to be analyzed.). Nine solid lines represent the track curves of the front steering angle at different speeds, with the dashed line representing the target angle. And the rise times and overshoots of steering angle tracking are also shown in Table 1. The figure shows that the dynamic and steady performance of the steering angle tracking varies at different
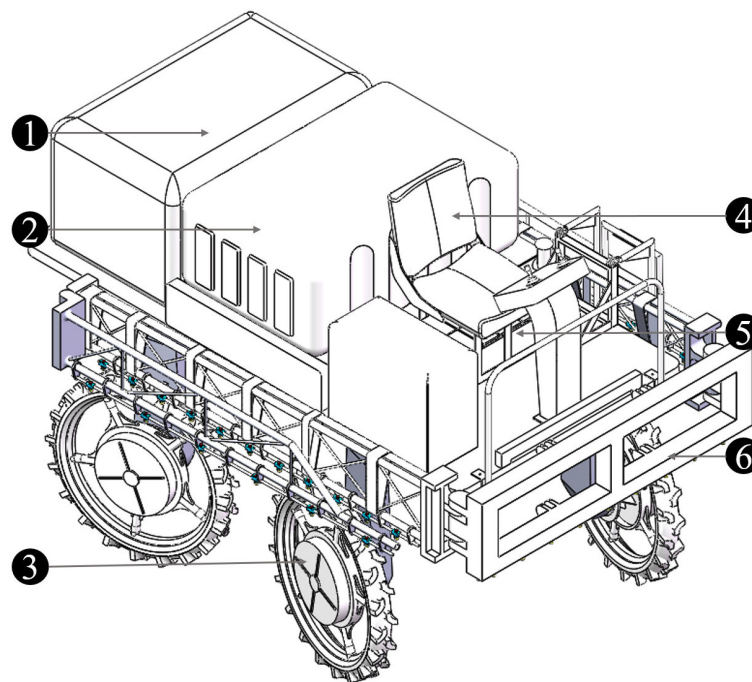
FIGURE 10
The four-wheel self-steering (4WSS) chassis with spraying system. 1: dust guard (petrol engine, generator, and water pump inside); 2: water tank; 3: wheel; 4: seat; 5: battery pack; 6: spray boom.

target speeds. Obviously, the curves can be classified into three control performances based on goal speed values. When the goal speed is less than 1.4 ms^{-1}, the rise times are less than 1.5 s and the overshoots are less than 4%. When the goal speed ranges over 1.4 ms^{-1}~1.6 ms^{-1}, a sudden increase of the rise times occurs that is over 2 s and the overshoots are still less than 4%. When the goal speed is above 1.6 ms^{-1}, the rise times slightly increase and the overshoots are over 6%. The results indicate that as speed increases, angle control performance gradually declines. The ability to maintain differential speed is required at all times to track the goal steering angle. The in-wheel motor speed margin shrinks when the in-wheel motor speed gets closer to its maximum value. As a result, the performances of controlling the chassis differential speed and angle both decline gradually. Rewrite the maximum steering angular velocity $\dot{\alpha}_{max}$ in Equation 28 as Equation 37, and then $\dot{\alpha}_{max}$ can be used to describe the steering capability. $v_{x,max}$ represents the chassis speed. Consequently, it can be said that the steering ability gradually deteriorates as the angle and speed increase. This explains why its steering control ability gradually declined as speed increased.
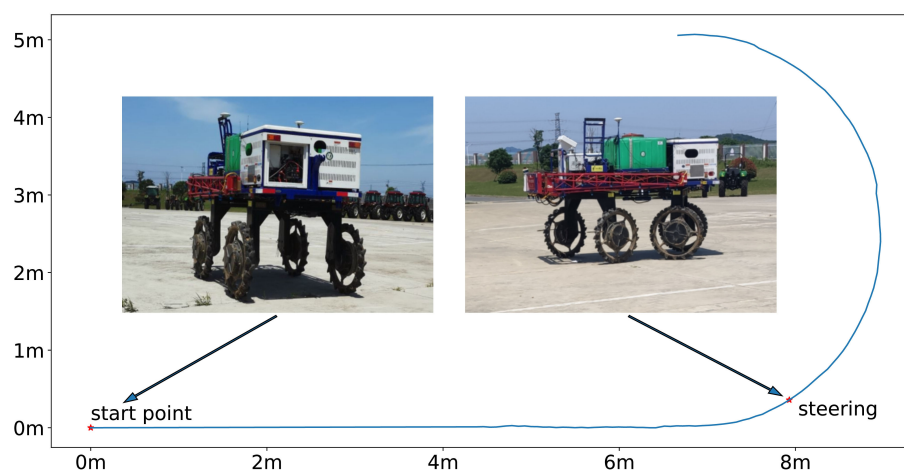
FIGURE 11
Speed and steering angle tracking test. The chassis holds still at the start point and steers after reaching the target speed.
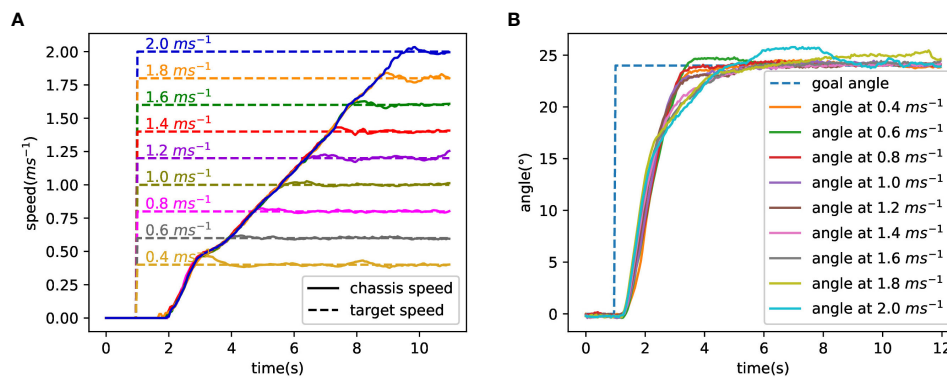
FIGURE 12
Test result of speed and steering angle. **(A)** Tracking curve at different target speeds. **(B)** The tracking curve of the front steering angle.

$$\dot{\alpha}_{max} = 2\frac{VL - |v_{x,max}|(L + D|sin\ \alpha|)}{DL} \quad (37)$$

Figure 13 illustrates the individual wheel speeds while steering at a targeted speed of 1 ms^{-1}. The target speed of four in-wheel motors is depicted by the dotted line, while the measured in-wheel motor speed is represented by the solid line. The various colors correspond to various motors. The figure shows that all four wheels have a speed of 1 ms^{-1} before steering. Then, the speeds of the *fr* and *rl* motors increase before decreasing to turn the chassis, while the speeds of the *fl* and *rr* decrease before increasing. After the transient process, the speeds of the right wheels converge to 1.4 ms^{-1}, and the speeds of the left wheels converge to 0.6 ms^{-1}. According to Equations 30–33, the target speeds of in-wheel motors are divided into two parts, as illustrated in Equations 38–40, named the kinematic part S_{inner}, S_{outer} and the P controller part $P_{controller}$. The chassis speed is mainly the kinematic part $S_{inner} = S_{outer} = v_T = 1$ ms^{-1} before steering. As the steering begins, the output of $P_{controller}$ controller part is a large value because of the maximum deviation of the steering angle and then decreases gradually with the convergence of the angle tracking. Finally, the outer and inner wheel speeds are $S_{outer} = 1.4$ and $S_{inner} = 0.6$ in order to maintain the differential steering.

$$S_{inner} = v_T\left(1 - \frac{D}{2I}\right) \quad (38)$$

$$S_{outer} = v_T\left(1 + \frac{D}{2I}\right) \quad (39)$$

$$P_{controller} = \dot{\alpha}_p\frac{D}{2} \quad (40)$$

3.2 Small turning radius

Measurements of the 4WSS turning radius were performed at a speed of 0.8 ms^{-1} on a dry field. The 4WSS chassis formed two closed circular trajectories when it turned at a fixed steering angle, as shown in Figure 14. During the test, the chassis was located in the center of the test site. Then, the operator set the steering angle to 24° and drove the chassis to turn 360°. The chassis drew two circular trajectories on the ground. The formed two circles were measured, where the inner radius was 1,367 mm and the outer radius was 2,877 mm. So, the measured turning

TABLE 1 Response characteristics of speed and steering angle.

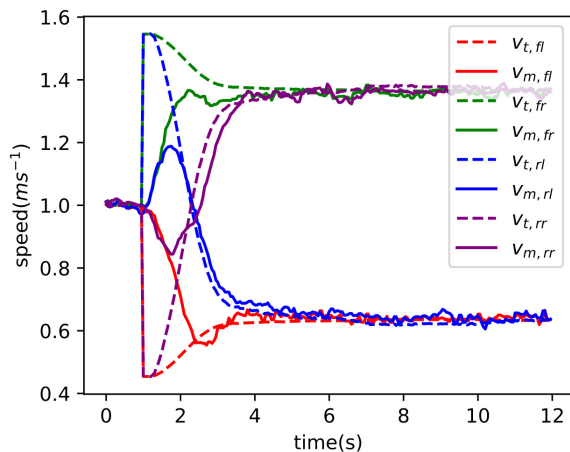| Test speed (ms^{-1})	Speed		Angle	
	Rise time (s)	Overshoot (%)	Rise time (s)	Overshoot (%)
0.4	1.8	16.3	1.4	2.3
0.6	2.6	3.2	1.5	3.3
0.8	3.4	2.9	1.5	2.2
1.0	4.1	2.8	1.5	1.9
1.2	4.9	2.2	1.5	0.9
1.4	5.7	2.3	2.1	0.9
1.6	6.3	1.7	2.2	1.9
1.8	6.9	2.3	2.2	6.1
2.0	7.7	1.7	2.4	7.5

FIGURE 13
Four-wheel speed when steering at 1 ms⁻¹.

radius was 2,877 mm. From kinematics analyses, Equation 41 was obtained. R_1 represented the theoretical radius for 4WSS chassis, and its result was determined to be 2,840 mm by substituting the parameter with the actual value. The error between the theoretical turning radius and the test result was within the allowable range.

$$R_1 = \frac{D}{2} + \frac{L}{2sin(\theta_{max})} \quad (41)$$

Compared to other types of chassis, such as those by Wang et al. (2017) and Zeng et al. (2019). Their theoretical equation for the turning radius of the chassis was denoted by R_2 and R_3 in Equations 42 and 43. If their chassis parameters were indeed consistent with the 4WSS chassis ($L = 1.7$ m, $D = 1.5$ m), then their respective theoretical turning radius would be 4,759 mm and 4,874 mm. So, the turning radius of the 4WSS chassis was smaller.

$$R_2 = \frac{D}{2} + \frac{L}{sin(\alpha_{max})}(1 - 0.5 + 0.5cos(\alpha_{max})) \quad (42)$$

$$R_3 = L\sqrt{1 + (cot(\alpha_{max}) + \frac{D}{2L})^2} \quad (43)$$

3.3 Walking in a muddy field

To test the obstacle-surmounting capability of the chassis in the paddy field, three different test scenarios were set up, respectively: driving in a muddy field, driving across a deep gully, and driving over a ridge between field blocks. In order to be close to the actual working environment, the water load tank of the chassis was filled with 500 L of water during the test.

The high-clearance chassis faced significant challenges in the muddy field environment. The soil in the field was soft and sticky, causing the chassis to frequently get stuck in the mud while driving, as illustrated in Figure 15A. During the muddy field test, the wheels sank to a depth of approximately 40 cm while moving, and the target speed ranged from 0.4 ms⁻¹ to 1.8 ms⁻¹. Despite these conditions, the 4WSS chassis exhibited smooth driving and steering capabilities.

As a kind of uncommon ground condition, the deep gully was inevitably encountered in the field. When traversing the deep gully, the chassis had to endure significant vibrations and heavy loads, especially when it was fully loaded. This posed a considerable challenge to both the structural integrity and power of the chassis. However, the 4WSS chassis offered a straightforward design without a transmission structure, making it less susceptible to damage. Additionally, the motor exhibited a robust overload capacity, enabling it to deliver substantial torque in a short time. The test was shown in Figure 15B. The speed of the test was set to 0.4 ms⁻¹, and the deep gully in the field was over 20 cm wide and deeper than 40 cm. Crossing a deep gully horizontally was easy, as the front two wheels were subjected to the same forces and could be crossed simultaneously unless both wheels completely fell into the

FIGURE 14
Turning trajectories of 24° steering angle.

FIGURE 15
Field testing of the four-wheel self-steering (4WSS) chassis in a muddy field with three typical scenarios. **(A)** Driving in a muddy field. **(B)** Driving across a deep gully. **(C)** Driving over a ridge between field blocks.

gully. Therefore, this test was chosen to go diagonally over a deep gully, working with the four wheels of the chassis plunging into the deep gully in turn and then climbing out.

To facilitate irrigation, the paddy field was usually divided into several blocks by ridges. So, the chassis needed to move across the field ridges when transferring between various fields. The test was shown in Figure 15C. The ridge was over 50 cm wide and 20 cm high, and the speed was set to 0.8 ms^{-1}. The chassis moved stably across the ridge.

4 Conclusion

This paper proposes a four-wheel independent electric drive 4WSS chassis, in which the four wheels are fixed to the front and rear steering bridges, respectively. The chassis is controlled by the four-wheel differential speed to steer or move forward. The linkage is designed to constrain the front and rear steering angle, improving the stability of steering. Benefiting from the steering bridge differential design, it has a better obstacle-surmounting ability in extreme conditions such as a muddy terrain. A kinematic model was developed according to the structural characteristics of the chassis, and the mathematical relationships between the four-wheel speeds, chassis speed, steering angle, and steering angular velocity were obtained. Based on the kinematic model of the chassis, an SDC was built. In the SDC, the control references were the target speeds and target steering angles obtained from the remote control. The feedback signals were the current steering angle measured by position sensors mounted on the front and rear steering bridges. The desired speeds for the four wheels were determined as outputs by the SDC.

The speed tracking test revealed a maximum overshoot of 16.3% at a target speed of 0.4 ms^{-1}. The steering angle tracking test showed that the performance of the steering angle control decreased as the speed rose. Therefore, the speed can approach 2.8 ms^{-1} when going straight but should be reduced to less than 2.0 ms^{-1} when turning at the maximum angle. Compared to other sprayer chassis, the 4WSS chassis has a smaller turning radius of 2,877 mm. And the chassis can move around with ease in conditions typical of the field, including muddy terrains, deep gullies, and ridges.

The 4WSS chassis is highly advantageous in the agricultural scene because it is capable of good passability at low speeds. Additionally, the chassis is designed closely in tandem with the future development direction of unmanned agricultural machinery. The advanced driving mode and steer-by-wire steering system eliminate the limitations associated with traditional agricultural machinery, showcasing significant potential in achieving an unmanned, intelligent, and information-driven chassis.

Data availability statement

The original contributions presented in the study are included in the article/Supplementary Material, further inquiries can be directed to the corresponding author. The code for the 4WSS Sprayer is confidential, however the code for a small similar chassis model with SDC is available at https://gitee.com/he-siwei/fwied/tree/kinematics_v0.

Author contributions

SH: Data curation, Investigation, Methodology, Software, Writing – original draft, Writing – review & editing. YS: Funding acquisition, Methodology, Supervision, Investigation, Conceptualization, Writing – review & editing. YZ: Data curation, Writing – original draft. HL: Supervision, Writing – review & editing.

Funding

Conflict of interest

The authors declare that the research was conducted in the absence of any commercial or financial relationships that could be construed as a potential conflict of interest.

Publisher's note

All claims expressed in this article are solely those of the authors and do not necessarily represent those of their affiliated organizations, or those of the publisher, the editors and the reviewers. Any product that may be evaluated in this article, or claim that may be made by its manufacturer, is not guaranteed or endorsed by the publisher.

Supplementary material

The Supplementary Material for this article can be found online at: https://www.frontiersin.org/articles/10.3389/fpls.2023.1258744/full#supplementary-material

References

Chen, Y., Mao, E., Li, W., Zhang, S., Song, Z., Yang, S., et al. (2020). Design and experiment of a high-clearance self-propelled sprayer chassis. *Int. J. Agric. Biol. Eng.* 13, 71–80. doi: 10.25165/j.ijabe.20201302.5262

Ding, K., Feng, J., Yu, J., and Wang, W. (2018). Simulation of roll stability control of high-clearance spray machine. *Comput. Simulation* 35, 130–134.

Hui, G., Hengfeng, C., Quangui, L., Zhiqiang, X., Guomin, G., and Xiaobo, X. (2018). Design and research on hydraulic system of high gap wheel self-propelled sprayer. *J. Agric. Mechanization Res.* 40, 51–56. doi: 10.13427/j.cnki.njyi.2018.10.010

Kuslits, M., and Bestle, D. (2019). Modelling and control of a new differential steering concept. *Vehicle System Dynamics* 57, 520–542. doi: 10.1080/00423114.2018.1473616

Li, Z., Shi, Y., Jiang, P., Hu, W., and Lin, W. (2018). Design and experimental research of high clearance universal operation chassis. *Food Machinery* 34, 100–105. doi: 10.13652/j.issn.1003-5788.2018.02.022

Li, W., Xue, T., Mao, E., Du, Y., Li, Z., and He, X. (2019). Design and experiment of multifunctional steering system for high clearance self-propelled sprayer. *Trans. Chin. Soc. Agric. Machinery* 50, 141–151. doi:10.6041/j.issn.1000-1298.2019.01.015

Liang, Y., Li, Y., Yu, Y., and Zheng, L. (2020). Integrated lateral control for 4WID/4WIS vehicle in high-speed condition considering the magnitude of steering. *Vehicle System Dynamics* 58, 1711–1735. doi: 10.1080/00423114.2019.1645343

Liu, Z., Li, R., Li, Z., Li, H., and Liu, Y. (2019). Design of hydraulic transmission system for selfpropelled sprayer's chassis. *Mach. Tool Hydraulics* 47, 72–75. doi: 10.3969/j.issn.1001-3881.2019.04.017

Liu, Y., Zong, C., Zhang, D., Zheng, H., Han, X., and Sun, M. (2021). Fault-tolerant control approach based on constraint control allocation for 4WIS/4WID vehicles. *Proc. Institution Mechanical Engineers Part D: J. Automobile Eng.* 235, 2281–2295. doi: 10.1177/0954407020982838

Mohanraj, D., Aruldavid, R., Verma, R., Sathiyasekar, K., Barnawi, A. B., Chokkalingam, B., et al. (2022). A review of BLDC motor: state of art, advanced control techniques, and applications. *IEEE Access* 10, 54833–54869. doi: 10.1109/ACCESS.2022.3175011

Oke, P., Nguang, S. K., and Wen, J. (2016). "H∞ dynamic output feedback control for independently driven four-wheel electric vehicles with differential speed steering," in *2016 IEEE International Conference on Information and Automation (ICIA)*. (Ningbo, China: IEEE), 567–572. doi: 10.1109/ICInfA.2016.7831886

Oksanen, T., and Linkolehto, R. (2013). Control of four wheel steering using independent actuators. *IFAC Proc. Volumes* 46, 159–163. doi: 10.3182/20130828-2-SF-3019.00061

Park, J. I., Jeon, K., and Yi, K. (2019). An investigation on the energy-saving effect of a hybrid electric-power steering system for commercial vehicles. *Proc. Institution Mechanical Engineers Part D: J. Automobile Eng.* 233, 1623–1648. doi: 10.1177/0954407018777579

Park, M., Wang, Z., Li, L., and Wang, X. (2023). Multi-objective building energy system optimization considering EV infrastructure. *Appl. Energy* 332, 120504. doi: 10.1016/j.apenergy.2022.120504

Ragheb, H., Aydin, M., El-Gindy, M., and Kishawy, H. (2013). Comparison of gradability performance of fuel cell hybrid electric and internal-combustion engine vehicles. *J. Power Sources* 221, 447–454. doi: 10.1016/j.jpowsour.2012.08.037

Sato, S., Jiang, Y. J., Russell, R. L., Miller, J. W., Karavalakis, G., Durbin, T. D., et al. (2022). Experimental driving performance evaluation of battery-powered medium and heavy duty all-electric vehicles. *Int. J. Electrical Power Energy Syst.* 141, 108100. doi: 10.1016/j.ijepes.2022.108100

Wang, H., Han, J., and Zhang, H. (2022). Lateral stability analysis of 4WID electric vehicle based on sliding mode control and optimal distribution torque strategy. *Actuators* 11, 244. doi: 10.3390/act11090244

Wang, J., Tang, H., Shen, H., Bai, H., and Na, M. (2017). Design and experiment of high clearance rollwaist multifunctional power chassis for paddy field. *Trans. Chin. Soc. Agric. Eng.* 33, 32–40. doi: 10.11975/j.issn.1002-6819.2017.16.005

Wang, J., Wang, Q., and Jin, L. (2008). "Modeling and simulation studies on differential drive assisted steering for EV with four-wheel-independent-drive," in *2008 IEEE Vehicle Power and Propulsion Conference*, (Harbin, China: IEEE). 1–7. doi: 10.1109/VPPC.2008.4677428

Wu, X., Xu, M., and Wang, L. (2013). "Differential speed steering control for four-wheel independent driving electric vehicle," in *2013 IEEE International Symposium on Industrial Electronics*. (Taipei, China: IEEE), 1–6. doi: 10.1109/ISIE.2013.6563667

Wu, X., Yang, L., and Xu, M. (2014). "Speed following control for differential steering of 4WID electric vehicle," in *IECON 2014 - 40th Annual Conference of the IEEE Industrial Electronics Society*. (Dallas, TX, USA: IEEE), 3054–3059. doi: 10.1109/IECON.2014.7048945

Zeng, S., Lui, J., Luo, X., Liu, S., Huang, D., and Mo, Z. (2019). Design and experiment of wheel-track compound power chassis for high clearance sprayer in paddy field. *J. South China Agric. Univ* 40, 14–22. doi: 10.7671/j.issn.1001-411X.201905070

Frontiers in Plant Science

Check for updates

Study on atomization mechanisms and spray fragmentation characteristics of water and emulsion butachlor

Wanting Yang[1†], Wei Zhong[1†], Weidong Jia[1*], Mingxiong Ou[1], Xiang Dong[1], Tie Zhang[2], Suming Ding[3], Li Jiang[1] and Xiaowen Wang[1]

[1]School of Agricultural Engineering, Jiangsu University, Zhenjiang, Jiangsu, China, [2]Science Innovation Center, Chinese Academy of Agriculture Mechanization Sciences Group Co., Ltd., Beijing, China, [3]Nanjing Institute of Agricultural Mechanization, Ministry of Agriculture and Rural Affairs, Nanjing, China

Agricultural chemicals are commonly used to control pests and weeds, but cause pesticide waste problems. Oil-based emulsions are often used as pesticide formulations to improve pesticide utilization. In this study, the spray visualization experiment of the water and oil-based emulsion butachlor is carried out using an ST flat fan nozzle at 0.1−0.5 MPa pressure. The dimensionless method is used to analyze the difference in liquid sheet fragmentation morphology and disintegration process and the influence of different fragmentation methods on droplet size. It is found that the hydrophobic components in pesticide have a significant effect on the morphology and process of atomization fragmentation. When spray liquid is water, the liquid sheet breaks up into liquid ligaments due to the Rayleigh instability, then the ligaments break up into droplets. The side view of a liquid sheet is a large-amplitude wave disturbance. When the spray liquid is the emulsion butachlor, holes are generated on the liquid sheet, then the holes break up into droplets. The fragmentation method of emulsion spray is the perforation mechanism. Compared with water spray, the presence of the pesticide butachlor increases the droplet size and spray angle and improves the uniformity of droplet size distribution but reduces the breakup length. The spray angle shows a power law dependence of the Weber number with a power of 0.17 for all conditions tested here. At 0.3 MPa, DV50 increases 25%, and span decreases from 1.187 to 1.172. This study could provide reference for the addition of agricultural additives, the improvement of spray operation efficiency, and the establishment of spray fragmentation mechanism.

KEYWORDS

agriculture, pesticide, atomization fragmentation, droplet size spectrum, spray

1 Introduction

At present, pesticide spraying is the most important method of modern agriculture to control crop diseases and insect pests. With the continuous progress of society and the gradual strengthening of environmental protection awareness, higher requirements have been put forward for pesticide spraying efficiency and pesticide utilization rate of plant protection machinery. How to increase the effective utilization rate of pesticides, reduce spray drift, and improve the foliar deposition has become the focus of research (Jun, 2012; Zhang et al., 2014; Wang et al., 2015).

The atomization process has a significant effect on the droplet size spectrum, and the droplet size has a very important effect on pesticide deposition and anti-drift spray (Yang et al., 2022). When the spray liquid contains oil-based emulsion, it would produce larger droplets than water spray when spraying through a flat fan nozzle, which is of great significance for controlling droplet drift (Hilz et al., 2012; Cryer and Altieri, 2017). From the early 1960s to the present, researchers have studied the influence of spray liquid characteristics on atomization (Wang et al., 2018). The decrease of surface tension in pure liquid leads to an increase in the growth rate in instability, which eventually leads to earlier liquid sheet breakup (Lefebvre and McDonell, 2017). However, studies have shown that surfactant solutions reduce surface tension and may lead to delayed breakups (Miller and Ellis, 2000). Surface tension is the most important physical property of spray liquids (Wang et al., 2018). How surface tension affects atomization fragmentation remains to be further explored. The visualization method could be used to study fragmentation physics well (Cloeter et al., 2010). The breakup length decreases with the increase of spray pressure. The appearance of hole structures on liquid sheet reduces the generation of droplets. When using emulsion-containing liquid spray, the emulsion droplets merge with the air/water interface of the liquid sheet, which enhances the disturbance in the turbulence and causes the perforation atomization (Hilz et al., 2012). In the atomization process of water and oil-in-water emulsions, the oil phase in the form of emulsions can shorten the length of the liquid sheet and expand the droplet size (Qin et al., 2010). The droplet size decreases with the increase of spray pressure (Negeed et al., 2011). Different nozzle structures affect the droplet size and velocity, and the addition of additives also affects the droplet size (Ellis and Tuck, 1999). The droplet size generated in the process of agricultural liquid atomization affects its coverage and off-target drift (Altieri and Cryer, 2018; Guler et al., 2020). Many studies have focused on the parameter of droplet volume median diameter, while the significant influence of droplet size divergence should be paid attention to in agricultural spraying.

These studies provide the basis and help for the establishment of atomization perforation regime. Although there are many studies on different liquid spray atomization mechanism, the current research on the atomization mechanism of perforation needs to be further improved. The influence of emulsion atomization mechanism on atomization quality is still a challenge (Zhao, 2012).

In this paper, the images of atomization and perforation process of water and emulsion are captured by the visualization method. The dimensionless analysis method is used to normalize the different physical properties of the spray liquid, which avoids the problem of inconsistent units of different physical properties. The spray atomization process is visualized by a high-speed camera, and the spray structure is quantitatively analyzed by image post-processing. The evolution of spray structure reflects the development of the instability of the spray liquid sheet. In addition, the effects of different atomization disturbance structures on droplet size distribution are described by measuring D_{V10}, D_{V50}, D_{V90}, and span. The effects of different spray structures on droplet size divergence are studied. It provides a reference for the use of plant protection spray adjuvants and the improvement of pesticide utilization.

2 Materials and methods

2.1 Material and equipment

The experiment was conducted in the Key Laboratory of Modern Agricultural Equipment and Technology, Ministry of Education, Jiangsu University. The experimental temperature is ambient temperature 23°C. The spray solutions used in the experiment are water and butachlor (CAS No: 23184-66-9, Lulilai, China). The water used in the experiment is tap water, with a surface tension of 0.0724 N/m and a density of 1.019×10^3 kg/m³. Butachlor is an oil-based emulsion pesticide, which is widely used in agricultural weed control. The concentration of butachlor in this study is 0.1%, the surface tension of this concentration is only 0.0417 N/m, and the density is 1.016×10^3 kg/m³.

The nozzle used in the experiment is the standard flat fan spray nozzle (Lechler GmbH, Germany) produced by Lechler GmbH. The nozzle type is ST 110-01. The instruments used in the experiment are the i-speed high-speed camera (OLYMPUS, UK) produced by OLYMPUS company and the winner318 industrial spray laser particle size analyzer (Winner Particle, China) produced by Winner Particle technology Co., Ltd.

2.2 Experiment setup

The images of water and butachlor atomization and fragmentation process are captured by a high-speed camera using a Lechler flat fan nozzle under different pressures of 0.1–0.5 MPa provided by a pressure spray system as shown in Figure 1. The droplet size of water and butachlor is measured by a laser particle size analyzer. A high-speed camera is placed in the direction of the fan-shaped liquid sheet plane to capture the morphological characteristics of the front of the spray liquid sheet. A second high-speed camera is placed on the side of the liquid sheet, and the structural feature information of the side view of the liquid sheet is recorded.

2.3 Spray visualization

The high-speed camera introduces fixed-mode noise (FPN) into the image through an image sensor. The light sensor captures the
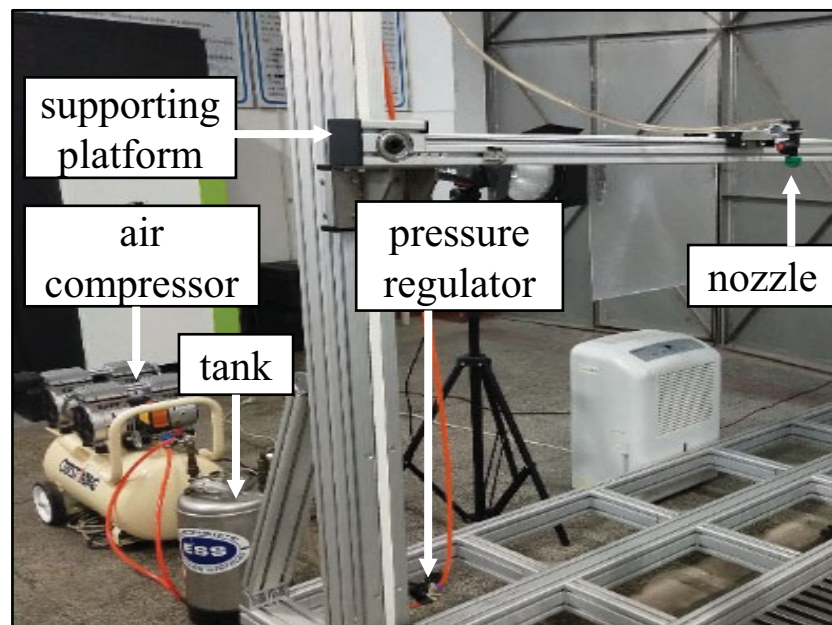
FIGURE 1
Pressure spray system includes supporting platform, air compressor, liquid tank, pressure regulator, and the spray nozzle.

light, converts it into an electronic copy of the optical image, and then stores the video image. The high-speed camera is set to 2,000 frames/s. Under the pressure of 0.1–0.5 MPa, the morphological differences of the water atomization process and butachlor atomization process in the front view and side view directions of liquid sheet were captured.

The breakup length is defined as the distance of the pieces of the sheet rupture from the main sheet to form ligaments. The spray angle is determined as the angle formed by the boundary of the liquid sheet near the nozzle parallel to the flat fan sheet. The diffusion angle is determined as the angle formed by the boundary of liquid sheet in the direction of the side view. The image processing software Image-Pro Plus is used to measure the breakup length by calculating the pixel length in the picture. The angles are measured by the flexible two-point method also using the image processing software Image-Pro Plus (Wang, 2014).

2.4 Droplet size measurement

At the distance of 50 cm from the nozzle outlet (Xiao et al., 2018), the droplet size spectrum of water and butachlor was measured by a laser particle size analyzer when using a standard flat fan nozzle. The droplet size was measured by the laser particle size analyzer according to the "Fraunhofer" diffraction principle and the typical parallel optical path design. The laser particle size analyzer uses a photoelectric detector to collect signals such as scattered light intensity and energy, and then calculates and interprets according to the scattering principle to obtain particle size information. Under the same working conditions, the instrument carries out three measurements and produces three

droplet size data. The most commonly used method to characterize the droplet size is through the volume median diameter D_{V50} (VMD). D_{Vm} is the diameter of the droplets with a cumulative distribution of m%. The relative span value (R) is the droplet distribution span/droplet spectrum width, which is an index to measure the droplet size distribution width (Dombrowski and Johns, 1963; Matthews et al., 2014). The test error is less than 3%. Under different pressure conditions of 0.1–0.5 MPa, the spraying distribution characteristics of droplet size was measured.

2.5 Dimensionless analysis

The dimensionless analysis method is used to analyze the obtained data. Dimensional analysis is an important method to explore the law of flow-through experiments, especially for those flow problems that are difficult to analyze theoretically. The dimensionless number generated by the fluid control equation can be used to describe the relevant physical changes in liquid sheet atomization (Altieri and Cryer, 2018). Within the accuracy range of this experiment, the viscosity has little effect on the droplet size (Kooij et al., 2018), and because of the significant correlation between surface tension and perforation mechanism in multiphase atomization mechanism, this study mainly focuses on the influence of surface tension and inertia force, that is, the Weber number on spray breakup mechanism (Yang et al., 2022). The surface tension of emulsion butachlor and water is measured by the CAM 101 (KSV, Finland) automatic tensiometer using the hanging drop method. The pendant drop method uses Laplace-Young fitting to fit the outline of the droplet to obtain surface tension. The Weber number is defined as (Tarnogrodzki, 1993):

$$We = \frac{\rho v^2 l}{\sigma} \qquad (1)$$

where ρ is liquid density (kg/m^3), v is characteristic velocity (m/s), σ is surface tension coefficient (N/m), and l is the characteristic length of the Weber number for the flat fan nozzle with an elliptical outlet, which is defined as:

$$l = 4* \frac{A}{X} \qquad (2)$$

where A is the area of the flat fan nozzle outlet (m^2) and X is the wetted perimeter (m).

Combining Equations (1) and (2) yields:

$$We = \frac{4A\rho v^2}{X\sigma} \qquad (3)$$

The Weber numbers of different surface tensions at different flow rates were measured to study the effect of the competition between surface tension and inertial force on the stability of liquid sheet and droplet breakup (Altieri et al., 2014). Using the dimensionless Weber number for dimensional analysis is helpful to find the functional relationship between physical quantities, especially for the complex fluid mechanics problem of agricultural spray.

3 Results

3.1 Morphological characteristics and evolution process of holes on liquid sheet

Figures 2A, B show the atomization process of water in the direction of front view of liquid sheet. When the spray liquid is water, the liquid at the nozzle outlet deforms due to the shear force and fluctuates during the contraction process. The liquid sheet with wave is formed due to the disturbance when leaving the nozzle outlet. There is an obvious corrugated structure on the liquid sheet formed by water spray (Nadeem et al., 2018). As the disturbance on the liquid sheet increases, the wave structure on the liquid sheet gradually tears into a liquid ligament. The liquid ligament continues

to break up into droplets due to Rayleigh–Taylor instability. These liquid ligaments are disintegrated into droplets by instability under the influence of surface tension (Gong et al., 2020; Wei et al., 2021).

Figure 3 shows the formation and development of holes when the spray liquid is a hydrophobic butachlor solution. The liquid mass leaves the nozzle outlet to form the liquid sheet, and the pre-hole structure could be observed on the liquid sheet as shown in Figure 3A. The position where the pre-hole structure exists on the liquid sheet would form a broken hole, and the single broken hole and the surrounding broken holes gradually expand to form a net structure as shown in Figure 3E. The net structure continues to break up into droplets. The downward speed of the hole is basically maintained at a constant speed proximity to spray liquid jet velocity. When the pre-hole structures on the liquid sheet just forms a hole, the initial expansion speed of the hole increases slowly, then the expansion speed of the hole expansion increases, and finally the droplet is broken along the grid.

The change of spray angle between water and butachlor is shown in Figures 4A, B. The spray angle indicates the change of spray swath and the rim disturbance of the liquid sheet. The spray angle of butachlor is 8° larger than that of water in the same operating pressure. The spray angle of water and butachlor has a similar change trend; that is, it increases slowly with the increase of the Weber number, and the increase gradually decreases. Sprays with pesticide butachlor lead to earlier breakup of the liquid sheet, droplet formation starting closer to the nozzle, and larger spray angles.

Combined with the dimensionless number analysis, the spray angle gradually increases with the increase of the Weber number. The spray angle remained at approximately 110° (Kooij et al., 2018). Quantitatively, the spray angle shows a power law dependence of the Weber number with a power of 0.17, which is suitable for all conditions tested here,

$$\theta_s \propto We^{0.17} \qquad (4)$$

where θ_s is the spray angle (°) and We is the Weber number (dimensionless).

The liquid sheet breakup length of water and emulsion butachlor varies with the Weber number, as shown in Figures 5A, B. It could be
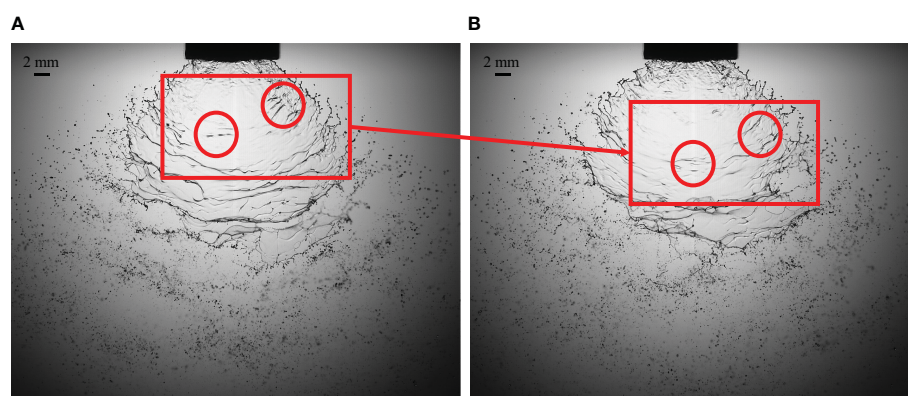

FIGURE 2
The features of wave structures in the water atomization process. The growth process of the typical liquid sheet unstable wave structures is marked by red circles. **(A)** the structural characteristics of the initial time of water atomization; **(B)** after 0.5 ms, the structure characteristics of water atomization.
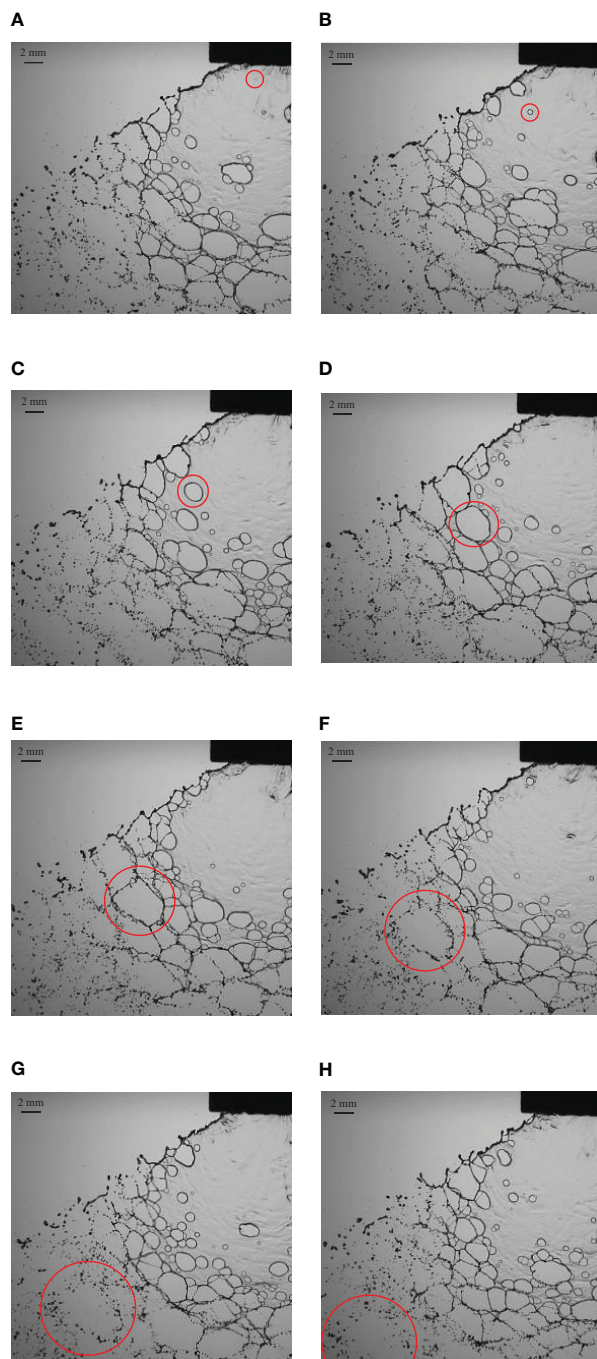
The evolution of hole structures in the emulsion butachlor atomization process. **(A)** 0 ms structure at the initial time; **(B)** 0.5ms structure; **(C)** 1 ms structure; **(D)** 1.5 ms structure; **(E)** 2 ms structure; **(F)** 2.5 ms structure; **(G)** 3 ms structure; **(H)** 3.5 ms structure.

seen that with the increase of the Weber number, the liquid sheet breakup length of water decreases slowly from 20 mm to approximately 16 mm, while the liquid sheet breakup length of butachlor increases slowly from approximately 7 mm to 12 mm, which changes less with the Weber number. It is obvious that the liquid sheet breakup length of butachlor is smaller than that of water.

With the presence of emulsion butachlor, the surface tension is different from the surface tension of water spray, which reduces the stability of the liquid sheet during spray, resulting in the formation of the liquid ligament closer to the nozzle, and making the atomization area of butachlor smaller. The liquid sheet breakup length of butachlor is shorter than that of water, which is consistent with the fact that the atomization breakup of butachlor occurs earlier (Ellis and Tuck, 1999; Xie et al., 2013).

As shown in Figures 6A, B, not only is the liquid sheet breakup length of butachlor less than that of water, but the liquid sheet expansion area of butachlor is significantly smaller than that of water as well. When the emulsion is used as the spray liquid, the liquid sheet fragmentation occurs in advance, while the spray angle increases (Gong et al., 2021). It indicates that emulsion butachlor advances the atomization process and changes the liquid sheet stability.

The droplets formed by the water spray and butachlor spray have different characteristics in morphology. It could be seen from Figure 7A that the liquid sheet formed by water atomization is broken into liquid ligaments due to oscillation disturbance, and the liquid ligaments destabilize and break up into droplets. The droplets are distributed from ligaments and gradually spread around (Qin et al., 2018). The droplet group formed by liquid ligament fragmentation also has the same wave-like distribution due to the disturbance. As shown in Figure 7B, when the spray liquid is emulsion butachlor, the morphology of the fragmentation process changes obviously, and holes appear on the liquid sheet to form the net structures. The fragmentation mechanism changes into perforation mechanism, and the droplets are also distributed around the net. It can be seen from the image that the droplet size formed by the water spray is smaller than that formed by the butachlor spray.

3.2 Disturbance and instability of liquid sheet

Water atomization and butachlor atomization also have different morphological characteristics from the side view of the liquid sheet. The fluctuation of the liquid sheet presents the stability of the liquid sheet.

It can be seen from Figure 8A that when the spray liquid is water, the disturbance fluctuation is more obvious and the fluctuation amplitude is larger. When the spray liquid is emulsion butachlor in Figure 8B, the fluctuation of the side is significantly reduced. The side view images of water atomization and butachlor atomization at the same position were intercepted respectively as shown in Figures 8C, D. It is obvious that the disturbance of the water spray is greater than that of butachlor. The appearance of droplets is earlier than that of the water spray in the side view image of butachlor.

As shown in Figures 9A, B, the diffusion angle increases with the increase of the Weber number. However, the increasing trend is weak. The diffusion angle of water is slightly larger than that of butachlor. This is consistent with the longer liquid sheet breakup length and more obvious swing of water. Moreover, all data collapse
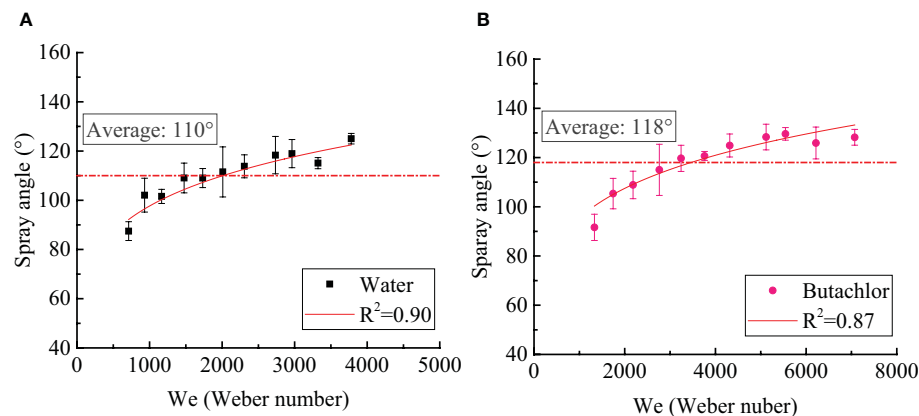
FIGURE 4
(A) Spray angle varies with the Weber number of water spray; **(B)** spray angle varies with the Weber number of butachlor spray.

on one line of diffusion angle, i.e.,

$$\theta_d \propto We \qquad (5)$$

where θ_d is the diffusion angle (°) and We is the Weber number (dimensionless).

3.3 Effect of emulsion butachlor on atomization droplet size

Droplet size is one of the key parameters affecting spray quality. Different atomization mechanisms significantly affect the droplet size spectrum. As shown in Table 1, the droplet size Dv_{50} (volume median diameter) of butachlor is larger than that of water (Altieri and Cryer, 2018; Post and Hewitt, 2018). This is consistent with the liquid sheet structure characteristics captured by the high-speed camera. Fine size droplets are easy to drift. The addition of emulsion additives could effectively increase D_{V50} and decrease D_{V10}, thereby reducing drift, and improving pesticide utilization (Altieri and Cryer, 2018).

The influence of spray process on the formation of droplets is further analyzed by analyzing the relative span. The relative span is a measure of droplet size distribution. The smaller the relative span, the narrower the droplet size spectrum, and the more consistent the droplet size. The droplet size decreases with the increase of spray pressure, regardless of spray type (water or butachlor), while the relative span increases with the increase of pressure. Butachlor emulsion spray not only increased the droplet size but also improved the uniformity of droplet size distribution. At 0.3 MPa, D_{V50} increased 25%, and the span decreased from 1.187 to 1.172. This may be attributed to the fact that the spray of emulsion butachlor changes the formation process of droplets and weakens the disturbance of the liquid sheet. The droplet size generated from the hole structure is more uniform than that generated from the surface wave structures. This result helps to improve the quality of sprays and reduces pesticide waste by adjusting pesticide formulations.

4 Discussion

Pesticide spraying is the primary means of controlling insects and weeds. The use of pesticides has a significant impact on crop yields and the health of surrounding ecosystems and workers
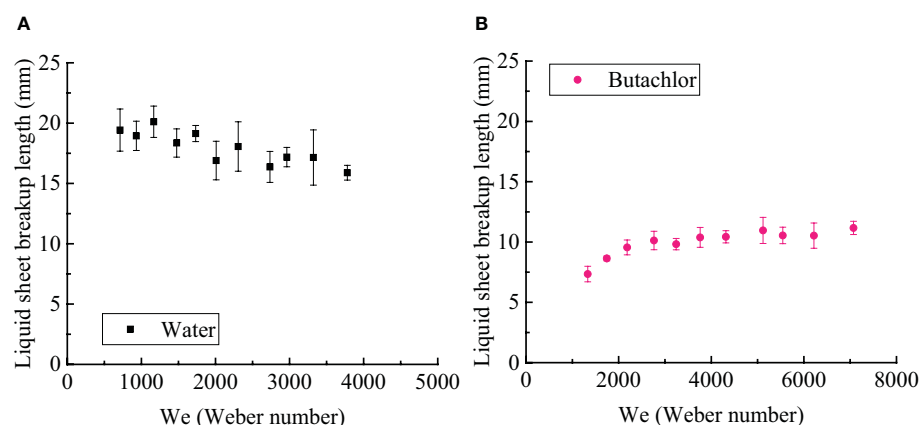
FIGURE 5
(A) Liquid sheet breakup length varies with the Weber number of water spray; **(B)** Liquid sheet breakup length varies with the Weber number of butachlor spray.
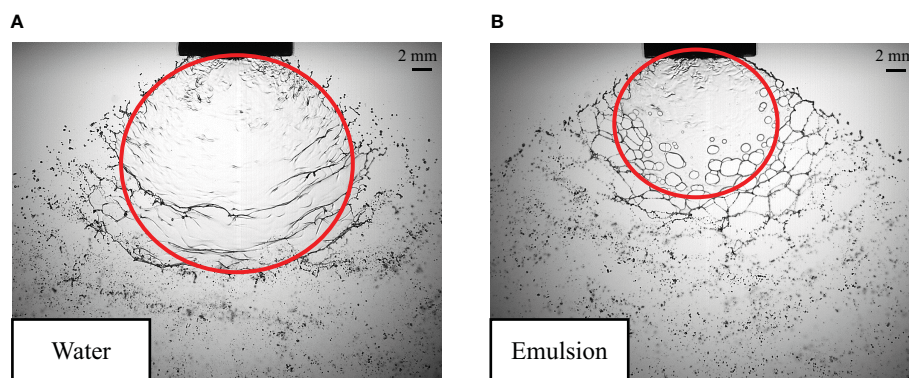
FIGURE 6
The liquid sheet area of water **(A)** and emulsion butachlor **(B)**.

(Paudel et al., 2020). However, the atomization mechanism of pesticide spraying is complex, and the relevant theoretical research is insufficient (Hilz et al., 2012). Taking water and emulsion concentrate pesticides as the research object aimed to deeply analyze the influence of emulsion concentrate pesticide atomization on atomized droplet size based on the study of the characteristics, development, and fragmentation process of the liquid sheet structure and the evolution process of fragmentation. The characteristics of the spray liquid sheet structure reflect the liquid sheet breakup dynamics (Li et al., 2020).

When the water is atomized, the structural characteristics of the liquid sheet are mainly the surface wave structures of continuous disturbance. This is because the main cause of the instability of the liquid sheet is the velocity difference between the liquid phase and the surrounding air phase. The existence of velocity difference leads to the generation of surface wave structures. With the development of surface wave, the liquid sheet breaks up to form droplets. Emulsion pesticide atomization has completely different structural characteristics; that is, it has completely different fragmentation mechanical properties. The presence of emulsion components leads to the appearance of hole
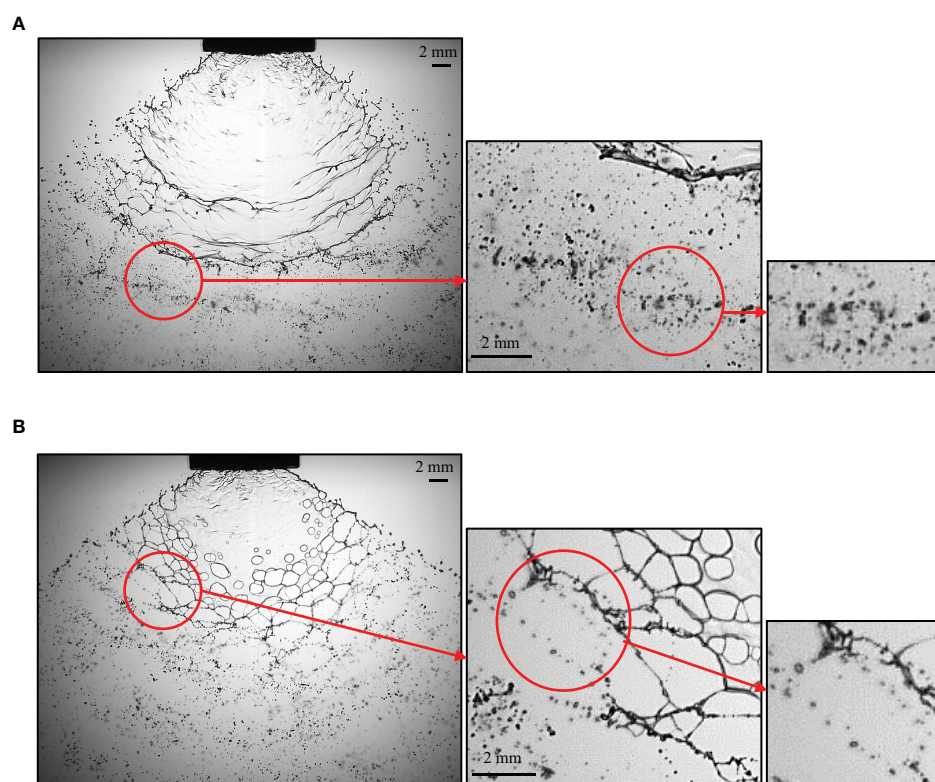
FIGURE 7
(A) Droplet morphology characteristics and formation of water spray; **(B)** Droplet morphology characteristics and formation of butachlor spray.
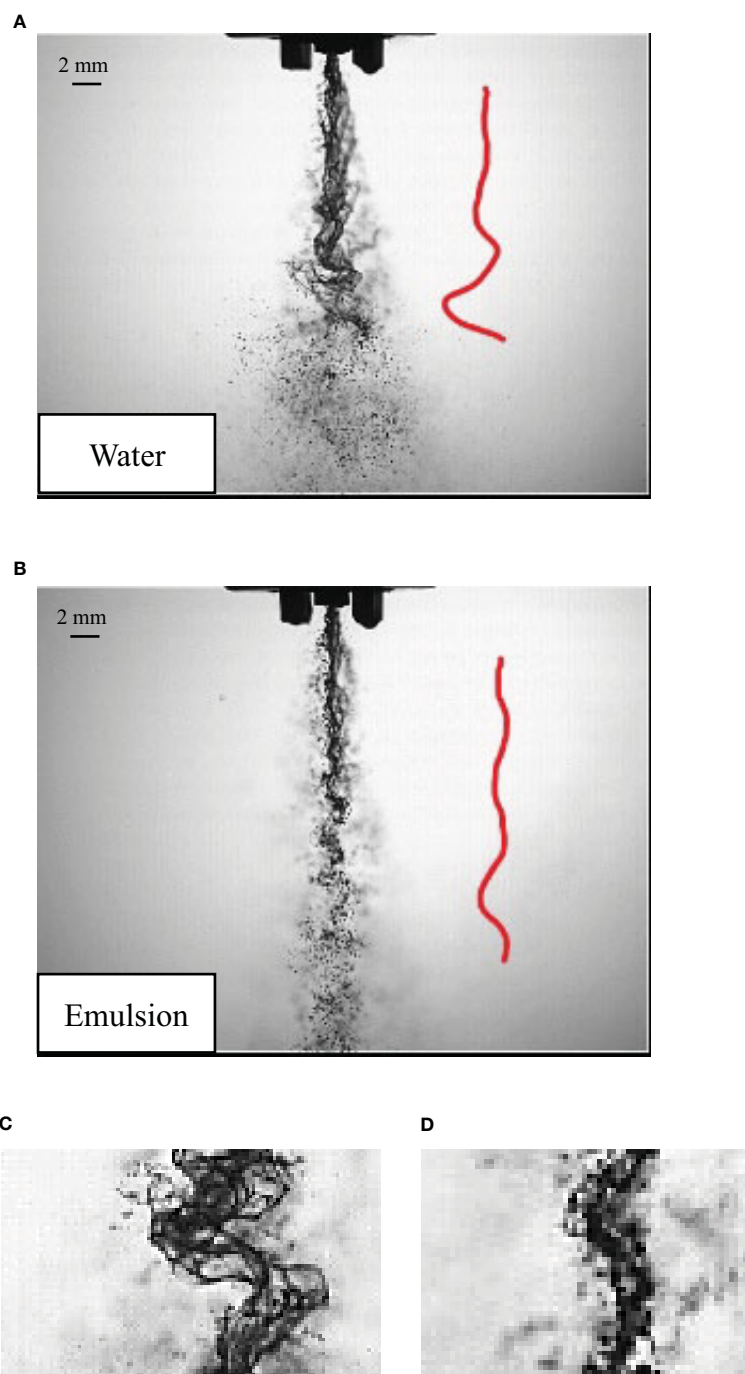
FIGURE 8
(A) The side view morphology of water spray; **(B)** The side view morphology of butachlor spray; **(C)** water morphology local; **(D)** butachlor morphology local.

structures on the liquid sheet (Goual et al., 2020; Siddharth, 2021). The existence of holes changes the instability process of liquid sheet and the formation of droplets (Li et al., 2021).

The development of liquid sheet is affected by surface tension and inertial force. Therefore, this study quantitatively studied the relationship between the Weber number and liquid sheet structure characteristics, which is used to characterize the process of liquid sheet instability and droplet formation. We found that the perforation mechanism slightly increased the spray angle (Kim et al., 2021).

Under the same surface tension, only the spray velocity is changed; that is, only the inertia force is changed. The spray angle of either mechanism shows the same trend with the Weber number; that is, it shows a power law relationship with the Weber number. When the inertia force is the same, the smaller the surface tension, the larger the spray angle. The size of the liquid sheet breakup length reflects the order of liquid sheet instability. The liquid sheet breakup length of the emulsion butachlor is smaller than that of water, which proves that the emulsion leads to the early breakage of the liquid sheet.
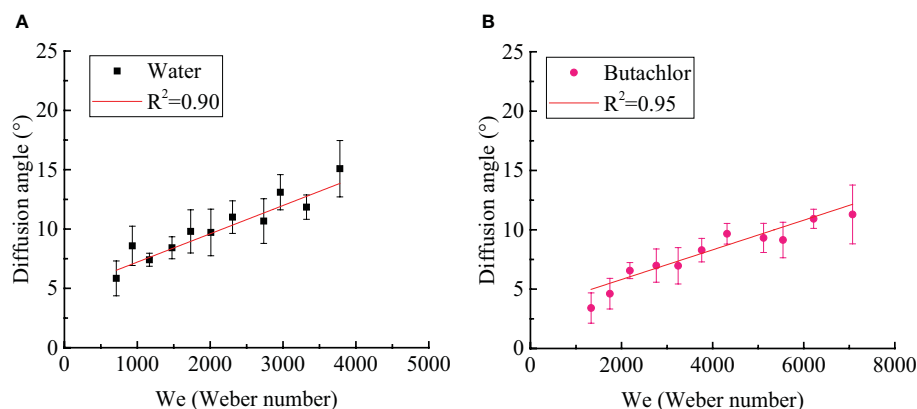
FIGURE 9

(A) Diffusion angle in water spray varies with the Weber number; **(B)** diffusion angle in butachlor spray varies with the Weber number.

Compared with water atomization, pesticide atomization is less affected by inertial force. The change trend of the diffusion angle with the Weber number also confirms each other. In summary, it leads to a larger droplet size and a more consistent droplet size spectrum of the emulsion pesticide butachlor atomization.

Emulsion pesticide sprays involve the complex multi-phase flow of water, oil, gas, and solid (Cryer et al., 2021). Their flow structure and flow characteristics are more complicated than those of pure water. Correlation studies involve a challenging scientific exploration and expansion of the theoretical system of single-phase fluid atomization. The purpose of reducing spray drift, improving atomization quality, and improving the effective utilization rate of pesticides could be achieved by preparing appropriate liquid and matching appropriate spray conditions to control spray stability, and then controlling the size and speed of droplets (Makhnenko et al., 2021).

5 Conclusions

In this paper, the atomization process through a standard flat fan nozzle of water and butachlor emulsion was visualized using a high-speed camera. By means of experimental research and dimensionless analysis, the differences of the atomization process

and droplet size spectrum between emulsion pesticide spray and water spray were compared:

(1) The spray angle of butachlor atomization is larger than that of water atomization. The spray angle shows a power law dependence of the Weber number with a power of 0.17 for all conditions tested here. However, the liquid sheet breakup length of emulsion butachlor is smaller than that of water.

(2) In the process of water atomization, the side view of the liquid sheet is a large waveform disturbance, while that of the butachlor atomization is a small waveform disturbance. In the meantime, the diffusion angle of water is also greater than that of butachlor.

(3) The atomization process and mechanism of water and emulsion butachlor are different. During water atomization, the fragmentation process in the direction of the fan-shaped liquid sheet plane shows that the liquid mass leaves the nozzle to form a liquid sheet. Wave structures are shown on the liquid sheet due to the disturbance. The unstable liquid sheet breaks up into liquid ligaments, and the liquid ligaments break up into droplets. The presence of butachlor led to the formation of pre-holes on the liquid sheet. The pre-holes developed into holes, and the holes formed a net structure and finally break up

TABLE 1 Dv_{50}, Dv_{10}, Dv_{90}, and relative span (uniformity of droplets size) for sprays produced with water and emulsion butachlor.

Spray liquid		0.1 MPa	0.2 MPa	0.3 MPa	0.4 MPa	0.5 MPa
Water	Relative Span	1.165	1.216	1.187	1.370	1.467
	Dv_{50} (μm)	229.563	178.668	156.067	146.817	138.365
	Dv_{10} (μm)	122.207	85.743	76.636	68.494	63.024
	Dv_{90} (μm)	389.548	302.935	261.809	269.643	265.973
Oil-based emulsion butachlor	Relative Span	1.067	1.2387	1.172	1.183	1.213
	Dv_{50} (μm)	387.474	234.55	194.57	178.46	165.608
	Dv_{10} (μm)	201.702	128.817	98.989	86.644	75.5
	Dv_{90} (μm)	615.113	419.26	326.967	297.812	276.434

into droplets. The size of the droplets formed by the atomization of butachlor is larger than that of water atomization due to the change of fragmentation mechanisms. The presence of emulsion improves the uniformity of spray droplet size distribution. The increase in droplet size is of great significance for spray anti-drift.

Data availability statement

The original contributions presented in the study are included in the article/supplementary material. Further inquiries can be directed to the corresponding author.

Author contributions

WY: Conceptualization, Data curation, Formal Analysis, Investigation, Methodology, Software, Validation, Visualization, Writing – original draft, Writing – review & editing. WZ: Conceptualization, Data curation, Formal Analysis, Investigation, Methodology, Software, Validation, Visualization, Writing – original draft, Writing – review & editing. WJ: Conceptualization, Funding acquisition, Project administration, Resources, Supervision, Writing – review & editing. MO: Conceptualization, Funding acquisition, Project administration, Resources, Supervision, Writing – review & editing. XD: Conceptualization, Project administration, Resources, Supervision, Writing – review & editing. TZ: Writing – review & editing. SD: Writing – review & editing. LJ: Writing – review & editing. XW: Writing – review & editing.

Funding

Acknowledgments

Conflict of interest

Author TZ is employed by the company Chinese Academy of Agriculture Mechanization Sciences Group Co., Ltd., Beijing, China.

The remaining authors declare that the research was conducted in the absence of any commercial or financial relationships that could be construed as a potential conflict of interest.

Publisher's note

All claims expressed in this article are solely those of the authors and do not necessarily represent those of their affiliated organizations, or those of the publisher, the editors and the reviewers. Any product that may be evaluated in this article, or claim that may be made by its manufacturer, is not guaranteed or endorsed by the publisher.

References

Altieri, A. L., and Cryer, S. A. (2018). Break-up of sprayed emulsions from flat-fan nozzles using a hole kinematics model. *Biosyst. Eng.* 169, 104–114. doi: 10.1016/j.biosystemseng.2018.02.006

Altieri, A., Cryer, S., and Acharya, L. (2014). Mechanisms, experiment, and theory of liquid sheet breakup and drop size from agricultural nozzles. *Atomization Sprays*, 24 (8). doi: 10.1615/AtomizSpr.2014008779

Cloeter, M. D., Qin, K., Patil, P., and Smith, B. (2010). "Planar laser induced fluorescence (PLIF) flow visualization applied to agricultural spray nozzles with sheet disintegration; Influence of an oil-in-water emulsion," In *Proc. ILASS-Americas 22nd Annual Conf.* (Cincinnati, USA: Institute for Liquid Atomization and Spray Systems).

Cryer, S. A., Altieri, A. L., Schmucker, A. L., and Day, K. M. (2017). Role of large inhomogeneities in initiating liquid sheet breakup in agricultural atomisation. *Biosyst. Eng.* 163, 103–115. doi: 10.1016/j.biosystemseng.2017.08.020

Cryer, S. A., Altieri, A. L., Schmucker, A. L., et al. (2021). Minimising atomisation drift potential by exploring the break-up of liquid sheets using multiphase methylated soybean and silicon oil emulsions. *Biosyst. Eng.* 202, 142–151. doi: 10.1016/j.biosystemseng.2020.12.004

Dombrowski, N., and Johns, W. R. (1963). The aerodynamic instability and disintegration of viscous liquid sheets. *Chem. Eng. Sci.* 18 (3), 203–214. doi: 10.1016/0009-2509(63)85005-8

Ellis, M. C. B., and Tuck, C. R. (1999). How adjuvants influence spray formation with different hydraulic nozzles. *Crop Prot.* 18 (2), 101–109. doi: 10.1016/S0261-2194(98)00097-0

Gong, C., Kang, C., Jia, W., Yang, W., and Wang, Y. (2020). The effect of spray structure of oil-based emulsion spray on the droplet characteristics. *Biosyst. Eng.* 198, 78–90. doi: 10.1016/j.biosystemseng.2020.08.001

Gong, C., Li, D., Kang, C., and Wang, Y. (2021). Visualisation of the evolution of perforations in oil-based emulsion sheets formed by flat-fan spray nozzles. *Biosyst. Eng.* 207, 68–80. doi: 10.1016/j.biosystemseng.2021.04.005

Goual, L., Zhang, B., and Rahham, Y. (2020). Nanoscale characterization of thin films at oil/water interfaces and implications to emulsion stability. *Energy Fuels* 35 (1), 444–455. doi: 10.1021/acs.energyfuels.0c03466

Guler, H., Zhang, Z., Zhu, H., Grieshop, M., and Ledebuhr, M. A. (2020). Spray characteristics of rotary micro sprinkler nozzles used in orchard pesticide delivery. *Transact ASABE* 63 (6), 1845–1853. doi: 10.13031/trans.13445

Hilz, E., Vermeer, A. W. P., Stuart, M. A. C., and Leermakers, F. A. M. (2012). Mechanism of perforation based on spreading properties of emulsified oils. *Atomization Sprays* 22 (12). doi: 10.1615/AtomizSpr.2013006728

Jun, Y. (2012). Experimental study based on nozzle spray uniformity. *Hunan Agric. Machinery* 39 (3), 55–60.

Kim, D. H., Lee, S., and Yoon, Y. (2021). Droplet size control in gas-liquid pintle injectors. *Trans. Japan Soc. Aeronautical Space Sci.* 64 (2), 91–100. doi: 10.2322/tjsass.64.91

Kooij, S., Sijs, R., Denn, M. M., Villermaux, E., and Bonn, D. (2018). What determines the drop size in sprays? *Phys. Rev. X* 8 (3), 031019. doi: 10.1103/PhysRevX.8.031019

Lefebvre, A. H., and McDonell, V. G. (2017). *Atomization and Sprays*. CRC press.

Li, H., Cryer, S., Acharya, L., and Raymond, J. (2020). Video and image classification using atomisation spray image patterns and deep learning. *Biosyst. Eng.* 200, 13–22. doi: 10.1016/j.biosystemseng.2020.08.016

Li, C., He, R., He, Z., Kumar, S. S., Fredericks, S. A., Hogan, C. J., et al. (2021). Spatially-resolved characterization of oil-in-water emulsion sprays. *Int. J. Multiphase Flow* 145, 103813. doi: 10.1016/j.ijmultiphaseflow.2021.103813

Makhnenko, I., Alonzi, E. R., Fredericks, S. A., Colby, C. M., and Dutcher, C. S. (2021). A review of liquid sheet breakup: Perspectives from agricultural sprays. *J. Aerosol Sci.* 157, 105805. doi: 10.1016/j.jaerosci.2021.105805

Matthews, G., Bateman, R., and Miller, P. (2014). *Pesticide application methods.* (Oxford: John Wiley & Sons).

Miller, P. C. H., and Ellis, M. C. B. (2000). Effects of formulation on spray nozzle performance for applications from ground-based boom sprayers. *Crop Prot.* 19 (8-10), 609–615. doi: 10.1016/S0261-2194(00)00080-6

Nadeem, M., Chang, Y. K., Venkatadri, U., Diallo, C., Harvard, P., and Nguyen-Quang, T.. (2018). Water quantification from sprayer nozzle by using particle image velocimetry (PIV) versus imagine processing techniques. *Pak. J. Agric. Sci.* 55 (1), 203–210. doi: 10.21162/PAKJAS/18.6679

Negeed, E. S. R., Hidaka, S., Kohno, M., and Takata, Y. (2011). Experimental and analytical investigation of liquid sheet breakup characteristics. *Int. J. Heat Fluid Flow* 32 (1), 95–106. doi: 10.1016/j.ijheatfluidflow.2010.08.005

Paudel, S., Sah, L. P., Devkota, M., Poudyal, V., Prasad, P., and Reyes, M. R. (2020). Conservation agriculture and integrated pest management practices improve yield and income while reducing labor, pests, diseases and chemical pesticide use in smallholder vegetable farms in Nepal. *Sustainability* 12 (16), 6418. doi: 10.3390/su12166418

Post, S. L., and Hewitt, A. J. (2018). Flat-fan spray atomization model. *Trans. ASABE* 61 (4), 1249–1256. doi: 10.13031/trans.12572

Qin, K., Cloeter, M., Tank, H., Liu, L., and Wilson, S. (2010). Modeling the Spray Atomization of Emulsion Embedded Agricultural Solutions. *J. ASTM Int.* 7 (10), 103040. doi: 10.1520/JAI103040

Qin, L., Yi, R., and Yang, L. (2018). Theoretical breakup model in the planar liquid sheets exposed to high-speed gas and droplet size prediction. *Int. J. Multiphase Flow* 98, 158–167. doi: 10.1016/j.ijmultiphaseflow.2017.09.010

Siddharth, K. S. (2021). "Dynamics of Annular Liquid Sheets Using Feature Correlation Velocimetry (FCV)," in *Advances in Engineering Design: Select Proceedings of FLAME 2020*, Springer Singapore. 211–219.

Tarnogrodzki, A. (1993). Theoretical prediction of the critical Weber number. *Int. J. multiphase Flow* 19 (2), 329–336. doi: 10.1016/0301-9322(93)90006-G

Wang, J., Mirynowski, E. M., Bittle, J. A., and Fisher, B. T. (2016). Experimental measurements of n-heptane liquid penetration distance and spray cone angle for steady conditions relevant to early direct-injection low-temperature combustion in diesel engines. *International J. Engine Res.* 17 (4), 371–390. doi: 10.1177/1468087415580916

Wang, X., He, X., Song, J., and Herbst, A. (2015). Effect of adjuvant types and concentration on spray drift potential of different nozzles. *Trans. Chin. Soc. Agric. Eng.* 31 (22), 49–55. doi: 10.11975/j.issn.1002-6819.2015.22.007

Wang, S., He, X., Song, J., Wang, S., Jia, X., and Ling, Y. (2018). Effects of xanthan gum on atomization and deposition characteristics in water and Silwet 408 aqueous solution. *Int. J. Agric. Biol. Eng.* 11 (3), 29–34. doi: 10.25165/j.ijabe.20181103.3802

Wei, Z., Zhu, H., and Zhang, Z. (2021). Droplet Size Spectrum, Activation Pressure, and Flow Rate Discharged from PWM Flat-Fan Nozzles. *Trans. ASABE* 1, 64. doi: 10.13031/trans.14100

Xiao, L., Zhu, H., Wallhead, M., Horst, L., Ling, P., and Krause, C. R. (2018). Characterization of Biological Pesticide Deliveries through Hydraulic Nozzles. *Trans. ASABE* 61 (3), 897–908. doi: 10.13031/trans.12698

Xie, C., He, X., and Song, J. (2013). Comparative research of two kinds of flat fan nozzle atomization process. *Trans. Chin. Soc. Agric. Eng.* 29 (5), 25–30. doi: 10.3969/j.issn.1002-6819.2013.05.004

Yang, W., Jia, W., Ou, M., Zhong, W., Jiang, L., and Wang, X. (2022). Effect of Physical Properties of an Emulsion Pesticide on the Atomisation Process and the Spatial Distribution of Droplet Size. *Agriculture* 12 (7), 949. doi: 10.3390/agriculture12070949

Zhang, W., He, X., Song, J., and Wang, C. (2014). Effect of adjuvant S240 on atomization of water dispersible granule and emulsion solution. *Trans. Chin. Soc. Agric. Eng.* 30 (11), 897–908, 61–67. doi: 10.3969/j.issn.1002-6819.2014.11.008

Zhao, H. (2012). *Study on atomization mechanism of coaxial airflow* PhD dissertation. (East China University of Science and Technology).

Check for updates

Dynamic stratified porosity computation from canopy interaction simulation between airflow and leaves

Huiyuan Cui[1†], Chengde Wang[2†], Fadian Lu[2], Xuemei Liu[1,3]* and Jin Yuan[1,3]

[1]College of Mechanical & Electronic Engineering, Shandong Agricultural University, Tai'an, China, [2]Forestry College, Shandong Agricultural University, Tai'an, China, [3]Shandong Provincial Key Laboratory of Horticultural Machinery and Equipment, Tai'an, China

The main goal of wind-driven spraying is to use assisted airflow to disrupt the structure of branches and leaves and broaden the air delivery channel, so as to achieve uniform droplet deposition in the middle and lower parts of the canopy. Due to the complex branch and leaf structure inside the canopy, there is currently no effective method to express the dynamic changes of canopy porosity and the law of airflow attenuation under assisted airflow. In this study, based on the two-way fluid-structure interaction numerical simulation method, the relating between the assisted airflow and the structural parameters of the cotton canopy is analyzed, and a new method for predicting and simulating the dynamic porosity of the canopy is proposed. Firstly, a two-way fluid-structure interaction model based on *Lattice Boltzmann* (LB) solver and *Finite Element* (FE) solver is developed to simulate the deformation motion of cotton leaves and the spatial distribution of airflow field, and the correctness of the numerical simulation is verified based on indoor measurement data. Secondly, the post-processing method of Computational Fluid Dynamics (CFD) is used to obtain images of leaves at different canopy positions under assisted airflow, and the porosity changes are calculated and analyzed by image processing. The research results show that under different initial wind speeds (5 m·s^{-1}, 10 m·s^{-1}, 15 m·s^{-1}), the maximum normalized mean absolute error (NMAE) between the simulated values and the measured values is 13.99%, 20.72% and 16.08%, respectively. The coefficient of determination (R^2) for linear fitting between simulated values and measured values is 0.9221. These validation results indicate the effectiveness of the numerical simulation method. The validated CFD model is applied to predict leaf deformation and porosity changes within the canopy under various wind loads and times. The application results have well revealed the interaction between crop leaves and airflow, and will be beneficial to make a better understanding of the effect of assisted airflow on droplet deposition.

KEYWORDS

stratified porosity, CFD, image processing, fluid-structure interaction, leaf deformation

1 Introduction

In the process of plant protection application, a large amount of pesticide misapplication will reduce the effectiveness of pesticide application and increase environmental pollution (Gil and Sinfort, 2005; Damalas and Eleftherohorinos, 2011; Tudi et al., 2021). The main goal of precision pesticide application is to achieve uniform coverage and deposition of pesticides in the target crop canopy (Khot et al., 2012; Li et al., 2021; Grella et al., 2022). The canopy characteristics of target plants directly affect the application mode and the droplet deposition effect (Duga et al., 2015; Xun et al., 2022). A complete understanding of the canopy characteristics of the target plant is important to evaluate the airflow velocity and turbulence levels within the canopy.

Canopy parameters are not only important indicators of growth and yield, but also important factors affecting pesticide interception and deposition (Olesen et al., 2003; Liu et al., 2020). In the late stage of crop growth, the stems and leaves of the plant population cover each other. Air-assisted sprayers can effectively deliver pesticides within dense canopies (Reichard et al., 1979; Derksen et al., 2008). The disturbance of the assisted airflow on the canopy branches and leaves can change the porosity of the canopy, thus widening the transmission channel of the pest control agent, which helps to achieve the droplet deposition at the lower canopy (Müller et al., 2018; Qiu et al., 2022). Scholars have conducted a large number of spray deposition field tests and wind tunnel tests on different target crops with different air-assisted sprayers.

Cross et al. (2001a, 2001b) conducted a series of field experiments on apple trees of different sizes to study the complex interaction between air-volume flow rate, spray-liquid flow rate, spray quality (droplet size distribution) and crop characteristics. Chen et al. (2013a; 2013b) measured the spray retention and non-target deposition at three crown growth stages (i.e. leaf stage, half leaf stage and full leaf stage), and found that increasing canopy density significantly reduced the amount of drift from the target. Duga et al. (2015) analyzed the spray deposition profiles in different pome fruit trees and concluded that tree characteristics such as total leaf cover, leaf wall porosity and tree volume strongly influenced total on-target deposition. These empirical spray studies indicate that spray deposition is caused by the complex interaction between the canopy and the air in canopy.

Crop spraying is a complex process involving the interaction of many parameters, such as pesticide dose and spray volume, spray-liquid distribution, droplet spectrum, air volume, sprayer speed, meteorological conditions and crop characteristics. In the past few decades, modeling approaches, especially computational fluid dynamics (CFD) models, have been effectively used to understand and characterize the crop spraying process (Badules et al., 2018; Zhang et al., 2018). Scholars adopted the averaging procedure to model airflow within a plant canopy without considering the flow details of individual elements (Wilson and Shaw, 1977; Raupach and Shaw, 1982). The canopy is considered as a porous medium to study the transport of airflow and droplets in canopy. The properties of porous medium are determined by the structural

parameters of the canopy (porosity, leaf density) (Da Silva et al., 2006; Cui et al., 2022; Zhang et al., 2022). Endalew et al. (2009), 2010 simulated the effect of large branches and airflow by adding a resistance term in the canopy. The leaves in the canopy have a large effect, especially on the crop canopy. Dorr et al. (2008) developed a turbulence probability model, which can combine the motion model of fog droplets with the three-dimensional structure of plants, and simulate the drift of pesticide droplets around different plant structures. These studies further illustrate the influence of canopy structure on airflow distribution and droplet deposition.

Optical porosity is an important indicator for quantitatively measuring canopy structure parameters. It is defined as the ratio of leaf gap area on a projection plane to the contour area of the canopy leaves (Loeffler et al., 1992; Zhu et al., 2003). To accurately describe and calculate porosity, researchers have conducted extensive studies using hemispherical photography (Qu et al., 2016), laser point clouds (Escolà et al., 2017), hyperspectral or thermal infrared techniques (Neinavaz et al., 2016) and physical and mathematical models (Giusti and Marsili-Libelli, 2006). However, these sensor-based calculation methods are costly and can only calculate the static porosity of canopy. In addition, the spatial distribution of leaves in canopy cannot be fully captured due to high canopy leaf density and heavy shading, especially in the late stages of crop growth. In fact, crops cultivated in the field have traceable patterns in growth and spatial distribution of leaves (Guo et al., 2009). According to these morphological characteristics (Liu et al. (2020, 2021a) specially studied the canopy porosity during spraying, proposed a 3D model to calculate the changes of canopy porosity, and realized the rapid prediction of crop canopy porosity. However, there is a strong interaction between leaves and airflow in the actual process of air-assisted spraying. The assisted airflow can not only move and deform the leaves, thus widening the droplet transport channel, but also improve the droplet transfer speed. It can effectively improve droplet deposition in the plant canopy and reduce drift (Panneton and Piché, 2005; Tang et al., 2021). Existing porosity calculation methods are difficult to express this physical process.

At present, the interaction between airflow and canopy is not clear. It is reflected in the following two aspects: one is how the airflow changes the deformation of the leaves, and the other is how the leaves affect the distribution of the airflow field. However, current research mainly calculates porosity based on the static structural characteristics of the canopy, and porosity is constantly changing in the actual spraying process. There is a lack of research on the quantitative description of porosity under assisted airflow, especially the dynamic changes in porosity. In our previous research, we studied a numerical simulation method for the fluid-structure interaction of leaves and spray airflow (Cui et al., 2023). In this study, we attempt to introduce the entire plant structure into numerical simulation and to calculate the real-time dynamic porosity. The relating between assisted airflow and canopy structural parameters is analyzed, and a new method for predicting and simulating canopy dynamic porosity is proposed.

2 Materials and methods

2.1 3D virtual cotton plant model and artificial cotton

In this paper, in order to build a 3D virtual plant model with reasonable simplification of the canopy, the main stems, fruiting branches, petioles, and leaves are mainly considered. According to previous studies (Liu et al., 2021a; Cui et al., 2022) and cotton field measurement data (Figure 1), the structural parameters of cotton, such as plant height, petiole length and diameter, and leaf shape are determined. The main stem nodes of cotton are divided into 20 segments. The 5-20 nodes are set as fruiting branch growth positions. The multiaxial branching of fruiting branches is simplified to straight branches, and the distance between nodes on the one fruiting branch is the same. The ratio of ovate, 3-lobed and 5-lobed leaves to the total number of leaves in a single cotton plant is 20%, 55% and 25%, respectively. Based on the collected phenotype data, the windward areas of ovate, 3-lobed and 5-lobed leaves are determined to be 4206.25 mm^2, 7859.10 mm^2 and 9823.00 mm^2, respectively.

The 3D phenotypic plant models are constructed in SolidWorks (2019, Dassault Systemes, FR) software. The cotton plant has a height of 130cm and is stratified into three layers (i.e., 0-50 cm along the main stem height direction as the lower layer, 50-90 cm as the middle layer, and 90-130 cm as the upper layer). Based on the morphological characteristics and growth pattern of cotton plants, a 3D virtual plant is constructed as shown in Figure 2A.

An artificial plant is built according to the morphological characteristics of the 3D virtual plant. The material of artificial cotton leaves is selected from cloth material based on the previous experiments of leaf deformation and spray retention (Liu et al., 2021a; Liu et al., 2021b). The main stem is made of PVC plastic pipe. Wire of suitable stiffness is used for the leaf stem and fruiting branch materials. The fruiting branches and leaves are placed on the pre-drilled holes in the main stem. The single artificial cotton plant is shown in Figure 2B.

2.2 Numerical approach

2.2.1 Lattice Boltzmann model

Lattice Boltzmann (*LB*) model is suitable for solving many complex scientific problems. In particular, it does not require tracing the interface between different phases when dealing with multiphase and multi-component flows. In addition, it has been proven to have reliable accuracy in dealing with problems on microscopic and macroscopic scales (Ran and Xu, 2009; Men et al., 2017; Cui et al., 2023).

The important basis of the *LB* model is the theory of molecular motion. And *LB* model has the following assumptions.

a. The velocity component of each moving molecule is calculated without considering the influence of adjacent molecules.
b. The collision between two molecules is only considered.
c. The trajectory of each moving molecule is calculated without considering environmental factors.

Based on the above assumptions, the equation of molecular motion calculation function f is obtained. The independent variables of the equation are spatial velocity position vector, molecular velocity vector and time. The assumption on the molecular collision term can be simplified to a single relaxation time Bhatnagar Gross Krook (BGK) collision operator (Aidun and Clausen, 2010; Zhang et al., 2020). This simplification can effectively reduce the computational power. The simplified equation is the Boltzmann-BGK equation, expressed as (Aidun and Clausen, 2010):

$$f_\alpha(\mathbf{r} + K_\alpha \delta_t, \ \mathbf{t} + \delta_t) - f_\alpha(r, t) = -\frac{1}{\tau}(f_\alpha(r, t) - f_\alpha^{eq}(r, t)) + \delta_t F_\alpha(\mathbf{r}, \mathbf{t}) \quad (1)$$

Where, r is the position vector; t is the time, s; f_α is a discrete velocity distribution function; K_α is discrete particle velocity vector; δ_t is the time step; τ is the dimensionless relaxation time, $\tau = \tau_0/\delta_t$; f_α^{eq} is a local equilibrium distribution function; F_α is the external force term.

Through the discrete process, particles may move and collide, meaning that particles can move from one node to another in adjacent time steps while colliding with other adjacent particles. In addition, the *LB* method can calculate the macroscopic characteristics of the fluid through the statistical analysis of particles in the computational domain, and establish the relating between microscopic particles and macroscopic phenomena. The model D_nQ_m can be expressed as n dimensions and m discrete velocities. In this study, the octree lattice structure of D_3Q_{27} is used, as shown in Figure 3.

FIGURE 1
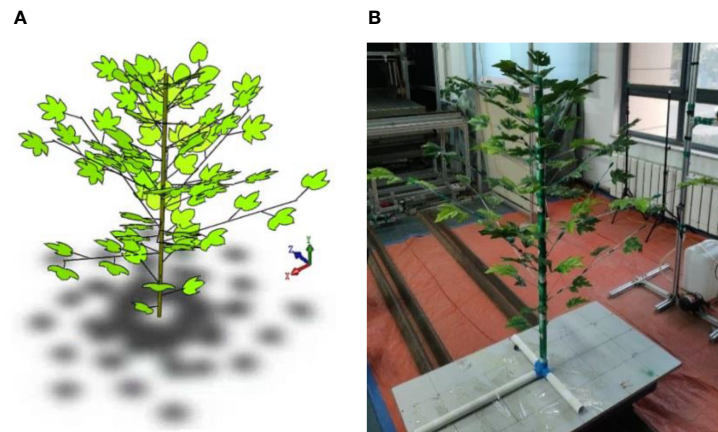Measurement of Cotton Phenotypic Parameters. **(A)** leaf, **(B)** petiole.

3D virtual cotton plant **(A)** and artificial cotton plant **(B)**.

2.2.2 Turbulence model

Large Eddy Simulation (LES) is used to model the turbulence distribution. This approach introduces an additional viscosity, called turbulent eddy viscosity to model the sub-grid turbulence (Weickert et al., 2010). The LES scheme adopts a wall-adapting local eddy viscosity model, which provides a consistent local eddy-viscosity and near-wall behavior (Ducros et al., 1998; Men et al., 2017; Zhang et al., 2020). The specific formulas are as follows:

$$U_t = (B_w\Delta)^2 \frac{(Q_{\alpha\beta}^d Q_{\alpha\beta}^d)^{3/2}}{(Q_{\alpha\beta}Q_{\alpha\beta})^{5/2} + (Q_{\alpha\beta}^d Q_{\alpha\beta}^d)^{5/4}} \quad (2)$$

$$Q_{\alpha\beta} = \frac{g_{\alpha\beta} + g_{\beta\alpha}}{2} \quad (3)$$

$$Q_{\alpha\beta}^d = \frac{1}{2}(g_{\alpha\beta}^2 + g_{\beta\alpha}^2) - \frac{1}{3}\varphi_{\alpha\beta}g_{rr}^2 \quad (4)$$

$$g_{\alpha\beta} = \frac{\partial_{\mu_\alpha}}{\partial_{x_\beta}} \quad (5)$$

Schematic diagram of the *LB model* of D$_3$Q$_{27}$.

Where, U_t, $B_w\Delta$, Δ, and $\varphi_{\alpha\beta}$ are turbulent eddy viscosity, filter scale, unit grid scale, and Kronecker symbol, respectively. $Q_{\alpha\beta}$ and $Q_{\alpha\beta}^d$ are the resolving scale strain rate tensors; $B_w(0.325)$ is a constant. $g_{\alpha\beta}$ $g_{\beta\alpha}$ and g_{rr} are the components of the strain rate tensor obtained from the second-order moment via the *LB* model. In the above equations, the subscripts α, β and r denote directions in space. The μ and x are velocity at a given distance from the wall and local flow direction tangential to the wall.

2.2.3 Boundary conditions and computational domain
2.2.3.1 Solid domain

In the fluid-structure coupling collaborative simulation, the setting size of stem and leaf parameters and the shape quality of mesh subdivision will have a significant impact on leaf deformation. The data interaction between the solid domain and the fluid domain should be completed by setting appropriate boundary conditions. It is necessary to establish the coupling environment required for collaborative simulation to ensure the accuracy of the simulation. The elements are divided in *Finite Element* (*FE*) solver, and the stem and leaf parameters and boundary conditions are set. Through two-way fluid-structure coupling, the change trend and deformation amount of leaves can be calculated, and then the dynamic porosity of leaves after deformation can be obtained.

The accurate and reasonable segmentation of *FE* mesh is the basis of *FE* solver analysis. High-quality mesh can not only ensure reasonable analysis results, but also shorten the simulation time. Therefore, selecting a suitable element segmentation method is particularly important. The numerical integration method of *FE* solver adopts Gaussian numerical integration, and the integration points of different element shapes are different. The C3D8R element of linear hexahedron reduction integral is used for the element subdivision of stems, leaves and petioles, which is used as a three-dimensional eight-node linear solid element, namely hexahedron element. Each node has six degrees of freedom and can bend in any direction. The combined element subdivision of cotton plant is shown in Figure 4. The number of elements is 16966, and the number of nodes is 41981 and the element size is 9mm.
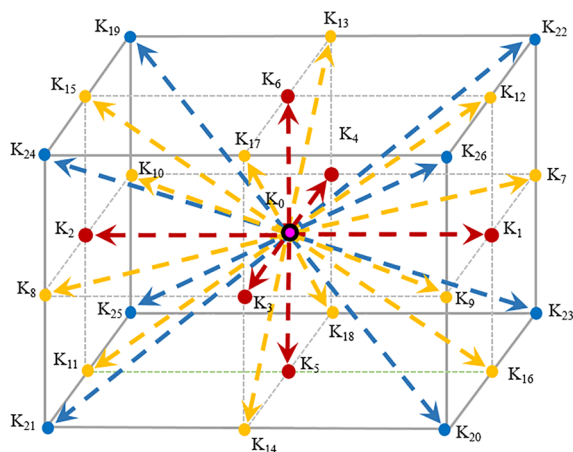
In the fluid-structure coupling analysis of assisted airflow and leaves, it is necessary to set the calculation attributes of the *FE* solver for the solid domain of stems and leaves.

(1) Material properties

The bending of stems and leaves affected by the assisted airflow is an elastic deformation phenomenon, so the elastic material parameters are used to simulate the stems and leaves. According to previous studies (Ma and Li, 2014; Liu et al., 2021a; Cui et al., 2023), the elastic modulus of cotton leaves is set to 46.5Mpa, the Poisson's ratio of leaves is 0.32, and the density of leaves is 700 kg·m^{-3}.

(2) Analysis step settings

In *FE* solver, the dynamic display analysis is set up. Since the spraying device drives the air curtain and nozzle to move in the actual spraying process. The initial value is verified according to the maximum time step of the fluid domain pilot site. The solid domain analysis step is set to 1s, and the field output adjusts 1s to 200 uniform time intervals, that is, there are 200 imaging effects within 1s.

(3) Boundary condition

According to the distribution and connection of stems and leaves, the location of stem is defined as a completely fixed constraint in the boundary conditions setting, namely 0 degrees of freedom. In the simulation process, it only bears the influence of airflow and no external force, so it is only necessary to set the corresponding contact attributes.

2.2.3.2 Fluid domain

The fluid domain model is the air domain model. The plant should be placed in the air domain. The air domain model is built in 3D modeling software. The size is 1500 mm long, 1500 mm wide and 1500 mm high. This model is saved in a file format that can

interface with the *LB* solver, and is named as 'air.stl'. The imported air fluid domain uses meshless modeling. The coordinate position of the fluid domain is adjusted to ensure that the branches and leaves are all in the flow field analysis domain. The location distribution of solid domain and fluid domain models is shown in Figure 5. The gravity acceleration applied to the fluid is set to -9.81m·s^{-2}. The default material 'Material 1' is used in the fluid domain, and its relevant parameters are set as follows: the molecular weight of air is 28.996 g·mol^{-1}, the density of air is 1.225 kg·m^{-3}, and the operating temperature is 289.35 K (16.2°C). The gas flowing at low speed is a Newtonian fluid, so the dynamic viscosity is set to 1.7894e-05 Pa ·s. In air-assisted spraying, the downward airflow can open the upper branches and leaves, which plays an important role in increasing the amount of droplets deposition in the lower and middle layers in dense canopy (Zhang et al., 2022; Zhu et al., 2022). In this study, we mainly consider the effect of downward airflow on porosity changes.
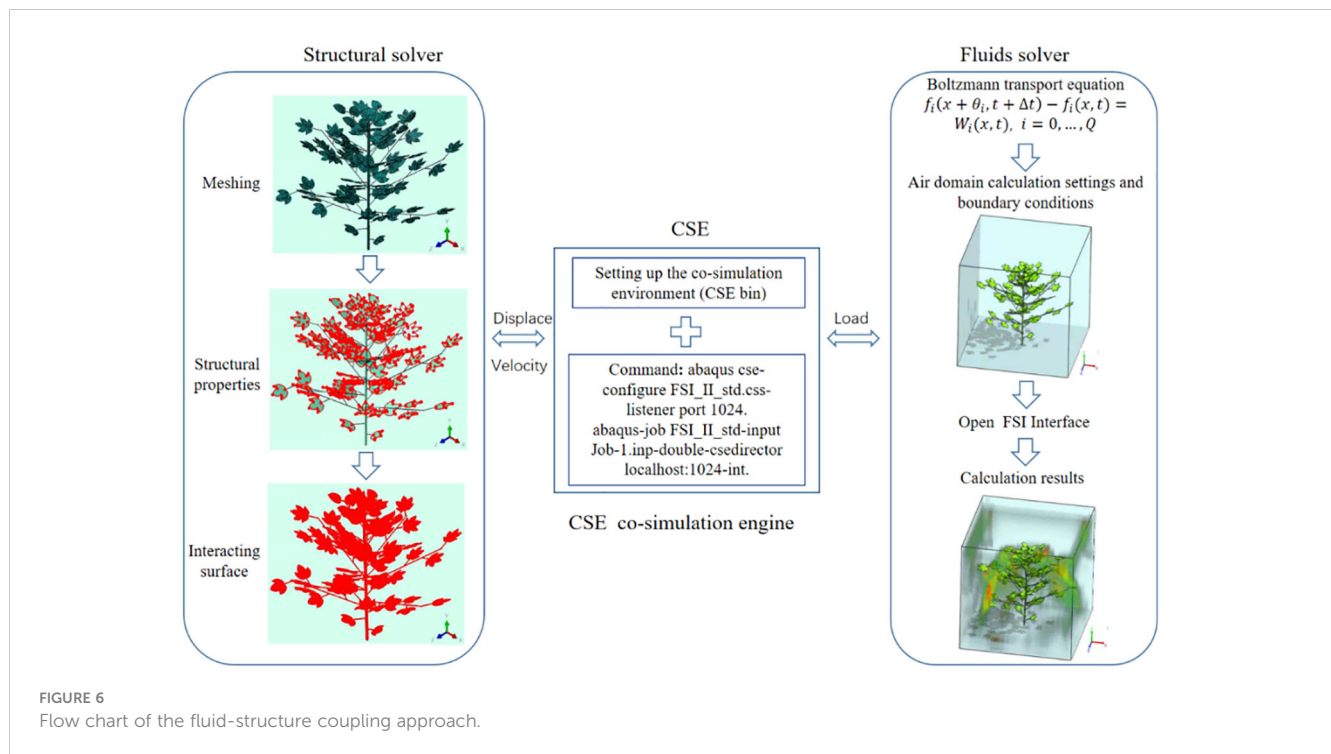
2.2.4 Fluid-structure coupling module

In *FE* solver, the contact surface with the fluid domain is set as the fluid-structure co-simulation boundary, as shown in Figure 6. After completing the above steps, set the calculation file in the Job module, name it *Job*-1, and export the.inp file. The recognition subroutine of fluid-structure coupling interface is set up in the.inp file. The flowchart of the fluid-structure coupling approach is shown in Figure 6.

2.2.5 Validation of numerical simulation

In order to make the experimental conditions controllable and avoid interference of uncontrollable factors in the natural environment, in this paper, we construct an artificial cotton plant based on the 3D virtual cotton plant (Dekeyser et al., 2014; Cui et al., 2022). To validate the numerical simulation, the differences between simulated and experimental values at the same position in the canopy are compared. The positions of the sampling points are

FIGURE 4
Schematic diagram of elements distribution in the structural explicit *FE* solver.

FIGURE 5
Schematic diagram of the distribution of cotton plant and air domain locations.

FIGURE 6
Flow chart of the fluid-structure coupling approach.
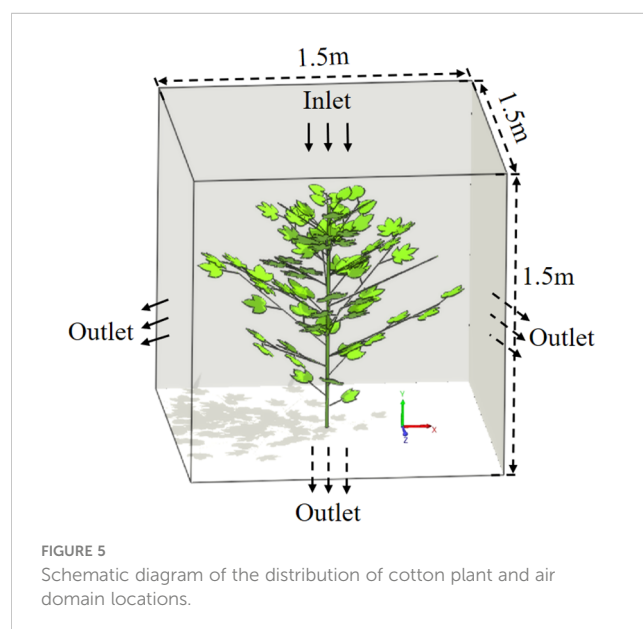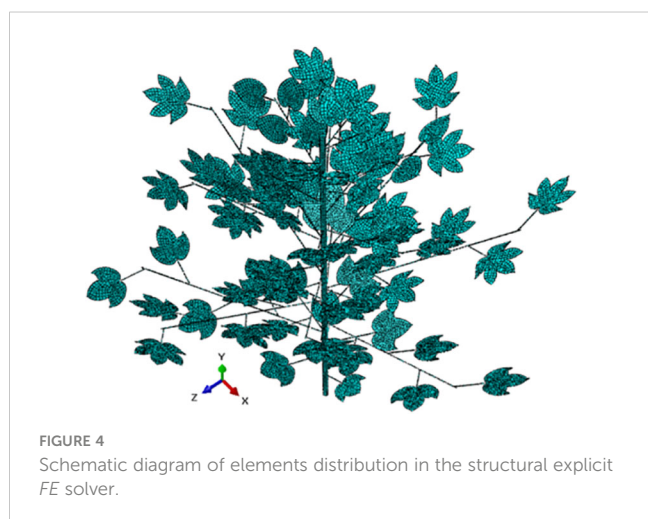
as shown in Figures 7A, B. In Figure 7B, the centrifuge (4-72-6A, FOSHAN CITY NANHAI POPULA FAN CO., LTD, China) is the wind source and the variable frequency speed controller is used to regulate the speed. The air velocity at the sampling points was measured separately by a hot-wire anemometer (Testo 405i, Titisee-Neustadt, Germany). The data measured by the hot-wire anemometer are exported to the computer terminal via Bluetooth.

In simulation, the airflow velocity at the sampling point is output through the detection line. The normalized mean absolute error (NMAE) between the measured and the simulated values of the upper, middle, and lower layers of the canopy were compared. The total difference was analyzed by fitting a linear equation.

2.3 Dynamic changes in canopy porosity based on image processing

Optical porosity is defined as the ratio of canopy leaf void area to contour plane area on a projection plane (Loeffler et al., 1992;

Zhu et al., 2003). It is related to plant density, structure and environmental conditions, and is a structural parameter closely related to flow and resistance characteristics near plants. In pesticide spraying, leaves are the main organ of droplet deposition. In addition to the size and position of the leaf, the leaf will bend and deform due to airflow disturbance, and the optical porosity will change accordingly.

Based on the 3D model of the plant and the fluid-structure coupling process, we propose a method to calculate the target canopy porosity by layering and zoning based on image processing. This method can obtain canopy dynamics images during the interaction between canopy and airflow through CFD post-processing, and then use image processing to calculate porosity at any canopy height. The specific process is as follows:

(1) Image acquisition. Using the layer plane as the reference plane, images of different canopy positions of three-dimensional cotton plant targets along the reference plane are captured and stored in *LB* solver (Figures 8A–C).
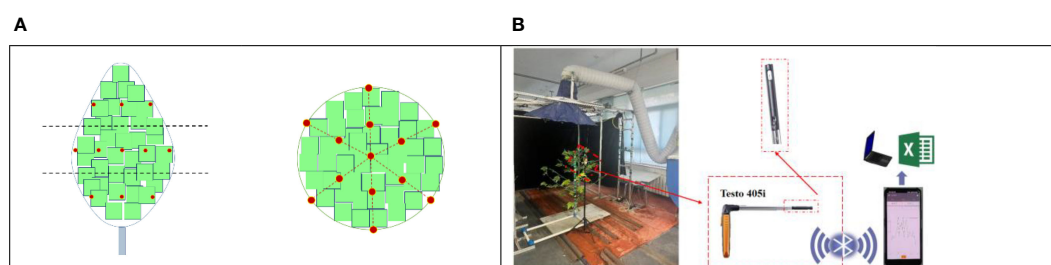
FIGURE 7
Distribution of sampling points **(A)** and indoor airflow measurement **(B)**.
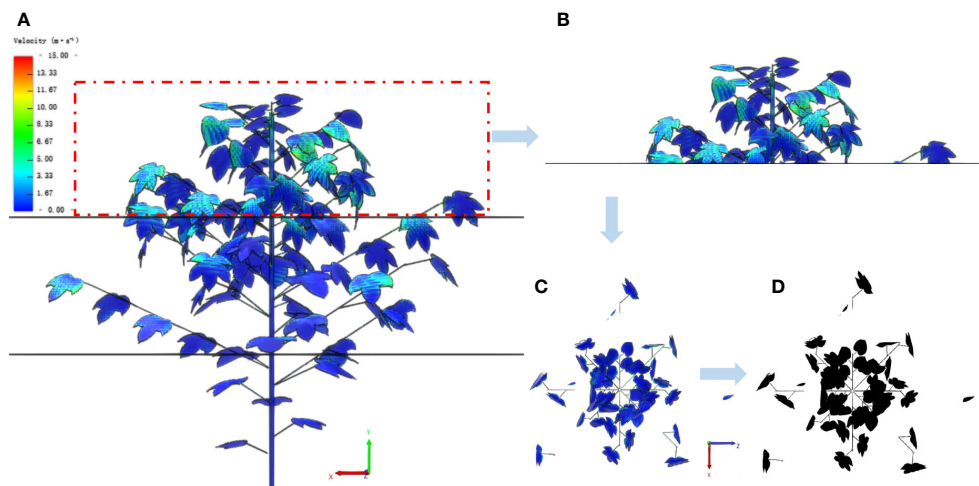
FIGURE 8
Calculation process of canopy stratified porosity. **(A)** The front view of a stratified cotton plant. **(B)** The front view of the upper layer. **(C)** The top view of the upper layer. **(D)** The image processing result of the top view.

(2) Image processing. Canopy projection images are processed by image denoising, gray scale processing, thresholding and binarization (Figure 8D).

(3) Determination of canopy outer edge. Determine the canopy projection along the outermost leaf edge of the canopy and calculate the projection area (S_i).

(4) Calculation of windward area. The pixel value occupied by the plant projection is counted, and according to the image and 3D plant leaf scale, the leaf windward area (A_i) at different canopy positions of the plant is calculated.

(5) Calculation of stratified porosity. The porosity of each layer can be calculated using the following formula: $P_i = \frac{A_i}{Si}$.

3 Results and discussions

3.1 Simulation validation results

In this study, in order to verify the reliability of the numerical simulation results, several sampling points are set up in the upper, middle, and lower layers of the artificial cotton planting target area. The initial airflow velocity values are 5 m·s^{-1}, 10 m·s^{-1} and 15 m·s^{-1}, respectively. The results are shown in Figure 9A. Under the initial air velocity of 5 m·s^{-1}, the normalized mean absolute error (NMAE) between the simulated value and the measured value of the upper, middle and lower parts of the canopy are 7.54%, 12.51% and 13.99%, respectively. Under the speed of 10 m·s^{-1}, the NMAE are
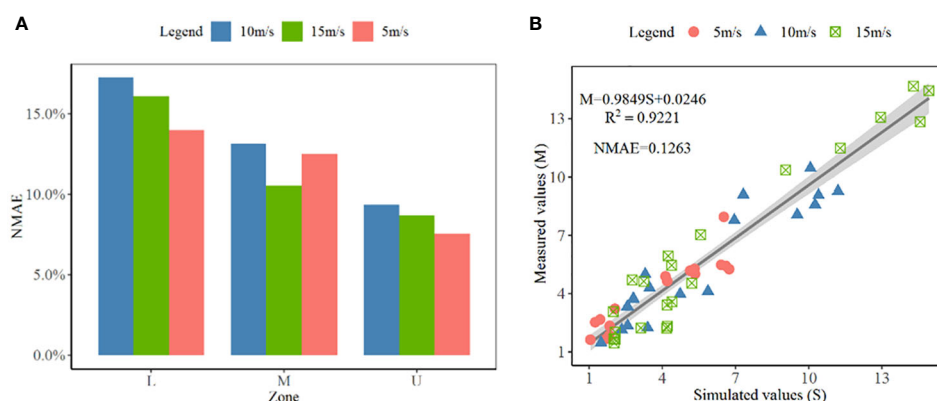
FIGURE 9
The comparative analysis between the measured values and the simulated values. **(A)** is the NMAE between simulated and measured values; **(B)** is the linear fitting analysis between simulated and measured values.

9.36%, 13.14% and 20.72%, respectively. Under the speed of 15 m·s^{-1}, the NMAE are 8.69%, 10.54% and 16.08%, respectively. The results show that the simulated airflow velocity distribution can reflect the attenuation of airflow velocity in the canopy. To further verify the accuracy of the simulation results, linear fitting analysis is performed on all simulated values (S) and measured values (M), as shown in Figure 9B. The expression of the linear equation is M=0.9849S+0.0246, and the coefficient of determination (R^2) is 0.9221. The fitting results indicate that the fluid-structure coupling method can effectively reflect the dynamic changes of canopy porosity.

3.2 Leaf deformation and porosity changes in the canopy at different airflow velocities

Figure 10 shows the leaf deformation and porosity changes within the canopy under the influence of different airflow velocities at 0.1s. Under 0 m·s^{-1}, 5 m·s^{-1}, 10 m·s^{-1} and 15 m·s^{-1}, the upper, middle and lower canopy leaves have different degrees of deformation, and the airflow velocity and vortex distribution changes are different.

In the absence of wind (0 m·s^{-1}), we export images at different heights of the canopy and calculated the porosity of the upper, middle, and lower layers as 49.95%, 59.85% and 49.16%,
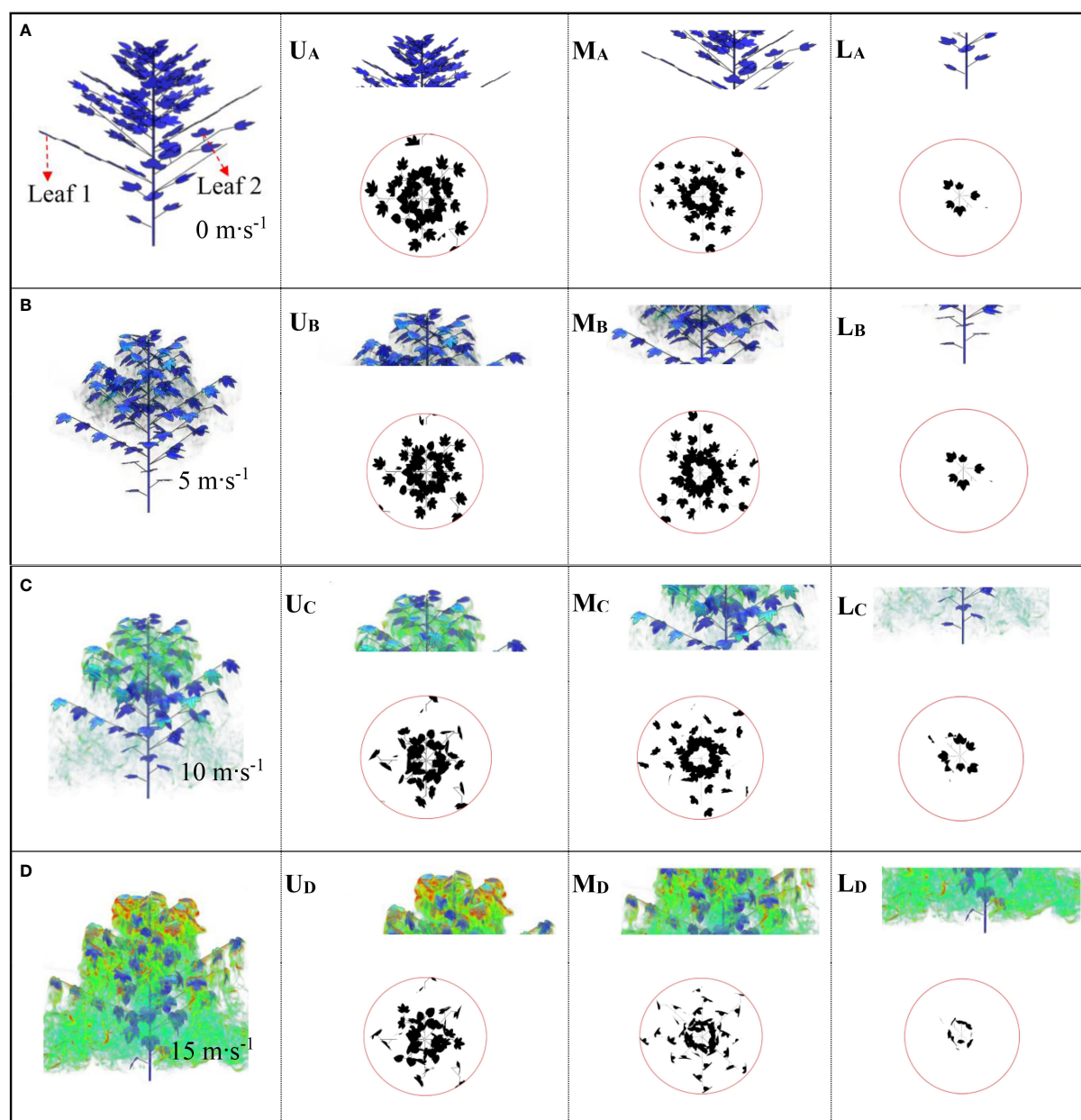
FIGURE 10
Airflow distribution at different initial wind speeds at 0.1s. **(A)** is 0 m·s-1; **(B)** is 5 m·s-1; **(C)** is 10 m·s-1; **(D)** is 15 m·s-1'. U, M and L represent the upper, middle, and lower layers of the canopy, respectively.

respectively (Figure 10A). When the airflow velocity reaches 5 m·s^{-1}, we find that the leaves at different heights showed slight twisting or bending deformation (Figure 10B). Compared with the velocity of 0 m·s^{-1}, the porosity at the same canopy position is 52.27%, 52.23% and 49.74%, respectively. Figure 10C shows the changes in leaves within the canopy at the same time when the airflow speed increases to 10 m·s^{-1}. The porosity at different canopy heights is 66.83%, 64.16% and 38.71%, respectively. As the flow rate increases, the plant shrinks its shape, rolls up its leaves and bends downstream, resulting in a decrease in its cross-sectional area and an increase in its fluidization degree. Figure 10D shows the changes in leaves within the canopy at the same time when the airflow speed increases to 15 m·s^{-1}, with the porosity of each layer being 68.07%, 73% and 62.35%, respectively. As the wind load increases, the leaves sway more and become more random. Compared with the initial state of 5 m·s^{-1}, the change ratio has increased by 36.28%, 21.97% and 26.83%, respectively. From the perspective of leaf deformation, when subjected to increased airflow load, the distribution of canopy branches and leaves will be reconfigured to reduce wind force and absorb momentum in the airflow, which is a reconstruction phenomenon (Ennos et al., 2000; Vollsinger et al., 2005; Kane et al., 2008; Miri et al., 2018). This behavior is often observed in plants with flat and thin leaves (Gillies et al., 2002). At higher wind speeds, plant resistance decreases and leaf deformation increases. However, in actual spraying operations, the distribution of vortices around the canopy changes greatly, which increases the drift of droplets in the atmosphere.

We derive the windward area and porosity at different canopy relative heights (CRHs) (10%, 20%,…, 100%) to further describe the changes in leaf deformation and porosity along the depth of the canopy. It is assumed that the initial porosity is defined as the porosity at different positions of the canopy under the condition of no wind (0 m·s^{-1}). The dynamic variation of porosity is defined as the change in porosity relative to the initial porosity at different relative heights of the canopy under wind conditions (5 m·s^{-1}, 10 m·s^{-1}, 15 m·s^{-1}). Figure 11A shows the changes in windward leaf area at different relative heights of the canopy under different initial velocities. From Figure 11A, it can be seen that the changes in leaf area at the bottom (CRH=10%) and top (CRH=90%) of the canopy are relatively small. While the changes in windward area in the middle of the canopy (CRH=20% -80%) are relatively large. Under low wind speed (5 m·s^{-1}), the maximum change in the windward area of leaves at different CRHs is 20%. As the airflow speed increases, the changes in the windward area of leaves within the canopy under 10 m·s^{-1} and 15 m·s^{-1} are significantly larger than those under low wind speed conditions. These results indicate that low wind speeds cause slight vibration of the leaves, while high wind speeds cause significant bending or deformation of the leaves. Figure 11B shows the dynamic changes in porosity at each relative height of the canopy. Under the three wind speed conditions of low (5 m·s^{-1}), medium (10 m·s^{-1}), and high (15 m·s^{-1}), the relative heights of the canopy with the largest changes in porosity are 40%, 70%, and 40%, respectively,

and the maximum changes in porosity are 11%, 26%, and 16%, respectively. The maximum change in porosity occurs in the middle of the canopy because the interaction between airflow and leaves becomes stronger in areas with denser leaves. Comparing Figures 11A, B, we find that there is consistency between the position with the largest change in leaf windward area and the position with the largest change in porosity. The specific modification form is as follows: 'the position with the largest change in porosity. Figures 11C–D and show the changes in velocity and vorticity at different relative heights of the canopy. As the depth of the canopy increases, the airflow velocity continues to decay. At CRH=80%, a significant change in vorticity occurred, which is related to the obstruction of airflow by the upper branches and leaves of the canopy.

3.3 Dynamic changes in porosity at different times

Figure 12 shows the dynamic changes in porosity at different times (0-1s) in the upper, middle and lower layers of the canopy at a wind speed of 5 m·s^{-1} (light breeze). At 0.1s, the upper leaves of the canopy begin to deform first due to the influence of the upper airflow, and the upper layer undergoes changes earlier than the middle and lower layers. From 0.2s to 0.5s, the leaves within the canopy continuously bend downward and deform. From the perspective of the curvature amplitude of most leaves in the canopy, the curvature degree of the canopy leaves is the highest at 0.6s. After 0.7s, the leaves gradually rebound. Due to the obstruction of airflow by the upper and middle branches and leaves within the canopy, the intensity of airflow decreases greatly when it reaches the lower part. The airflow ultimately causes only slight deformation of the leaves in the lowest layer, indicating that under the action of a small airflow (light breeze), the deformation amplitude of the canopy leaves is small and they sway slightly up and down.

Figure 13 shows the deformation of internal branches and leaves in the canopy under airflow disturbance at different times when the assisted airflow velocity is 10 m·s^{-1} (moderate wind). At 0.1s, the airflow has just reached the top of the canopy. At 0.2s to 0.4s, the canopy leaves begin to gradually bend downward. Compared to the initial wind speed of 5 m·s^{-1}, the leaf reaches its maximum deformation at 0.5s. At this moment, the maximum porosity of the entire canopy indicates that the moment when the wind speed increases and the maximum leaf deformation occurs is relatively late. After 0.6s, the deformation amplitude of most leaves in the canopy shows a slight rebound. A small number of leaves have a large rebound amplitude and even show a reversal trend, especially the leaves at the bottom of the canopy have obvious deformation (0.9s to 1.0s). This may be caused by the vortices formed under the canopy. Due to the obstruction of the upper leaves, the assisted airflow under the canopy gradually decreases, and the intensity of the vortices on

FIGURE 11
Changes in windward area (A), porosity (B), velocity (C), and vorticity (D) at different CRHs.
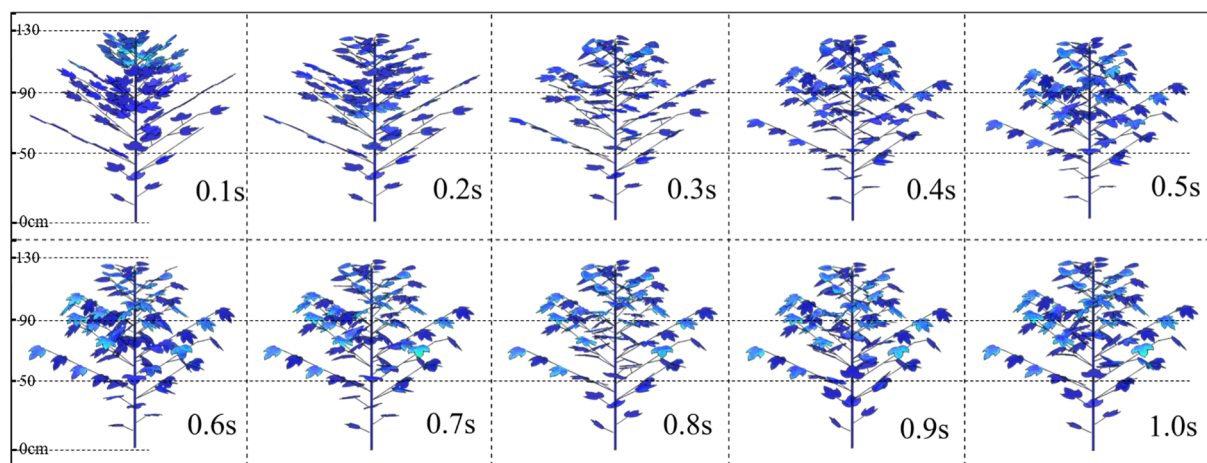

FIGURE 12
Changes in canopy leaf morphology at different times under 5 m·s⁻¹.

the back of the lower leaves is greater than that of the assisted airflow on the front. This leaf inversion is very important for the uniform deposition in the middle and lower parts of the canopy during spraying.

Figure 14 shows the deformation of internal branches and leaves in the canopy under airflow disturbance at different times when the assisted airflow velocity is 15 m·s⁻¹ (high wind speed). At

0.2s, the airflow has reached the lower part of the canopy and caused deformation of the lowest leaves. As the airflow gradually enters the interior of the canopy, the leaf deformation amplitude reaches its maximum value at 0.4s, which is earlier than the maximum moment of leaf deformation under medium (10 m·s⁻¹) and low (5 m·s⁻¹) wind speeds, indicating that the leaves are susceptible to deformation under high wind speeds. After 0.5s,
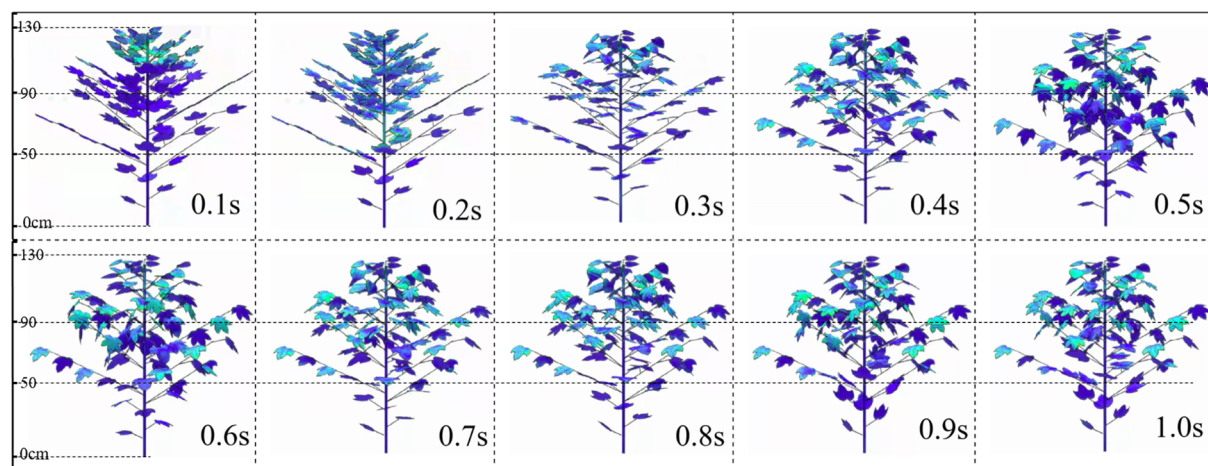
FIGURE 13
Changes in canopy leaf morphology at different times under 10 m·s^{-1}.
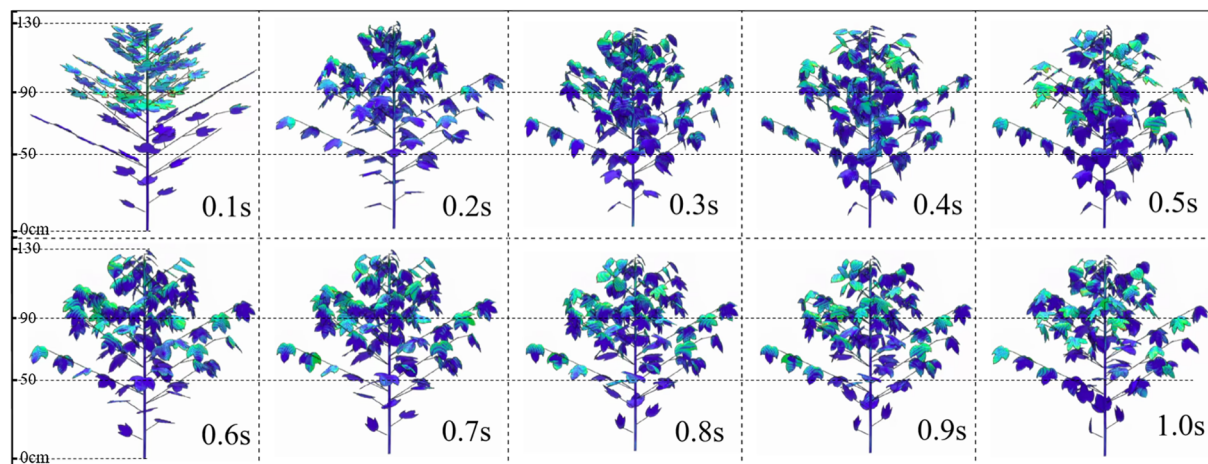
FIGURE 14
Changes in canopy leaf morphology at different times under 15 m·s^{-1}.

the leaves in the canopy become disorderd, floating up and down, and some of the leaves undergo reversals, especially for 0.9s and 1.0s. From the perspective of leaf deformation, the degree of leaf deformation will not increase as the airflow velocity continues to increase. However, a higher velocity can lead to an increase in airflow disturbance outside the canopy, which leads to the possibility of spray droplets drift.

4 Conclusions

In this study, a new method based on CFD simulation and image processing is proposed to calculate the dynamic changes in porosity caused by leaf deformation under assisted airflow. A two-way fluid-structure interaction model is developed based on LB solver and FE solver. The model achieves a quantitative and intuitive analysis of the deformation of leaves in the canopy under the action of assisted airflow. The fluid-solid interaction model is validated by indoor experiments. The results of CFD post-processing are analyzed using image processing algorithms, and the stratified dynamic porosity in the canopy is calculated at different velocities and different times. This study provides an idea to clarify the dynamic changes of porosity in canopy during air-assisted spraying and to analyze the mechanism of increasing droplet deposition in canopy by assisted airflow.

Compared with previous static porosity studies, this study can better reveal the dynamic interaction phenomenon between crop leaves and airflow. However, the developed CFD model still needs further improvement. In order to accurately predict the dynamic porosity of the canopy, 3D leaf modeling should consider more details. In addition, the effect of different directional assisted airflow on the canopy structure should be considered.

Data availability statement

Author contributions

Funding

Acknowledgments

Conflict of interest

The authors declare that the research was conducted in the absence of any commercial or financial relationships that could be construed as a potential conflict of interest.

Publisher's note

All claims expressed in this article are solely those of the authors and do not necessarily represent those of their affiliated organizations, or those of the publisher, the editors and the reviewers. Any product that may be evaluated in this article, or claim that may be made by its manufacturer, is not guaranteed or endorsed by the publisher.

References

Aidun, C. K., and Clausen, J. R. (2010). Lattice-Boltzmann method for complex flows. *Annu. Rev. fluid mechanics* 42, 439–472. doi: 10.1016/j.soilbio.2017.12.011

Badules, J., Vidal, M., Boné, A., Llop, J., Salcedo, R., Gil, E., et al. (2018). Comparative study of CFD models of the air flow produced by an air-assisted sprayer adapted to the crop geometry. *Comput. Electron. Agric.* 149, 166–174. doi: 10.1016/j.compag.2017.09.026

Chen, Y., Ozkan, H. E., Zhu, H., Derksen, R. C., and Krause, C. R. (2013a). Spray deposition inside tree canopies from a newly developed variable-rate air-assisted sprayer. *Trans. ASABE* 56 (6), 1263–1272. doi: 10.13031/trans.56.9839

Chen, Y., Zhu, H., Ozkan, H. E., Derksen, R. C., and Krause, C. R. (2013b). Spray drift and off-target loss reductions with a precision air-assisted sprayer. *Trans. ASABE* 56 (6), 1273–1281. doi: 10.13031/trans.56.10173

Cross, J. V., Walklate, P. J., Murray, R. A., and Richardson, G. M. (2001a). Spray deposits and losses in different sized apple trees from an axial fan orchard sprayer: 1. Effects of spray liquid flow rate. *Crop Prot.* 20 (1), 13–30. doi: 10.1016/S0261-2194(00)00046-6

Cross, J. V., Walklate, P. J., Murray, R. A., and Richardson, G. M. (2001b). Spray deposits and losses in different sized apple trees from an axial fan orchard sprayer: 2. Effects of spray quality. *Crop Prot.* 20 (4), 333–343. doi: 10.1016/S0261-2194(00)00163-0

Cui, H., Wang, C., Liu, X., Yuan, J., and Liu, Y. (2023). Dynamic simulation of fluid-structure interactions between leaves and airflow during air-assisted spraying: A case study of cotton. *Comput. Electron. Agric.* 209, 107817. doi: 10.1016/j.compag.2023.107817

Cui, H., Wang, C., Liu, X., Yuan, J., Liu, Y., and Song, L. (2022). Cotton canopy airflow simulation and velocity attenuation model based upon 3D phenotype and stratified sub-regional porous medium. *Comput. Electron. Agric.* 201, 107282. doi: 10.1016/j.compag.2022.107282

Damalas, C. A., and Eleftherohorinos, I. G. (2011). Pesticide exposure, safety issues, and risk assessment indicators. *Int. J. Environ. Res. Public Health* 8 (5), 1402–1419. doi: 10.3390/ijerph8051402

Da Silva, A., Sinfort, C., Tinet, C., Pierrat, D., and Huberson, S. (2006). A Lagrangian model for spray behavior within vine canopies. *J. aerosol Sci.* 37 (5), 658–674. doi: 10.1016/j.jaerosci.2005.05.016

Dekeyser, D., Foqué, D., Duga, A. T., Verboven, P., Hendrickx, N., and Nuyttens, D. (2014). Spray deposition assessment using different application techniques in artificial orchard trees. *Crop Prot.* 64, 187–197. doi: 10.1016/j.cropro.2014.06.008

Derksen, R. C., Zhu, H., Ozkan, H. E., Hammond, R. B., Dorrance, A. E., and Spongberg, A. L. (2008). Determining the influence of spray quality, nozzle type, spray volume, and air-assisted application strategies on deposition of pesticides in soybean canopy. *Trans. ASABE* 51 (5), 1529–1537. doi: 10.13031/2013.25301

Dorr, G., Hanan, J., Adkins, S., Hewitt, A., O'Donnell, C., and Noller, B. (2008). Spray deposition on plant surfaces: a modelling approach. *Funct. Plant Biol.* 35 (10), 988–996. doi: 10.1071/FP08056

Ducros, F., Nicoud, F., and Poinsot, T. (1998). Wall-adapting local eddy-viscosity models for simulations in complex geometries. *Numerical Methods Fluid Dynamics* VI, 293–299 Available at:. https://www.imag.umontpellier.fr/~nicoud/PDF/ICFD_WALE.pdf.

Duga, A. T., Ruysen, K., Dekeyser, D., Nuyttens, D., Bylemans, D., Nicolai, B. M., et al. (2015). Spray deposition profiles in pome fruit trees: Effects of sprayer design, training system and tree canopy characteristics. *Crop Prot.* 67, 200–213. doi: 10.1016/j.cropro.2014.10.016

Endalew, A. M., Debaer, C., Rutten, N., Vercammen, J., Delele, M. A., Ramon, H., et al. (2010). A new integrated CFD modelling approach towards air-assisted orchard spraying. Part I. Model development and effect of wind speed and direction on sprayer airflow. *Comput. Electron. Agric.* 71 (2), 128–136. doi: 10.1016/j.compag.2009.11.005

Endalew, A. M., Hertog, M., Delele, M. A., Baetens, K., Persoons, T., Baelmans, M., et al. (2009). CFD modelling and wind tunnel validation of airflow through plant canopies using 3D canopy architecture. *Int. J. Heat Fluid Flow* 30 (2), 356–368. doi: 10.1016/j.ijheatfluidflow.2008.12.007

Ennos, A. R., Spatz, H. C., and Speck, T. (2000). The functional morphology of the petioles of the banana, Musa textilis. *J. Exp. Bot.* 51 (353), 2085–2093. doi: 10.1093/jexbot/51.353.2085

Escolà, A., Martínez-Casasnovas, J. A., Rufat, J., Arnó, J., Arbonés, A., Sebé, F., et al. (2017). Mobile terrestrial laser scanner applications in precision fruticulture/horticulture and tools to extract information from canopy point clouds. *Precis. Agric.* 18, 111–132. doi: 10.1007/s11119-016-9474-5

Gil, Y., and Sinfort, C. (2005). Emission of pesticides to the air during sprayer application: A bibliographic review. *Atmospheric Environ.* 39 (28), 5183–5193. doi: 10.1016/j.atmosenv.2005.05.019

Gillies, J. A., Nickling, W. G., and King, J. (2002). Drag coefficient and plant form response to wind speed in three plant species: Burning Bush (Euonymus alatus), Colorado Blue Spruce (Picea pungens glauca.), and Fountain Grass (Pennisetum

setaceum). *J. Geophysical Research: Atmospheres* 107 (D24), ACL–A10. doi: 10.1029/2001JD001259

Giusti, E., and Marsili-Libelli, S. (2006). An integrated model for the Orbetello lagoon ecosystem. *Ecol. Model.* 196 (3-4), 379–394. doi: 10.1016/j.ecolmodel.2006.02.016

Grella, M., Gioelli, F., Marucco, P., Zwertvaegher, I., Mozzanini, E., Mylonas, N., et al. (2022). Field assessment of a pulse width modulation (PWM) spray system applying different spray volumes: duty cycle and forward speed effects on vines spray coverage. *Precis. Agric.* 23 (1), 219–252. doi: 10.1007/s11119-021-09835-6

Guo, Y., Zhao, C., Zhu, Y., Li, C., Sun, H., and Cao, W. (2009). Morphogenesis model with relation to light and temperature condition for above-ground organs in cotton. *Acta Agronomica Sin.* 35 (11), 2101–2106. doi: 10.3724/SP.J.1006.2009.02101

Kane, B., Pavlis, M., Harris, J. R., and Seiler, J. R. (2008). Crown reconfiguration and trunk stress in deciduous trees. *Can. J. For. Res.* 38 (6), 1275–1289. doi: 10.1139/X07-225

Khot, L. R., Ehsani, R., Albrigo, G., Larbi, P. A., Landers, A., Campoy, J., et al. (2012). Air-assisted sprayer adapted for precision horticulture: Spray patterns and deposition assessments in small-sized citrus canopies. *Biosyst. Eng.* 113 (1), 76–85. doi: 10.1016/j.biosystemseng.2012.06.008

Li, X., Giles, D. K., Niederholzer, F. J., Andaloro, J. T., Lang, E. B., and Watson, L. J. (2021). Evaluation of an unmanned aerial vehicle as a new method of pesticide application for almond crop protection. *Pest Manage. Sci.* 77 (1), 527–537. doi: 10.1002/ps.6052

Liu, X., Liu, X., Li, Y., Yuan, J., and Li, H. (2021a). Predicting spray deposit distribution within a cotton plant canopy based on canopy stratification porosity and Gaussian process models. *Biosyst. Eng.* 204, 1–14. doi: 10.1016/j.biosystemseng.2020.12.018

Liu, X., Liu, X., Li, Y., Yuan, J., Song, L., Li, H., et al. (2020). Estimation model of canopy stratification porosity based on morphological characteristics: a case study of cotton. *Biosyst. Eng.* 193, 174–186. doi: 10.1016/j.biosystemseng.2020.02.018

Liu, X. M., Song, L. Q., Cui, H. Y., Liu, Y. C., Liu, X. H., and Wu, M. Q. (2021b). Decoupling on influence of air droplets stress and canopy porosity change on deposition performance in air-assisted spray. *Nongye Jixie Xuebao/Transactions Chin. Soc. Agric. Machinery* 52 (8), 117–126+137. doi: 10.6041/j.issn.1000-1298.2021.08.011

Loeffler, A. E., Gordon, A. M., and Gillespie, T. J. (1992). Optical porosity and windspeed reduction by coniferous windbreaks in Southern Ontario. *Agroforestry Syst.* 17 (2), 119–133. doi: 10.1007/BF00053117

Ma, L. F., and Li, L. Z. (2014). The topology optimization simulation study on the process of natural selection of leaf veins. *Chin. J. Appl. Mech.* 01), 132–136+12. doi: 10.11776/cjam.31.01.B027

Men, Y., Lai, Y., Dong, S., Du, X., and Liu, Y. (2017). Research on CO dispersion of a vehicular exhaust plume using Lattice Boltzmann Method and Large Eddy Simulation. *Transportation Res. Part D: Transport Environ.* 52, 202–214. doi: 10.1016/j.trd.2017.03.012

Miri, A., Dragovich, D., and Dong, Z. (2018). The response of live plants to airflow–Implication for reducing erosion. *Aeolian Res.* 33, 93–105. doi: 10.1016/j.aeolia.2018.06.002

Müller, M., Rakocevic, M., Caverzan, A., Boller, W., and Chavarria, G. (2018). Architectural characteristics and heliotropism may improve spray droplet deposition in the middle and low canopy layers in soybean. *Crop Sci.* 58 (5), 2029–2041. doi: 10.2135/cropsci2017.11.0653

Neinavaz, E., Skidmore, A. K., Darvishzadeh, R., and Groen, T. A. (2016). Retrieval of leaf area index in different plant species using thermal hyperspectral data. *ISPRS J. photogrammetry Remote Sens.* 119, 390–401. doi: 10.1016/j.isprsjprs.2016.07.001

Olesen, J. E., Jørgensen, L. N., Petersen, J., and Mortensen, J. V. (2003). Effects of rates and timing of nitrogen fertilizer on disease control by fungicides in winter wheat.

2. Crop growth and disease development. *J. Agric. Sci.* 140 (1), 15–29. doi: 10.1017/S0021859602002897

Panneton, B., and Piché, M. (2005). Interaction between application volume, airflow, and spray quality in air-assisted spraying. *Trans. ASAE* 48 (1), 37–44. doi: 10.13031/2013.17938

Qiu, W., Guo, H., Cao, Y., Li, X., Wu, J., Chen, Y., et al. (2022). An electrical vortex air-assisted spraying system for improving droplet deposition on rice. *Pest Manage. Sci.* 78 (10), 4037–4047. doi: 10.1002/ps.7023

Qu, Y., Meng, J., Wan, H., and Li, Y. (2016). Preliminary study on integrated wireless smart terminals for leaf area index measurement. *Comput. Electron. Agric.* 129, 56–65. doi: 10.1016/j.compag.2016.09.011

Ran, Z., and Xu, Y. (2009). Entropy and weak solutions in the thermal model for the compressible Euler equations. *Int. J. Modern Phys. C* 20 (10), 1493–1519. doi: 10.1142/S0129183109014369

Raupach, M. R., and Shaw, R. H. (1982). Averaging procedures for flow within vegetation canopies. *Boundary-layer meteorology* 22 (1), 79–90. doi: 10.1007/BF00128057

Reichard, D. L., Fox, R. D., Brazee, R. D., and Hall, F. R. (1979). Air velocities delivered by orchard air sprayers. *Trans. ASAE* 22 (1), 69–0074. doi: 10.13031/2013.34968

Tang, Q., Zhang, R. R., Chen, L. P., Li, L. L., and Xu, G. (2021). Research progress of key technologies and verification methods of numerical modeling for plant protection unmanned aerial vehicle application. *Smart Agric.* 3 (3), 1. doi: 10.12133/j.smartag.2021.3.3.202107-SA004

Tudi, M., Daniel Ruan, H., Wang, L., Lyu, J., Sadler, R., Connell, D., et al. (2021). Agriculture development, pesticide application and its impact on the environment. *Int. J. Environ. Res. Public Health* 18 (3), 1112. doi: 10.3390/ijerph18031112

Vollsinger, S., Mitchell, S. J., Byrne, K. E., Novak, M. D., and Rudnicki, M. (2005). Wind tunnel measurements of crown streamlining and drag relationships for several hardwood species. *Can. J. For. Res.* 35 (5), 1238–1249. doi: 10.1139/x05-051

Weickert, M., Teike, G., Schmidt, O., and Sommerfeld, M. (2010). Investigation of the LES WALE turbulence model within the lattice Boltzmann framework. *Comput. Mathematics Appl.* 59 (7), 2200–2214. doi: 10.1016/j.camwa.2009.08.060

Wilson, N. R., and Shaw, R. H. (1977). A higher order closure model for canopy flow. *J. Appl. Meteorology (1962-1982)* 16 (11), 1197–1205. doi: 10.1175/1520-0450(1977

Xun, L., Garcia-Ruiz, F., Fabregas, F. X., and Gil, E. (2022). Pesticide dose based on canopy characteristics in apple trees: Reducing environmental risk by reducing the amount of pesticide while maintaining pest and disease control efficacy. *Sci. Total Environ.* 826, 154204. doi: 10.1016/j.scitotenv.2022.154204

Zhang, H., Qi, L., Wan, J., Musiu, E. M., Zhou, J., Lu, Z., et al. (2022). Numerical simulation of downwash airflow distribution inside tree canopies of an apple orchard from a multirotor unmanned aerial vehicle (UAV) sprayer. *Comput. Electron. Agric.* 195, 106817. doi: 10.1016/j.compag.2022.106817

Zhang, H., Qi, L., Wu, Y., Musiu, E. M., Cheng, Z., and Wang, P. (2020). Numerical simulation of airflow field from a six–rotor plant protection drone using lattice Boltzmann method. *Biosyst. Eng.* 197, 336–351. doi: 10.1016/j.biosystemseng.2020.07.018

Zhang, B., Tang, Q., Chen, L. P., Zhang, R. R., and Xu, M. (2018). Numerical simulation of spray drift and deposition from a crop spraying aircraft using a CFD approach. *Biosyst. Eng.* 166, 184–199. doi: 10.1016/j.biosystemseng.2017.11.017

Zhu, Y., Guo, Q., Tang, Y., Zhu, X., He, Y., Huang, H., et al. (2022). CFD simulation and measurement of the downwash airflow of a quadrotor plant protection UAV during operation. *Comput. Electron. Agric.* 201, 107286. doi: 10.1016/j.compag.2022.107286

Zhu, J. J., Matsuzaki, T., and Gonda, Y. (2003). Optical stratification porosity as a measure of vertical canopy structure in a Japanese coastal forest. *For. Ecol. Manage.* 173 (1-3), 89–104. doi: 10.1016/S0378-1127(01)00813-1

frontiers | Frontiers in Plant Science

Check for updates

Study on the movement mechanism of rice stem under the action of canopy-opening device based on explicit dynamics simulation

Lin-long Jing, Xin-hua Wei*, Qi Song and Fei Wang

Key Laboratory of Modern Agricultural Equipment and Technology, Ministry of Education of the
People's Republic of China, Institute of Agricultural Engineering, Jiangsu University, Zhenjiang, China

The dense canopy of rice causes attenuation of droplet dispersion during
pesticide application. The canopy-opening device can increase droplet
deposition in the middle and lower canopy of rice by causing disturbance to
the rice canopy. However, the conditions for use of the canopy-opening device
are difficult to determine. Rice morphological structure parameters and material
parameters were measured to study the movement mechanism of the rice stems
under the action of the canopy-opening device, and the canopy-opening
process was then simulated using the explicit dynamic method. The simulation
scene of the rice canopy-opening process considered the combination of three
different heights and three different driving velocities of the canopy-opening
device. The movement mechanism of the rice stems under the operation of the
canopy-opening device was investigated, and the entire movement process was
separated into two stages: contact and oscillation. The simulation results and
high-speed photography experimental results show a strong correlation, with a
correlation coefficient of 0.733. The simulation results indicate that when the
canopy-opening device is closer to the ground and the driving velocity is higher,
the disturbance to the rice stem during the contact stage is stronger. However,
for the oscillation stage, there exists a critical value for both the height and driving
velocity of the canopy-opening device. During the oscillation stage, there is a
critical value for both the height and driving velocity of the canopy-opening
device. The numerical-based explicit dynamics approach was employed in this
work to investigate the rice canopy motion mechanism, and this study has a
definite reference value for the investigation of complicated motion mechanisms
in the field crop production process.

KEYWORDS

canopy-opening device, explicit dynamics, rice, motion mechanism, canopy deposition

1 Introduction

When spraying pesticides, the rice canopy structure has a great influence on the spread and retention of droplets (Farooq and Salyani, 2004; Da Silva et al., 2006; Gaskin et al., 2013). A dense canopy is formed in the middle and late stages of rice growth. The permeability of spraying in the rice canopy decreases as leaf density increases (Liu et al., 2021), as does spray uniformity (Xu et al., 2021). The effect of disease prevention and treatment on the middle and lower canopy of rice will be reduced. The main diseases and insect pests affecting rice growth during the middle and late stages are sheath blight, rice planthopper, and rice blast. These pests typically affect the middle and lower canopy of the rice plant and can cause significant damage to rice production throughout the year (Lee, 1983; Savary et al., 2000; Skamnioti and Gurr, 2009; Heong et al., 2016; Liu et al., 2016). To improve the effectiveness of rice plant protection operations, it is critical to optimize the spraying method. To improve droplet penetration, and raise droplet deposition quantity in the middle and lower canopy of rice.

The canopy-opening device is a device that can cause disturbance to the crop canopy. Usually composed of conduits or pipes installed in front of the spray arm, it has the characteristics of simple structure, high reliability, and minimal mechanical damage to plants. The canopy-opening device can effectively open the internal space of the crop canopy (Wu and Wei, 2019) and is not affected by the characteristics of the canopy (Prado et al., 2016), making it easier for droplets to reach the middle and lower layers of the canopy, improving the permeability and uniformity of droplets in the crop canopy (Wang et al., 2021).

The spatial position relationship between the canopy-opening device and the spray boom is shown in Supplementary Figure 1. The canopy-opening device (Supplementary Figure 1A) is typically mounted on the lower front of the spray boom. The hydraulic system controls the lifting and lowering of the canopy-opening device and the spray boom. The distance between the canopy-opening device and the spray boom can be adjusted in the vertical direction, ranging from 0 to 0.5 meters (Supplementary Figure 1B), and in the horizontal direction, ranging from 0 to 0.5 meters (Supplementary Figure 1C). Before spraying, the canopy-opening device is adjusted to be inside the rice canopy. As the sprayer advances, the canopy-opening device pushes the movement of the rice canopy, effectively opening up the internal space of the crop canopy (Wu and Wei, 2019), making it easier for droplets to reach the middle and lower layers of the canopy and solving the problem of branch and leaf shading.

The function of the canopy-opening device can greatly enhance droplet penetration and uniformity in the crop canopy (Wang et al., 2021). It can improve droplet deposition rate by 8.6~18.0% for varied nozzles (Womac et al., 2022). However, determining the position of the canopy-opening device is challenging. If the location is too high, it is difficult to open the rice canopy; if it is too low, the rice will be harmed. There are several elements that influence canopy-opening effect, however the influence rule of each component on canopy-opening effect is unclear.

Zhu et al. established a mathematical model according to the physical characteristics of soybean plants to determine the best position of the canopy-opening device (Zhu et al., 2008). It should be noted that in this study, only greenhouse soybean was utilized as the research object, and only the location of the canopy-opening device was investigated. According to the characteristics of rice plants, Wu and Wei analyzed the canopy-opening process through transient dynamic simulation and investigated the mathematical relationship between time and displacement at different canopy-opening device positions (Wu and Wei, 2019). The influence of driving velocity on the canopy's motion mechanism, on the other hand, had not been studied. Most of these studies had been conducted under considerations of static or quasi-static loading cases, small strain deformation, short time, small displacement, and linear contact assumptions through implicit solvers (Celik, 2017).

In solving dynamic problems, explicit finite element method (FEM) and implicit FEM are commonly used. The explicit method is essentially an incremental method used to determine the dynamic response of the structure (Celik, 2017). One advantage of the explicit process over the implicit process is that it is easier to solve complex contact problems, without iteration and convergence issues, and as the model size increases, the explicit method is more cost-effective than the implicit method. Rice canopy-opening process is a long-time (>1s), low-velocity and large displacement dynamic and complex contact process. In this context, the explicit solution approach has been pointed out to be valuable in solving loading cases such as dynamic contact events (Wakabayashi et al., 2008; SolidWorks Doc., 2010; Lee, 2012; Wu and Gu, 2012; ANSYS Doc., 2016). As a result, displacement caused by the rice canopy-opening process can be considered a nonlinear dynamics application covered by the aforementioned explicit dynamics system, and the use of explicit dynamic simulation can well reveal the kinematic characteristics of stamping, collision, drop, etc.

The contribution of this study is to simulate the process of rice canopy-opening through the explicit dynamic simulation method, and to study the movement mechanism of the rice canopy under the action of the canopy-opening device. Rice morphological structure parameters and material parameters were measured, and a relationship model was established between the position and driving velocity of the canopy-opening device and the maximum displacement of the canopy-opening process in this study. The relationship model was tested by high-speed photography. It may be used as a reference point for simulations of different crops as well as the optimization of canopy-opening device, installation location, sinking position, and driving velocity. Provided an optimization idea for improving the droplet permeability in dense crop canopy.

2 Materials and methods

Select 300 disease- and insect-free rice plants at the heading stage on the RunGuo Agricultural Base in Zhenjiang City in Jiangsu Province (32°54′19′′N, 116°23′28′′E) on Sep 6, 2021. The rice varieties studied were 'Longliangyou 2010' (Supplementary

Figure 2). The row spacing of rice plants was 18 cm and the plant spacing per row was 10 cm. The temperature was 26.27°C, the humidity was 75.38%. The collected rice was used for the measurement of rice morphological structure parameters and material parameters, and the relevant detection measurements were completed within 24 hours.

2.1 The simulation model of rice canopy-opening process

Rice morphological structure parameters and material parameters were used as the basis for explicit dynamics simulation. All measurements and tests of morphological structure parameters and material parameters were carried out at the physical property analysis laboratory of the Agricultural Engineering Institute (Jiangsu University, Zhenjiang, China). The morphological structure parameters of the canopy-opening device and rice were taken for modelling the canopy-opening device and rice geometry as the first step. A simulation model of the rice canopy process was created using the material parameters and geometric models of the rice plant and the canopy-opening device. The simulation model of the rice canopy-opening process was simulated after modeling. The simulation results were post-processed, and the movement mechanism of the rice canopy was analyzed.

2.1.1 Measurement of morphological structure parameters

To establish a geometry structure model of rice and canopy-opening device, the morphological structure parameters of rice plants and canopy-opening device must be determined experimentally. The parameters (plant height, number of leaves, leaf area, leaf width, stem length, stem diameter, stem wall thickness) of rice plants were measured (Figure 1) (Shu and Wei, 2019). To simplify the rice structure, the stem and leaves are considered primarily. Rice morphological structural parameters were measured and averaged using 100 selected rice plants.

Some measurements of morphological structure parameters on the whole rice plant and the test results are shown in Supplementary Table 1. The geometric model and morphological parameters of canopy-opening device are shown in the Figure 2.

2.1.2 Measurement of rice material parameters

The three-point bending test method (Figure 3A) was adopted for the measurement of the elastic modulus of rice stems (Kokubo et al., 1989; Crook and Ennos, 1994). This method is based on the bending theory of the beam to measure the elastic modulus and indirectly calculates the elastic modulus by measuring the force-displace (Timoshenko and Gere, 1973). An SMS Texture Analyzer (TA.XT PlusC., Godalming, UK) was used for measurement. Remove blades from petioles and nodes before treatment. The elastic modulus of rice stem were measured and averaged using
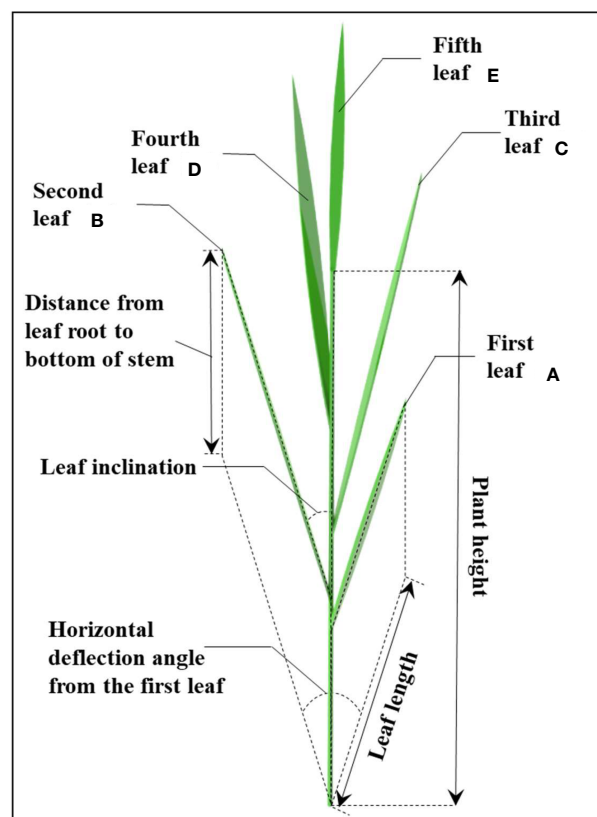

FIGURE 1
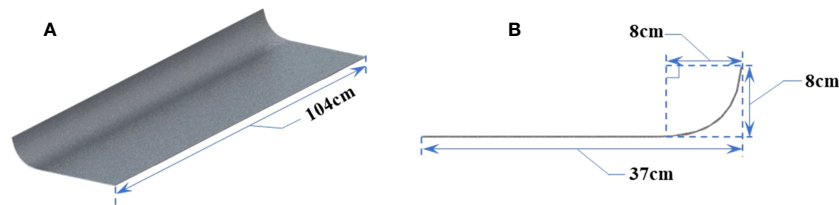The geometric relation and spatial distribution of rice stem and leaves.

FIGURE 2
The geometric model and morphological parameters of canopy-opening device. **(A)** Oblique view, **(B)** Side view.

100 selected rice plants (Figure 4B). The experimental design of the three-point bending method to measure the elastic modulus of rice is shown in Figure 4A. The setting parameters of SMS texture analyzer are shown in the Figure 4C.

The deformation characteristics of the rice stem specimen under quasistatic compressive stress were revealed by three-point bending tests (Figure 3). Under this compressive loading, the stem specimen displayed almost linear deformation behavior up to an initial bio-yield point. Beyond this point, permanent (plastic) deformation was observed and then the stem specimen collapsed. It is estimated that the force of the canopy-opening device on the rice stem cannot reach the bio-yield point of the rice material. So,

the deformation of the rice in this process was simplified to elastic deformation. Therefore, it was only necessary to calculate the elastic modulus of the rice stem in this process, which represents the elastic modulus of the rice stem.

The calculation formula for elastic modulus E is shown in Formula (1):

$$E = \frac{PL^3}{48YI} \qquad (1)$$

where E is the modulus of elasticity, measured in N m^{-2}; P is the magnitude of the bending force, measured in N; L represents the length of the test sample, measured in mm; Y represents the size of
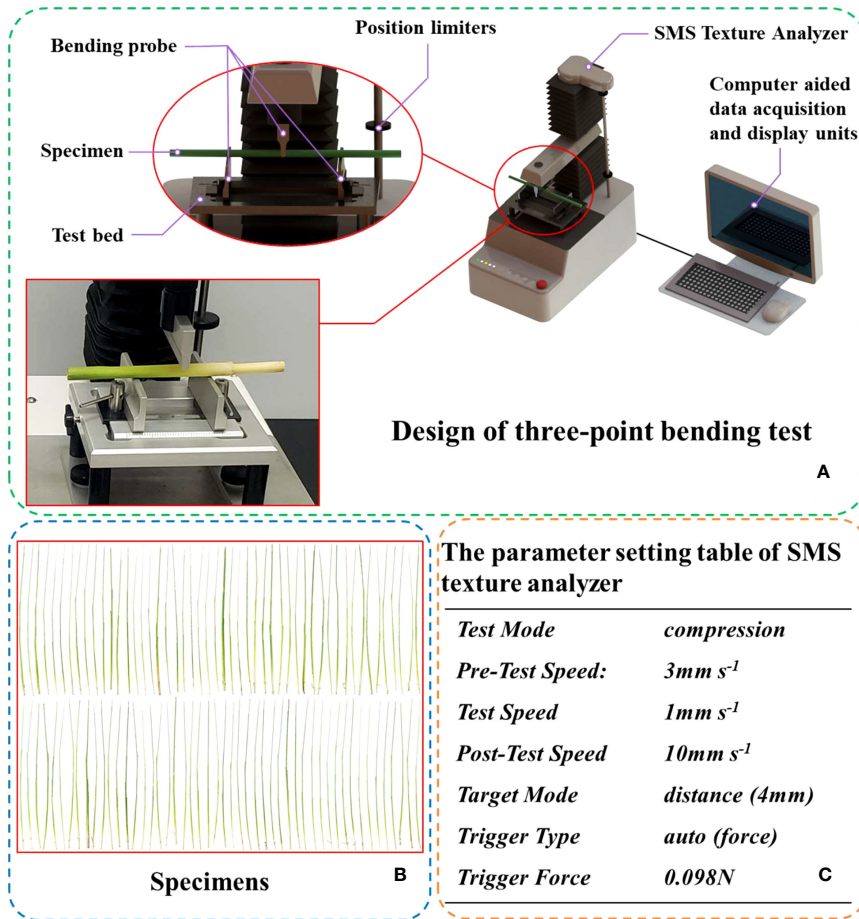

FIGURE 3
The set-up for the three-point bending test. **(A)** Design of three-point bending test, **(B)** All specimens used in the measurement of rice elastic modulus, **(C)** The parameter setting table of SMS texture analyzer.
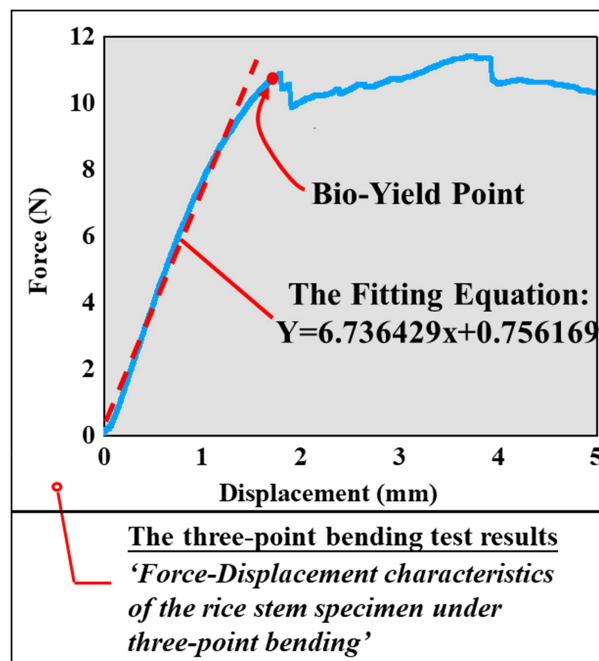
FIGURE 4
The force-displacement characteristics of the single rice stem specimen.

the bending deflection, measured in mm; and I is expressed as the magnitude of the moment of inertia of the section, measured in mm^4.

The formula for calculating the moment of inertia of the section is shown in Formula (2).

$$I = \frac{\pi}{4}\left[ab^3 - (a-t)\cdot(b-t)^3\right]$$ (2)

In formula (2), a represents the long half-axis of the cross-section in millimeters (mm), while b represents the short half-axis of the cross-section, in mm. t represents the average wall thickness of the rice stem in mm.

The above formula (1) can be transformed into:

$$E = \frac{1}{48}\cdot\frac{P}{Y}\cdot\frac{L^3}{I}$$ (3)

Figure 3 displays the force-displacement curve of a rice stem collected using an SMS texture analyzer. Blue line before biological yield point represents the elastic deformation section of the rice stem. A straight-line fitting was performed on this section, as illustrated by the white line in the figure. The fitting equation, Y=6.736429x+0.756169, yielded a slope of k=6.736429, which corresponds to $\frac{P}{Y}$ in formula (3). The calculation parameters a, b, t, and L were obtained through experiments. By combining Formula (2) and Formula (3), the elastic modulus of each rice stem was calculated.

Tensile tests and electrical measurements were used to conduct Poisson's ratio test studies on rice stems. The axial strain of the surface of the test piece was measured by the tensile test, and the

transverse strain of the surface of the test piece was simultaneously measured by the electrical measurement, to measure the Poisson's ratio of the rice stem specimen (Figure 5A). Tensile tests were performed on an SMS texture analyzer. When preparing the rice stem specimen, the specimen should be straight, the two ends should be smoothed with sandpaper, and the two ends must be kept flush. The Poisson's ratio of rice stem were measured and averaged using 100 selected rice plants. The size of the prepared specimen should be measured separately to reduce the error. Both ends of the specimen were wrapped with soft elastic rubber to reduce the damage of the fixture to the specimen (Figure 5A). Tension was applied to the specimen at a loading rate of 2 mm s^{-1}. Tension and displacement changes were measured by a texture analyzer, and force-displacement-time records were obtained before specimen failure.

Electrical measurement is one of the methods commonly used in stress analysis experiments in engineering. The resistance strain gauge was attached to the measured point in the middle of the rice stem sample using a strong cyanoacrylate adhesive. The strain value generated while the rice stem specimen was subjected to the tensile test was converted into the resistance change of the strain gauge, and then the resistance variable of the strain gauge was measured by the strain analyzer, and the transverse strain value of the rice stem was directly converted and output (Figure 5B). The parameters of the strain gage used in this test are shown in Supplementary Table 2.

The calculation formula of Poisson's ratio is shown in formula (4).

$$\varepsilon = \left|\frac{\varepsilon_p{}'}{\varepsilon_p}\right|$$ (4)

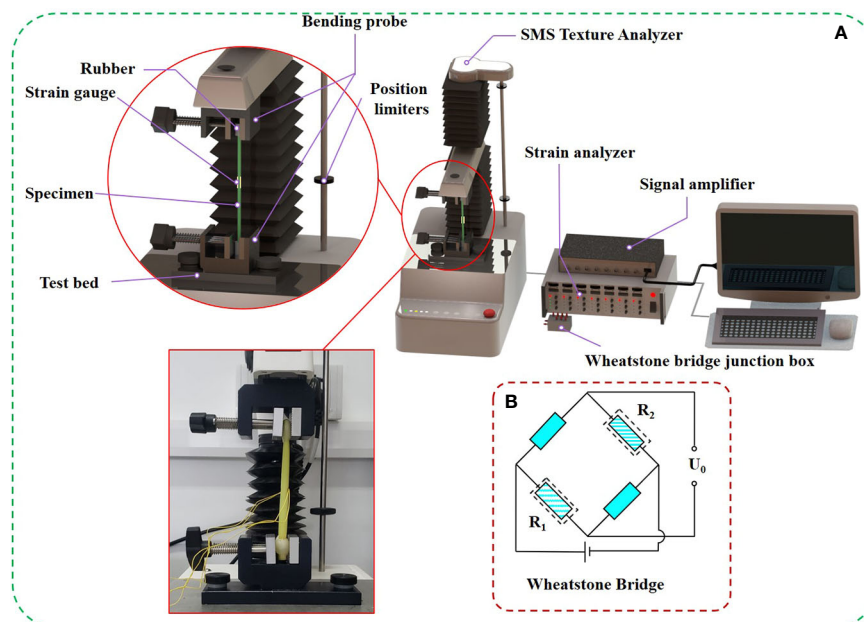**FIGURE 5**
Measurement of poisson's ratio in rice. **(A)** The set-up for the tensile and electrometric method testing, **(B)** The principle of electrical measurement.

In Equation (4), ε is Poisson's ratio; ε_p is the axial strain; ε_p' is the transverse strain.

2.2 Simulation condition and parameter setting

In this study, a 3D model of rice canopy-opening dynamics was established by using SolidWorks software (SolidWorks 2019, Dassault Systems SolidWorks Corporation, USA). Each rice plant is assigned a random rotation angle to obtain the spatial position of the rice leaves in the population (Figure 6). The mesh of the model was divided by HyperMesh software (HyperMesh 10, Altair Engineering, Inc., Troy, MI). Using HyperMesh software, the material characteristics of the rice and canopy-opening devices in Table 1 were established in their respective geometric models. Simultaneously, HyperMesh was utilized to pre-process the model of the rice canopy-opening process, including limitations, contact, speed, and so on. The process of rice canopy-opening was numerically simulated by LS-DYNA software (LS-DYNA 11.0, Livermore Software Technology Corporation, Livermore, CA, United States). LS-DYNA software was used as a dynamic analysis and was considered for the canopy-opening process simulation due to its capability of analyzing complex contacts and large dynamic deformations.

According to the basic principles of the finite element method, a 3D geometric model was meshed to develop a finite element model (Figure 6). The model includes eight rice plants (two clusters) and a canopy-opening device. To obtain more accurate numerical simulation results, shell mesh unit was used to preliminary divide the mesh (Figure 6). The rice leaves and the connection of leaves and stems were meshed sub-dividing, which are shown in Figures 6. After the sub-division was completed, the total finite element model had

31518 units and 33780 nodes. In HyperMesh, set the simulation time to 3 seconds, and make the rice stem's bottom a fixed restriction. Contact is the sort of contact interaction attribute specified for two surfaces in HyperMesh, and hard contact is the usual behavior for this interaction.

To analyze the movement mechanism of the rice canopy, combinations of various canopy-opening heights and driving velocities were simulated through explicit dynamics simulation. Specifically, nine simulation combinations were created, consisting of three different heights of the canopy-opening device from the ground (0.5, 0.6, 0.7 m) and three different driving velocities (0.8, 1.2, 1.6 m/s). Explicit time integration typically requires smaller time steps than implicit time integration. Therefore, the LS-DYNA software's explicit dynamics module was used to simulate these combinations. Result analysis was performed using LS-PrePost 4.5 (Livermore Software Technology Corporation, USA).

To conduct a numerical simulation of the rice canopy opening process, the HyperMesh software was used for pre-processing in this study. The rice plants were modeled as non-rigid bodies, while the canopy-opening device was modeled as a rigid body. To simulate the contact process, the automatic general contact type was selected. Subsequently, the LS-DYNA software was used to perform the numerical simulation of the rice canopy opening process. An explicit time integration method was used in the simulation process, with a smaller time step selected to obtain more accurate results. For the boundary conditions, the bottom of the rice stem was fixed with respect to rotation and transition in all directions, while the canopy-opening device was only allowed to translate along the X positive half-axis direction.

In the HyperMesh software, the MATL3 element type was used to model the rice plants. The rice plants were modeled as linear viscoelastic tissue. The canopy-opening device, which was folded from a
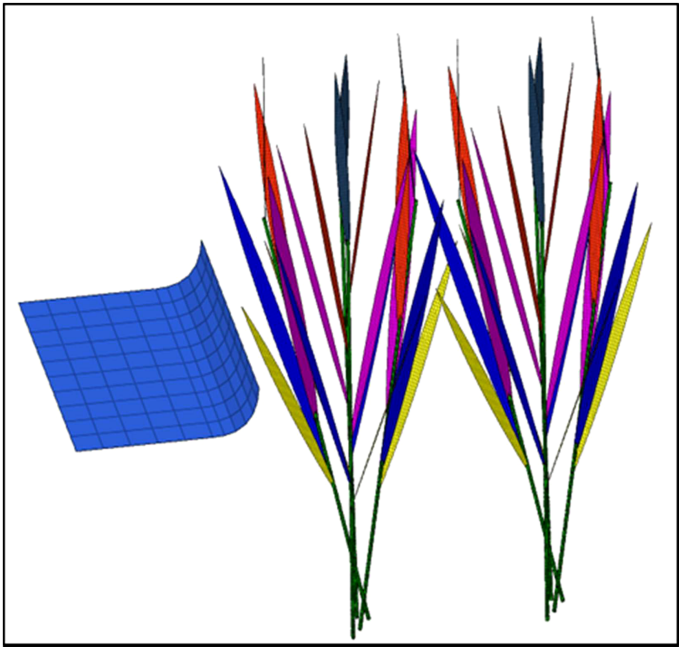
FIGURE 6
The canopy-opening 3D model and mesh generation.

TABLE 1 Material properties of the rice and the canopy-opening device used in the simulation.

Material properties used in FEM-based simulation			
Materials	Modulus of elasticity (MPa)	Poisson's ratio	Density (kg m^{-3})
Crop			
Rice (Longliangyou 2010)	158.8218	0.32	1815.69
The canopy-opening device			
Stainless steel	193000	0.310	7750

1000×500×2.6 mm steel plate, was modeled using the MATL20 element type with an elastic modulus of 193000 MPa and a density of 7750 kg m^{-3}. To account for the non-rigid characteristics of rice plants, shell elements were used to model the rice plant in HyperMesh, with a mesh size of 0.001mm for element size and a mixed mesh type of triangular and quadrilateral elements. The final rice plant model consisted of 33648 nodes and 31408 elements. Similarly, shell elements were used to model the canopy-opening device, with an element size of 0.1 and 0.2 mm and quadrilateral elements used to generate a mesh consisting of 132 nodes and 110 elements.

2.3 Assessment verification

The high-speed camera (i-speed716, ix-cameras Company, Woburn, MA, USA) at maximum frame rate of 500,000 fps was utilized to track the movement trajectory of the rice stem under the action of the canopy-opening device in the real scene to evaluate the validity of the simulation results. Similarly, to the simulation combination, 9 actual combination situations were seted, and

three distinct driving velocities (0.8, 1.2, 1.6 m s^{-1}) of the canopy-opening device and different heights of the canopy-opening device from the ground (0.5, 0.6, 0.7 m) were examined. Each combination was repeated three times. Using ProAnalyst software (version 1.5.6.8, Xcitex Company, Woburn, MA, USA) to extract the three-dimensional coordinate motion trajectory of the rice canopy, and compared with the simulation results.

3 Result and discussion

3.1 Analysis of simulation results

The model for the rice canopy-opening process was created in Hypermesh software and simulated using LS-DYNA software. A video recording of the rice canopy-opening process was also made. As an example of the simulation, the seven frames representing the canopy-opening process were taken from the video in chronological order and arranged according to the timeline, and divide the canopy-opening process into three stages, as shown Figure 7. In

the first stage, the canopy-opening device has not been in contact with the rice, and the rice is in a static state. At this time, the upper canopy of the rice is relatively dense, and there is no obvious gap between the two clusters of rice (Figure 7A). In the second stage, the canopy-opening device moves to the right at a certain speed and begins to come into contact the rice, and the rice stems bend toward the forward direction of the canopy-opening device under the action of the canopy-opening device (Figure 7B). When the canopy-opening device entirely leaves the first cluster of rice, it begins to rebound in the opposite direction of the canopy-opening device's forward motion (Figure 7C). Because of the varied positions, the rice stems that first encountered the canopy-opening device rebounded earlier than those that came later. A gap emerged in the canopy of the first cluster of rice at this time (Figure 7D). In the third stage, the canopy-opening device completely leaves the rice (Figure 7E). The first cluster of rice has rebounded in the opposite direction to the forward direction of the canopy-opening device (Figure 7F), the second cluster of rice is about to start to rebound, and there is a large gap between the two clusters of rice (Figure 7G).

In the explicit dynamics simulation of the canopy-opening process, not only the contact process between the canopy-opening device and the rice stem, but also the rebound oscillation motion process of the rice stem after the canopy-opening device leaves were also considered.

To analyze the simulation results of the rice canopy opening process, the process was divided into two stages: the contact stage and the oscillation stage. The stage in which the canopy-opening device makes contact with the rice stem was defined as the contact stage, while the stage in which the rice stem rebounds and oscillates after the device leaves was defined as the oscillation stage. It can be seen from Figure 8 that when the canopy-opening device starts to contact with the rice stem, the rice stem is displaced by force, and reaches the maximum displacement in the contact stage when it leaves the canopy-opening device. As the canopy-opening device moved away from the rice stem, the rice stem began to rebound and entered the oscillation stage, and the displacement and the amplitude of the oscillation gradually decreased.

As shown in Figures 9–11, the fluctuation of rice stem displacement with time while keeping the same height of the canopy-opening device and increasing the velocity of the canopy-opening device. When the height of the canopy-opening device is 0.5m and its velocity is 0.8m/s, the rice stems experience its maximum displacement roughly one second after coming into contact with the canopy-opening device (Figure 9). The faster the velocity of the canopy-opening device, the sooner the rice stems will reach the maximum displacement in the contact stage. This conclusion is also applicable when the canopy-opening device height is 0.6 m and 0.7 m (Figures 10, 11). Furthermore, when the driving velocity of the canopy-opening device increases, the oscillation amplitude of the rice stems increases and the oscillation period decreases.

Figure 12 shows that the highest displacement of the contact stage between the rice stems and the canopy-opening device may be created when the deriving velocity of the canopy-opening device was 1.6 m s^{-1}. From Figure 12, it can be concluded that, when the deriving velocity of the canopy-opening device is constant, the maximum displacement of the rice stem during the contact stage decreases as the height of the canopy-opening device above the ground increases. This is because the lower the height of the canopy-opening device above the ground, the greater the bending
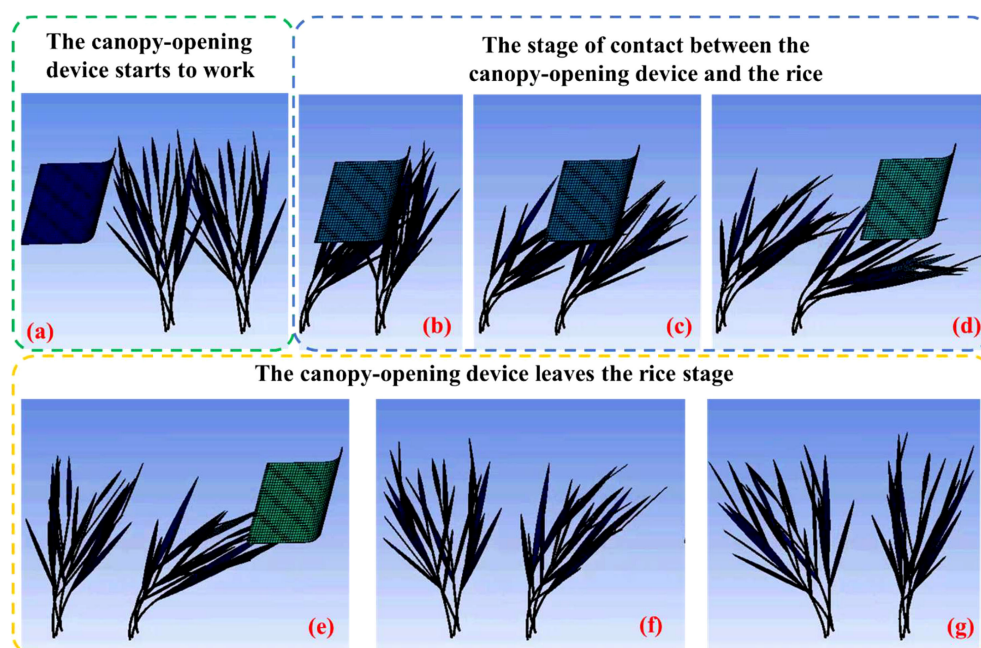

FIGURE 7
Simulation of a rice canopy-opening process. **(A)** The canopy-opening device starts to work, **(B-D)** The stage of contact between the canopy-opening device and the rice, **(E-G)** The canopy-opening device leaves the rice stage.
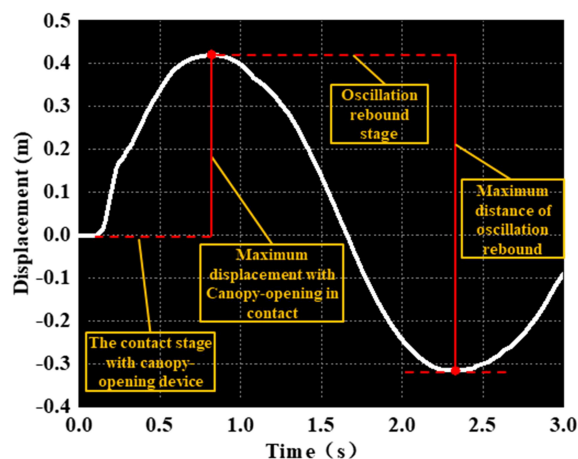
FIGURE 8
Schematic diagram of the characteristics of the canopy-opening process.

of the rice stem, and the larger the displacement. If the device continues to lower and the height above the ground decreases further, the displacement may increase, but the canopy-opening device may also damage the rice stem. When the canopy-opening device was 0.7 m above the ground, it is positioned in the upper portion of the rice canopy, and the contact and action time between the canopy-opening device and the rice stem was short, a considerable displacement could not be obtained.

When the height of the canopy-opening device above the ground is constant, the overall trend of the maximum
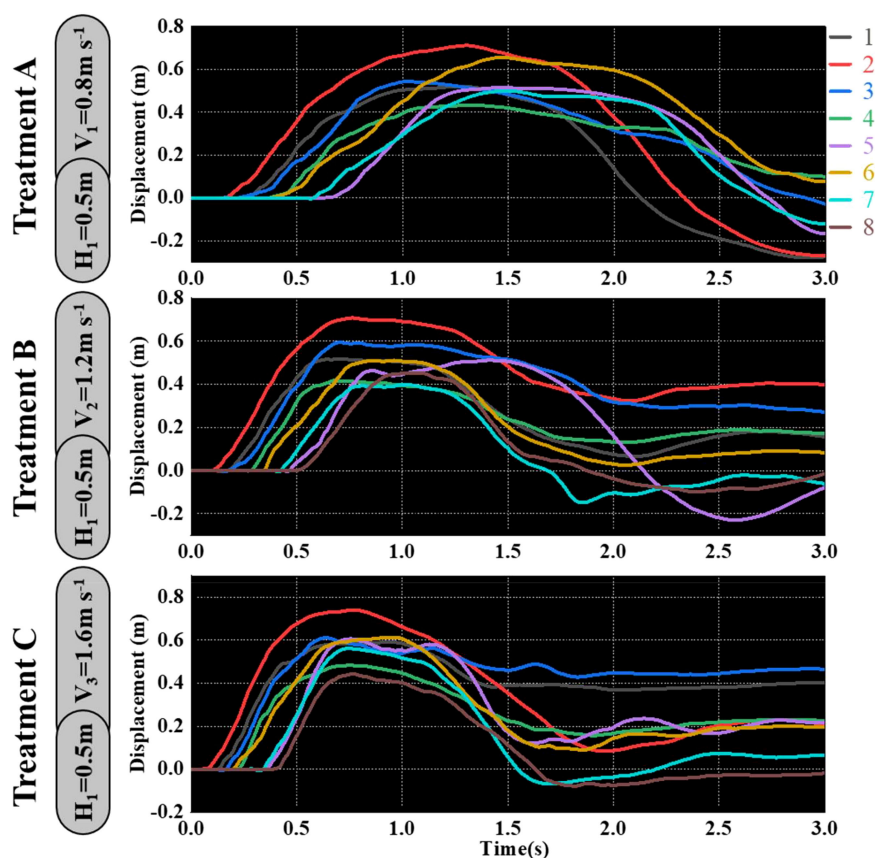
FIGURE 9
When the canopy-opening device is 0.5m above the ground, the relationship between time and displacement of rice stems without the effect of velocity. (1) 1~8 are rice plants in different positions.
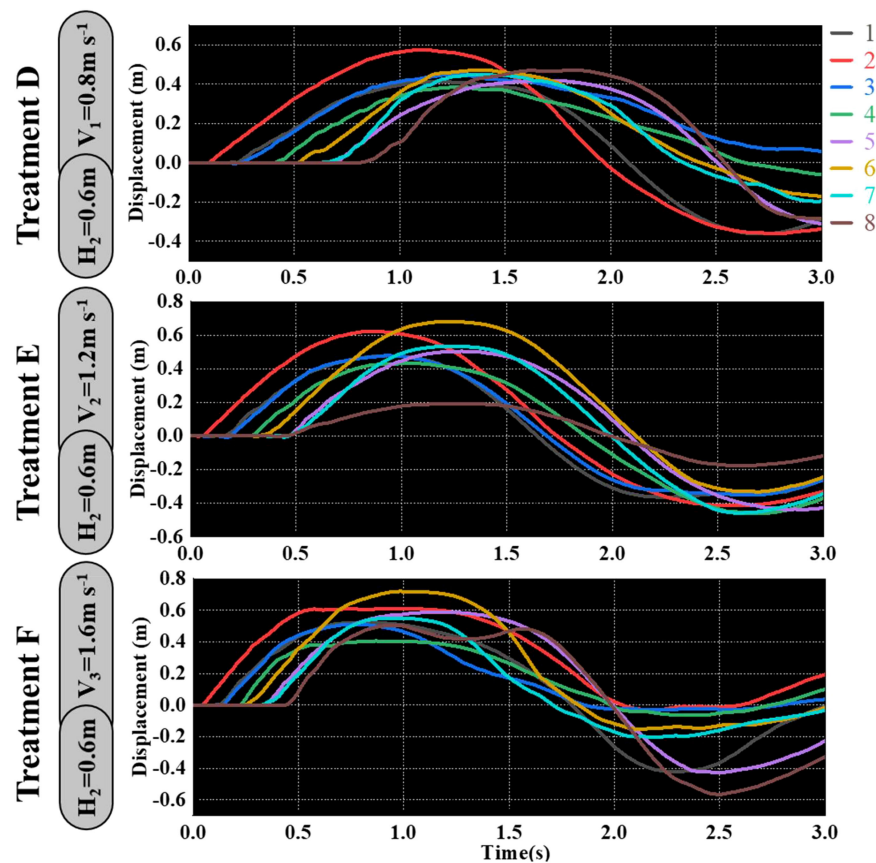
FIGURE 10
When the canopy-opening device is 0.6m above the ground, the relationship between time and displacement of rice stems without the effect of velocity.

displacement of the rice stem during the contact stage increases as the deriving velocity increases. It is obvious that reducing the deriving velocity will decrease the impact energy of the canopy-opening device on the rice stem. However, when the canopy-opening device is 0.5m above the ground, the rice stem shows a trend of first decreasing and then increasing in the oscillation stage as the deriving velocity increases.

Figure 13 shows the maximum displacement of rice stem during the oscillation stage under different treatments and the maximum displacement of rice stem measured by high-speed photography experiments. It can be seen that when the canopy-opening device is 0.6m above the ground and the deriving velocity of the canopy-opening device is 1.2m s^{-1} (Treatment E), the maximum displacement of rice stem is the largest, approximately 1.04m.

Under the same deriving velocity of the canopy-opening device, the maximum displacement of rice stem generated by oscillation stage first increases and then decreases with the increase of the height of the canopy-opening device. When the height is 0.6m, the maximum displacement is greater than that of other heights. At the same height, increasing the deriving velocity of the canopy-opening device cannot obtain a better maximum displacement of rice stem. On the contrary, when the height of the canopy-opening device is 0.5m and 0.7m, the maximum displacement of rice stem

generated by the canopy-opening device decreases with the increase of deriving velocity. When the height of the canopy-opening device is 0.6m, the maximum displacement of rice stem generated by the canopy-opening device increases first and then decreases with the increase of deriving velocity, reaching the maximum value at the deriving velocity of 1.2m s^{-1}.

Figure 14 provides the trend of the total energy of rice canopy model under different treatments. It can be seen from the Figure 14 that the total energy of the model increases first and then decreases with the increase of time; under the same height of the canopy-opening device, the larger the deriving velocity, the higher the total energy of the model; the larger the deriving velocity, the earlier the model reaches the maximum total energy; under the same deriving velocity, the higher the height, the lower the total energy of the model. However, due to the interaction between the canopy-opening device and rice stem during the oscillation stage, the total energy of the model decays rapidly after reaching the maximum value when the deriving velocity is high. It can be seen from Figure 14 that under Treatment E, the total energy of the model decays slower after reaching the maximum value. Therefore, when the canopy-opening device is 0.6m above the ground and the deriving velocity is 1.2m s^{-1}, the interference intensity on rice stem during the oscillation stage is the highest, and a larger canopy gap can be obtained.
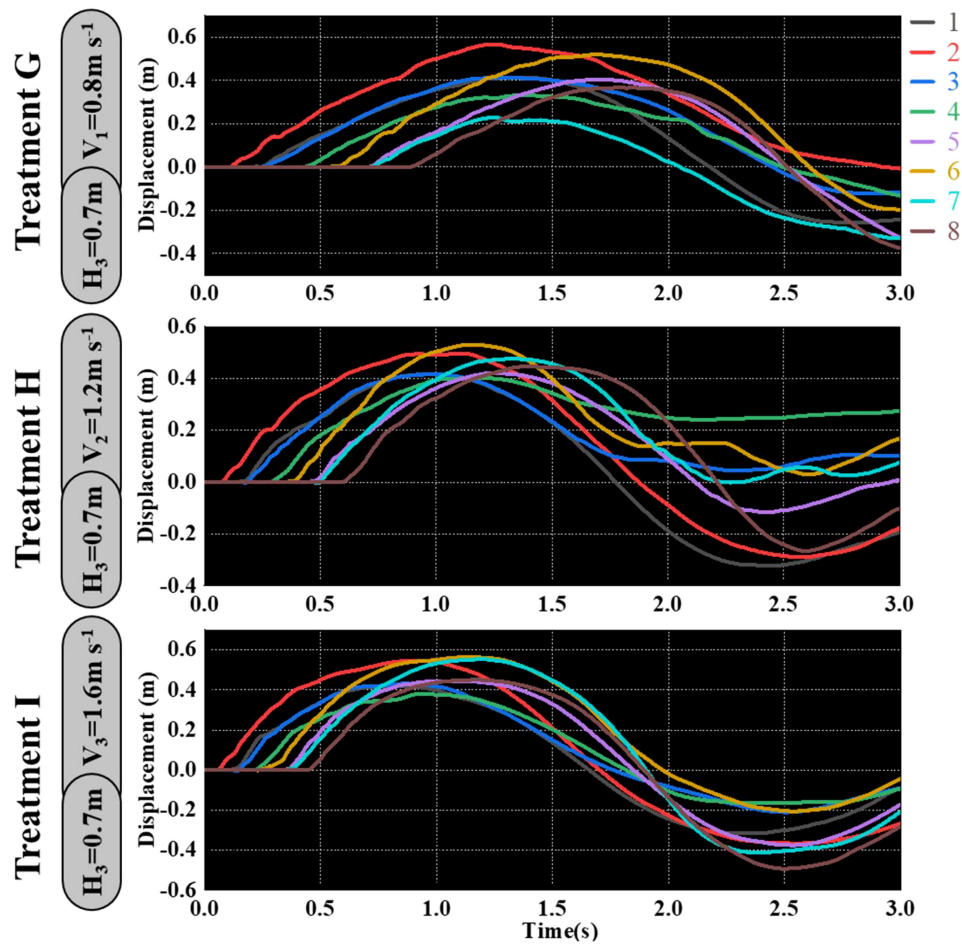
FIGURE 11
When the canopy-opening device is 0.7m above the ground, the relationship between time and displacement of rice stems without the effect of velocity.
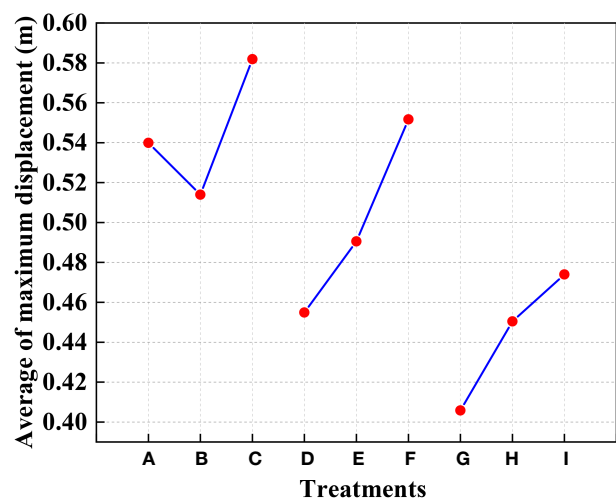

FIGURE 12
The average of the maximum displacement of rice stems under different treatments in the contact stage. (1) **(A-I)** are different experimental treatments in Figures 9−11.
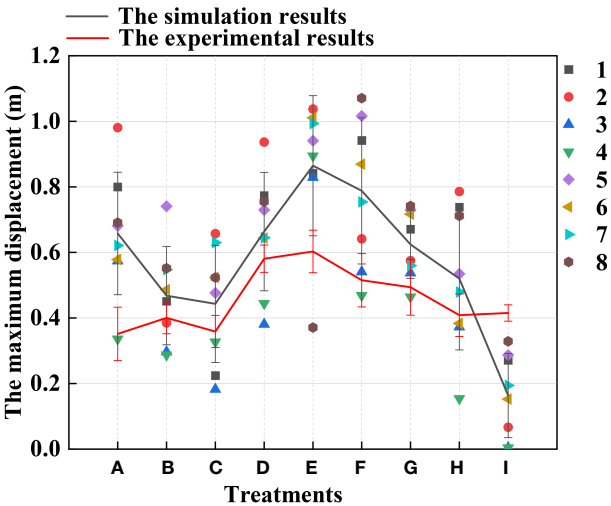
FIGURE 13
Comparison of the difference between the experimental results and the simulation results in the oscillation stage. (1) The point in the Figure is the maximum displacement of the rice stems in the oscillation stage under the simulation result.
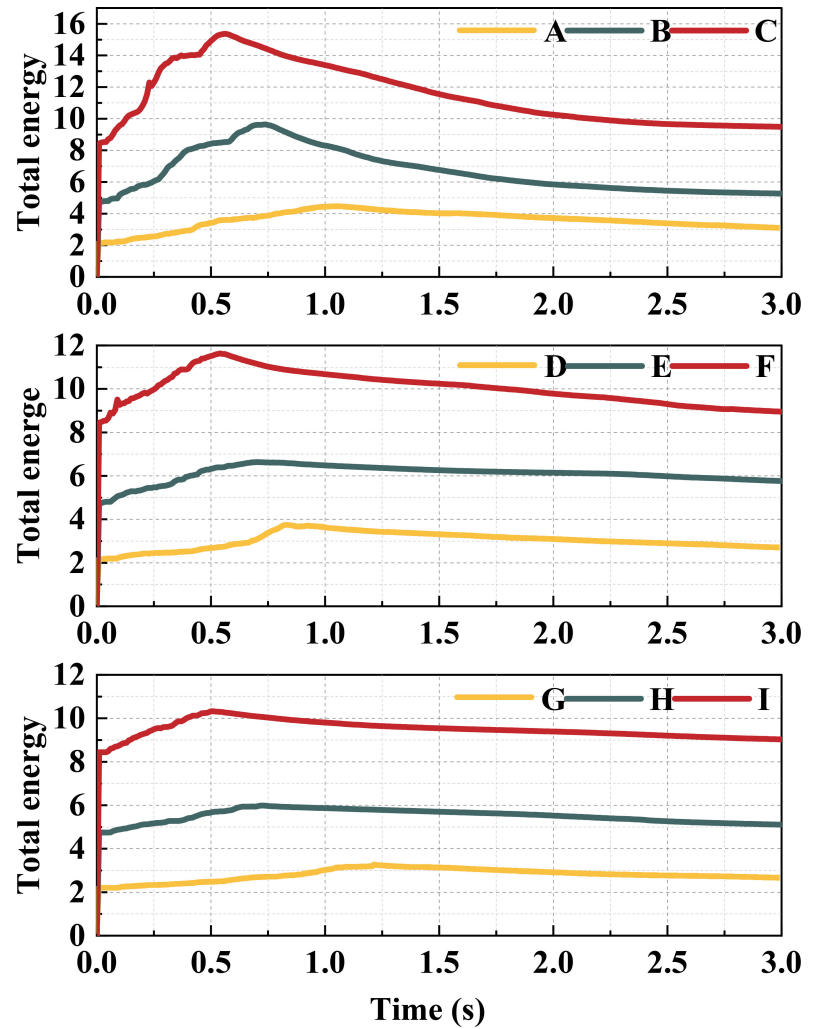

FIGURE 14
The total energy of canopy opening model under different treatments.

3.2 Comparison of test results and simulations

Simulation results were verified by high-speed testing. The movement of rice plants due to the action of the canopy-opening was recorded using high-speed photography (Figure 15). Calibrate the movement track of the rice stem by the length of the known black and white area in the calibration group. According to the track plots of rice plants, the average value of the maximum displacement of the rice stems after being acted by the canopy-opening device was calculated.

When the canopy-opening device leaves rice plants, rice plants exhibited a rebound-oscillation movement due to its elasticity. Figure 13 shows the average value of the greatest displacement of rice stems in the simulation results and experimental results during the oscillation stage. Figure 16 compares the simulated and measured values during the oscillation stage when the height of the canopy-opening device from the ground was 0.5 m. Figures 17, 18 show similar comparisons when the height of the canopy-opening device from the ground was 0.6 m and 0.7 m respectively. It showed that the relative difference between the simulation data and the test data was

consistent. Because the field test was affected by too many uncontrollable factors (such as wind force, and wind direction), the occlusion of blades also affects the test data. Therefore, there are large fluctuations in the test data. However, values similar to the measured values can still be found in the simulation values. Comparison of the maximum displacement of rice stem in the oscillation stage between high-speed photography experiment results and simulation results (Figure 13) and the errors shown in Table 2, the minimum and maximum errors in predicting the maximum displacement in the oscillation stage are 12.12% and -162.50%, respectively. The error caused under Treatment I is the largest, which may be due to the unstable relative height between the canopy-opening device and the rice under field conditions, resulting in a larger maximum displacement of the rice stems in the oscillation stage. If we exclude the extreme condition of Treatment I (with the deriving velocity and high height of the canopy-opening device), the correlation coefficient between the simulation results and the high-speed photography experiment results is 0.733, indicating a good correlation between the simulation results and the high-speed photography experiment results.
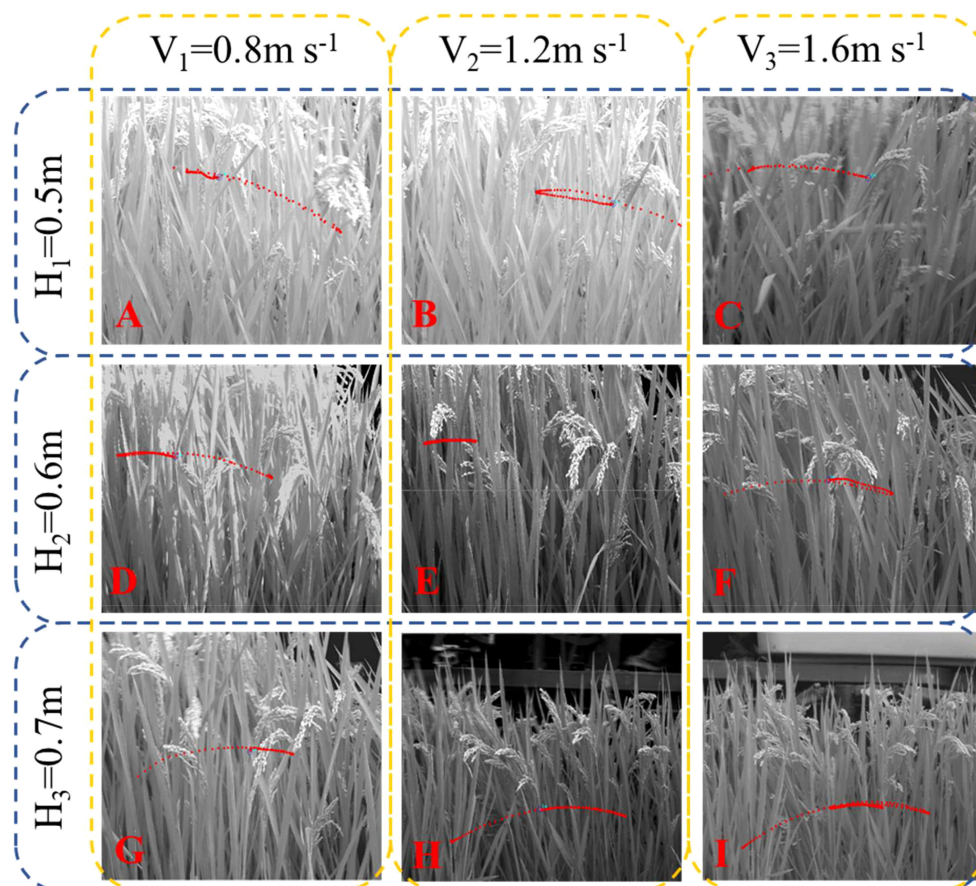

FIGURE 15
Maximum displacement of rice stems during oscillation stage captured by high-speed photography.
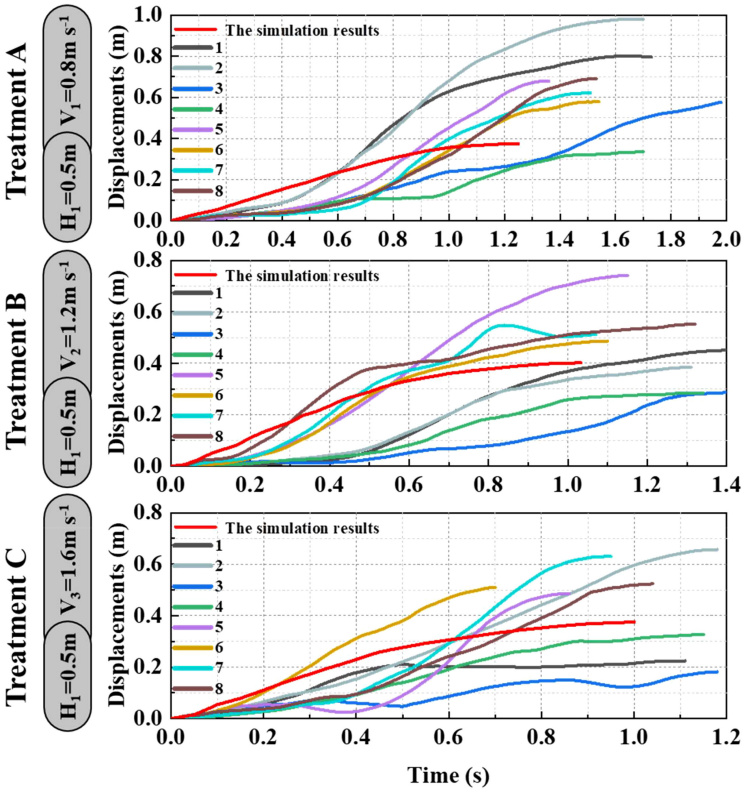
FIGURE 16
The simulation and experimental results during the oscillation stage when the height of the canopy-opening device from the ground was 0.5 m. (1) 1~8 are rice plants in different positions.
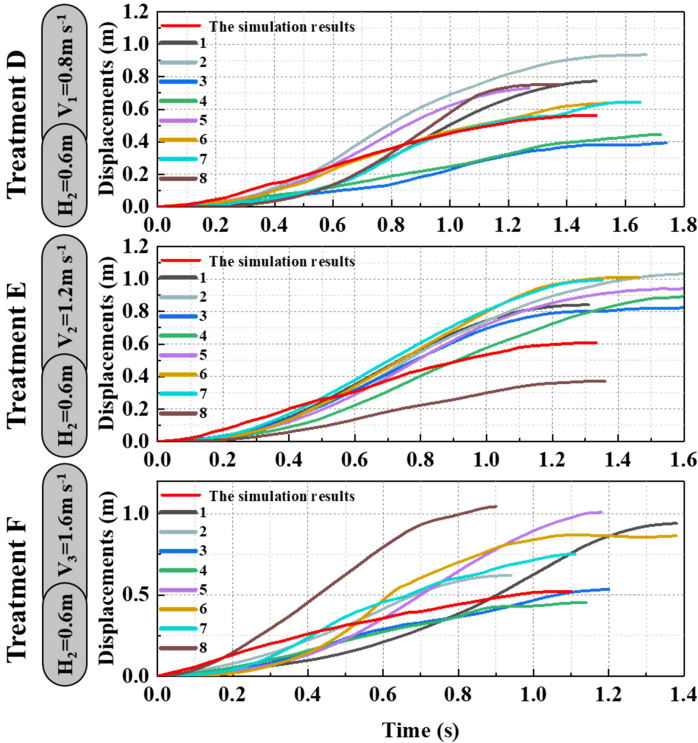

FIGURE 17
The simulation and experimental results during the oscillation stage when the height of the canopy-opening device from the ground was 0.6 m.
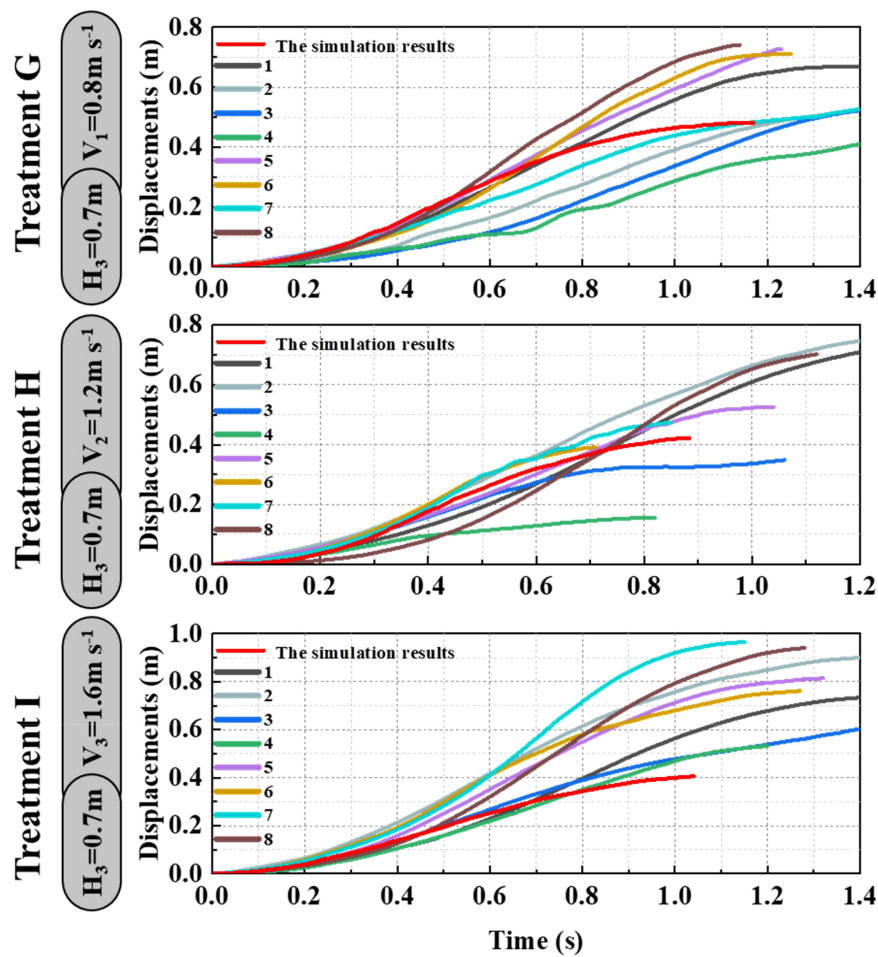
FIGURE 18
The simulation and experimental results during the oscillation stage when the height of the canopy-opening device from the ground was 0.7 m.

TABLE 2 The results of rice canopy opening in the oscillation stage.

Treatments	Average of maximum displacement in oscillation stage (m)		
	Simulation	Experimental	Error (%)
A	0.66	0.35	46.97
B	0.47	0.40	14.89
C	0.44	0.36	18.18
D	0.66	0.58	12.12
E	0.86	0.60	30.23
F	0.79	0.52	34.18
G	0.62	0.49	20.97
H	0.52	0.41	21.15
I	0.16	0.42	-162.50

4 Conclusion

The main purpose of this study is to simulate the rice canopy opening process using an explicit dynamic method and investigate its disturbance mechanism. The morphological and material parameters of rice were measured, and the simulation model of the rice canopy opening process was established. The canopy opening process was simulated using an explicit dynamic method. When analyzing the simulation results, the canopy opening process was divided into two stages: contact stage and oscillation stage.

The simulation results show that in the contact stage, the maximum displacement of the rice stem increases with the decrease in the height of the canopy opening device from the ground and the increase in deriving velocity. In the oscillation stage, there is a critical value for the height and deriving velocity of the canopy-opening device, and heights and deriving velocities that are too high or too low cannot increase the maximum displacement of the rice stem. When the height of the canopy-opening device is 0.6 m and the deriving velocity is 1.2 m s^{-1}, the disturbance intensity of the canopy-opening device to the rice stem is the maximum in the oscillation stage. The total energy of the model increases with the decrease in the height of the canopy-opening device and the increase in its deriving velocity, but the increase in deriving velocity also increases the rapid decay of the total energy of the model. High-speed photography experimental results show that there is a certain error between the simulation results in the oscillation stage and the high-speed photography experimental results. However, if extreme processing is removed, the simulation results and experimental results show a strong correlation, with a correlation coefficient of 0.733. However, the error between the simulated rice stem displacement and the observed displacement is large during the process of the canopy opening. This is because the canopy opening process is a very complex physical phenomenon influenced by many factors, such as the growth status of the rice and the material properties of the rice stem. Therefore, even with accurate physical parameters and fine grid division in the simulation, it is difficult to completely replicate the actual situation. However, increasing the number of rice plants in the simulation model can better reflect the interaction between rice plants in reality, which maybe help to reduce the error between the simulation and real results. This is also our next work.

Data availability statement

The original contributions presented in the study are included in the article/Supplementary Material. Further inquiries can be directed to the corresponding author.

References

Conflict of interest

The authors declare that the research was conducted in the absence of any commercial or financial relationships that could be construed as a potential conflict of interest.

Publisher's note

Supplementary material

The Supplementary Material for this article can be found online at: https://www.frontiersin.org/articles/10.3389/fpls.2023.1252247/full#supplementary-material

ANSYS Documentation (2016). *Release Notes: Explicit Dynamics Analysis* (Release 17.1. ANSYS Inc).

Celik, H. K. (2017). Determination of bruise susceptibility of pears (Ankara variety) to impact load by means of FEM-based explicit dynamics simulation. *Postharvest Biol. Technol.* 128, 83–97. doi: 10.1016/j.postharvbio.2017.01.015

Crook, M. J., and Ennos, A. R. (1994). Stem and root characteristics associated with lodging resistance in four winter wheat cultivars. *J. Agric. Sci.* 123, 167–174. doi: 10.1017/S0021859600068428

Da Silva, A., Sinfort, C., Tinet, C., Pierrat, D., and Huberson, S. (2006). A Lagrangian model for spray behaviour within vine canopies. *J. Aerosol Sci.* 37 (5), 658–674. doi: 10.1016/j.jaerosci.2005.05.016

Farooq, M., and Salyani, M. (2004). Modeling of spray penetration and deposition on citrus tree canopies. *Trans. ASAE* 47 (3), 619. doi: 10.13031/2013.16091

Gaskin, R. E., Manktelow, D. W., Cook, S., and May, W. A. (2013). Effects of canopy density on spray deposition in kiwifruit. *New Z. Plant Prot.* 66, 194–198. doi: 10.30843/nzpp.2013.66.5607

Heong, K. L., Cheng, J., and Escalada, M. M. (2016). *Rice planthoppers* (Springer).

Kokubo, A., Kuraishi, S., and Sakurai, N. (1989). Culm strength of barley: correlation among maximum bending stress, cell wall dimensions, and cellulose content. *Plant Physiol.* 91, 876–882. doi: 10.1104/pp.91.3.876

Lee, F. N. (1983). Rice sheath blight: A major rice disease. *Plant Dis.* 67, 829–832. doi: 10.1094/PD-67-829

Lee, H. H. (2012). *Finite element simulation with ANSYS Workbench* Vol. 14 (Kansas City, KS: SDC Publications), 608, ISBN: .

Liu, W. C., Liu, Z. D., Huang, C., Lu, M. H., Liu, J., and Yang, Q. P. (2016). Statistics and analysis of crop yield losses caused by main diseases and insect pests in recent 10 years. *Plant Prot* 42 (05), 1–9. doi: 10.3969/j.Issn.0529-1542.2016.05.001

Liu, X., Liu, X., Li, Y., Yuan, J., and Li, H. (2021). Predicting spray deposit distribution within a cotton plant canopy based on canopy stratification porosity and Gaussian process models. *Biosyst. Eng.* 204, 1–14. doi: 10.1016/j.biosystemseng.2020.12.018

Prado, E. P., Dal Pogetto, M. H. F. D. A., De Cerqueira, D. T. R., Raetano, C. G., and Costa, S.Í.D.A. (2016). Construction and practical application of a canopy opener device. *Engenharia Agricola* 36 (6), 1126–1135. doi: 10.1590/1809-4430-Eng.Agric.v36n6p1126-1135/2016

Savary, S., Willocquet, L., Elazegui, F. A., Castilla, N. P., and Teng, P. S. (2000). Rice pest constraints in tropical Asia: Quantification of yield losses due to rice pests in a range of production situations. *Plant Dis.* 84 (3), 357–369. doi: 10.1094/PDIS.2000.84.3.357

Skamnioti, P., and Gurr, S. J. (2009). Against the grain: safeguarding rice from rice blast disease. *Trends Biotechnol.* 27 (3), 141–150. doi: 10.1016/j.tibtech.2008.12.002

SolidWorks Documentation (2010). *SolidWorks Simulation Premium: Nonlinear.Training Manual Serial No: 22658021044 ENG0001* (USA: Dassault Systemes SolidWorks Corporation).

Timoshenko, S. P., and Gere, J. M. (1973). *Mechanics of materials* (New York, NY, USA: Van Nostrand Reinhold Company).

Wakabayashi, N., Ona, M., Suzuki, T., and Igarashi, Y. (2008). Nonlinear finite element analyses: advances and challenges in dental applications. *J. dentist.* 36, 463–471. doi: 10.1016/j.jdent.2008.03.010

Wang, S. L., Li, X., Lei, X. H., Gu, Y., Herbst, A., Bonds, J., et al. (2021). Influences of canopy-pushing plate on droplet drift and deposition characteristics of boom sprayer. *Plant Prot.* 47 (1), 68–73. doi: 10.16688/j.zwbh.2019541

Womac, A. R., Ozkan, E., Zhu, H., Kochendorfer, J., and Jeon, H. (2022). Status of spray penetration and deposition in dense fieldcrop canopies. *J. ASABE* 65 (5), 1107–1117. doi: 10.13031/ja.15091

Wu, S., and Wei, X. (2019). Mechanical interaction between a canopy opener and rice stalks based on the transient dynamic analysis. *Biosyst. Eng.* 178, 256–263. doi: 10.1016/j.biosystemseng.2018.12.004

Wu, S. R., and Gu, L. (2012). *Introduction to the Explicit Finite Element Method for Nonlinear Transient Dynamics* (John Wiley & Sons).

Xu, D. J., Xu, G. C., Xu, L., Wang, C. B., Hu, S. N., Gu, Z. Y., et al. (2021). Study on the statistical index of uniformity of pesticide deposition and distribution of foliage spraying in rice field. *Modern Agrochem.* 020 (005), 38–44. doi: 10.3969/j.issn.1671-5284.2021.05.005

Zhu, H., Derksen, R. C., Ozkan, H. E., Reding, M. E., and Krause, C. R. (2008). Development of a canopy opener to improve spray deposition and coverage inside soybean canopies: part 2: opener design with field experiments. *Trans. ASABE* 51 (6), 1913–1922. doi: 10.13031/2013.25390

Design and test of powerful air-assisted sprayer for high stalk crops

Youyi Miao[1†], Xiao Chen[1†], Yan Gong[1,2*], Dejiang Liu[1,2], Jian Chen[1], Guo Wang[1] and Xiao Zhang[1]

[1]Nanjing Institute of Agricultural Mechanization, Ministry of Agriculture and Rural Affairs, Nanjing, China, [2]Western Agricultural Research Center, Chinese Academy of Agricultural Sciences, Changji, China

The canopies of high stalk crops, such as maize, intersect the rows at the later stages of growth, making conventional sprayers unable to enter the field for spraying. Air-assisted sprayers are often used to improve the deposition of droplets inside the canopy. In this study, the sprayer structure, the air-assisted system, and the spraying system were designed. The air-assisted conveyor system characteristics were numerically analyzed, and the wind-field distribution was tested. The wind-field distribution results showed that the near-ground wind speed exceeded 5 m s^{-1} in the sampling interval from 10 to 35 metres. The wind field covered a concentrated spatial area with a downward pressure trend, resulting in better drift resistance and penetration. Field tests for droplet distribution were conducted at three maize heights to verify the powerful air-assisted sprayer's technical performance and working quality. The test results showed that the droplet deposition and coverage decreased gradually along the range direction, and the top layer had the highest deposition and coverage across the canopy. The upper canopy of 0 to 12 metres range demonstrated a greater extent of coverage and deposition. The peak deposition area expanded from 9 to 33 metres in the lower canopy, with an average value of 3.77 µg cm^{-2}. The droplet coverage within the 30 to 60 metres range only amounted to 15% to 18% of the total coverage.

KEYWORDS

powerful air-assisted sprayer, high stalk crops, gas-liquid combined spraying, sprayer, wind-field distribution

1 Introduction

Maize planting area in China has reached 43,324 thousand hectares, constituting 25.7% of the total crop planting area in 2021. Maize canopies intersect the rows in the later stages of growth, making conventional sprayers unable to enter the field for spraying operations. Once encountering aggressive pests and diseases, it is often difficult to effectively control, leading to a significant reduction in maize yields or even a failure of the harvest. This poses a serious threat to China's food security. Fall armyworm invaded twenty-six domestic

provinces in 2019, threatening over 50% of the crop planting area in China (Yang et al., 2019; Wang and Lu, 2020). The timing of pest control is critical. Once a pest infestation is identified, all spraying operations must be completed in a very short time (Wang et al., 2014; Kumar et al., 2021).

Air-assisted spray is an advanced application technology recommended by the Food and Agriculture Organization of the United Nations (FAO) (Czaczyk, 2012; Gu et al., 2022). In agricultural pest control, pneumatic sprayers equipped with large axial-flow or centrifugal fans have been widely used in developed countries (Khot et al., 2012; Sinha et al., 2019). Hong et al. (2018) designed an air-assisted sprayer that integrated air-assisted, variable spraying, and intelligent targeting technologies, which could be used for pests and diseases of fruit trees with different canopy shapes. Thakare et al. (2015) evaluated an air-assisted sleeve boom sprayer machine and achieved effective pest control.

Derksen et al. (2008) utilized the Jacto air-assist sprayer equipped with JA3 hollow-cone nozzles in soybean canopy. This specific method generated the highest concentration accumulation of fungicide residues on leaves in the lower part of the canopy. The Italian company TIFONE has developed a series of wind-driven long-range sprayers for maize, soybeans, and other crops. These sprayers have a maximum range of 30 metres and are designed with horizontal inflow ducts, similar to wind-driven sprayers used in orchards.

In recent years, Chinese scholars have made significant advancements in orchard wind-delivery technology and equipment, focusing on enhancing efficiency and reducing volume spraying. Li et al. (2021) designed and constructed an air-fed sprayer equipped with an axial fan and annular nozzle. The dimensions and placement of the nozzle were determined through computational fluid dynamics (CFD) fluid simulation. Zhou et al. (2015) developed an air-assisted electrostatic sprayer combined with air-assisted spraying and electrostatic spraying technology. With the development of Unmanned Aerial Vehicle (UAV), field crop spraying by plant protection UAV was widely accepted (Qin et al., 2023). Hussain et al. (2022) compared the spraying effect of different HBL dosages and sprayer volumes of KMS (Knapsack manual sprayers) and UAV sprayers on maize crop growth and development. The results showed that the droplet deposition of UAV (15 30 L ha^{-1}) was higher than KMS; the average deposition was between 0.05 and 0.06 μL cm^{-2}. However, the UAV sprayer had a poor droplet coverage rate, which was below 10%. The low coverage results were similar to Sarri et al. (2019). The plant protection UAV equipment has the features of mobile flexibility and high operational efficiency. However, the protection effect for high stalk crops still needs to be improved due to poor penetration and extremely small number of droplets (Abd. Kharim et al., 2019; Guo et al., 2020; Zhan et al., 2022; Chang et al., 2023).

Studies have shown that the effective deposition of droplets inside the canopy can be improved by the air-assisted spray system. However, there is a lack of research and application of wind-delivered application technology and ground equipment for field crops in China. Wang et al. (2021) designed a crawler self-propelled corn interrow sprayer that could meet the space requirements for

plant protection operations under the narrow row of corn leaves below 600 mm. The high clearance boom sprayer with an air-assisted system is commonly employed for maize crops due to its good spray uniformity and control effects. However, the equipment will be invalid when the height of the maize exceeds the ground clearance of the equipment (Wang et al., 2015; Wei et al., 2016; Wu et al., 2018).

In this study, a powerful air-assisted remote sprayer was developed to overcome the challenges of mechanized plant protection for maize and other crops in China. The wind field distribution characteristics were numerically analyzed, and wind field distribution tests and prototype droplet deposition distribution tests were conducted in maize fields to provide a new type of application technology and equipment that is economical and efficient for pest and disease control in this crop.

2 Materials and methods

2.1 Structural composition and working principle

The powerful air-assisted sprayer structure consists of a spraying system, an air-assisted conveyor system, a power transmission system, and a traction frame, as is shown in Figure 1. The spraying system is composed of a diaphragm pump (3), a distribution valve (1), a pesticide tank (5), and spray components (10). The air-assisted conveyor system is comprised of a multi-wing centrifugal fan (8), a turbine casing (12), a deflector duct (11), a deflector cap (9), a turbine casing rotating mechanism (13) and a frame (14). The power transmission system is composed of a universal joint (4), a drive shaft (6), and a gearbox (7). The gearbox (7) is connected to the output shaft of the diaphragm pump (3) through the universal joint (4). The multi-wing centrifugal fan (8) is mounted on the gearbox (7). The powerful air-assisted sprayer is connected to the tractor through the tractor frame (2), and the tractor power output shaft links to the input shaft of the diaphragm pump (3). The turbine casing rotating mechanism (13) is driven by the hydraulic system of tractor.

The powerful air-assisted sprayer is towed and powered by a tractor and can be used on field roads. The air-assisted conveyor system has the capability to generate secondary atomization while pushing droplets to a longer distance, significantly enhancing the delivery range and penetration of the droplets.

2.2 Design of the air-assisted conveyor system

The air-assist conveyor system is the core technology of powerful air-assisted sprayer. Its working performance directly impacts the conveyance distance and the penetration capacity of droplets. The air-assisted conveyor system for plant protection in high stalk crops requires higher air volumes, faster speeds, and uniform airflow direction compared to orchard air-assist sprayers.
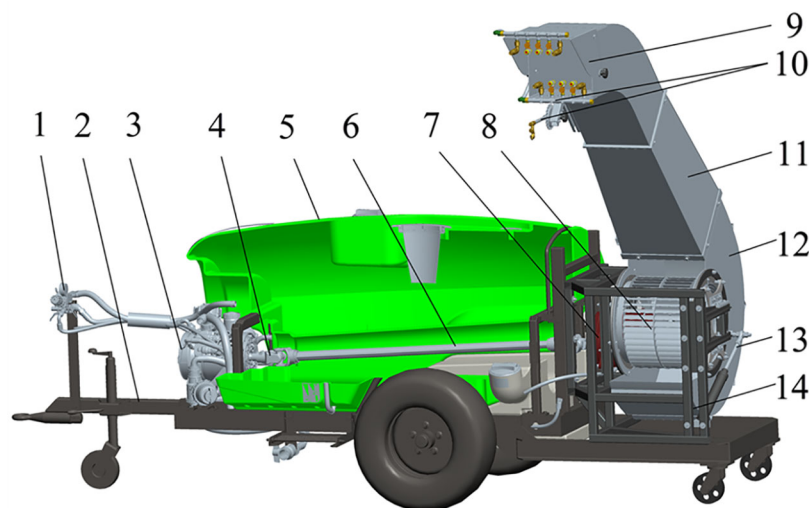
FIGURE 1

Structure of powerful air-assisted sprayer. 1. distribution valve 2. tractor frame 3. diaphragm pump 4. universal joint 5. pesticide tank 6. drive shaft 7. gearbox 8. multi-wing centrifugal fan 9. deflector cap 10. spray components 11. deflector duct 12. turbine casing 13. turbine casing rotating mechanism 14. frame.

2.2.1 Overall structure of air-assisted deflector duct

The structure of the air-assisted deflector duct is shown in Figure 2, which is composed of turbine casing (1), contraction section (2), straight section A (3), arc section (4), straight section B (5), and deflector shield (6). The contraction section (2) is a trapezoidal structure that further augments the velocity and pressure of the wind. The arc section (4) connects straight section A (3) and straight section B (5), forming an angle of 135°. This design not only redirects the flow field but also minimizes wind energy loss effectively.

The deflector shield (6) is set in the upper part of the air outlet of the deflector duct, and the angle can be adjusted from 0° to -5°. The adjustable angle of the deflector shield can also meet the varying requirements of different meteorological conditions in the field for spraying. This feature allows the shield to effectively mitigate the adverse effects of air movement in the environment, reducing the drift of insecticide droplets to non-target areas. By adjusting the angle of the deflector shield to form a downward airflow, it is possible to enhance the dispersion of pesticide droplets towards the target crop, particularly in the lower areas.

Figure 3 illustrates the steering mechanism motion sketches of deflector duct. The turbine casing is designed to coincide with the fixed-ring and fan axis, ensuring no alteration to the airflow in the turbine casing or deflector duct. This ensures that the application equipment maintains spraying consistency and stability without wasting extra wind energy.

Equation (1) shows the correlation between the telescopic length of the cylinder and the rotation angle of the inflow air cylinder.

$$X_3 = \sqrt{X_1^2 + X_2^2 - 2X_1 * X_2 * cos(\alpha + \beta)} \qquad (1)$$

Where X_1 is the distance from fan axis A to hinge point B of hydraulic cylinder on frame, mm; X_2 is the distance from fan axis A to hinge point C of hydraulic cylinder on turbine casing, mm; X_3 is the hydraulic cylinder telescopic length, mm; α is the initial angle of deflector duct, °; β is the adjustable angle of deflector duct, °.

The designed parameter of α is 74°, X_1 is 1136 mm, and X_2 is 586 mm. Inserting the known values obtains a result of hydraulic cylinder telescopic length range from 1126 to 1526 mm, and 47° adjustable angle of deflector duct.
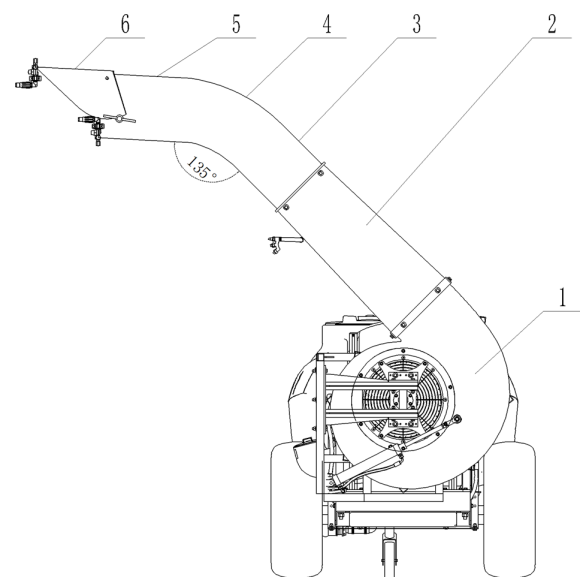

FIGURE 2

Structure of air-assisted deflector duct. 1. turbine casing 2. contraction section 3. straight section A 4. arc section 5. straight section B 6. deflector shield.
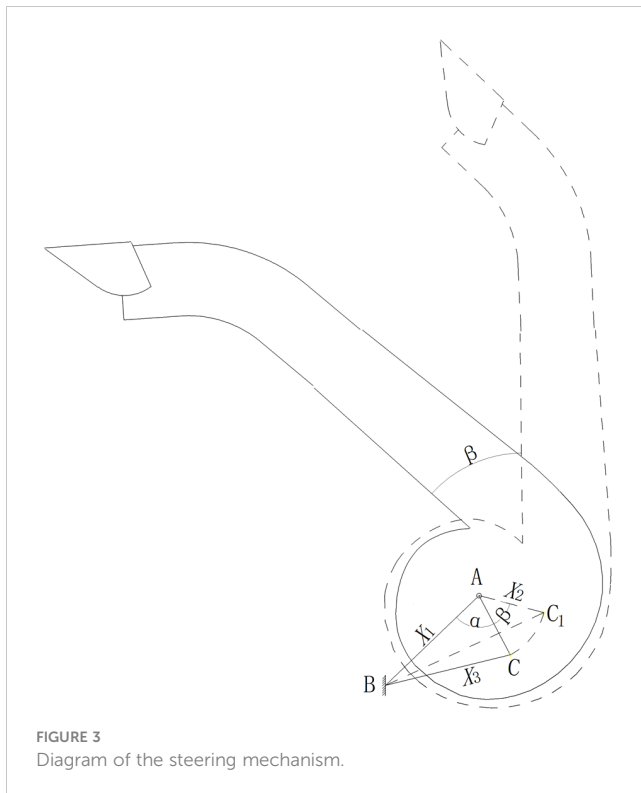
FIGURE 3
Diagram of the steering mechanism.

FIGURE 4
Structure of the turbine casing steering mechanism. 1. turbine casing 2. frame 3. fan 4. fixed-ring 5. hydraulic cylinder.

2.2.2 Design of turbine casing steering mechanism

To avoid uneven stresses and deformations in the structure of the air-assisted system caused by the heavy weight of deflector duct, the turbine casing is constructed with the double support structure.

As shown in Figure 4, the turbine casing (1) coincides with the fixed-ring (4) and fan (3) axis; the hydraulic cylinder (5) is hinged on the frame (2) at one end and on the turbine casing (1) at the other end. By adjusting the telescopic length of the hydraulic cylinder (5), the turbine casing (1) (together with the deflector duct) is driven to revolve on the flange of fixed-ring (4), thus changing the spray angle at the outlet of conveyor system.

2.2.3 Calculation of air volume of powerful air-assisted system

The design of the fan and the calculation of the air volume in the powerful air-assisted system are mainly based on the replacement principle and the end velocity principle (Dai, 2008; Ru et al., 2022). The main function of the designed air-assisted system is to transport the airflow from the fan to the far side. The replacement principle's space volume should be the area between the sprayer outlet and the top of the crop canopy.

As shown in Figure 5A, according to the replacement principle, with the sprayer's driving speed and the fan's constant rotation speed, the air volume generated by fan per second is equal to the volume of the rectangular.

The calculation of the required air volume is given by Equation (2).
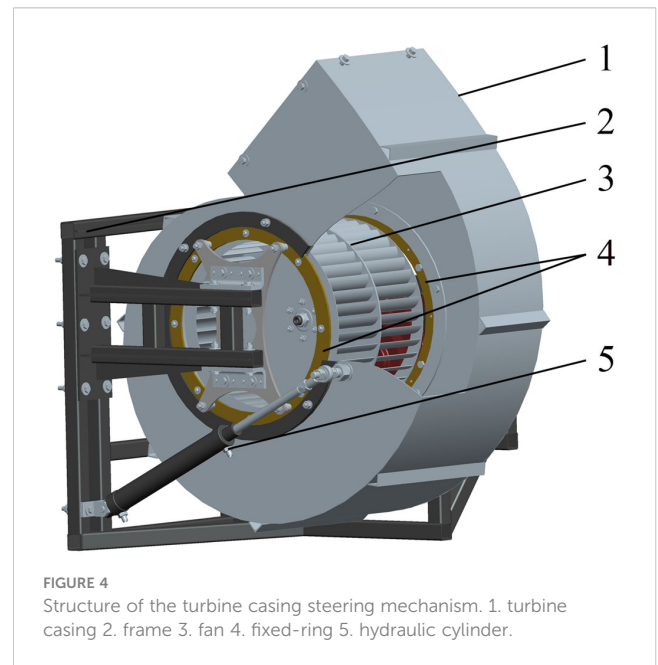
$$Q_1 = L_1 H_1 v K_1 \qquad (2)$$

Where Q_1 is the air volume generated by ducts, m³ s⁻¹; L_1 is the range of sprayer, m; H_1 is the height between the sprayer outlet and the top of crops, m; v is the driving speed of sprayer, m s⁻¹; K_1 is the coefficient of air attenuation and loss, $K_1 = 1.3{\sim}1.6$. Although the horizontal direction wind loss of the outlet is small, the fan under pressure wind will be blown into the crop inside, taking $L_1 = 50$ m, $K_1 = 1.4$. According to Equation (2), the required air volume Q_1 is 7 m³ s⁻¹.

As shown in Figure 5B, according to the end velocity principle, the airflow must keep a certain velocity when it reaches the end of its range. This ensures that crop leaves could be flipped by the airflow at a distance in the direction of the shot to improve droplet penetration and adhesion.

The initial velocity must satisfy the following Equation(3).

$$L_2 v_1 \geq L_3 v_2 K_2 \qquad (3)$$

Equation(3) can be used to obtain:

$$v_1 \geq \frac{L_3 v_2 K_2}{L_2} \qquad (4)$$

Where v_1 is the initial velocity, m s⁻¹; v_2 is the end velocity, m s⁻¹, $v_2 = 2{\sim}4$ m s⁻¹; L_2 is the length of duct outlet, m; L_3 is the length at the end of the range area, m; K_2 is the coefficient of air resistance, $K_2 = 1.3{\sim}1.8$.

According to the design parameter and cultivation requirement of crops, take $L_3 = 3$ m, $v_2 = 3$ m s⁻¹, $L_2 = 0.35$ m. Considering the resistance against the airflow because of dense crop canopy in late growth period, take $K_2 = 1.8$. According to the Equation (4), the required initial velocity v_1 is not less than 46 m s⁻¹.

2.2.4 Design of multi-wing centrifugal fan

The designed multi-wing centrifugal fan with double inlet must satisfy the flow rate $Q_1{\geq}7$ m³ s⁻¹, $v_1{\geq}46$ m s⁻¹. The full pressure of
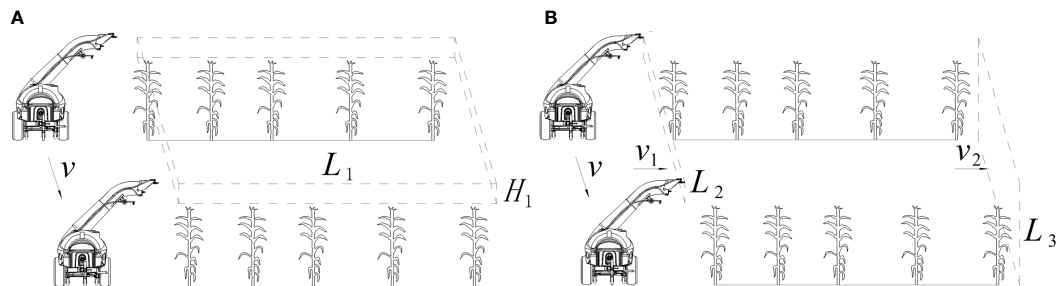
FIGURE 5
Calculation principle of powerful air-assisted system. **(A)** Replacement principle. **(B)** End speed principle.

the fan mainly consists of the dynamic pressure loss and static pressure loss (friction pressure loss and local pressure loss), which is calculated as Equation (5).

$$\begin{cases} P_{\mathrm{d}} = \frac{1}{2}\rho v_1^2 \\ P_{\mathrm{f}} = \lambda \frac{\rho v_1^2}{2D} L \\ P_{\mathrm{l}} = \xi \frac{1}{2}\rho v_1^2 \\ P_{\mathrm{tF}} = P_{\mathrm{d}} + P_{\mathrm{f}} + P_{\mathrm{l}} \end{cases} \tag{5}$$

Where P_{d} is the dynamic pressure loss, Pa; P_{f} is the friction pressure loss, Pa; P_{l} is the local pressure loss, Pa; P_{tF} is the full pressure, Pa; ρ is air density, kg m^{-3}; λ is the friction coefficient; D is the equivalent diameter, m; L is the length of deflector duct, m; ξ is the local resistance coefficient.

The selected values of each parameter are: ρ=1.21 kg m^{-3}, λ=0.18, D=0.44 m, L=2.46 m, ξ=0.31, According to Equation (5), the full pressure P_{tF} is 2965 Pa.

The designed impeller rotation speed is 2200 r min^{-1}. The specific speed can be calculated by Equation (6).

$$n_s = 5.54 n \frac{\left(\frac{Q_1}{2}\right)^{1/2}}{p_{\mathrm{tF}}^{3/4}} \tag{6}$$

Where n_{s} is the specific speed; n is the impeller rotation speed, r min^{-1}.

The calculated specific speed of multi-wing centrifugal fan is 56.75, which belongs to the range of forward-bladed impeller centrifugal fans. Table 1 shows the main structural parameters of multi-wing centrifugal fan.

2.2.5 Simulation of the air-assisted conveyor system

The numerical calculation was carried out for the air-assisted conveyor system by Fluent. To improve the accuracy of the simulation results and computational efficiency, mesh refinement was performed on centrifugal fan. The volume was meshed with poly-hexcore body, size from 2 mm to 20 mm. The total number of elements was 3,080,962.

The control equations were Navier-Stokes equations, the turbulence was calculated by Realizable k-ε model. The near-wall equations were in standard wall function, The pressure-velocity coupling was in Coupled algorithm, and the pressure discrete format was in PRESTO! Format. The momentum, energy and turbulence dissipation equations were in second-order windward format, and the computational convergence residuals were set to 0.0001. The inlet and outlet were given pressure inlet and pressure outlet boundary conditions, and the value was set to zero during simulation experiments. The impeller area was set as a rotating area, and the Frame Motion model was used to set the rotating area speed at 2200 r min^{-1}.

2.3 Design of the spraying system

To achieve uniform distribution of pesticide droplets in the full spray range, the nozzle combination was designed with multi-heads hydraulic nozzle, high-pressure long-shot nozzle, and cone nozzle (Figure 6A). As shown in Figure 6B, in the range from 0 to 15 metres, the airflow has not yet deposited in the region, this area of the crop using multi-heads hydraulic nozzle spraying method. The multi-heads hydraulic nozzle is mounted on the out wall of the deflector duct, and the installation height from the ground is 1.5 metres. In the range from 15 to 50 metres, using the air-assisted method to transport the droplets to this interval. The high-pressure long-shot nozzle and cone nozzle are distributed on the upper and lower sides of the deflector shield air outlet. The strong airflow generated by the fan makes two kinds of nozzles spraying pesticide droplets to remote distribution, effectively covering target crops in the deposition area. The parameter of spraying system is shown in Table 2.

TABLE 1 Basic structural parameters of multi-wing centrifugal fan.

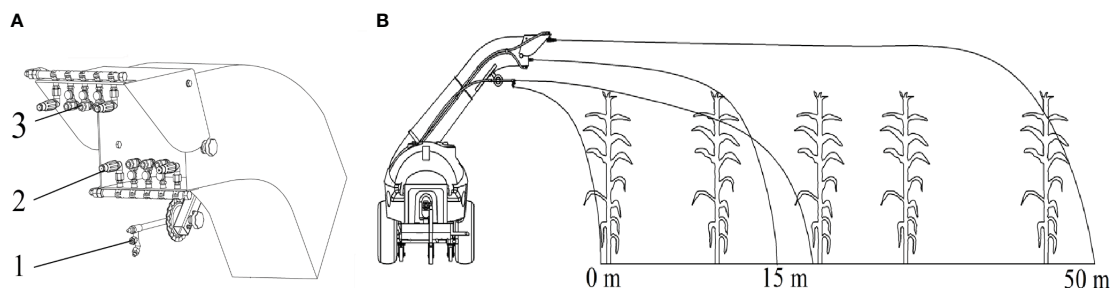| Parameters	value
Inner diameter of impeller D_1/mm	360
Outer diameter of impeller D_2/mm	450
Number of blades z/pcs	42
Impeller width b/mm	324
Turbine casing width B/mm	400
Blade inlet angle β_{1A}/°	69
Blade outlet angle β_{2A}/°	131

FIGURE 6
Working principle of the spraying system. **(A)** Structure of spraying system: 1. multi-heads hydraulic nozzle 2. high-pressure long-shot nozzle 3. cone nozzle. **(B)** Distribution of spraying range.

TABLE 2   Technical parameter of spraying system.

Parameters	Quantity	Working pressure/ MPa	Flow rate/ L min^{-1}
Multi-heads hydraulic nozzle	1	4.0	19
High-pressure long-shot nozzle	4	4.0	8.4
Cone nozzle	6	4.0	6.5

2.4 Experimental design and methods

2.4.1 Design and measurement of the wind-field distribution test

The wind-field distribution test was conducted in the wind-filed lab of XINYI Agricultural Machine Co. Ltd, Taizhou, Zhejiang Province. A tractor of 100 HP was applied to drive the centrifugal fan. The sampling grid frame was a rectangle frame with 2750 mm×3000 mm, divided into several grids of 250 mm×250 mm (Figure 7A). Before testing, a cartesian coordinate was set with the center of the fan outlet as the wind measurement origin, the horizontal direction as the X-axis and the vertical direction as the Y-axis.

The sprayer was located stably on the ground, and the fan outlet was adjusted to a horizontal status by rotating the hydraulic cylinder. The sampling grid frame was located vertically to the X-axis. The wind speed value at each node was measured by KA33 thermal sphere anemometer, and each node was measured in turn from the center to the surrounding area until the measured wind speed value was less than 2 m s^{-1}. The sampling grid frame was moved at intervals of 5 metres along the range direction, and the wind speed values at each node at the corresponding position were measured separately (Figure 7B).

2.4.2 Design of spray field test

The spray field test was conducted in maize planting base of the Institute of Farmland Irrigation of CAAS, Shangqiu, Henan Province (Figure 8). The maize row spacing was 0.4 metres and the plant spacing was 0.5 metres. Three trials were conducted at different growth height of maize at 1.4, 1.7 and 2 metres named as TM1, TM2 and TM3. The sprayer was towed by a 100 hp tractor and operated at travel speeds of 3.6 km h^{-1}.

The fluorescent tracer dye, Allura Red was used as spray tracer to verify the droplet deposition and coverage performance. The tracer was dissolved in water at about 5 g L^{-1}. The filter paper (Φ90 mm) and water-sensitive paper (26 mm×76 mm, Syngenta) were applied to collect the spray droplets. The visible spectrophotometer
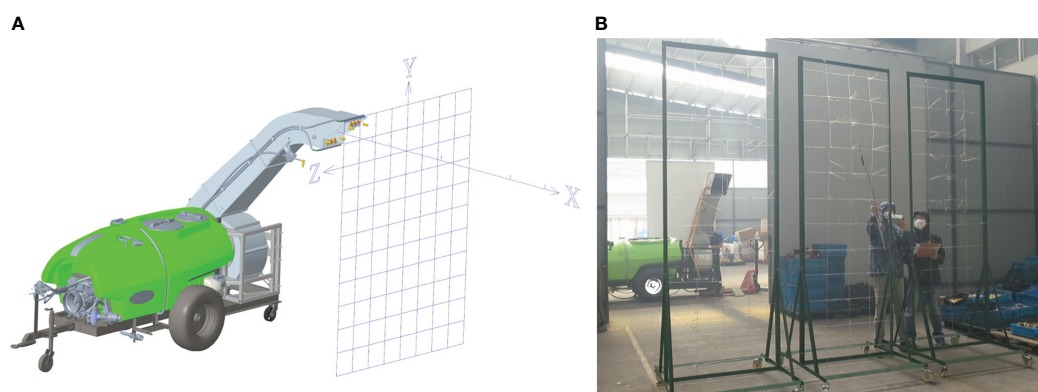

FIGURE 7
Wind-field distribution measurement method. **(A)** Sampling grid frame. **(B)** Wind-field distribution test.

FIGURE 8
Field test.

(V5100, Developed Shanghai METASH Instruments Co., Ltd) and the droplet analysis software of DepositScan (Developed by USDA) were applied to determine and analyze droplet deposition and coverage on filter paper and water-sensitive paper.

In this study, according to the maize cultivation spacing, twenty-one plants of maize with an interval of 3 metres each were selected as an experimental row along the spray range. Along the travel direction of sprayer, three same experimental rows as mentioned above with an interval of 5 metres were selected. For TM1, three layers of filter paper were fixed on the leaves from the top leaf with an interval of 50 cm. For TM2 and TM3, four layers of filter paper were fixed on the leaves from the top leaf with an interval of 50 cm. Meanwhile, beside each filter paper, one piece of water-sensitive paper was fixed for each layer. After spraying was completed, the filter paper and water-sensitive paper were collected (in less than 10 min) and placed in resealable plastic bags.

2.5 Data analysis

2.5.1 The determination of droplet deposition

The filter paper was placed individually into a glassware filled with 20 mL of water and kept soaking for 3~4 hours to make sure that the Allura Red was completely eluted. A certain amount of liquid was pipetted into the glass cuvette, and placed into the spectrophotometer to measure the absorbance of the liquid. According to Equation (7), the absorbance of the liquid was converted to the value of droplet deposition on the filter paper.

$$p = \frac{\rho_{(A)} \times V}{S} = \frac{(24.83 \times A + 0.031) \times V}{S} \quad (7)$$

Where p is the droplet deposition value, $\mu g \ cm^{-2}$; $\rho_{(A)}$ is the mass concentration of washed-out Allura Red, $mg \ L^{-1}$; A is the absorbance of Allura Red liquid; V is the volume of water used to soak the filter paper, mL; S is the area of filter paper, cm^2.

2.5.2 The determination of droplet coverage

The parameters of droplet size, droplet number and droplet coverage on water-sensitive paper were analyzed by the image processing software DepositScan. The recycled water-sensitive paper was scanned in grayscale mode with a resolution of 600 DPI, and then the scanned images were imported into DepositScan to analyze the droplet coverage.

3 Results and discussion

3.1 Simulation test

As shown in Figure 9, the velocity distribution inside the deflector duct is evenly distributed. Due to the influence of airflow space, the wind speed on the impeller surface is higher in the area close to the turbine casing outlet than in the narrow area of the turbine casing. The cross-section gradually contracts, and the wind speed gradually increases after the airflow enters the contraction section. The wind speed on the outside of the arc section is lower than the wind speed on the inside because of air flow is blocked by the wall. After the airflow is guided to the outlet of deflector duct, the airflow direction is consistent with the outlet direction, leading to a decrease in overall turbulence. The average wind speed at the outlet reaches 65.3 m s^{-1}, and the outlet air volume flow rate is 7.85 m^3 s^{-1}.

Figure 10 shows the pressure distribution of air-assisted deflector duct. The full pressure of the deflector duct is well distributed and the average full pressure at the outlet is 3200 Pa (Figure 10A). Dynamic pressure is the main contributor to the total pressure in the deflector duct. The dynamic pressure is higher around the impeller and at the outlet, and the trend is consistent with the airflow velocity field distribution (Figure 10B). The static pressure increases gradually in the direction of the impeller diameter, with the highest pressure at the wall of turbine casing
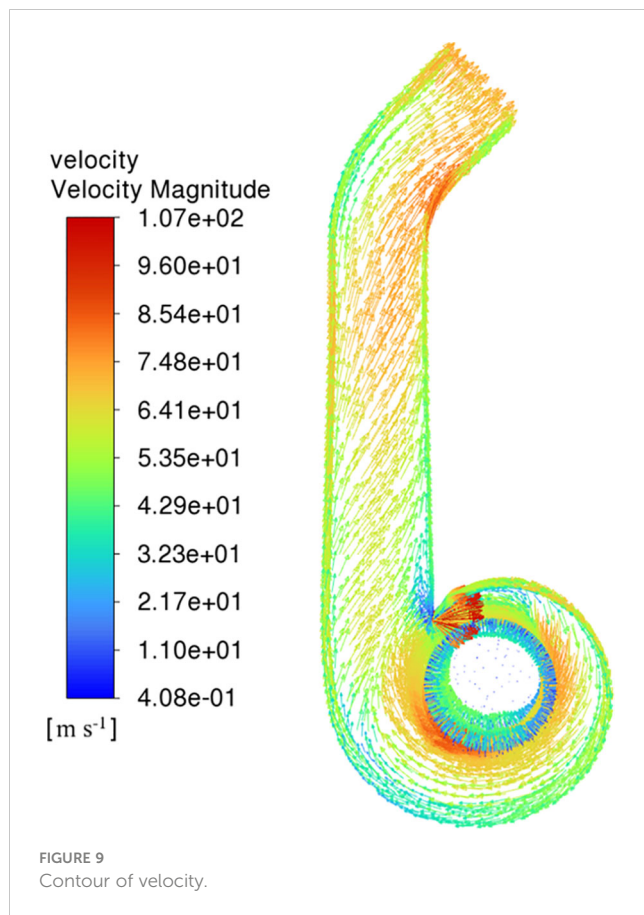
and contraction section, and then decreases gradually in the direction of the outlet (Figure 10C).

3.2 Test of wind-field distribution

The wind-field distribution results were shown in Figure 11, the wind-field range of the sampling grid frame at 5 m from the air outlet was concentrated, and the maximum wind speed of the cross

section was large than 30 m s^{-1}. With the increase of the distance from the outlet, the wind-field of the sampling plane was expanded gradually, and at the 10 metres sampling position, the lower boundary of the wind-field was expanded to the ground, while the upper boundary of the wind field was not significantly raised. The near-ground wind speed exceeded 5 m s^{-1} in the sampling interval from 10 to 35 metres, which showed the downward pressure effect of the wind-field. When the sampling distance reached 40 metres, the maximum wind speed area gradually disappeared, and the overall wind speed of the sampling plane became stable, with an average wind speed of 3.8 m s^{-1}. The wind speed further decreased at 50 metres position, but the average wind speed at the node in the sampling grid frame still met the effective wind speed of more than 2 m s^{-1}.

3.3 Field test

3.3.1 Distribution of droplet deposition

The distribution of droplet deposition for three trials was shown in Figure 12. In Figure 12A, there was a clear trend of decreasing in droplet deposition along the direction of range for all three trials. The TM1 trial had an average deposition of 5.9 μg cm^{-2} in the top layer, 3.2 μg cm^{-2} in the second layer and 2.1 μg cm^{-2} in the third layer. A reduction of 45.7% in the second layer and a reduction of 64.4% in the third layer compared to the first layer. The highest deposition across the canopy was in the top layer. TM3 had the highest deposition and TM1 had the lowest deposition in the top layer of the three trials. This indicated that there was a positive correlation between deposition levels and proximity to the outlet. The droplet deposition was significantly higher in the top layer compared to the other layers within the 0 to 6 metres range.

In the multi-heads hydraulic nozzle range of 0 to 15 metres, the deposition in the top layer of TM1, TM2, and TM1 was 15.7 μg cm^{-2}, 14.1 μg cm^{-2}, and 11.7 μg cm^{-2}, respectively (Figure 12B). This was more than three times the average value of the layer in which it was located. In the second layer, the area of peak deposition concentration was observed within the range of 9 to 21 metres. In the third layer, the
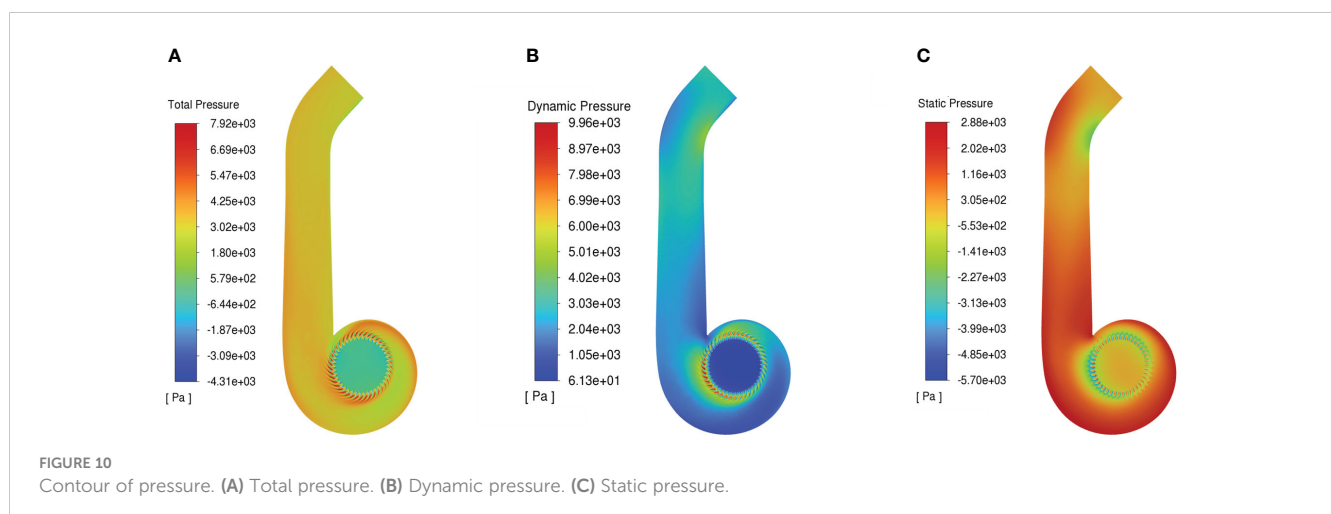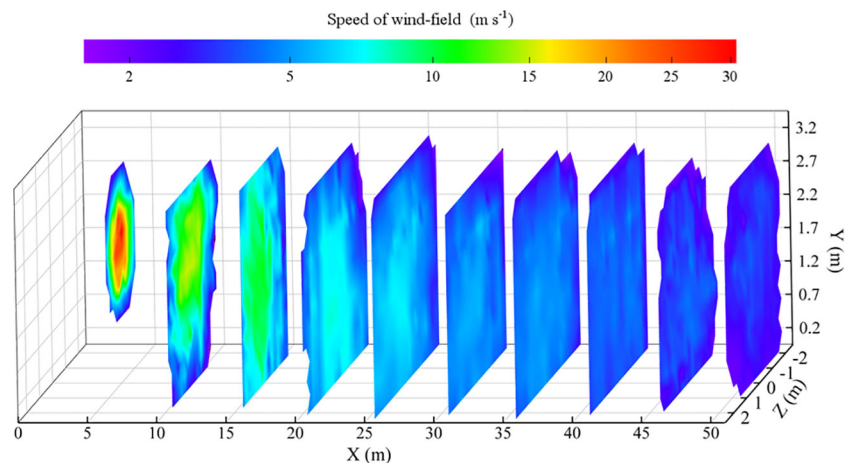
FIGURE 11
Cloud map of wind-field distribution.

area of peak deposition extended from 9 to 33 metres, exhibiting an average value of 3.77 µg cm^{-2}. This indicated that as the range expanded, deposition in the lower and middle layers of the crop distributed further, reflecting the advantages of a downward-pressure wind field. In the bottom layer, droplet deposition could still be presented in TM2 and TM3 with a mean value of 1.59 µg cm^{-2} and

1.61 µg cm^{-2}. The well-distributed deposition indicated the effective penetration of the wind field.

3.3.2 Distribution of droplet coverage

The distribution of droplet coverage for three trials was shown in Figure 13. The average coverage of TM1 was 22.8% in the top
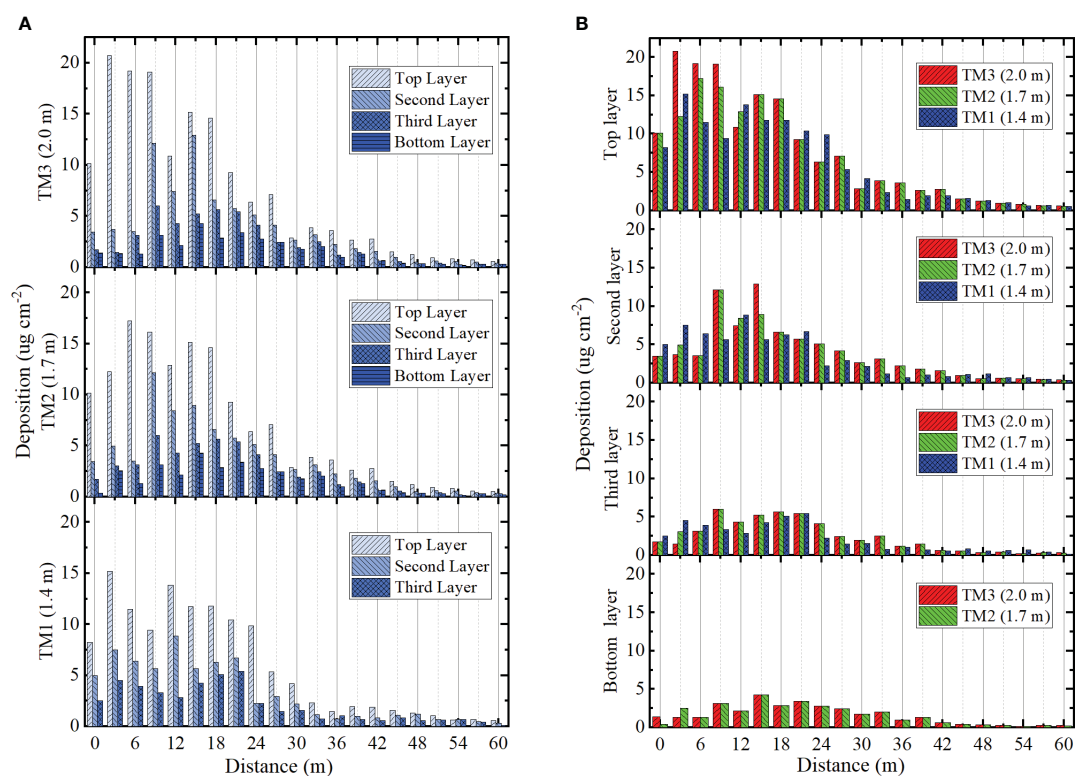

FIGURE 12
The deposition distribution of canopy. **(A)** Deposition distribution of three trials. **(B)** Deposition distribution in four layers.
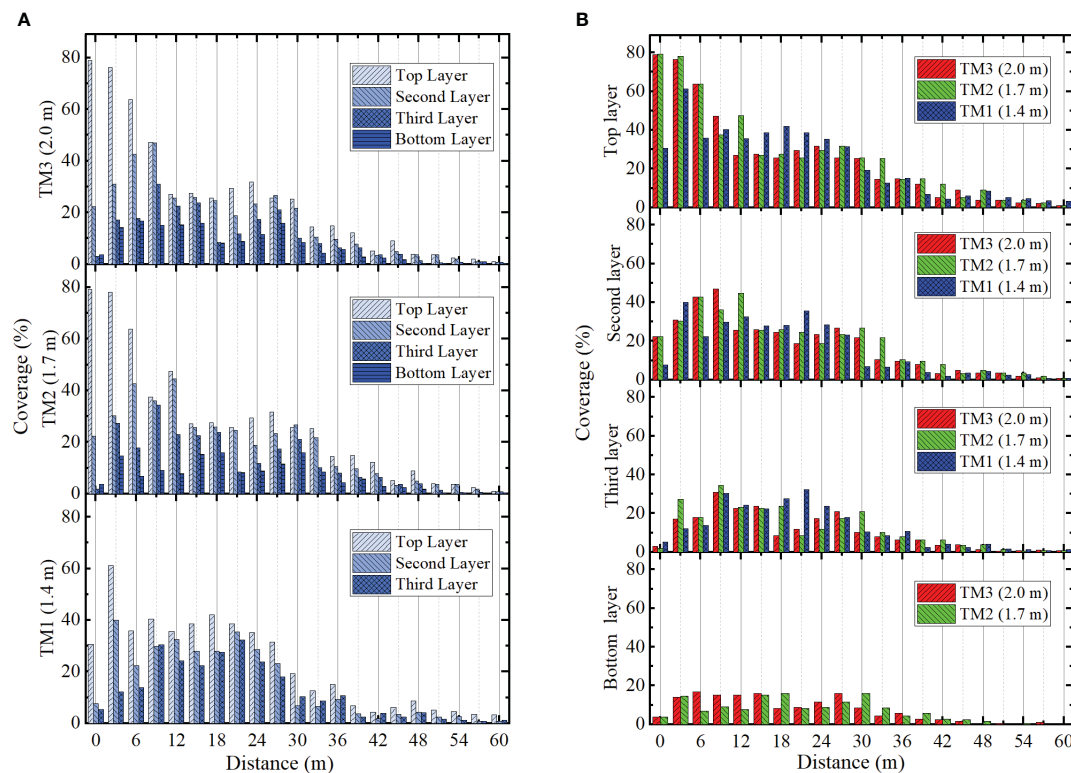
FIGURE 13

The coverage distribution of canopy. **(A)** Coverage distribution of three trials. **(B)** Coverage distribution in four layers.

layer, 15.2% in the second layer and 12.3% in the third layer (Figure 13A). The average coverage of TM2 was 26.9% in the top layer, 18.5% in the second layer, 12.0% in the third layer and 6.9% in the bottom layer. The average coverage of TM3 was 25.1% in the top layer, 17.0% in the second layer, 10.3% in the third layer and 7.3% in the bottom layer. TM2 and TM3 exhibited superior coverage than TM1. TM2 demonstrated better coverage than TM3 in the initial three layers and had inferior coverage in the bottom layer. In the range of 0 to 30 metres, the average coverage of TM1, TM2, and TM3 in the top three layers was measured as 28.9%, 30.4%, and 27.6% respectively. Conversely, in the range of 30 to 60 metres, the average coverage of TM1, TM2, and TM3 in the top three layers was measured as only 4.9%, 6.7%, and 4.8% respectively. Although the three trials satisfied the design requirements for droplet coverage within the 30 to 60 metres range, the spray coverage achieved only amounted to 15% to 18% of the total coverage.

In the top layer, TM1 exhibited more extensive coverage than TM2 and TM3 within the 12 to 24 metres range (Figure 13B). After 24 metres, the trend was consistent with TM2 and TM3. In the second layer, the coverage of the three trails exhibited consistency with the top layer from 12 to 24 metres. TM2 and TM3 maintained their dominance in the 24 to 42 metres range. In the third layer, the coverage of three trials experienced a decrease to 5% after 39 metres. In the bottom layer, the distribution of TM2 and TM3 coverage exhibited greater uniformity and still reached 2% at 45 metres range.

4 Conclusions

1. In view of the difficulty of plant spraying after the canopies cross the rows of maize and other crops, a powerful air-assisted remote sprayer which could be sprayed on the field road was designed. The adjustable air-assisted conveyor system and combined gas-liquid remote uniform spraying system were designed to achieve uniform and effective droplet coverage over the entire spraying area.

2. The wind-field test results showed that the wind field could reach more than 50 metres. The near-ground wind speed exceeded 5 m s^{-1} within the sampling interval from 10 to 35 metres. The wind field covered a concentrated spatial area and had a downward pressure trend, resulting in better drift resistance and penetration, which helped to transport droplets to the middle and lower parts of the crop.

3. The field test showed that the droplet deposition and coverage decreased gradually along the range direction, and the top layer had the highest deposition and coverage across the canopy. The upper canopy of the range of 0 to 12 metres range demonstrated a greater extent of coverage and deposition. However, there was no significant enhancement in the lower canopy, indicating that the multi-heads hydraulic nozzle has limited ability to penetrate this area.

The peak deposition area expanded from 9 to 33 metres in the lower canopy, with an average value of 3.77 µg cm^{-2}. This indicated that as the range extended, deposition in the lower and middle crop layers dispersed further, reflecting the advantages of a downward-pressure wind field.

Data availability statement

The original contributions presented in the study are included in the article/supplementary material. Further inquiries can be directed to the corresponding author.

Author contributions

YM: Conceptualization, Methodology, Validation, Writing – original draft, Writing – review & editing. XC: Formal Analysis, Methodology, Validation, Writing – review & editing. YG: Conceptualization, Funding acquisition, Project administration, Resources, Supervision, Writing – review & editing. DL: Investigation, Methodology, Writing – review & editing. JC: Resources, Writing – review & editing. GW: Data curation, Visualization, Writing – review & editing. XZ: Data curation, Investigation, Writing – review & editing.

Funding

Acknowledgments

Conflict of interest

The authors declare that the research was conducted in the absence of any commercial or financial relationships that could be construed as a potential conflict of interest.

Publisher's note

All claims expressed in this article are solely those of the authors and do not necessarily represent those of their affiliated organizations, or those of the publisher, the editors and the reviewers. Any product that may be evaluated in this article, or claim that may be made by its manufacturer, is not guaranteed or endorsed by the publisher.

References

Abd. Kharim, M. N., Wayayok, A., Mohamed Shariff, A. R., Abdullah, A. F., and Husin, E. M. (2019). Droplet deposition density of organic liquid fertilizer at low altitude UAV aerial spraying in rice cultivation. *Comput. Electron. Agr.* 167, 105045. doi: 10.1016/j.compag.2019.105045

Chang, K., Chen, S., Wang, M., Xue, X., and Lan, Y. (2023). Numerical simulation and verification of rotor downwash flow field of plant protection UAV at different rotor speeds. *Front. Plant Sci.* 13, 1087636. doi: 10.3389/fpls.2022.1087636

Czaczyk, Z. (2012). Influence of air flowdynamics on droplet size in conditions of air-assisted sprayers. *Atomization Spray.* 22 (4), 275–282-275 – 282. doi: 10.1615/AtomizSpr.2012003788

Dai, F. (2008). Selection and calculation of the blowing rate of air-assisted sprayers. *Plant Prot.* 34 (6), 124–127. doi: 10.3969/j.issn.0529-1542.2008.06.032

Derksen, R. C., Zhu, H., Ozkan, H. E., Hammond, R. B., Dorrance, A. E., and Spongberg, A. L. (2008). Determining the influence of spray quality, nozzle type, spray volume, and air-assisted application strategies on deposition of pesticides in soybean canopy. *Trans. ASABE* 51 (5), 1529–1537. doi: 10.13031/2013.25301

Gu, C., Zou, W., Wang, X., Chen, L., and Zhai, C. (2022). Wind loss model for the thick canopies of orchard trees based on accurate variable spraying. *Front. Plant Sci.* 13, 1010540. doi: 10.3389/fpls.2022.1010540

Guo, Q., Zhu, Y., Tang, Y., Hou, C., He, Y., Zhuang, J., et al. (2020). CFD simulation and experimental verification of the spatial and temporal distributions of the downwash airflow of a quad-rotor agricultural UAV in hover. *Comput. Electron. Agr.* 172, 105343. doi: 10.1016/j.compag.2020.105343

Hong, S.-W., Zhao, L., and Zhu, H. (2018). CFD simulation of airflow inside tree canopies discharged from air-assisted sprayers. *Comput. Electron. Agr.* 149, 121–132. doi: 10.1016/j.compag.2017.07.011

Hussain, M., Wang, Z., Huang, G., Mo, Y., Kaousar, R., Duan, L., et al. (2022). Comparison of droplet deposition, 28-homobrassinolide dosage efficacy and working efficiency of the unmanned aerial vehicle and knapsack manual sprayer in the maize field. *Agronomy* 12, 385. doi: 10.3390/agronomy12020385

Khot, L. R., Ehsani, R., Albrigo, G., Larbi, P. A., Landers, A., Campoy, J., et al. (2012). Air-assisted sprayer adapted for precision horticulture: Spray patterns and deposition

assessments in small-sized citrus canopies. *Biosyst. Eng.* 113 (1), 76–85. doi: 10.1016/j.biosystemseng.2012.06.008

Kumar, S. P., Roul, A. K., Nandede, B. M., Bikram, J., and Chethan, C. R. (2021). Development of small tractor operated boom sprayer for effective control of weeds in maize. *Indian J. Weed Sci.* 53 (2), 173–178. doi: 10.5958/0974-8164.2021.00032.0

Li, J. P., Bian, Y. L., Huo, P., Wang, P. F., Xue, C. L., and Yang, X. (2021). Design and experimental optimization of spray device for air-fed annular nozzle of sprayer. *Trans. Chin. Soc Agric. Mach.* 52 (9), 79–88. doi: 10.6041/j.issn.1000-1298.2021.09.009

Qin, W. C., Chen, P. Y., and Wang, B. K. (2023). Productivity model and experiment of field crop spraying by plant protection unmanned aircraft. *Front. Plant Sci.* 14, 1168228. doi: 10.3389/fpls.2023.1168228

Ru, Y., Chen, X. Y., Liu, B., Wang, S. J., and Lin, M. (2022). Optimized design and performance test of axial flow orchard sprayer air delivery system. *Trans. Chin. Soc Agric. Mach.* 53 (5), 147–157. doi: 10.6041/j.issn.1000-1298.2022.05.015

Sarri, D., Martelloni, L., Rimediotti, M., Lisci, R., Lombardo, S., and Vieri, M. (2019). Testing a multi-rotor unmanned aerial vehicle for spray application in high slope terraced vineyard. *J. Agric. Eng.* 50 (1), 38–47. doi: 10.4081/jae.2019.853

Sinha, R., Ranjan, R., Khot, L. R., Hoheisel, G. A., and Grieshop, M. J. (2019). Drift potential from a solid set canopy delivery system and an axial–fan air–assisted sprayer during applications in grapevines. *Biosyst. Eng.* 188, 207–216. doi: 10.1016/j.biosystemseng.2019.10.015

Thakare, S. K., Saraf, V. V., and Deshmukh, M. (2015). Field evaluation of air assisted sleeve boom sprayer. *Madras Agric. J.* 102 (September), 273–276. doi: 10.29321/maj.10.001117

Wang, B., Zhang, D., Yang, L., and Wang, L. (2014). Gate-type spray system of high-frame corn spayer. *Trans. Chin. Soc Agric. Mach.* 45 (6), 104–111. doi: 10.6041/j.issn.1000-1298.2014.06.017

Wang, J., Dong, X., Yan, H., Wang, J., Zhang, T., and Zeng, Y. (2015). Experiment on spraying performance of air-assisted boom sprayer in corn field. *Trans. Chin. Soc Agric. Mach.* 46 (7), 79–84. doi: 10.6041/j.issn.1000-1298.2015.07.012

Wang, L., and Lu, Y. Y. (2020). Spreading trend predication of fall armyworm, Spodoptera frugiperda, in year of 2020 in China. *J. Environ. Entomol.* 42 (5), 1139–1145. doi: 10.3969/j.issn.1674-0858.2020.05.13

Wang, W., Xie, J., Chen, L., Liu, L., Quan, L., and Liu, L. (2021). Design and experiment of 3YZ-80A crawler self-propelled corn interrow sprayer. *Trans. Chin. Soc Agric. Mach.* 52 (09), 106–114. doi: 10.6041/j.issn.1000-1298.2021.09.012

Wei, X. H., Shao, J., Xie, L. G., and Lv, X. L. (2016). Design and experiment of air-assisted cotton boom sprayer with separating row and spraying in inside and upper canopy. *Trans. Chin. Soc Agric. Mach.* 47, 101–107 and 190. doi: 10.6041/j.issn.1000-1298.2016.01.014

Wu, Y. Q., Lin, L. H., Hou, J., Yuan, J., Liu, X. M., and Liu, X. F., (2018). Design and experiment of high clearance boom sprayer with air-assisted system. *J. Agric. Sci.* 40 (07), 55–61. doi: 10.13427/j.cnki.njyi.2018.07.010

Yang, P. Y., Zhu, X. M., Guo, J. F., and Wang, Z. Y. (2019). Strategy and advice for managing the fall armyworm in China. *Plant Prot.* 45 (4), 1–6. doi: 10.16688/j.zwbh.2019260

Zhan, Y. L., Chen, P. C., Xu, W. C., Chen, S. D., Han, Y. F., Lan, Y. B., et al. (2022). Influence of the downwash airflow distribution characteristics of a plant protection UAV on spray deposit distribution. *Biosyst. Eng.* 216, 32–45. doi: 10.1016/j.biosystemseng.2022.01.016

Zhou, L. F., Zhang, L., Ding, W. M., Xue, X. Y., and Sun, Z. (2015). Droplet coverage response surface models and influencing factors of air-assisted electrostatic spray. *Trans. Chin. Soc Agric. Eng.* 31(Supp. 2), 52–59. doi: 10.11975/j.issn.1002-6819.2015.z2.008

Research on a UAV spray system combined with grid atomized droplets

Xiuyun Xue[1,2,3,4], Yu Tian[1], Zhenyu Yang[1], Zhen Li[1,2,3,4]*,
Shilei Lyu[1,2,3,4], Shuran Song[1,2,3] and Daozong Sun[1,2,3]

[1]College of Electronic Engineering (College of Artificial Intelligence), South China Agricultural
University, Guangzhou, China, [2]Division of Citrus Machinery, China Agriculture Research System
of Ministry of Finance the People 's Republic of China and Ministry of Agriculture and Rural
Affairs of the People 's Republic of China, Guangzhou, China, [3]Guangdong Provincial Agricultural
Information Monitoring Engineering Technology Research Center, Guangzhou, China, [4]Pazhou
Lab, Guangzhou, China

Backgrounds: UAVs for crop protection hold significant potential for application in mountainous orchard areas in China. However, certain issues pertaining to UAV spraying need to be addressed for further technological advancement, aimed at enhancing crop protection efficiency and reducing pesticide usage. These challenges include the potential for droplet drift, limited capacity for pesticide solution. Consequently, efforts are required to overcome these limitations and optimize UAV spraying technology.

Methods: In order to balance high deposition and low drift in plant protection UAV spraying, this study proposes a plant protection UAV spraying method. In order to study the operational effects of this spraying method, this study conducted a UAV spray and grid impact test to investigate the effects of different operational parameters on droplet deposition and drift. Meanwhile, a spray model was constructed using machine learning techniques to predict the spraying effect of this method.

Results and discussion: This study investigated the droplet deposition rate and downwind drift rate on three types of citrus trees: traditional densely planted trees, dwarf trees, and hedged trees, considering different particle sizes and UAV flight altitudes. Analyzing the effect of increasing the grid on droplet coverage and deposition density for different tree forms. The findings demonstrated a significantly improved droplet deposition rate on dwarf and hedged citrus trees compared to traditional densely planted trees and adopting a fixed-height grid increased droplet coverage and deposition density for both the densely planted and trellised citrus trees, but had the opposite effect on dwarfed citrus trees. When using the grid system. Among the factors examined, the height of the sampling point exhibited the greatest influence on the droplet deposition rate, whereas UAV flight height and droplet particle size had no significant impact. The distance in relation to wind direction had the most substantial effect on droplet drift

rate. In terms of predicting droplet drift rate, the BP neural network performed inadequately with a coefficient of determination of 0.88. Conversely, REGRESS, ELM, and RBFNN yielded similar and notably superior results with a coefficient of determination greater than 0.95. Notably, ELM demonstrated the smallest root mean square error.

1 Introduction

Agricultural aviation crop protection has significant advantages such as low terrain restrictions, high spray efficiency, and the ability of downdrafts to promote droplet deposition on both sides of the leaves (He et al., 2017). However, the formulation used in the current unmanned aerial vehicle (UAV) crop protection spraying operation is typically based on ground-based machinery. Due to the limited payload capacity of UAVs, the application rate per unit area needs to be reduced to ensure a certain operational efficiency. To achieve the same operational effect, it is necessary to increase the concentration of the liquid and reduce the size of the droplets. However, high-concentration and small-droplet sprays are prone to problems such as pesticide evaporation and drift, resulting in pesticide waste and pollution (Hilz and Vermeer, 2013; Lou et al., 2018). Therefore, there is an urgent need to develop efficient crop spraying techniques for agricultural aviation to reduce secondary disasters and improve the utilization rate of agricultural pesticides (Hu et al., 2022).

To improve the deposition rate and reduce the drift rate of pesticide solutions on targets, researchers have explored the relationship between the number of rotors, flight speed, and altitude of unmanned aerial vehicles (UAVs) and the quality of droplet deposition and spraying effectiveness, aiming to further improve the efficiency of UAV plant protection spraying. Martinez-Guanter (2020) compared the drift of wind-sent sprayers and ultra-low volume variable sprayers using water-sensitive paper set up between fruit trees, and the experimental results showed that ultra-low volume UAVs could effectively reduce drift and improve pesticide utilization. Hunter et al. (2020) used UAV imagery for pest mapping and combined it with UAV sprayers to provide a new strategy for integrated pest management, which could improve pesticide use efficiency, reduce pesticide use, and improve the detection and control of weed escape and delay the evolution of weed resistance to herbicides. Sarri et al. (2019) collected droplets using water-sensitive paper and studied the distribution of droplet deposition and spraying efficiency in a small mountain vineyard using a spray gun, a backpack sprayer, and a UAV. The results showed that the working capacity of the UAV was twice that of the spray gun and 1.6 times that of the backpack sprayer. The coverage

and deposition density of droplets were influenced by the sampling point location and the type of sprayer used. Biglia et al. (2022) investigated the effect of different UAV spraying parameters on crown spray deposition and coverage, and the experimental results showed that the flight mode had the greatest impact on spraying efficiency. Compared with the broadcast spraying mode, the strip spraying mode could increase the average crown deposition by 209% and reduce the average ground loss by 54%.

Currently, when unmanned aerial vehicles (UAVs) are used for crop spraying, the droplet size of the spray is small, which makes it susceptible to drift under the influence of environmental wind and downwash from the UAV. The larger the droplet size, the less likely it is to drift, but the deposition rate of the droplets decreases accordingly. It is often difficult to balance between a high deposition rate and low drift in UAV spraying. To address this issue, the characteristic of secondary atomization of liquid droplets after hitting a mesh can be utilized. UAVs can spray larger droplets first and then these droplets can hit the mesh and atomize into smaller droplets when approaching the target, thus achieving the advantages of low drift for larger droplets and high deposition rate for smaller droplets.

When droplets interact with a mesh, they undergo various dynamic processes such as collision, penetration, and fragmentation, which are influenced by both mesh parameters and droplet properties. Liao et al. (2022) analyzed the dynamic behavior of liquid film on stainless steel mesh surface using CFD simulations and studied the effects of different experimental conditions on the wetted area and film thickness. Ryu et al. (2017) investigated the phenomena of droplet penetration or adhesion during the process of droplet impact on mesh structures, and explored the impact factors such as droplet collision velocity, size, and mesh properties. The experimental results showed that droplets are more likely to undergo penetration and fragmentation after impact on the mesh as the droplet velocity or size increases. In addition, superhydrophobic surfaces are more likely to cause droplet penetration or rebound as a whole than ordinary surfaces. Sun et al. (2023) used high-speed cameras to study the liquid flow and rupture behavior of two liquid jets after impact on a stainless steel mesh. Kooij et al. (2019) investigated the effects of droplet properties and mesh impact

velocity on the maximum spreading diameter and water droplet penetration mass after droplet impact on the mesh using experiments and simulation. Soto et al. (2018) studied the process of droplet impact on single holes and meshes and found that a conical atomization zone is formed beneath the mesh when the droplet impacts on the mesh, and the spray angle of this atomization zone increases as the velocity gradually increases. Moreover, when the velocity reaches a certain level, the spray angle tends to a fixed size that is related to the properties of the mesh, and when the velocity increases further, there is no significant change in the spray angle. Sidawi et al. (2022) investigated the spray mass fraction that penetrates through the mesh after conical spraying impacts a vertical and horizontal mesh. Moitra et al. (2021) studied the water leap phenomenon before penetration, penetration speed, and the distribution of droplets beneath the mesh after penetration by changing droplet properties (density, surface tension, and viscosity) and metal mesh properties (aperture and wire diameter).

Grid atomization technology uses a fine, structurally regular grid that allows droplets to pass through and break into smaller particle sizes upon impact, a characteristic that provides new and efficient system design ideas for agricultural plant protection spraying. The application of this technology can effectively improve the utilization rate of liquid solution and reduce waste. In this technique, the droplets form a jet after impacting the grid, and then the jet is broken into sub-droplets under the action of Rayleigh-Plateau instability, thus realizing the fine treatment of droplets and the optimization of spraying effect. The droplet impact grid process is shown in Figure 1. However, the current theoretical study mainly focuses on the case of a single droplet impacting the grid, in order to better apply the grid atomization technology in plant protection spraying, it is necessary to carry out an in-depth study on the impact of the spray composed of multiple droplets with the grid, and reasonably extend the theoretical study of a single droplet to the spray system, and further improve the theory through experimental verification.

Machine learning is a branch of artificial intelligence that can quickly discover potential patterns behind data, reduce model computation complexity, and increase model construction speed. Compared with CFD simulation, it reduces computation complexity and improves efficiency (Mosavi et al., 2018). Machine learning methods have been well applied in agriculture, biomedical and other fields (McKinney et al., 2006; Yildiz et al., 2017; Wenwen et al., 2018). Guo et al. (2020) used machine learning methods to predict the droplet size in the overlapping area of dual UAV nozzles. He et al. (2022) established quantitative models of different hollow cone nozzles' volume median diameter (VMD) and relative span (RS) based on machine learning methods.

This study employed a combination of UAV spraying and grid atomization to examine the impact of UAV flight altitude, droplet size, and the presence of a grid on droplet deposition on target trees and downwind drift. Four machine learning methods were utilized to forecast droplet deposition and drift, resulting in the development of quantitative models. Significantly, this study represents the pioneering attempt to integrate UAVs with grid atomization to achieve a balance between high droplet deposition and minimal drift, while employing machine learning techniques for the prediction of droplet deposition and drift.

2 Materials and methods

2.1 UAV spray test method

The DJI T40 plant protection UAV used in the spray experiments features a coaxial dual-rotor design and is equipped with intelligent mapping, binocular visual perception, dual spray systems, and active phased array radar. The key parameters of the T40 are presented in Table 1.

Before conducting the UAV spraying experiment, a distilled water solution with a concentration of 0.5 g/L of methyl orange dye was prepared as the spray liquid. Water-sensitive paper (Chongqing LiuLiu Shanxia Plant Protection Technology Co., Ltd., with a rectangular shape of 76 mm × 26 mm), filter paper (Shanghai Peninsula Industrial Co., Ltd., with a pore size of 0.22 μm and a circular shape with a diameter of 50 mm), and nylon rope (Xiangyu Rope Net) were used as droplet collection devices. A wind speed meter (WindMaster Pro, Gill Ltd., UK) was used to monitor the environmental wind during the experiment. An oscillator and a UV spectrophotometer (UV-752, Shanghai Tianpu Analytical Instrument Co., Ltd.) were used to process the droplet collector to obtain data.

The experiment was conducted at the Citrus Research Institute in Ganzhou City, Jiangxi Province, from August 22 to 27, 2022. Prior to commencing the experiment, four air-suspended droplet samplers were designed and constructed using rigid PVC pipes with a diameter of 20 mm. These samplers were shaped as rectangular frames measuring 2 m × 1 m in height and width. To measure the
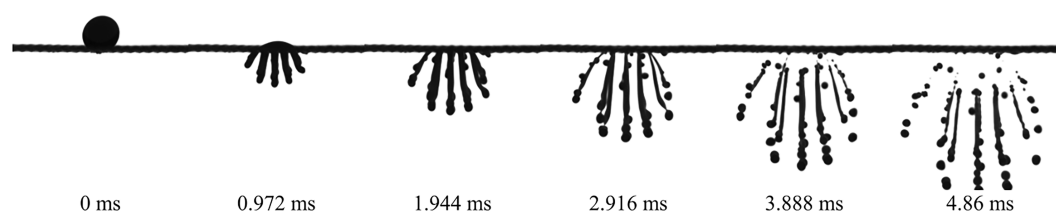

| 0 ms | 0.972 ms | 1.944 ms | 2.916 ms | 3.888 ms | 4.86 ms |

FIGURE 1
The process of liquid droplets impacting the mesh and breaking (ms= milliseconds).

Key parameters of UAV	
Work box volume	40 L
Number of nozzles	2
Nozzle type	Centrifugal nozzle
Atomized particle size	50 - 300 μm
Spray width	4 - 11 m
maximum flow	6 L/min * 2

drift rate of airborne droplets, samplers were positioned at distances of 3, 5, 10, and 15 m downwind from the fruit trees, starting from the UAV spraying edge. Six different heights were considered for testing, with measurements taken at varying distances from the ground. Each air-suspended droplet sampler featured a 1 m long nylon rope, with nylon ropes set at 0.3 m intervals along the sampler frame. Six nylon ropes were allocated to each sampler, resulting in a total of 24 nylon ropes used for droplet collection in a single experiment. Both ends of each nylon rope were securely fastened to the frame using 25 mm snap hooks, ensuring that the ropes remained taut and free from any bending or deformation.

In order to assess the dispersion pattern of drifting droplets on the ground in the downwind direction, the experimental setup followed the guidelines outlined in the ISO 22866 field testing standard for spray drift. Three Plastic Petri dishes, each with a diameter of 15 cm, were positioned at distances of 3, 5, 10, and 15 m downwind from the unmanned aerial vehicle spray swath edge. These Petri dishes were placed parallel to the flight path of the UAV. Within each dish, a water-sensitive paper and a filter paper were carefully arranged. A total of 12 Plastic Petri dishes were employed in a single testing session. The three fruit tree planting areas are shown in Figure 2A and the experimental layout is shown in Figure 2B.

For the experiment, an open flat area adjacent to a fruit tree was chosen as the designated test zone. The selected area exhibited no prominent obstacles in its immediate vicinity. To determine the drone flight route, the direction of the environmental wind was taken into consideration. The airborne droplet samplers were aligned parallel to each other, following the downwind direction and perpendicular to the wind direction. The ground drift collection device was positioned adjacent to the airborne droplet samplers, running parallel to them.

A 3D wind speed sensor bracket was erected near the test site, ensuring it did not interfere with the spraying process. Along the UAV flight route, two trees with similar growth conditions were identified. Above one of these trees, an aluminum frame with dimensions of 2.5 m (length) × 0.7 m (width) × 2 m (height) was installed. This aluminum frame featured a mesh attached to it, characterized by an aperture size of 350 μm. Refer to Figure 3 for a visual representation of this setup.

During the course of the experiment, two fruit trees were divided into three levels: upper, middle, and lower, with a 0.5 m gap between each level. Each level was further subdivided into three lines: front, middle, and back, with a spacing of 0.5 m. Additionally, each level was divided into left, middle, and right lines, and sampling points were established at the intersections of these lines, resulting in a total of 27 sampling points.

The three levels were labeled as A, B, and C, with A1, A2, and A3 representing the front, middle, and back positions of level A, respectively. The left, middle, and right points were denoted as A1-1, A1-2, A1-3, A2-1, A2-2, A2-3, A3-1, A3-2, and A3-3. At each sampling point, two water-sensitive papers and two filter papers were fixed using paperclips on the front and back sides, without overlapping. The morphology of the three fruit trees is shown in Figure 4A, and the water-sensitive paper arrangement of the target fruit trees is shown in Figure 4B.

In accordance with the ISO 22866 standard, the acceptable wind speed for lateral environmental wind drift tests ranged from 1.0 to 5.0 m/s (at a height of 2 m), with a permissible wind direction angle
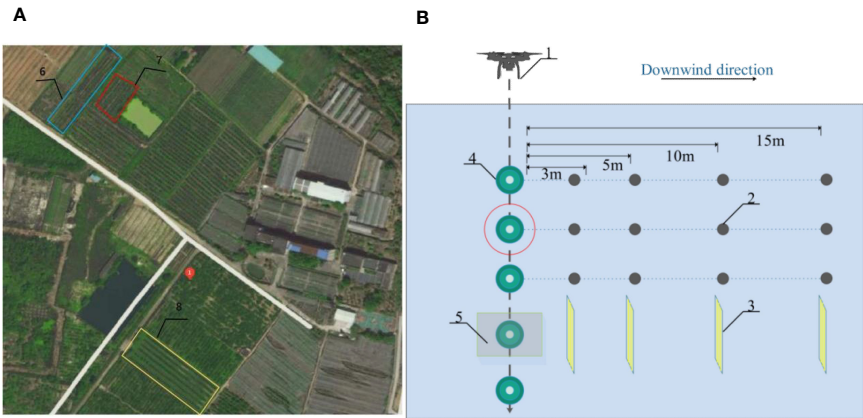

FIGURE 2
Schematic diagram of UAV test ((A) Three fruit tree planting areas (B) Experimental sampling point layout 1. Plant protection UAV; 2. Ground fog droplet collection device; 3. Aerial fog droplet sampler; 4. Citrus tree; 5.350mm aperture mesh; 6.Trellised citrus tree planting areas; 7.Dwarfed citrus tree planting areas; 8.Densely planted citrus tree planting areas).

FIGURE 3
Placement of mesh.

deviation of 90° ± 30° from the flight route. The flow rate of the plant protection UAV was calibrated, and real-time monitoring of wind speed and direction was carried out. Once the wind speed and direction met the standard requirements and remained stable for one minute, a methylene orange solution was introduced into the tank.

The experimental trees comprised three types of citrus trees, namely dwarf, hedge-style, and dense planting. The flight path of the UAV was pre-determined, with the UAV flying vertically over the trees at a height of 2, 3, or 4 m. The UAV maintained a speed of 2 m/s while spraying pesticide at a rate of 50 L/hm2. The nozzle sprayed droplets with sizes of very coarse, medium, and very fine, according to the instructions in the plant protection UAV manual, the three particle sizes are 140μm, 100μm and 60μm respectively.

The UAV followed the designated tree route, conducting spraying during the flight. After completing one spraying operation, the UAV avoided the sampling point area to prevent interference with the data. It then returned to the takeoff point.

Once the water-sensitive papers, filter papers, and nylon ropes at the sampling points were completely dry, they were collected using forceps and immediately placed in self-sealing plastic bags sized 22 cm × 15 cm to avoid cross-contamination between samples. Each experimental condition was repeated three times, and the final data was averaged. After concluding the full day of experiments, all samples (including water-sensitive papers, filter papers, and nylon ropes) were transported to a cool, dark storage location for further analysis and uniform processing.
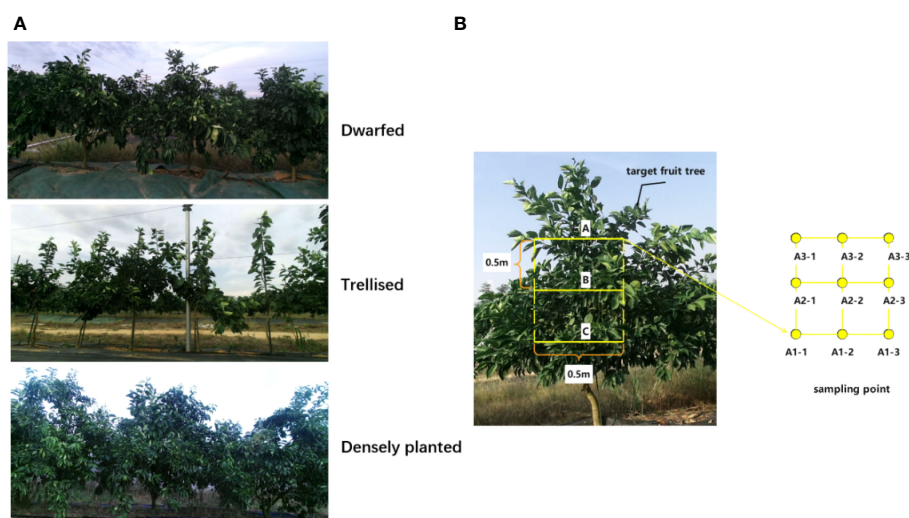

FIGURE 4
Three forms of trees and target fruit tree sampling site layout ((**A**) Three tree-shaped fruit trees (**B**) Sampling point arrangement of target fruit trees).

2.2 Machine learning methods

Prior to training the quantitative model, the dataset in this study was divided into training and prediction sets at a ratio of 3:1, ensuring the model's robustness. To explore the meaningful relationship between the independent and dependent variables, a one-way ANOVA analysis was conducted on the data using SPSS software.

The study employed four primary machine learning algorithms, which are as follows:

(1) Multi-dimensional non-linear regression analysis was conducted using the REGRESS function in MATLAB software, which employs orthogonal least squares method and has been widely used in biomedical and financial fields (Arnisigo et al., 2008; Steed et al., 2009; Lü et al., 2014). The REGRESS function calculates the estimated ratio of the observation value residuals to their standard deviation using orthogonal least squares method. The resulting value is t-distributed with a certain degree of freedom, and the function returns the offset of the t-distribution confidence interval with the residuals as the center (Hoaglin and Kempthorne, 1986). The significance of the model was evaluated using the F statistic, with a significance level of 0.05 in this study, and the confidence interval for the estimated values was set at 95%.

(2) The Back Propagation Neural Network (BPNN) belongs to the multi-layer feedback network category. It uses the Back Propagation algorithm for training, which does not require an explicit functional relationship between input and output vectors before training. The algorithm uses gradient descent to iteratively adjust the biases and weights of each layer in the network to minimize the error between predicted and expected outputs. During the Back Propagation process, the network updates the weight values of each neuron to adjust the parameters of the neural network, improving its predictive ability. When the error reaches its minimum value, the calculated output of the input value is closest to the expected output, which is used as the predicted value.

(3) Extreme Learning Machine (ELM) is a type of feedforward neural network that does not require gradient-based backpropagation to adjust weights. Instead, ELM sets the weight values using the Moore-Penrose generalized inverse matrix and has only one hidden layer, resulting in extremely fast computation speeds (Huang et al., 2006).

(4) The Radial Basis Function Neural Network (RBFNN) is a feedforward neural network with a 3-layer structure, consisting of an input layer, a hidden layer with radial basis functions (RBF) as activation functions, and an output layer. This machine learning method is widely used for classification and regression analysis due to its fast training speed and strong generalization ability (Schalkoff, 1997).

2.3 Performance evaluation

2.3.1 Droplet deposition rate/drift rate analysis method

The water-sensitive papers from the samples were scanned using a scanner at a grayscale resolution of 600 dpi. The obtained images were subsequently processed using ImageJ software to determine the density and coverage of the spray deposition. As for the filter paper samples, they were placed in plastic self-sealing bags along with 50 mL of distilled water. These bags were subjected to oscillation at a frequency of 200 r/min for a duration of 30 minutes to extract the chemicals. The resulting eluates were then analyzed using a UV-Vis spectrophotometer to measure the absorbance specifically at a wavelength of 465 nm. Based on these measurements, the deposition and drift amounts were calculated.

To measure the deposition and drift of droplets on filter paper and nylon rope, a UV-752 UV/visible spectrophotometer (Shanghai Tiantu Analytical Instrument Co., Ltd.) was used to calibrate the concentration-absorbance relationship. A linear regression equation was derived through linear fitting, correlating the methyl orange concentration (a) in mg/L with the absorbance value (b) of the test solution. For the filter paper, 10 mL of distilled water was added to the self-sealing bag containing the sample. Similarly, for the nylon rope, 50 mL of distilled water was added to its respective self-sealing bag. These bags were then oscillated on an oscillator at a frequency of 200 r/min for a duration of 30 minutes. Subsequently, 3 mL of eluent was extracted using a pipette, and its absorbance value was measured at a detection wavelength of 465 nm using the UV-752 UV/visible spectrophotometer. The methyl orange concentration was determined by utilizing the previously established regression curve. Finally, the deposition rate of droplets was calculated based on Formulas 1, 2.

$$\beta = \frac{Ce_1 \times V}{Ce_2 \times S} \tag{1}$$

$$\beta_{dep\%} = \frac{\beta}{\beta_v} * 100\% \tag{2}$$

Where β is the deposition of droplets per unit area(μL/cm^2); Ce_1 is the concentration of methyl orange in the elution solution(mg/L); V is the volume of elution solution added(μL); Ce_2 is the concentration of methyl orange in the spray solution(mg/L); S is the area of the droplet collector(cm^2); $\beta_{dep\%}$ is the deposition/drift rate(%); β_v is the application rate(L/m^2).

2.3.2 Analysis method of droplet ground drift rate

In this study, the Average Average Drift Rate (AADR) is used to indicate the extent of droplet drift. AADR represents the average of all data means at each downwind distance during each spray operation. The calculation is shown in Formulas 3:

$$AADR = \frac{\sum_{i=1}^{n} \bar{\beta}_{dep\%i}}{n} \tag{3}$$

Where $\overline{\beta}_{dep\%i}$ is the mean drift rate of the i-th group at downwind distance; n represents the number of sampling groups at different downwind distances.

According to ISO 22866 standard, the percentage of cumulative drift of droplets $\beta_{total\%}$ from the edge of the spray plume to a downwind distance x, relative to the total drift, is defined as the cumulative drift ratio of droplets $\beta_{cum\%}$. The downwind distance at which $\beta_{cum\%}$ reaches 90% is defined as the 90% cumulative drift distance $x_{90\%}$. The calculation method is shown in Formulas 4, 5:

$$\beta_{cum\%} = \frac{\int_1^x \beta_{dep\%}(x)dx}{\beta_{total\%}} \times 100\% \qquad (4)$$

$$\beta_{total\%} = \int_1^{x_m} \beta_{dep\%}(x)dx \qquad (5)$$

Where $\beta_{dep\%}(x)$ represents the drift rate at a downwind distance of $x(\%)$; x_m represents the distance from the edge of the spray plume to the farthest ground-level droplet collector(m).

2.3.3 Analysis method of droplet drift rate in air

h_r represents the relative feature height, indicating the relative position of the center of droplet drift distribution on the droplet collection framework. A higher relative feature height indicates a greater extent of airborne droplet drift at the current downwind distance. The calculation method for the relative feature height is shown in Formula 6:

$$h_r = \frac{s \cdot \sum_{i=1}^{n_p} \beta_{dep\%i} h_i}{h_{max}} \qquad (6)$$

Where s represents the distance between each nylon rope in the airborne droplet sampler (0.3 m); n_p represents the number of nylon ropes on each droplet collection device ($n_p = 10$); $\beta_{dep\%i}$ represents the drift rate of droplets on the i-th nylon rope; h_i represents the height of the i-th nylon rope in meters; h_{max} represents the height of the highest nylon rope ($h_{max} = 1.8m$).

2.3.4 Quantitative model analysis method

This study evaluates the performance of various machine learning quantitative models using the Coefficient of Determination (R^2) and Root Mean Squared Error (RMSE). R^2, also known as the multiple correlation coefficient, is defined as the ratio of variances in the regression model. This definition makes it a measure of the success rate of predicting the dependent variable from the independent variables (Nagelkerke, 1991). R_t^2 and R_p^2 are the determination coefficients for the training set and the prediction set, respectively, indicating the accuracy of the predictive model. RMSE is used to measure the error of the model, including the Root Mean Squared Error of the training set (RMSET) and the Root Mean Squared Error of the prediction set (RMSEP). A smaller RMSE indicates better performance and higher accuracy of the model. R2 and RMSE can be calculated using Formulas 7, 8.

$$R^2 = \left(\frac{\sum_{i=1}^N (\hat{y}_i - \overline{\hat{y}})(y_i - \overline{y})}{\sqrt{\sum_{i=1}^N (\hat{y}_i - \overline{\hat{y}})^2 (y_i - \overline{y})^2}} \right)^2 \qquad (7)$$

$$RMSE = \sqrt{\frac{\sum_{i=1}^N (y_i - \hat{y}_i)^2}{N - 1}} \qquad (8)$$

where y_i and $\hat{y}_i$ are the measured value and the predicted value of the i-th sample, $\overline{y}$ and $\overline{\hat{y}}$ are the average values of measured and predicted values, respectively; N is the number of samples.

3 Results and discussion

3.1 Droplet coverage and deposition density

The images of water-sensitive paper were processed using ImageJ software to quantify the coverage and deposition density of droplets at each sampling point. Subsequently, the average droplet coverage and deposition density on the front and back surfaces of leaves from various tree forms, with and without a grid, were calculated. The results are presented in Figures 5, 6.

The analysis of Figure 5 reveals that, in the absence of grid placement, the average droplet coverage on the front side of the fruit trees across the three tree forms ranged from 2.96% to 6.89%, while on the reverse side it varied between 0.16% and 0.77%. With grid placement, the average droplet coverage on the front side of the fruit trees of the three tree forms ranged between 3.29% and 9.22%, and between 0.5% and 1.34% on the reverse side. The introduction of the grid led to an improvement in droplet coverage on the reverse side for all three tree forms, resulting in an increase of 0.27% for dwarfed citrus trees, 0.57% for trellised citrus trees, and 0.34% for densely planted types. Conversely, the grid placement resulted in a decrease in droplet coverage by 2.5% on the front side of dwarfed citrus trees, while increasing droplet coverage by 4.24% on trellised citrus trees, and exhibiting the most significant increase of 5.98% on the densely planted citrus trees.

The analysis of Figure 6 reveals that, in the absence of the grid, the average droplet deposition density on the front side of the three forms of tree ranged from 28.45 drops per square centimeter to 53.45 drops per square centimeter, while on the reverse side it varied between 2.46 drops per square centimeter and 34.14 drops per square centimeter. With the grid placement, the average droplet deposition density on the front side of the three tree forms ranged between 24.9 drops per square centimeter and 110.71 drops per square centimeter, and between 7.29 drops per square centimeter and 35.48 drops per square centimeter on the reverse side. The introduction of the grid led to an improvement in the mean droplet deposition density on the reverse side of the three tree forms, although the improvement was not statistically significant. However, the addition of grids had a significant impact on the frontal droplet deposition density for trellised and the densely planted citrus trees. The frontal droplet deposition density increased
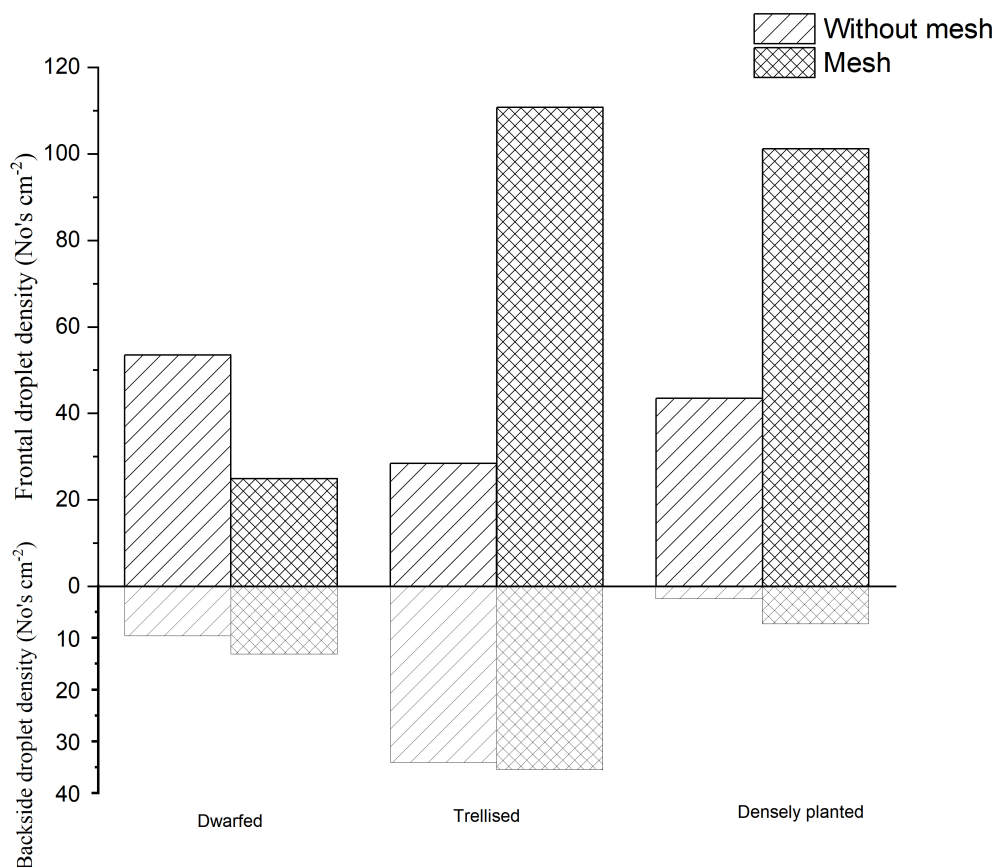
FIGURE 5
Coverage of droplets in different tree forms.

by 82.26 drops per square centimeter (289%) for the densely planted citrus trees and by 57.62 drops per square centimeter (132%) for the densely planted citrus trees. In contrast, the mean frontal droplet deposition density of dwarfed citrus trees decreased by 28.55 drops per square centimeter due to the addition of the grid.

Increasing the grid has shown clear improvements in droplet deposition density and coverage on the front side of trellised and the densely planted citrus trees. However, for dwarfed citrus trees, the addition of the grid resulted in a decrease in droplet deposition density and coverage on the front side of the tree. This can be attributed to the fixed height of the grid, which causes dwarfed citrus trees to be farther away from the grid compared to the other two types of trees. The droplets produced by the grid undergo a second atomization, resulting in smaller particle sizes. These smaller droplets are more susceptible to drift during their movement towards the dwarfed citrus trees. As a result, the droplets may not reach the intended target as effectively, leading to a decrease in droplet deposition density and coverage on the front side of the dwarfed citrus trees.
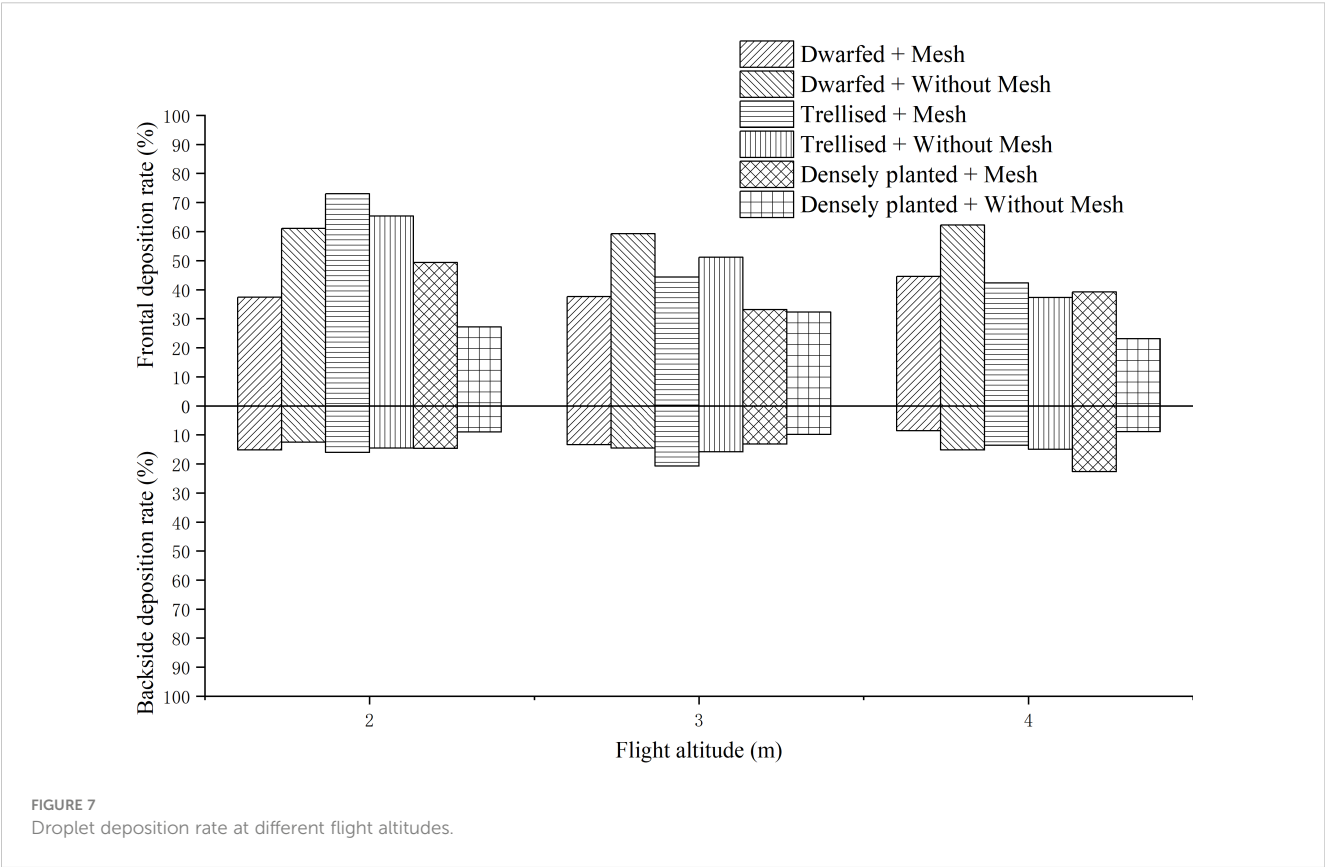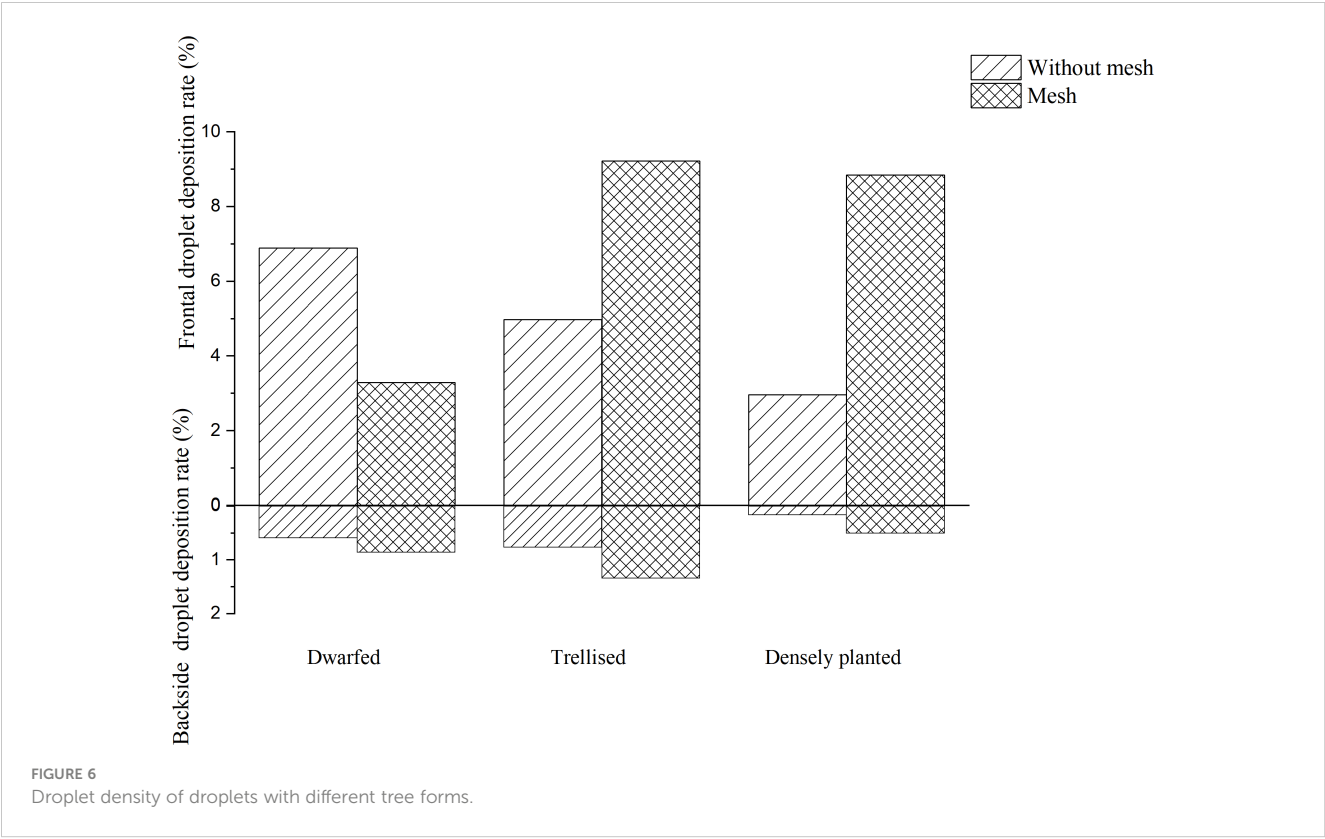
3.2 Droplet deposition rate

The deposition rates of droplets on the adaxial and abaxial surfaces of three citrus tree leaf forms at different flight heights were determined by measuring filter papers, as shown in Figure 7.

Based on the observations from Figure 7, it can be noted that the deposition rates of droplets on the upper (adaxial) surface of the leaves range from 23% to 73%, while the deposition rates on the lower (abaxial) surface range from 8.57% to 22.61%. As the flight height of the UAV increases, the deposition rate on the adaxial surface gradually decreases. The maximum deposition rate of 52.21% is observed at a flight height of 2 m, which is higher by 9.26 and 10.76 percentage points compared to the rates at 3 m (42.95%) and 4 m (41.45%), respectively. On the other hand, the flight height has a lesser impact on the deposition rate on the abaxial surface, as the rates remain relatively consistent across the three flight heights.

Among the three forms of citrus trees, the densely planted trees exhibit the lowest deposition rate on the adaxial surface, with an average of 34.04%. In contrast, the average deposition rates on the adaxial surface of dwarfed and trellised citrus trees exceed 50%, measuring at 50.34% and 52.22%, respectively. This indicates that the deposition rates on dwarfed and trellised citrus trees are higher compared to traditionally densely planted citrus trees. This can be attributed to the smaller canopy size of dwarfed and trellised citrus trees, which allows droplets to penetrate the canopy and deposit on the lower parts.

The average deposition rates of droplets with and without the placement of grids on citrus trees are 44.51% and 46.55%, respectively. This suggests that the placement of grids has

FIGURE 6
Droplet density of droplets with different tree forms.

FIGURE 7
Droplet deposition rate at different flight altitudes.

minimal effect on the deposition rate of droplets on citrus trees, resulting in only a 2.04 percentage point decrease on average.

The deposition rates of droplets on the adaxial and abaxial surfaces of three citrus tree leaf forms at different droplet sizes, as measured using filter papers on citrus trees, are shown in Figure 8.

Based on the observations from Figure 8, it can be noted that among the three different sizes of droplets, the deposition rate on the upper (adaxial) surface is highest for medium-sized droplets, averaging at 55.39%. The deposition rates for very coarse and very fine droplets are comparatively lower, measuring at 45.48% and 45.86%, respectively. This discrepancy in deposition rates can be attributed to certain factors.

Very coarse droplets have a tendency to rebound from the leaf surface, making it challenging for them to adhere effectively. As a result, their deposition rates are lower compared to medium-sized droplets. On the other hand, very fine droplets are more susceptible to environmental winds and the downwash airflow generated by the UAV. These factors contribute to the drift of the fine droplets, reducing their ability to deposit on the leaf surface and resulting in lower deposition rates.

The deposition rates of droplets on the adaxial and abaxial surfaces of the upper, middle, and lower layers of leaves in three citrus tree forms, as measured using filter papers on citrus trees, are shown in Figure 9.

Based on the observations from Figure 9, it can be noted that the deposition rates of droplets on the upper (adaxial), middle, and lower layers of the citrus tree canopy range from 16.68% to 83.89%.

On the lower (abaxial) surface, the deposition rates range from 8.60% to 24.42%.

The deposition rate on the adaxial surface gradually decreases as we move from the upper layer to the lower layer of the canopy. In the upper layer, the average deposition rate is 66.91%, which is higher by 19.52 and 34.48 percentage points compared to the rates in the middle layer (47.39%) and lower layer (32.43%), respectively. However, the deposition rates on the abaxial surface show little variation across the different layers of the canopy.

Among the layers of the canopy, the disparity in deposition rates between the upper (adaxial) and lower (abaxial) surfaces is most pronounced in the upper layer. The deposition rate on the adaxial surface is 4.5 times higher than that on the abaxial surface in the upper layer, while in the middle and lower layers, this ratio decreases to 3.5 and 2.3 times higher, respectively. As the height decreases, the difference in deposition rates between the adaxial and abaxial surfaces also decreases.

In the presence of grids, the deposition rate on the adaxial surface is 3.1 times higher than that on the abaxial surface, whereas in their absence, this ratio increases to 3.9 times higher. This indicates that the placement of grids on citrus trees can enhance the deposition of droplets on the abaxial surface, consequently increasing the overall deposition rate. The grids facilitate this improvement by causing secondary atomization of droplets upon impact. This process leads to reduced movement velocity and droplet size, thereby enhancing the adherence of droplets to the abaxial surface of the leaves.
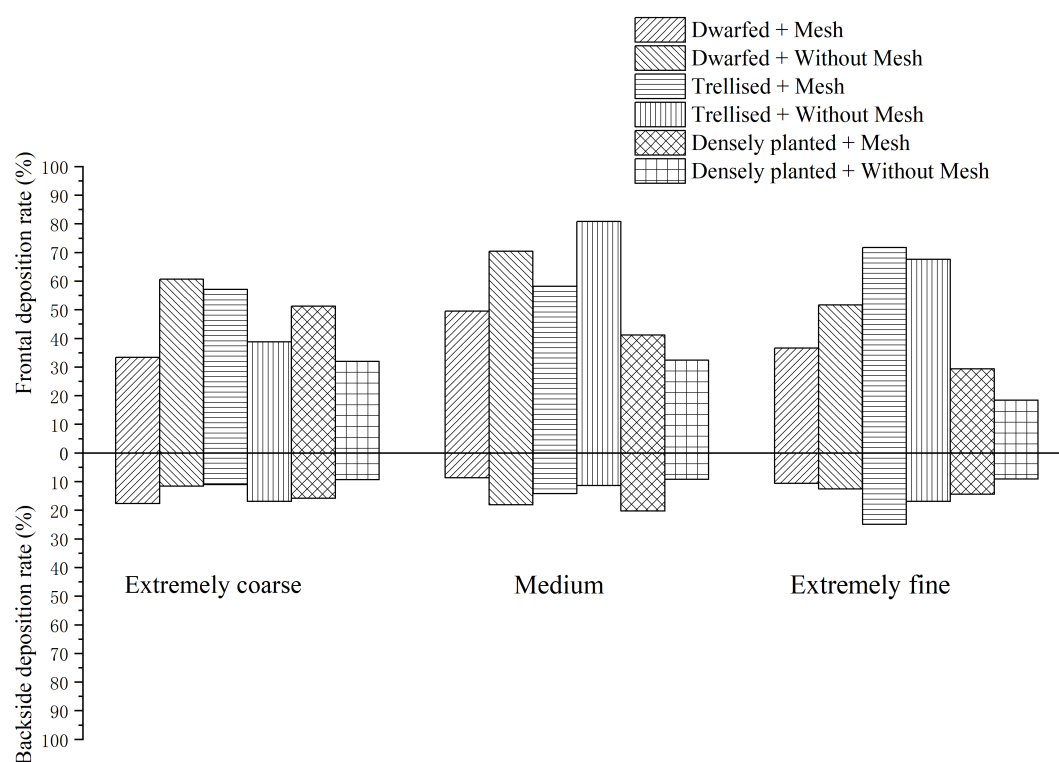

FIGURE 8
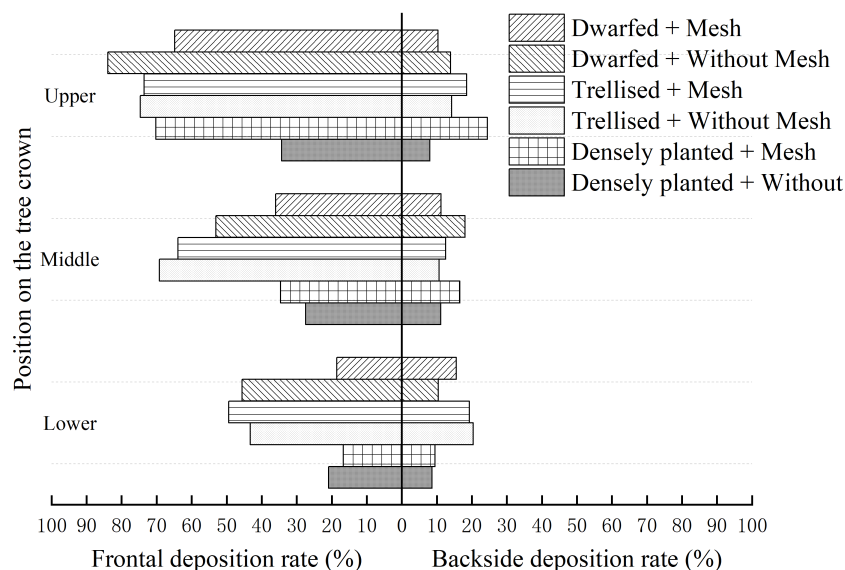Droplet deposition rate under different droplet sizes.

FIGURE 9
Droplet deposition rate in upper, middle and lower layers of tree canopy.

3.3 Ground droplet drift

The non-linear regression analysis of the mean drift rate was conducted using Origin 2018 software, and the fitted curve was plotted as shown in Figure 10. The analysis aimed to examine the effects of changes in downwind distance, different flight heights, and droplet sizes on the mean drift rate.

Based on the observations from Figure 10, it can be noted that the drift rate of sprayed droplets from the UAV gradually diminishes as it extends to a distance of 15 m. However, under certain conditions, the drift rate of droplets at the 15 m mark can still exceed 3%. This indicates that the actual drift distance of droplets at this point is greater than 15 m. The most rapid decrease in drift rate occurs within the range of 3 to 5 m. The
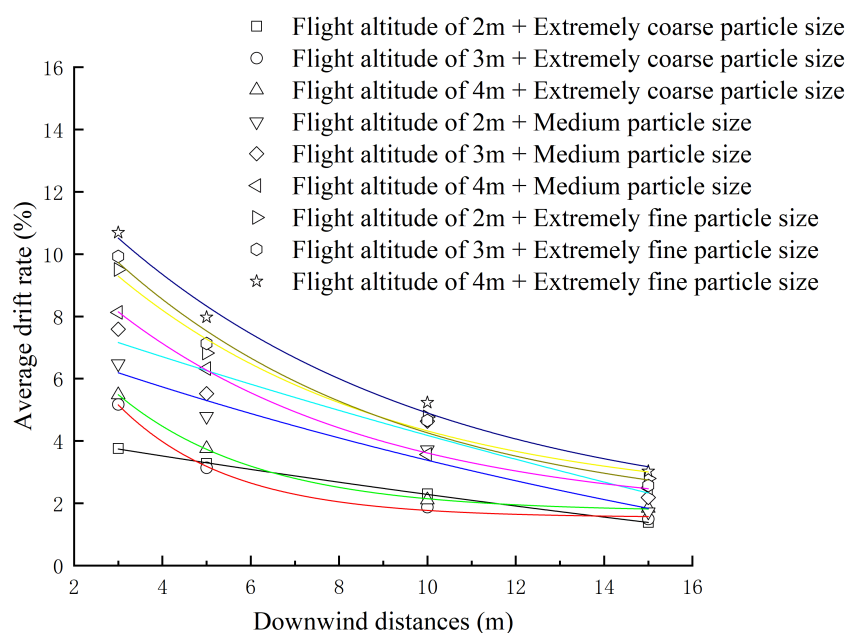

FIGURE 10
Variation of average drift rate of ground sampling points with downwind distance and its exponential function regression curve under various test conditions.

drift rate of UAV spraying exhibits an exponential relationship with the downwind distance, with a decrease in drift rate as the downwind distance increases.

Figure 11 displays the Average Absolute Drift Rate (AADR) of droplets under different operational parameters of the plant protection UAV.

Based on the observations from Figure 11, it is evident that both droplet size and UAV flight height have a significant impact on the Average Absolute Drift Rate (AADR) of droplets. The AADR decreases as the droplet size increases and increases with higher UAV flight heights. The lowest AADR, at 2.68%, is observed with a UAV flight height of 2 meters and the droplet size classified as "coarse." In contrast, the highest AADR is 6.73%, representing an increase of 4.05 percentage points.

Figure 12 displays the 90% cumulative drift distance of droplets under different operational parameters of the plant protection UAV.

Based on the observations from Figure 12, it can be noted that the 90% Cumulative Drift Distance (CDD) ranges from 8.6 to 13.5 meters. The 90% CDD increases as the droplet size decreases, indicating that larger droplets result in a decrease in the 90% CDD by 2 to 5 meters. In contrast, the UAV flight height has minimal influence on the 90% CDD. For coarse or medium droplet sizes, the 90% CDD increases with increasing flight height, reaching its maximum at 4 meters. However, for extremely fine droplets, the 90% CDD is highest at a flight height of 3 meters. When the droplet

size is kept constant, the difference in the 90% CDD is within 1.2 meters.

3.4 Droplet drift in the air

The results obtained from the calculation of relative feature heights based on the vertical drift rates of droplets at different downwind distances are presented in Figure 13. It can be observed that the relative feature height decreases as the downwind distance increases. At downwind distances of 3m and 5m, the relative feature height increases with higher flight heights and smaller droplet sizes, indicating an increase in droplet drift. This observation aligns with the analysis of ground-level droplet drift.

At downwind distances of 10m and 15m, the relative feature height still increases with decreasing droplet size, while the flight height has minimal influence on the relative feature height at this point.

3.5 Prediction of droplet deposition rate

In the experiment conducted on the DJI T40 plant protection UAV, significance analysis was performed to examine the influence of flight altitude, droplet size, and sampling height on the droplet deposition rate. The results of the analysis are presented in Table 2.
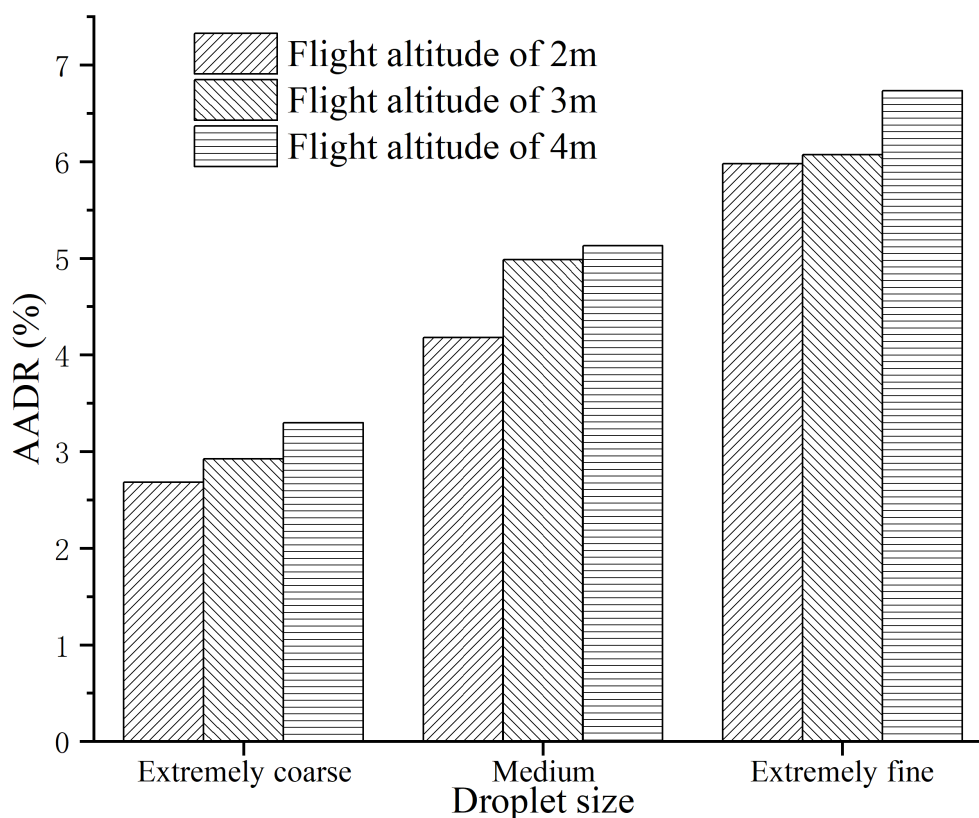

FIGURE 11
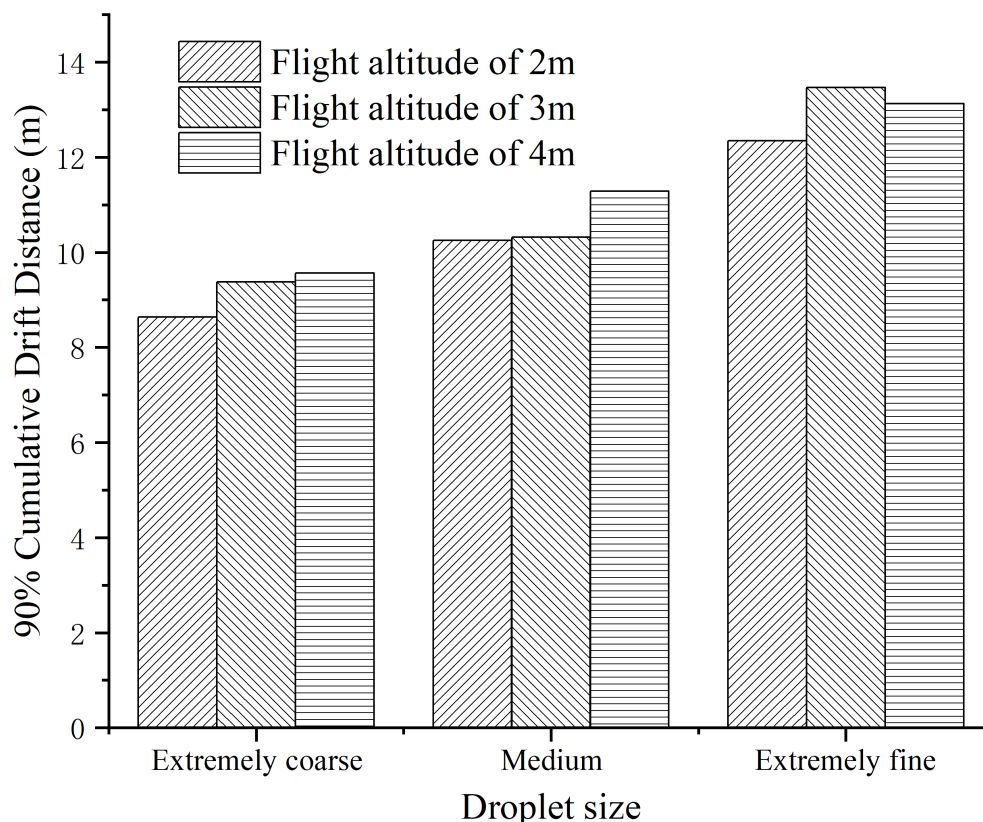*AADR of ground droplets under different operating parameters.*

FIGURE 12
90% cumulative drift distance of ground droplets under different operating parameters.

Comparing different flight altitudes on the droplet deposition rate, three flight altitudes were selected for analysis. According to Table 2, there is no significant relationship observed between flight altitude and the droplet deposition rate.

Analyzing the impact of droplet size on the droplet deposition rate, three different droplet sizes were analyzed. The results in Table 2 indicate that there is no significant relationship between droplet size and the droplet deposition rate.

When examining the effects of different sampling heights on the droplet deposition rate, three specific sampling heights were chosen. Based on the results presented in Table 2, a significant relationship is observed between the droplet deposition rates at different sampling heights. The droplet deposition rate at a sampling height of 2 m shows a significant difference compared to the rates at 1 m and 1.5 m sampling heights. However, there is no significant difference in the droplet deposition rates between the 1 m and 1.5 m sampling heights.

In order to analyze the relationship between unmanned aerial vehicle (UAV) flight height, droplet size, sampling height, and the deposition rate of droplets on target trees, four different machine learning methods were employed. These methods include REGRESS, BP neural network, ELM, and RBFNN. Prediction models were established using these methods to predict the deposition rate of droplets on target trees. Figure 14 displays the prediction results obtained from the four machine learning methods.

From the observations in Figure 14, it can be seen that none of the four modeling methods achieved satisfactory results in predicting the deposition rate of droplets. The highest coefficient of determination (R^2) obtained among the four methods for both training and prediction sets is 0.6677. The limited success in prediction may be attributed to the weak regularity of the experimental data or the insufficient amount of data available for training and prediction in machine learning models. Moreover, it is noteworthy that the unmanned aerial vehicle flight height, droplet size, and sampling height did not show a significant impact on the deposition rate, which aligns with the conclusion drawn during the data preprocessing stage that these factors do not have a substantial influence on the deposition rate.

3.6 Prediction of droplet drift rate

The results of the significance analysis for the DJI T40 crop-spraying UAV experiment between flight height, droplet size, downwind distance, and drift rate are presented in Table 3. When examining the impact of different flight heights on the drift rate, a significance analysis was conducted considering three flight heights. According to Table 3, it can be inferred that there is no significant relationship between the flight height and the drift rate. However, it is observed that the drift rate tends to increase with higher flight heights. Overall, these results suggest that flight height does not
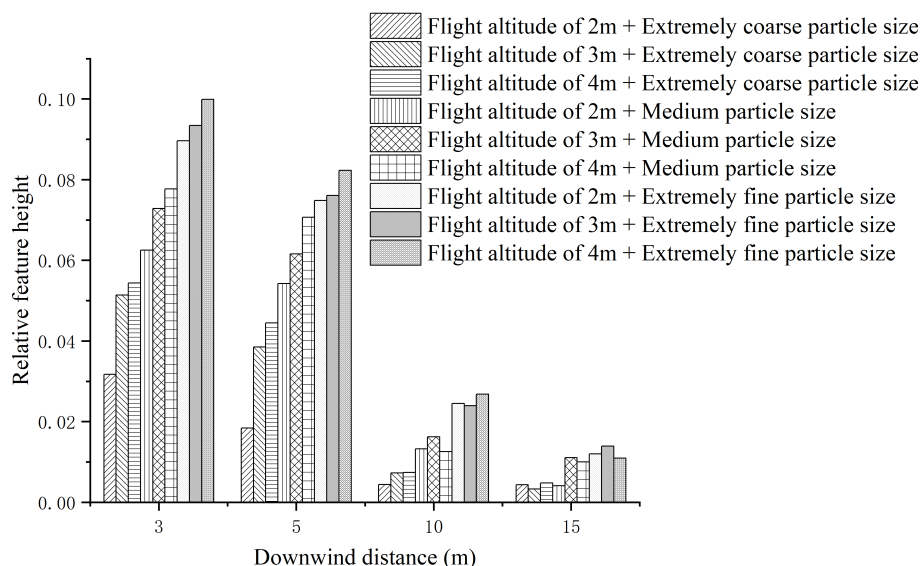
FIGURE 13
Relative characteristic height of droplets at different downwind distances and different test parameters.

have a statistically significant effect on the drift rate for the DJI T40 crop-spraying UAV experiment. Nevertheless, it should be noted that there is a general trend of increased drift rate with higher flight heights.

In the analysis of the effects of different droplet sizes on drift rate, a significance analysis was performed considering three droplet sizes. According to Table 3, it can be observed that there is a significant relationship between droplet size and drift rate. Specifically, smaller droplets lead to higher drift rates. This observation aligns with the actual observations, indicating that smaller droplets are more prone to drifting during the DJI T40 crop-spraying UAV experiment.

In the analysis of the effects of different downwind distances on drift rate, a significance analysis was conducted considering four

downwind distances. According to Table 3, it can be observed that there is a significant relationship between downwind distance and drift rate. The drift rate decreases as the downwind distance increases. This finding aligns with the actual drift pattern of the droplets, indicating that the further the downwind distance, the lower the potential for drift during the DJI T40 crop-spraying UAV experiment.

In order to analyze the relationship between flight height, droplet size, downwind distance, and drift rate in plant protection UAV spraying, four machine learning methods were employed: REGRESS, BP neural network, ELM, and RBFNN. These methods were used to establish predictive models for the drift rate of droplets in plant protection UAV spraying. The predictive results of the four machine learning methods are displayed in Figure 15.

From Figure 15, it can be observed that all four selected modeling methods have good simulation performance in predicting the volume median diameter distribution of droplets. The R_t^2 and R_p^2 values for the training and prediction sets are all above 0.85. However, the BP neural network model shows relatively poorer performance, with lower values of coefficient of determination (R_t^2) and root mean square error compared to the other models. The ELM, REGRESS, and RBFNN models exhibit better and more similar modeling results, with R_t^2 and R_p^2 values above 0.95 for both the training and prediction sets. These three modeling methods can be effectively applied in predicting droplet drift rates. Among them, ELM demonstrates the smallest root mean square error, making it a preferred choice for predicting droplet drift rates.

TABLE 2 Droplet deposition rates at different flight altitudes, droplet sizes, sampling points.

		Deposition rate
Flight altitude/m	2	0.373 ± 0.175^a
	3	0.376 ± 0.304^a
	4	0.445 ± 0.357^a
Droplet size/μm	60	0.367 ± 0.173^a
	100	0.495 ± 0.379^a
	140	0.333 ± 0.253^a
Sampling point height/m	1	0.186 ± 0.124^a
	1.5	0.360 ± 0.215^a
	2	0.648 ± 0.263^b

The deposition rate data in the table is the mean ± standard deviation, dimensionless; The same small letters indicate that there is no significant difference in droplet deposition rate under different droplet sizes, and the significance level setting p=0.05.
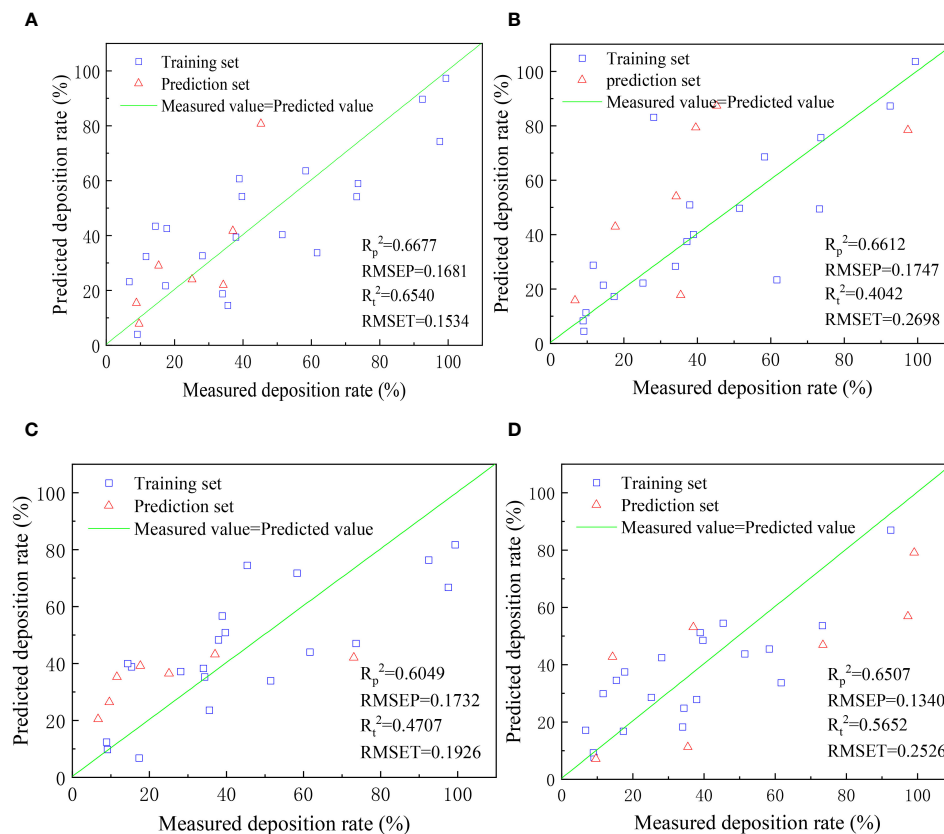
4 Conclusion

In this study, based on grid atomized droplet technology and machine learning technology, a spraying method combining grid

FIGURE 14
Scatter plot of measured and predicted droplet deposition rates ((A) REGRESS, (B) BP Neural Network, (C) ELM, (D) RBFNN).

atomization and plant protection UAV is proposed, and the impact test of UAV spraying and grid is carried out to study the principle of grid atomized droplet and the influence of different operating parameters on droplet particle size, deposition and drift, and the spraying model is constructed with machine learning technology to

TABLE 3 Droplet deposition rates at different flight altitudes, droplet sizes, downwind distances.

		Deposition rate
Flight altitude/m	2	0.043 ± 0.024^a
	3	0.047 ± 0.030^a
	4	0.051 ± 0.028^a
Droplet size/μm	60	0.063 ± 0.029^a
	100	0.048 ± 0.021^b
	140	0.030 ± 0.014^c
Downwind distance/m	3	0.074 ± 0.024^a
	5	0.054 ± 0.018^b
	10	0.037 ± 0.013^c
	15	0.022 ± 0.006^d

The drift rate data in the table is the mean ± standard deviation; The same small letters indicate that there is no significant difference in droplet drift rate under different downwind distances, and the significance level setting p=0.05.

predict the spraying effect of this system. The main research results and conclusions are as follows:

(1) Field experiments were conducted utilizing the DJI T40 plant protection UAV to investigate the deposition rate and downwind drift of droplets on three different types of citrus trees: dwarfed, hedgerow, and densely planted. The experiments were carried out under various conditions, including three droplet sizes (coarse, medium, and fine) and three UAV flight heights (2, 3, and 4 m), both with and without the presence of a grid. The findings yielded from the experimental analysis indicate notable observations. Firstly, the deposition rate of droplets on dwarfed and hedgerow citrus trees was observed to be considerably higher in comparison to traditional densely planted citrus trees. This observation highlights the significant influence of tree type and arrangement on droplet deposition. Secondly, the inclusion of a grid resulted in a slightly reduced deposition rate of droplets on citrus trees as opposed to the absence of a grid. However, this disparity was not deemed statistically significant. Furthermore, when considering the grid condition, there was minimal discrepancy in the deposition rate of droplets on citrus trees between the coarse and fine droplet sizes. This suggests that the use of a grid contributes to a consistent deposition rate irrespective of droplet size. Additionally, it
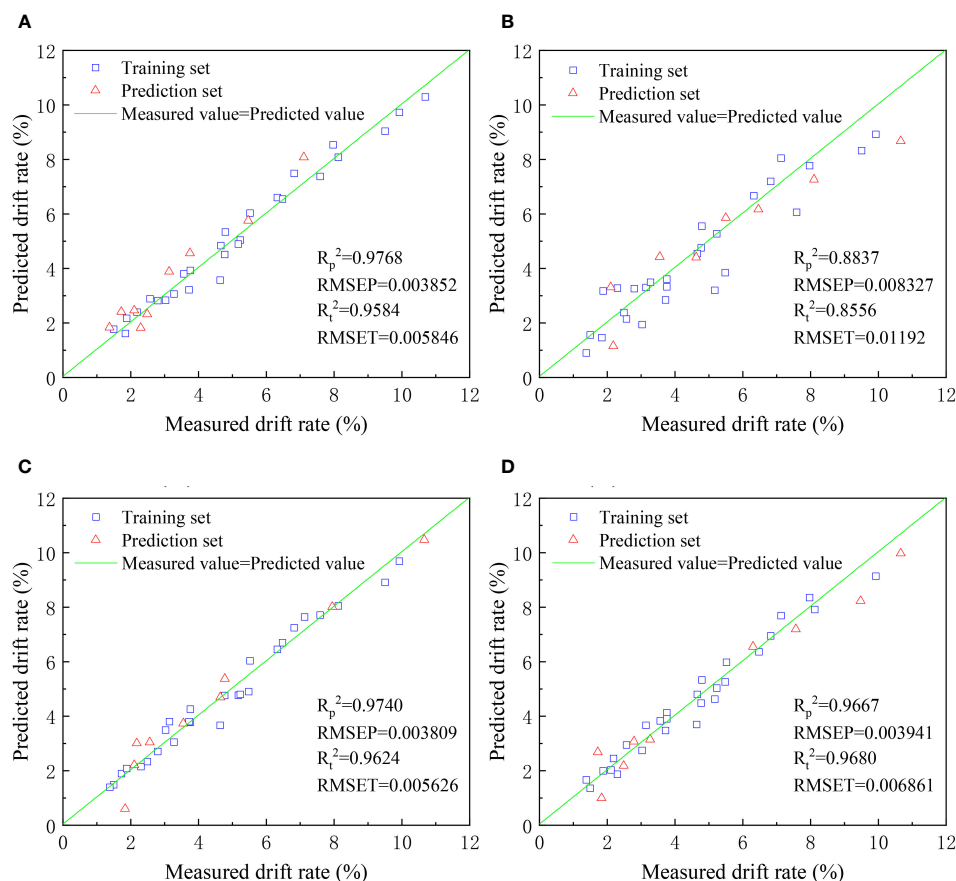
FIGURE 15
Scatter plot of measured and predicted droplet drift rate ((**A**) REGRESS, (**B**) BP Neural Network, (**C**) ELM, (**D**) RBFNN).

was observed that when employing a coarse droplet size, the drift rate of droplets was lower compared to utilizing a fine droplet size. This finding indicates that opting for a coarser droplet size effectively mitigates drift during pesticide spraying operations. In light of these findings, it can be concluded that deploying a grid on citrus trees along with the utilization of a coarse droplet size facilitates the sustenance of a high deposition rate of droplets on citrus trees while concurrently reducing drift. As a result, there is an improvement in the overall efficiency of pesticide utilization in citrus tree spraying operations. Fixed-height grids have improved droplet coverage and deposition density for both hedgerow and densely planted fruit trees, while dwarf fruit trees are farther away from the grid than other fruit trees, so they have the opposite effect on dwarf fruit trees, and adjustable-height grids will be considered in the subsequent study, while how to arrange the grids more conveniently and solve the problem of cost are also issues that need to be considered when they are put into practical use in the future.

(2) In order to predict the droplet size, deposition rate, and downwind drift of droplets following the impact with the grid, machine learning techniques were employed. Appropriate machine learning methods were carefully selected for prediction and validation, enabling the analysis of the influence of various operational parameters on droplet size, deposition, and drift subsequent to grid collision. The experimental findings indicate that the horizontal distance from the nozzle exerts the greatest impact on the volume median diameter of droplets, followed by the vertical distance from the nozzle. On the other hand, the grid aperture has the least influence on droplet size. Concerning droplet deposition rate, the sampling point height emerges as the most influential factor, whereas UAV flight height and droplet size exhibit negligible effects. In terms of droplet drift rate, the downwind distance is found to have the greatest impact, followed by droplet size, while UAV flight height exerts the least influence. Among the four machine learning methods assessed, the BP neural network and ELM (Extreme Learning Machine) demonstrate favorable performance in predicting droplet size. However, the BP neural network exhibits suboptimal performance in predicting droplet drift rate. On the other hand, ELM, REGRESS, and RBFNN (Radial Basis Function Neural Network) display similar performance characteristics. Therefore, ELM can be given priority when predicting both droplet size and drift rate. To summarize, the

utilization of machine learning techniques enables effective prediction of droplet size, deposition rate, and downwind drift after interaction with the grid. The experimental results highlight the varying influences of different operational parameters on these droplet characteristics. Additionally, the evaluation of various machine learning methods identifies ELM as a preferential choice for accurate predictions of droplet size and drift rate.

Data availability statement

The raw data supporting the conclusions of this article will be made available by the authors, without undue reservation.

Author contributions

XX: Writing – review & editing, Conceptualization, Data curation, Formal analysis, Methodology, Project administration, Supervision, Writing – original draft. YT: Conceptualization, Data curation, Formal analysis, Investigation, Methodology, Writing – original draft, Writing – review & editing. ZY: Conceptualization, Data curation, Formal analysis, Investigation, Methodology, Writing – original draft, Writing – review & editing. ZL: Funding acquisition, Supervision, Writing – review & editing. SL: Conceptualization, Supervision, Validation, Writing – review & editing. SS: Conceptualization, Supervision, Validation, Writing – review & editing. DS: Conceptualization, Supervision, Validation, Writing – review & editing.

Conflict of interest

The authors declare that the research was conducted in the absence of any commercial or financial relationships that could be construed as a potential conflict of interest.

Publisher's note

All claims expressed in this article are solely those of the authors and do not necessarily represent those of their affiliated organizations, or those of the publisher, the editors and the reviewers. Any product that may be evaluated in this article, or claim that may be made by its manufacturer, is not guaranteed or endorsed by the publisher.

References

Arnisigo, B. A., Van, D., Rogers, C., Wei, A., and Friesen, J. (2008). Monthly streamflow prediction in the volta basin of west africa: a sisonarmax polynomial modelling. *Phys. Chem. Earth* 33, 141–150. doi: 10.1016/j.pce.2007.04.019

Biglia, A., Grella, M., Bloise, N., Comba, L., Mozzanini, E., Dicembrini, L., et al. (2022). Uav-spray application in vineyards: flight modes and spray system adjustment effects on canopy deposit, coverage, and off-target losses. *Sci. Total Environ.* 845, 157292. doi: 10.1016/j.scitotenv.2022.157292

Guo, H., Zhou, J., Liu, F., He, Y., Huang, H., and Wang, H. (2020). Application of machine learning method to quantitatively evaluate the droplet size and deposition distribution of the uav spray nozzle. *Appl. Sci.* 10, 1759. doi: 10.3390/app10051759

He, X. K., Bonds, J., Herbst, A., and Langenakens, J. (2017). Recent development of unmanned aerial vehicle for plant protection in east asia. *Int. J. Agric. Biol. Eng.* 10, 18–30. doi: 10.3965/j.ijabe.20171003.3248

He, Y., Wu, J., Fu, H., Sun, Z., Fang, H., and Wang, W. (2022). Quantitative analysis of droplet size distribution in plant protection spray based on machine learning method. *Water (Basel)* 14, 175. doi: 10.3390/w14020175

Hilz, E., and Vermeer, A. (2013). Spray drift review: the extent to which a formulation can contribute to spray drift reduction. *Crop Prot.* 44, 75–83. doi: 10.1016/j.cropro.2012.10.020

Hoaglin, D. C., and Kempthorne, P. J. (1986). [Influential observations, high leverage points, and outliers in linear regression]: comment. *Stat. Sci.* 1, 379–416. doi: http://www.jstor.org/stable/2245482

Hu, P., Zhang, R., Yang, J., and Chen, L. (2022). Development status and key technologies of plant protection uavs in china: a review. *Drones* 6, 354. doi: 10.3390/drones6110354

Huang, G. B., Zhu, Q. Y., and Siew, C. K. (2006). Extreme learning machine: theory and applications. *Neurocomputing* 70, 489–501. doi: 10.1016/j.neucom.2005.12.126

Hunter, J. E., Gannon, T. W., Richardson, R. J., Yelverton, F. H., and Leon, R. G. (2020). Integration of remote-weed mapping and an autonomous spraying unmanned aerial vehicle for site-specific weed management. *Pest Manage. Sci.* 76, 1386–1392. doi: 10.1002/ps.5651

Kooij, S. A., Moqaddam, A. M., de Goede, T. C., Derome, D., Carmeliet, J., and Bonn, D. (2019). Sprays from droplets impacting a mesh. *J. Fluid Mechanics* 871, 489–509. doi: 10.1017/jfm.2019.289

Liao, H., Jiang, L., Yu, H., Liu, Z., Fu, J., Chu, G., et al. (2022). Numerical studies of dynamic behavior of liquid film on single-layer wire mesh with different wettabilities. *Front. Chem. Sci. Eng.* 16, 1672–1680. doi: 10.1007/s11705-022-2205-8

Lou, Z., Fang, X., Han, X., Lan, Y., and Wei, F. (2018). Effect of unmanned aerial vehicle flight height on droplet distribution, drift and control of cotton aphids and spider mites. *Agronomy* 8, 187. doi: 10.3390/agronomy8090187

Lü, Y., Zhang, L., Feng, X., Zeng, Y., Fu, B., Yao, X., et al. (2014). Recent ecological transitions in China: greening, browning, and influential factors. *Rep* 5, 8732. doi: 10.1038/srep08732

Martinez-Guanter, J. (2020). Spray and economics assessment of a uav-based ultra-low-volume application in olive and citrus orchards. *Precis. Agric.* 21, 226–243. doi: 10.1007/s11119-019-09665-7

McKinney, B. A., Reif, D. M., Ritchie, M. D., and Moore, J. H. (2006). Machine learning for detecting gene-gene interactions. *Appl. Bioinf.* 5, 77–88. doi: 10.2165/00822942-200605020-00002

Moitra, S., Roy, T., Ganguly, R., and Megaridis, C. M. (2021). Jet impact on superhydrophobic metal mesh. *Langmuir* 37, 2891–2899. doi: 10.1021/acs.langmuir.0c03301

Mosavi, A., Ozturk, P., and Chau, K. (2018). Flood prediction using machine learning models: literature review. *Water* 10, 1536. doi: 10.3390/w10111536

Nagelkerke, N. (1991). A note on a general definition of the coefficient of determination. *Biometrika* 78, 691–692. doi: 10.2307/2337038

Ryu, S., Sen, P., Nam, Y., and Lee, C. (2017). Water penetration through a superhydrophobic mesh during a drop impact. *Phys. Rev. Lett.* 118, 14501. doi: 10.1103/PhysRevLett.118.014501

Sarri, D., Martelloni, L., Rimediotti, M., Lisci, R., Lombardo, S., and Vieri, M. (2019). Testing a multi-rotor unmanned aerial vehicle for spray application in high slope terraced vineyard. *J. Agric. Eng* 50,38-47. doi: 10.4081/jae.2019.853

Schalkoff, R. J. (1997). Artificial neural networks. *New York:McGraw-Hill Higher Educ.*

Sidawi, K., Bouchard, D. J., Boscariol, C., and Chandra, S. (2022). Penetration of water spray droplets through wire mesh. *Atomization Sprays* 32,47-66. doi: 10.1615/AtomizSpr.2022042722

Soto, D., Girard, H., Le Helloco, A., Binder, T., Quéré, D., Varanasi, K.K., et al. (2018). Droplet fragmentation using a mesh. *Phys. Rev. Fluids* 3, 083602. doi: 10.1103/PhysRevFluids.3.083602

Steed, C. A., Swan, J. E., Jankun-Kelly, T. J., and Fitzpatrick, P. J. (2009). Guided analysis of hurricane trends using statistical processes integrated with interactive parallel coordinates. *IEEE Symposium Visual Analytics Sci. Technol*, 19-26. doi: 10.1109/VAST.2009.5332586

Sun, Z., Liao, H., Wang, L., Jiang, L., Zhang, X., Wang, B., et al. (2023). Liquid flow and breakage behaviors of two liquid jets impacting on the wire mesh with different impinging angles. *Chem. Eng. J.* 454, 140036. doi: 10.1016/j.cej.2022.140036

Wenwen, K., Zhang, C., Huang, W., Liu, F., and He, Y. (2018). Application of hyperspectral imaging to detect sclerotinia sclerotiorum on oilseed rape stems. *Sensors* 18, 123. doi: 10.3390/s18010123

Yildiz, B., Bilbao, J. I., and Sproul, A. B. (2017). A review and analysis of regression and machine learning models on commercial building electricity load forecasting. *Renewable Sustain. Energy Rev.* 73, 1104–1122. doi: 10.1016/j.rser.2017.02.023

Frontiers in Plant Science

Reducing environmental exposure to PPPs in super-high density olive orchards using UAV sprayers

Luis Sánchez-Fernández[1], María Barrera-Báez[1], Jorge Martínez-Guanter[2] and Manuel Pérez-Ruiz[1]*

[1]Departamento de Ingeniería Aeroespacial y Mecánica de Fluidos, Área de Ingeniería Agroforestal, Universidad de Sevilla, Seville, Spain, [2]Digital Marketing Manager Iberia at Corteva Agriscience, Sevilla, Spain

The increasing demand for optimizing the use of agricultural resources will require the adoption of cutting-edge technologies and precision farming management. Unmanned Aerial Vehicle (UAV) sprayers seem promising due to their potential to perform precision or spot spraying, particularly in woody crop environments where total surface spraying is unnecessary. However, incorporating this technology is limited by the lack of scientific knowledge about the environmental risks associated with UAV sprayers and the strict legal framework. Nonetheless, these spraying systems' characteristic downwash airflow and the limited swath width can potentially mitigate drift in hedgerow crops. During our study we performed comparative studies aimed to compare the airborne drift, soil, and crop depositions between a conventional orchard sprayer and a UAV sprayer in a commercial superhigh-density orchard in the South Iberian Peninsula in 2022. Our findings reveal that, in superhigh-density olive orchards, the UAV sprayer presents a substantial reduction in airborne drift, while soil depositions showed no significant differences compared to those of a conventional terrestrial orchard sprayer. Crop depositions were significantly lower when utilizing the UAV sprayer. These results suggest that introducing UAV spraying technology in Mediterranean agricultural systems, under specific scenarios, can effectively reduce the environmental impact of crop spraying and encourage the responsible use of plant protection products (PPPs).

1 Introduction

The United Nations expects the population to grow by two billion people over the next 30 years (United Nations, 2022), for which agriculture must provide food, fiber, and fuel. The estimated increase in calorie consumption that comes with the economic growth of developing countries will require an expansion of approximately 70% in agricultural production

(Searchinger et al., 2018). Increasing agricultural yield is not an easy task, especially in the context of climate change, which is expected to cause a significant reduction in precipitation in the Mediterranean region, one of the main agricultural areas in the world (Masson-Delmotte et al., 2019). Increasing the agricultural area at the expense of natural ecosystems is not sustainable, so the increased agricultural yield must come from sustainable intensification. Moreover, there is increasing concern about the environmental impact of PPPs. This concern has resulted in strategies, such as the Farm to Fork initiative, that aims to reduce the use of PPPs in Europe by 50% over the next decade.

Some technologies with the potential to contribute to solving this challenge have already been developed. Unmanned aerial vehicles (UAVs) are becoming increasingly popular in the agricultural industry due to their adaptability and versatility. UAVs are now being utilized for various agricultural tasks, including the precise application of PPPs with a high spatial resolution (Huang et al., 2009). In some situations, spraying UAVs might be more suitable than conventional spraying systems since they can spray areas that are difficult for workers or machinery to access, such as hilly or muddy plots. Some studies suggest that the use of spraying UAVs has several advantages over conventional terrestrial spraying systems, especially when compared to orchard (Sánchez-Fernández et al., 2023) and backpack sprayers (Wang et al., 2018; Sarri et al., 2019; Xiao et al., 2020).

Spraying UAVs can perform variable and spot spraying, reducing the application's environmental impact and contributing to the sustainability of agricultural systems. They are more time efficient than conventional terrestrial sprayers, and they can spray approximately $4\,ha\cdot h^{-1}$, a significantly higher surface than a knapsack sprayer (Giles and Billing, 2015), while reducing the exposition to the operator. Furthermore, several studies suggest that the downwash airflow generated by the UAVs' rotors may contribute to the penetration of the spray into the crop (He et al., 2017; Tang et al., 2017). Moreover, batteries power most commercial spraying UAVs, and their use might contribute to reducing the dependency on fossil fuels. However, there are still unknown aspects of the flight and structural parameters of UAVs that might affect the spray depositions, such as the distance between the rotors, their number, or the lifted weight (da Cunha et al., 2021). More studies in this field are needed to fully understand how all these parameters affect spraying UAVs' depositions.

Spraying UAV technology, while promising, still faces significant limitations. The limited payload capacity of these systems restricts their application to ultra-low volume rates. Technologically, the payload limitation is being overcome by developing larger and heavier UAVs. However, one of the most vital limitations of this technology, especially in Europe, is the strict legal framework. UAV spraying is considered aerial spraying in most parts of Europe and, consequently, banned, except under exceptional circumstances and with minimal active ingredients approved. Comparative studies such as this are needed to determine if, under specific scenarios, UAV spraying systems can help reduce environmental exposure to PPPs compared to conventional terrestrial orchard sprayers.

Olive tree (*Olea europaea*) is the main permanent crop worldwide and one of the main crops in the Mediterranean region, covering 11.5 million hectares. Olive production is restricted to the Mediterranean climate areas, but a globally dispersed growing demand exists. As a result, the surface dedicated to olive orchards increases steadily to 162,000 hectares yearly (Vilar et al., 2018). Recently, superhigh-density orchards have gained prominence and represent most new plantations. Moreover, some traditional olive orchards are converted to superhigh-density or hedgerow orchards yearly due to their reduced human labor requirements, earlier returns on investment, consistency in yield, and efficient management (Lindell et al., 2023). Furthermore, some studies suggest that super high-density orchards may have some environmental benefits over traditional production systems, and they exhibit a lower impact on climate change per ton of production (Ben Abdallah et al., 2021). Currently, the spraying of PPPs in super high-density olive orchards is performed by terrestrial mist blowers. Introducing spraying UAVs in olive orchards has the potential to mitigate the environmental impact of these operations under specific conditions, supporting the sustainability of agricultural systems. Some studies assessing the drift generated by UAV sprayers have been published (Liu et al., 2020; Wang et al., 2021; Dengeru et al., 2022; Li et al., 2022). Nevertheless, the deposition parameters and airborne drift associated with UAV sprayers in superhigh-density olive orchards are still unknown. Our study is the first to compare the airborne drift, soil, and crop depositions generated by a UAV sprayer to those caused by a conventional orchard sprayer in super-high density olive orchards.

This study assesses the potential advantages of UAV spraying systems compared to conventional terrestrial systems concerning airborne drift and crop and soil depositions within specific conditions, particularly in superhigh-density hedgerow olive orchards. This study involves a comparative analysis of the airborne drift, crop, and soil depositions resulting from using a UAV sprayer and conventional terrestrial mist blower. Our trials were conducted in a representative commercial superhigh-density olive orchard whose characteristics and agricultural practices are common to orchards of the same type in the Mediterranean region. Our hypothesis states that UAV sprayers may generate less airborne drift while maintaining similar soil depositions to conventional terrestrial atomizers. Conventional orchard sprayers typically project the spray horizontally onto the crop's canopy, resulting in a substantial portion of the applied volume passing through the canopy as drift.

Conversely, UAVs spray vertically, directing the spray downward over the crop with the assistance of the downwash airflow generated by the rotors. This downward airflow might promote spray penetration into the canopy, mitigating airborne drift. In specific scenarios, adopting UAV sprayers can help reduce the use of PPPs, consequently safeguarding and expanding areas of environmental interest adjacent to agricultural areas.

The chosen crop for our study is superhigh density olive-orchards. These orchards hold significant importance in the region, accounting for 46.7% of the total agricultural surface

(SIGPAC, 2021). Andalusia contains 61% of the total olive surface of Spain, the main olive producer in the world.

2 Materials and methods

2.1 Study area and target crop

The focus crop of this study was a superhigh-density olive (*Olea europaea*) orchard. Drift trials were conducted from June to September 2022, during phenological growth stages 71 and 75 according to the BBCH scale. The study occurred at Bujalmoro farm (37°13'N, 5°55'W), a commercial superhigh-density olive orchard in Andalusia (South Iberian Peninsula). The olive trees were fully developed and planted at a planting frame of 4 m x 1.5 m (1667 trees·ha^{-1}) in 2018. The trees' height measured from the ground was 3 m, the hedgerow width was 1.66 m, and the measured canopy volume was 10555 m^3·ha^{-1}. Andalusia has typical Mediterranean climatic conditions characterized by mild winters and hot and dry summers. The average rainfall and reference evapotranspiration (ET$_o$) registered in the orchard have been 484 mm and 1442 mm, respectively, for the last 25 years. The characteristics and the management of the orchard are representative of the superhigh-density commercial orchards of the region and the Mediterranean area.

2.2 Spraying systems

2.2.1 Orchard sprayer

In our study, we compared the airborne drift, soil, and crop depositions of two spraying systems: a conventional orchard sprayer and an autonomous UAV spraying system (Figure 1). A tractor-mounted mist blower (Zebra Axial 600, HARDI International, Nørre Alslev, DK) was attached to a Claas Elios 240 (Claas, Harsewinkel, DE), 73 kW tractor. This is the typical sprayer used in the region's olive orchards and woody crops. The mist blower has six ceramic hollow cone nozzles (Albuz ATR-80, Solcera, Evreux, FR) on each side. The two bottom nozzles were yellow, the two middle ones were orange, and the top were red. The top red nozzle at each side of the mist blower was closed to adjust the sprayed area to the crop's height. The mist blower operated with the rear intake at 280 rpm and 10 bar, spraying 13.5 L·min^{-1}. The

final application rate at a 0.7 m·s^{-1} speed was 800 L·ha^{-1}. The proper function of the mist blower was checked following ISO 16122 (2015) under the same working conditions.

2.2.2 Autonomous UAV sprayer

The UAV spraying system is a prototype hexacopter equipped with an RTK-GNSS system (Here3+, HexAero Pte. Ltd, SG), a 16 L tank, and four green hollow cone nozzles (KZ-80 06, Ningbo Licheng Agricultural Spray Technology Co., Ltd, Yuyao, CN) placed just below the frontal rotors. Determining the swath width is a crucial factor in UAV sprayers. We conducted an indoor trial using three sampling lines to evaluate the spraying UAV swath width without the influence of the wind. In each sampling line, we fixed 26 x 76 mm water-sensitive papers (Syngenta, Basel, CH) every 0.4 m; each line was 3 m from each other. During the swath width trials, we assessed the depositions of the UAV sprayer at 1 m, 2 m, and 3 m high. Flight speed was the same used during the field trials, 1.5 m·s^{-1}. The spraying height of the field trials was 1.5 m above the canopy. With these flight parameters, the final application rate was 40 L·ha^{-1}. The image analysis software ImageJ (ImageJ 1.52p, NIH, EEUU) analyzed the water-sensitive paper. The proper function of the nozzles in the UAV sprayer was checked following ISO 16122 (2015).

2.3 Experimental design

The experimental plot was surrounded by farmlands covered in grassy crops that were mowed and ploughed to establish a drift measurement area free of crops and obstacles of 40 m in length and 50 m wide, meeting the requirements of ISO 22522 (2007) and ISO 22866 (2005), in which the trials were conducted. The spraying area measured 80 m in length and 40 m in width. Soil and crop deposition trials were performed together in the spraying area, while airborne drift trials occurred in the adjacent drift area. The area was sprayed three times for each trial and sprayer. After each repetition, collectors (Figure 2) were meticulously collected and replaced to ensure accurate data collection and analysis.

Weather conditions were monitored using three weather stations (WH3000SE PRO, Shenzhen Fine Offset Electronics Co., Ltd, Guangdong, CN) placed 1 m above the canopy in the drift area. Only trials carried out under acceptable weather conditions according to ISO 22866 (2005) were considered for this study. As
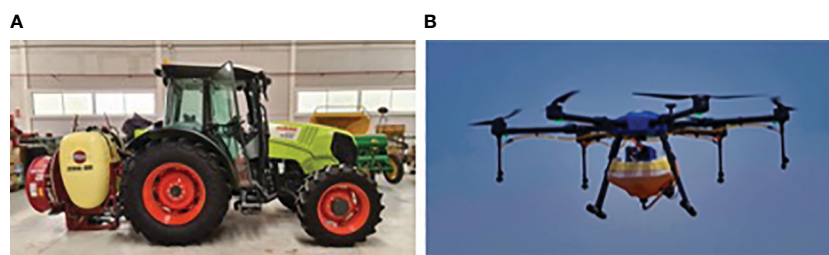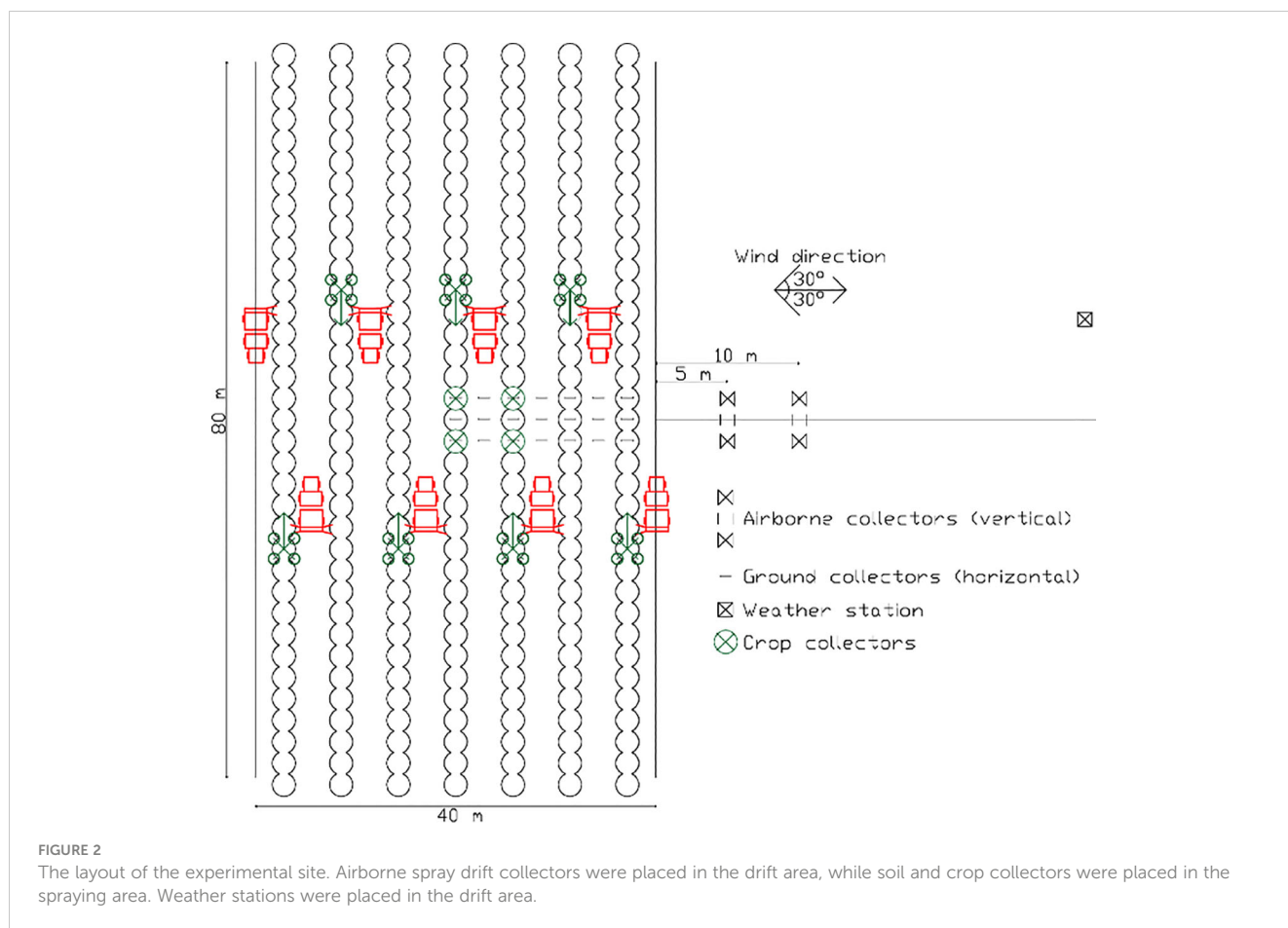

FIGURE 1
(A) Typical orchard sprayer currently used by farmers and **(B)** UAV sprayer used in our study.

FIGURE 2
The layout of the experimental site. Airborne spray drift collectors were placed in the drift area, while soil and crop collectors were placed in the spraying area. Weather stations were placed in the drift area.

for the tracer, we employed Tartrazine (E-102, Seimex & Procona Ltd., Valencia, ES). Given the differences in the spraying parameters between the two tested spraying systems (conventional vs ultra-low volume spraying), we applied different concentrations of tracer to ensure the same amount of tracer was sprayed in the spraying area. The conventional terrestrial sprayer utilized a 0.6 g·L^{-1} concentration, while the UAV sprayer sprayed a higher 12 g·L^{-1} concentration. Following application, we allowed the collectors to dry for five minutes before carefully placing them into individual zip bags. These bags were then stored in cool and dark conditions to prevent degradation. Samples were taken from the tanks of both spraying systems for a thorough analysis to determine the precise amount of tracer sprayed.

The airborne drift was measured 5 and 10 m downwind from the sprayed area. The collector used was a PETG filament with a diameter of 2.85 mm (KIMYA, Nantes, FR), which was vertically arranged on 6 m tall poles in an array. We placed two filaments at each sampling distance. Sampling of airborne drift was performed at regular intervals of 0.5 m, starting from the ground level up to a height of 6 m. To evaluate soil depositions under the hedgerow and interrow areas, we established three sampling lines perpendicular to the hedgerow, spaced every 5 m at the center of the spraying area (Figure 3). Each sampling line was comprised of a total of 7 data collection points. This setup allowed us to sample intra-row and interrow surfaces within the spraying area. To measure crop depositions, we chose four representative trees around the spraying area's center (Figure 2). To understand the spray distribution within the canopy, each selected tree was sampled at three different heights: 1, 2, and 3 m from the ground. We evenly positioned four absorbent paper collectors (CANSON, Annonay, FR) at each height per sampling tree, each collector had a surface of 5 x 5 cm.

2.4 Depositions calculation

Once in the laboratory, the tartrazine from each collector was extracted using a known volume of deionized water. To determine the amount of tartrazine present, the absorbance of the wash-off water was measured at a wavelength of 425 nm using a spectrophotometer (Cary UV-Vis Compact, Agilent Technologies, Inc., Santa Clara, USA) Equation 1. Blank collectors were analyzed to eliminate any potential influence of the collectors and deionized water on the absorbance readings. Using a calibration curve previously done with the same spectrophotometer, the spray deposit of each collector was calculated based on the amount of tartrazine extracted Equation 2. Additionally, we analyzed the samples extracted from the sprayers'

tanks before and after each repetition to determine the precise concentration of tartrazine sprayed:

$$SD = \frac{(\rho_{smpl} - \rho_{blk}) \cdot F_{cal} \cdot V_{dil}}{\rho_{spray} \cdot A_{col}} \quad (1)$$

where SD represents the deposit extracted from each collector ($\mu L \cdot cm^{-2}$); ρ_{smpl}, the absorbance (dimensionless) of the sample washing; ρ_{blk}, the absorbance (dimensionless) of the blank collectors washing; F_{cal}, the calibration factor; V_{dil}, the volume of the deionized water used to dilute the tracer from the collector (μL); ρ_{spray}, the absorbance (dimensionless) of the tank solution; and A_{col}, the area of the collector (cm^2).

The percentage of spray drift on a collector ($D_\%$) was calculated considering the projected area of each collector. Finally, the deposit was expressed as a percentage of the total volume sprayed in the same area using the following expression:

$$D_\% = \frac{SD \cdot 10000}{\beta_v} \quad (2)$$

where βv is the spray application volume per hectare ($L \cdot ha^{-1}$) and is given by the following Equation 3:

$$\beta_v = \frac{T_{flow} \cdot 600}{R_{spac} \cdot V} \quad (3)$$

where T_{flow} is the total nozzle flow rate ($L \cdot min^{-1}$); R_{spac} is the distance between crop lines (m); and V is the velocity of the sprayer ($km \cdot h^{-1}$).

2.5 Data analysis

The effect of the spraying system on the airborne, soil, and crop depositions at every distance and height was evaluated using a one-way analysis of variance (ANOVA) coupled with Fisher's least significant difference (LSD) test (Fisher, 1936). Before conducting the analysis, we ensured that the data met the necessary assumptions for these tests. The Shapiro-Wilk test (Shapiro and Wilk, 1965) was employed to assess the normality of the data, while Levene's test (Levene, 1960) was used to examine the homogeneity of variance. All statistical tests were carried out with a confidence level of 95%. The results were analyzed using the R statistics software (R Core Team, 2022).

3 Results

3.1 Sprayer UAV swath width

Figure 4 presents spray coverage distribution at different horizontal distances from the flight path of our UAV, this swath width trial was repeated at three different heights: 1 m (a), 2 m (b), and 3 m (c). As shown in Figure 4, almost no coverage is detected after 1.5 m from the UAV's flight path for the three tested heights. As Figure 4 suggests, we observed a higher spray coverage when flying lower. Still, after 2 m high, the coverage seems to stabilize with height, and no further reduction in coverage is observed when

FIGURE 3

(A) Aerial view of the experimental area showing the position of soil and airborne collectors. **(B)** Array used to place the airborne collectors. **(C)** The soil collector was used in our trials.
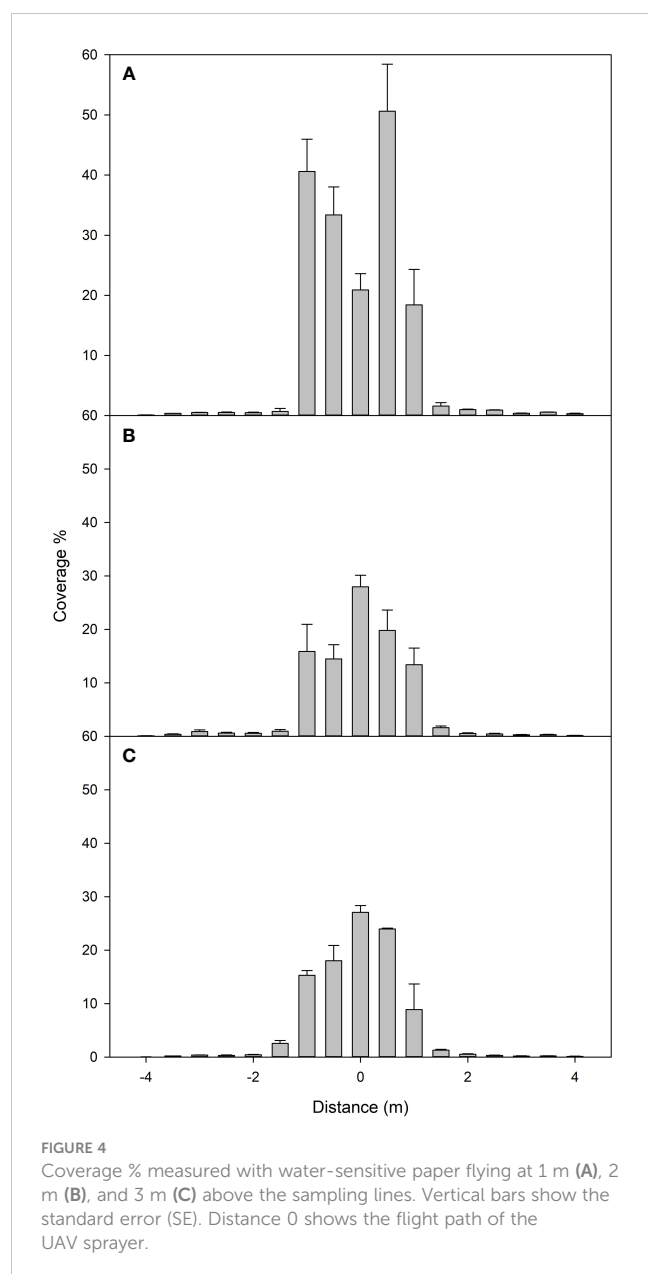
increasing height to 3 m. When analyzing the standard error across different height measurements, a consistent decrease is observed with increasing heights, indicating a trend toward spray homogenization at increasing heights. Our data (Table 1) also shows how the variation coefficient decreases with height.

3.2 Airborne spray drift

Values of airborne spray drift show significant differences between both sprayers at 5 and 10 m downwind from the sprayed area for every height (p< 0.05). As shown in Figure 5, the statistical analysis did not show significant differences in the airborne deposit generated by the UAV sprayer at 5 and 10 m downwind from the sprayed area. However, the terrestrial sprayer caused significantly less airborne drift at 10 m downwind from the sprayed area when compared to the airborne drift captured by the sampling array

TABLE 1 Results of the swath width trials performed indoors.

Flying Height (m)	Swath width (m)	CV (%)
1	2.25	28.13
2	2.5	27.13
3	2	25.84

placed at 5 m. Our results show that the UAV sprayer generated significantly less airborne drift under our conditions than our conventional terrestrial orchard sprayer.
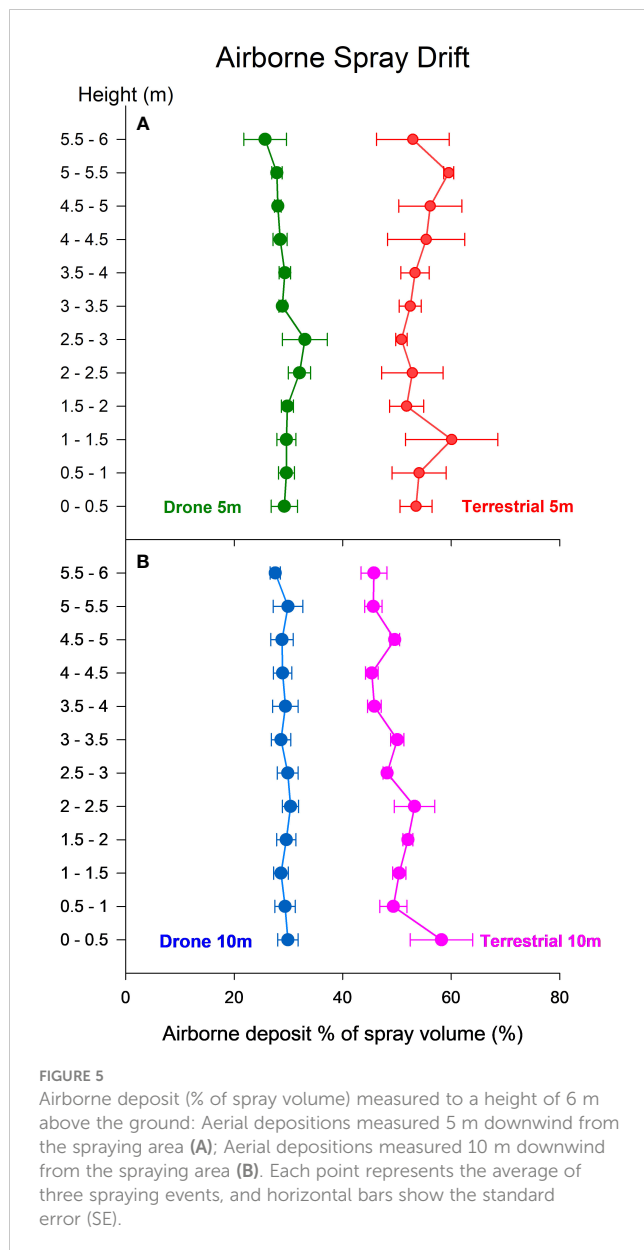
3.3 Soil depositions

Our soil deposition results (Figure 6) suggest that the total % of spray volume that reached the soil was similar between the sprayers, with no statistically significant differences in the total % of spray volume collected. However, our results showed statistically significant differences between the sprayers at specific positions. At intra-row places (4, 8, and 12 m), the terrestrial orchard sprayer demonstrated significantly higher soil depositions than the UAV sprayer. The UAV sprayer exhibited more variability in soil depositions at each sampled position when compared to the terrestrial orchard sprayer.

3.4 Crop depositions

As some of our data did not meet the assumptions for ANOVA, we also employed the Kruskal-Wallis test (Kruskal and Wallis, 1952). As depicted in Figure 7, our analysis revealed distinctions in crop deposition between the terrestrial orchard sprayer and the UAV sprayer at each sampled height. Specifically, the terrestrial orchard sprayer showed a significantly higher crop deposition at every sampled height than the UAV sprayer. However, the data dispersion suggests that the terrestrial orchard sprayer displayed less homogeneity in crop depositions at every sampled height. Moreover, the spatial distribution of crop deposition varied between the two sprayers. The terrestrial orchard sprayer generated higher depositions at 2 m above the ground in the middle section of the hedgerow. By contrast, the UAV sprayer showed a higher crop deposition at the top part of the canopy, at a height of 3 m above the ground. Our data did not show significant differences between the depositions generated by the UAV sprayer at 1 and 2 m from the ground.

4 Discussion

We evaluated airborne drift and mass balance distribution to assess spray deposition and drift. In our analysis of swath width, we observed a decrease in the coefficient of variation (CV) as the height increased. This might suggest that the spray's distribution trended to become more homogenized at higher altitudes, potentially due to the effect of the turbulence generated by the downwash airflow. In

FIGURE 5
Airborne deposit (% of spray volume) measured to a height of 6 m above the ground: Aerial depositions measured 5 m downwind from the spraying area **(A)**; Aerial depositions measured 10 m downwind from the spraying area **(B)**. Each point represents the average of three spraying events, and horizontal bars show the standard error (SE).
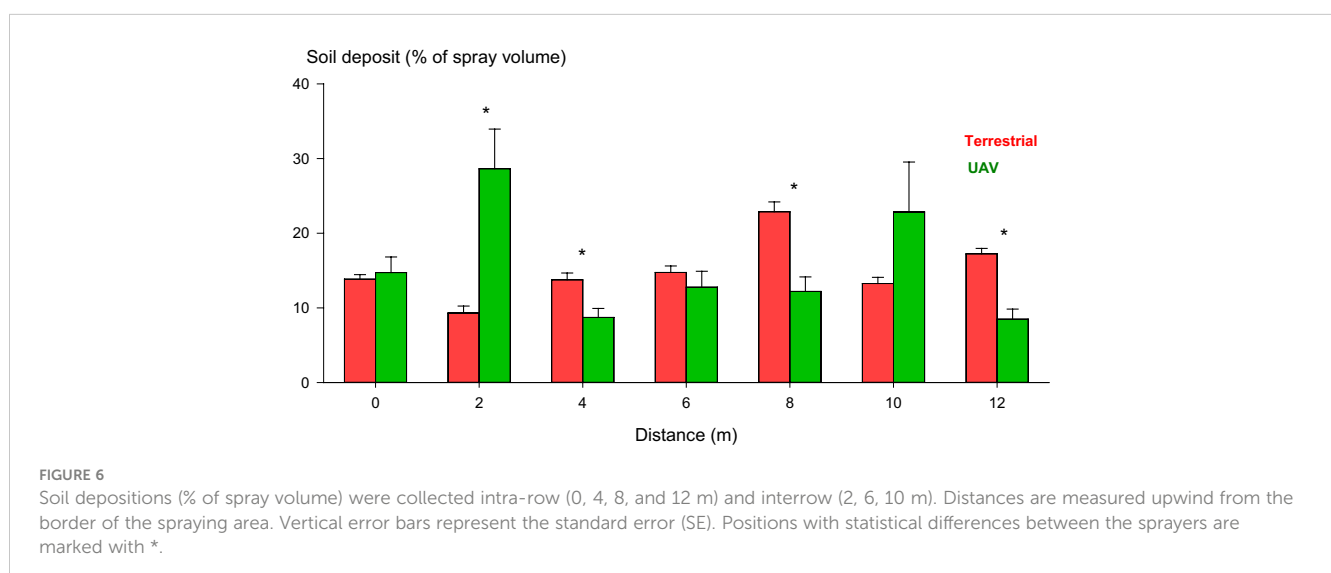
our study, the flight height had a limited influence on the UAV's swath width. This suggests that, within the range of 1 to 3 m, the swath width was more dependent on other factors, such as the spacing between the rotors and the characteristics of the downwash airflow generated by these rotors.

Our results suggest that UAV sprayers generate significantly less airborne drift than conventional orchard sprayers. These results align with the findings of previous work (Sánchez-Fernández et al., 2023), which observed reduced sedimented spray drift from a UAV sprayer compared to a conventional terrestrial orchard sprayer. Our experiments observed no statistically significant differences in the airborne spray drift among the various heights tested for any of the studied sprayers. However, our data shows a trend of increasing airborne spray drift as height decreases; this phenomenon seemed stronger for the terrestrial orchard sprayer at 10 m downwind from the spraying area. This trend is consistent with observations in similar studies (van de Zande et al., 2014; Torrent et al., 2017; Gil et al., 2018; Wang et al., 2021).

The influence of the vortex generated by rotor blades interacting with the air and the interplay between the UAV's wind field and the canopy can affect droplet deposition, as suggested in previous studies (Xue et al., 2014; Guo et al., 2019). Spraying at lower altitudes facilitates a more efficient projection of the spray onto the crop below, whereas, at higher altitudes, the vortex can emerge, leading to increased drift. Our airborne spray drift results support our hypothesis that downward spraying of the UAV sprayer results in less drift than a terrestrial orchard sprayer, even at heights of 1.5 m above the olive hedgerow, corresponding to a spraying height of 4 m above the ground. The mentioned vortex occurs at this height and induces significantly more drift than lower-altitude spraying. Despite the presence of the vortex and its potentially harmful effects, the UAV sprayer still generated significantly lower airborne spray drift than the terrestrial orchard sprayer.

In terms of soil depositions, our study revealed significantly higher depositions for the terrestrial orchard sprayer in the intra-row sampled positions. However, no statistically significant differences were observed in soil depositions for the inter-row

FIGURE 6
Soil depositions (% of spray volume) were collected intra-row (0, 4, 8, and 12 m) and interrow (2, 6, 10 m). Distances are measured upwind from the border of the spraying area. Vertical error bars represent the standard error (SE). Positions with statistical differences between the sprayers are marked with *.
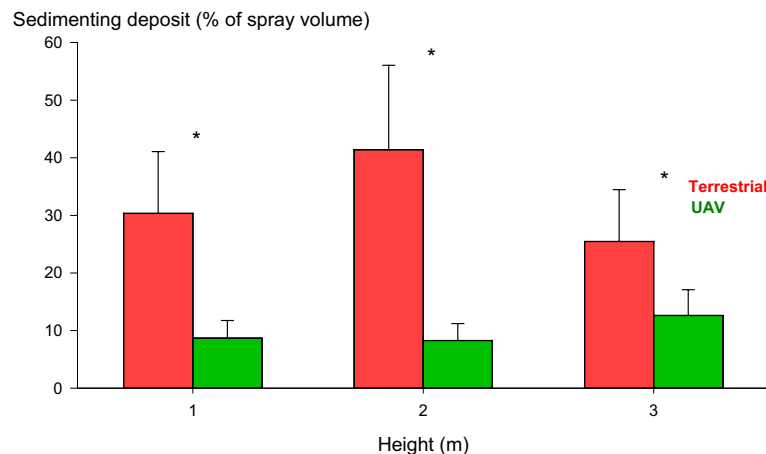
FIGURE 7
Crop depositions (% of spray volume) collected at 1, 2, and 3 m height measured from the ground. Vertical error bars show the standard error (SE). Positions with statistical differences between the sprayers are marked with *.

sampled positions. Additionally, our results suggest a higher spray variability when using the UAV sprayer than the conventional orchard sprayer. These soil spray deposition results align with previous studies, suggesting that UAV sprayers tend to have lower droplet density and deposition uniformity. The spray drift generated by the conventional orchard sprayer while spraying adjacent rows generated soil depositions comparable to those generated by the UAV sprayer. Although no statistically significant differences were observed in the soil depositions collected from the inter-row positions, this result holds significant meaning, especially considering that the terrestrial orchard sprayer was a mist blower whose spraying area was adapted to the canopy's surface, that it did not spray the soil, and that the swath width of our UAV sprayer was wider than the hedgerow width. In hedgerow crops, the swath width of the UAV sprayer becomes especially important, ideally it should be equal to or narrower than the hedgerow width to prevent the spraying of the crop's interrow space. In our study, the swath width of the UAV sprayer was 2.25 m, while the hedgerow width was, on average, 1.66 m. This excessive swath width may be why we did not find significant differences in soil depositions between the two tested sprayers. Further optimization of this parameter may reduce the UAV's soil depositions. Maintaining an appropriate swath width is essential to prevent off-target spray drift, which can decrease spraying efficiency and increase environmental exposure to plant protection products (PPPs). Commercial UAV sprayers cannot adapt their swath width to woody orchards' heterogeneous and changing characteristics. Further research is needed in this aspect to ensure the precision of this technology in spraying applications.

Regarding crop depositions, our results show that the UAV sprayer's crop depositions are significantly limited compared to the crop depositions generated by the conventional orchard sprayer. This behavior can be attributed to the distinct spraying parameters employed by the two spraying systems: the terrestrial orchard sprayer applies a high volume laterally to the canopy, while the UAV sprayer projects an ultra-low volume spray downward from the top of the canopy. The higher spray volume of the terrestrial orchard sprayer promotes better penetration but also leads to increased run-off from the canopy to the soil, which explains the higher soil depositions detected when using the conventional orchard sprayer. The terrestrial orchard sprayer generated more crop depositions in the middle section of the hedgerow, while the UAV sprayer produced more crop depositions at the top part of the canopy. This characteristic crop deposition pattern observed in the 7nbsp;UAV sprayer is expected, given that drones spray from above the canopy. The phenomenon has been previously documented (Zhang et al., 2016; Martinez-Guanter et al., 2020; Li et al., 2021). The UAV sprayer did not exhibit statistical differences in crop depositions at the middle and lower levels of the canopy. This crop deposition pattern suggests that the downwash airflow associated with the UAV sprayer promotes better penetration and homogenizes the spray distribution at the middle and lower sections of the canopy.

5 Conclusion

This study demonstrates that UAV sprayers offer a significant advantage in reducing airborne drift compared to conventional orchard sprayers, particularly in super-high-density olive orchards. Our results also suggest that UAV sprayers generate soil depositions similar to conventional orchard sprayers. However, the practicality of using UAV sprayers may vary depending on the specific context and the desired crop depositions. Our findings suggest that UAV sprayers may be particularly well-suited for systemic or bait products that do not require extensive crop coverage for their efficacy. Moreover, in scenarios where spot spraying is necessary, UAV sprayers could prove valuable and efficient. Introducing UAV sprayers for systemic or bait PPPs, particularly in cases where ultra-low volume or spot spraying is effective, seems promising for reducing environmental exposure.

The findings presented in this work can be useful for quantifying the implications and the impact of the introduction of UAV sprayers in the Mediterranean agricultural environment and assessing the benefits of this technology to reduce the use and mitigate the consequences of plant protection product spraying. Introducing UAV sprayer technology might offer advantages in reducing the usage of PPPs and addressing their environmental impacts. However, further research is needed to fully understand how the spraying parameters affect the performance of UAV sprayers and to find ways of adapting UAV sprayers' swath width to the requirements of each crop.

Data availability statement

The raw data supporting the conclusions of this article will be made available by the authors, without undue reservation.

Author contributions

LS-F: Data curation, Formal analysis, Investigation, Methodology, Writing – original draft, Writing – review & editing. MB-B: Data curation, Investigation. JM-G: Conceptualization, Funding acquisition. MP-R: Funding acquisition, Investigation, Writing – original draft.

Funding

Acknowledgments

Conflict of interest

The authors declare that the research was conducted in the absence of any commercial or financial relationships that could be construed as a potential conflict of interest.

Publisher's note

All claims expressed in this article are solely those of the authors and do not necessarily represent those of their affiliated organizations, or those of the publisher, the editors and the reviewers. Any product that may be evaluated in this article, or claim that may be made by its manufacturer, is not guaranteed or endorsed by the publisher.

Supplementary material

The Supplementary Material for this article can be found online at: https://www.frontiersin.org/articles/10.3389/fpls.2023.1272372/full#supplementary-material

References

Ben Abdallah, S., Elfkih, S., Suárez-Rey, E. M., Parra-López, C., and Romero-Gámez, M. (2021). Evaluation of the environmental sustainability in the olive growing systems in Tunisia. *J. Clean Prod* 282. doi: 10.1016/j.jclepro.2020.124526

da Cunha, J. P. A. R., de Alvarenga, C. B., Rinaldi, P. C. N., Gregorio Marques, M., and Zampiroli, R. (2021). Use Of Remotely Piloted Aircrafts For The Application Of Plant Protection Products. *Engenharia Agricola* 41, 245–254. doi: 10.1590/1809-4430-eng.agric.v41n2p245-254/2021

Dengeru, Y., Ramasamy, K., Allimuthu, S., Balakrishnan, S., Kumar, A. P. M., Kannan, B., et al. (2022). Study on spray deposition and drift characteristics of UAV agricultural sprayer for application of insecticide in redgram crop (Cajanus cajan L. Millsp.). *Agronomy* 12. doi: 10.3390/agronomy12123196

Fisher, R. A. (1936). Design of experiments. *Br. Med. J.* 1, 554. doi: 10.1136/bmj.1.3923.554-a

Gil, E., Llorens, J., Gallart, M., Gil-Ribes, J. A., and Miranda-Fuentes, A. (2018). First attempts to obtain a reference drift curve for traditional olive grove's plantations following ISO 22866. *Sci. Total Environ.* 627, 349–360. doi: 10.1016/j.scitotenv.2018.01.229

Giles, D. K., and Billing, R. C. (2015). Deployment and performance of a uav for crop spraying. *Chem. Eng. Trans.* 44, 307–312. doi: 10.3303/CET1544052

Guo, S., Li, J., Yao, W., Zhan, Y., Li, Y., and Shi, Y. (2019). Distribution characteristics on droplet deposition of wind field vortex formed by multi-rotor UAV. *PloS One* 14. doi: 10.1371/journal.pone.0220024

He, X. K., Bonds, J., Herbst, A., and Langenakens, J. (2017). Recent development of unmanned aerial vehicle for plant protection in East Asia. *Int. J. Agric. Biol. Eng.* 10, 18–30. doi: 10.3965/j.ijabe.20171003.3248

Huang, Y., Hoffmann, W. C., Lan, Y., Wu, W., and Fritz, B. K. (2009). Development of a spray system for an unmanned aerial vehicle platform. *Appl. Eng. Agric.* 25, 803–809. doi: 10.13031/2013.29229

ISO 16122. (2015). *Agricultural and forestry machines - Inspection of sprayers in use* (Geneva, Switzerland: ISO Int Organ Stand). Available at: www.aenor.es.

ISO 22522. (2007). *Crop protection equipment - Field measurement of spray distribution in tree and bush crops* (Geneva, Switzerland: ISO Int Organ Stand).

ISO 22866. (2005). *Equipment for crop protection - Methods for field measurement of spray drift* (Geneva, Switzerland: ISO Int Organ Stand).

Kruskal, W. H., and Wallis, W. A. (1952). Use of ranks in one-criterion variance analysis. *J. Am. Stat. Assoc.* 47, 583–621. doi: 10.2307/2280779

Levene, H. (1960). Robust Tests for Equality of Variances. *Contributions to Probability Stat* (Palo Alto), 278–292.

Li, X., Giles, D. K., Niederholzer, F. J., Andaloro, J. T., Lang, E. B., and Watson, L. J. (2021). Evaluation of an unmanned aerial vehicle as a new method of pesticide application for almond crop protection. *Pest Manag Sci.* 77, 527–537. doi: 10.1002/ps.6052

Li, L., Hu, Z., Liu, Q., Yi, T., Han, P., Zhang, R., et al. (2022). Effect of flight velocity on droplet deposition and drift of combined pesticides sprayed using an unmanned aerial vehicle sprayer in a peach orchard. *Front. Plant Sci.* 13. doi: 10.3389/fpls.2022.981494

Lindell, C. A., Irish-Brown, A., Rothwell, N. L., and Wallis, A. E. (2023). Pest and disease risk and management in high-density perennial crops: Current knowledge and areas of future research. *Crop Prot.* 165. doi: 10.1016/j.cropro.2022.106150

Liu, Y., Li, L., Liu, Y., He, X., Song, J., Zeng, A., et al. (2020). Assessment of spray deposition and losses in an apple orchard with an unmanned agricultural aircraft system in China. *Trans. ASABE* 63, 619–627. doi: 10.13031/TRANS.13233

Martinez-Guanter, J., Agüera, P., Agüera, J., and Pérez-Ruiz, M. (2020). Spray and economics assessment of a UAV-based ultra-low-volume application in olive and citrus orchards. *Precis Agric.* 21, 226–243. doi: 10.1007/s11119-019-09665-7

Masson-Delmotte, V., Zhai, P., Pörtner, H.-O., Roberts, D., Skea, J., Shukla, P. R., et al. (2019). *Global warming of 1.5°C An IPCC Special Report on the impacts of global warming of 1.5°C above pre-industrial levels and related global greenhouse gas emission pathways, in the context of strengthening the global response to the threat of climate change, sustainable development, and efforts to eradicate poverty* (Cambridge, UK and New York, NY, USA: Science Officer Science Assistant Graphics Officer Working Group I Technical Support Unit). Available at: www.environmentalgraphiti.org. doi: 10.1017/9781009157940

R Core Team. (2022). *R: A language and environment for statistical computing.* Available at: https://www.R-project.org/.

Sánchez-Fernández, L., Barrera, M., Martínez-Guanter, J., and Pérez-Ruiz, M. (2023). Drift reduction in orchards through the use of an autonomous UAV system. *Comput. Electron Agric.* 211. doi: 10.1016/j.compag.2023.107981

Sarri, D., Martelloni, L., Rimediotti, M., Lisci, R., Lombardo, S., and Vieri, M. (2019). Testing a multi-rotor unmanned aerial vehicle for spray application in high slope terraced vineyard. *J. Agric. Eng.* 50, 38–47. doi: 10.4081/jae.2019.853

Searchinger, T. D., Wirsenius, S., Beringer, T., and Dumas, P. (2018). Assessing the efficiency of changes in land use for mitigating climate change. *Nature* 564, 249–253. doi: 10.1038/s41586-018-0757-z

Shapiro, S. S., and Wilk, M. B. (1965). An Analysis of Variance Test for Normality (Complete Samples). *Biometrika* 52, 591–611. doi: 10.2307/2333709

SIGPAC. (2021). "Agricultural plots geographical information system," (Government of Andalusia).

Tang, Q., Zhang, R., Chen, L., Xu, M., Yi, T., and Zhang, B. (2017). Droplets movement and deposition of an eight-rotor agricultural UAV in downwash flow field. *Int. J. Agric. Biol. Eng.* 10, 47–56. doi: 10.3965/j.ijabe.20171003.3075

Torrent, X., Garcerá, C., Moltó, E., Chueca, P., Abad, R., Grafulla, C., et al. (2017). Comparison between standard and drift reducing nozzles for pesticide application in citrus: Part I. Effects on wind tunnel and field spray drift. *Crop Prot.* 96, 130–143. doi: 10.1016/j.cropro.2017.02.001

United Nations. (2022). *World population prospects 2022: summary of results* (New York, USA: United Nations publication).

van de Zande, J. C., Michielsen, G. P., Stallinga, H., and van Velde, P. (2014). *International advances in pesticide application* (Wellesbourne, Warwick, UK: Association of Applied Biologists).

Vilar, J., Pereira, J. E., Ghedira, A., and Reyes, F. (2018). *INTERNATIONAL OLIVE GROWING worldwide analysis and summary* (Jaén, Spain: Fundación Caja Rural de Jaén).

Wang, C., Herbst, A., Zeng, A., Wongsuk, S., Qiao, B., Qi, P., et al. (2021). Assessment of spray deposition, drift and mass balance from unmanned aerial vehicle sprayer using an artificial vineyard. *Sci. Total Environ.* 777. doi: 10.1016/j.scitotenv.2021.146181

Wang, G., Li, X., Andaloro, J., Chen, P., Song, C., Shan, C., et al. (2018). Deposition and biological efficacy of UAV-based low-volume application in rice fields. *Int. J. Precis. Agric. Aviation* 1, 65–72. doi: 10.33440/j.ijpaa.20200302.86

Xiao, Q., Du, R., Yang, L., Han, X., Zhao, S., Zhang, G., et al. (2020). Comparison of droplet deposition control efficacy on phytophthora capsica and aphids in the processing pepper field of the unmanned aerial vehicle and knapsack sprayer. *Agronomy* 10. doi: 10.3390/agronomy10020215

Xue, X. Y., Tu, K., Qin, W. C., Lan, Y.B., and Zhang, H. H. (2014). Drift and deposition of ultra-low altitude and low volume application in paddy field. *Int. J. Agric. Biol. Eng.* 7, 23–28. doi: 10.3965/j.ijabe.20140704.003

Zhang, P., Deng, L., Lyu, Q., He, S. L., Yi, S. L., de Liu, Y., et al. (2016). Effects of citrus tree-shape and spraying height of small unmanned aerial vehicle on droplet distribution. *Int. J. Agric. Biol. Eng.* 9, 45–52. doi: 10.3965/j.ijabe.20160904.2178

Frontiers in
Plant Science

Cultivates the science of plant biology and its applications

The most cited plant science journal, which advances our understanding of plant biology for sustainable food security, functional ecosystems and human health.

Discover the latest Research Topics

See more →

frontiers | Research Topics